STUDY ON THE COUPLED FLOW, HEAT AND MASS TRANSFER PROCESSES IN A LIQUID DESICCANT DEHUMIDIFIER

LUO YIMO

Ph.D

The Hong Kong Polytechnic University

2014

The Hong Kong Polytechnic University

Department of Building Services Engineering

Study on the Coupled Flow, Heat and Mass Transfer Processes in a Liquid Desiccant Dehumidifier

Luo Yimo

A thesis submitted in partial fulfillment of the requirements for the Degree of Doctor of Philosophy

July, 2014

CERTIFICATE OF ORIGINALITY

I hereby declare that this thesis is my own work and that, to the best of my knowledge and belief, it reproduces no material previously published or written, nor material that has been accepted for the award of any other degree or diploma, except where due acknowledgement has been made in the text.

I also declare that the intellectual content of this thesis is the product of my own work, even though I may have received assistance from others on style, presentation and language expression.

_____(Signed)

_____Luo Yimo_____(Name of student)

Department of Building Services Engineering

The Hong Kong Polytechnic University

Hong Kong SAR, China

July, 2014

ABSTRACT

Abstract of thesis entitled: Study on the coupled flow, heat and mass transfer processes in a liquid desiccant dehumidifier

Submitted by: Luo Yimo

For the degree of: Doctor of Philosophy

At The Hong Kong Polytechnic University in July, 2014.

At present, a large amount of energy is needed to create a livable indoor environment. It is estimated that the buildings sector consumed 28% ~ 30% of the total final energy in China. Among all the power-driven equipment in buildings, chillers for air conditioning are well-known for their high power consumption in buildings. This study concentrates on solar energy based liquid desiccant air-conditioning to reduce latent cooling load of central air-conditioning systems. Due to the separate control of temperature and humidity, a liquid desiccant air conditioning system can save up to 40% of energy compared to a conventional vapor compression system. Thus, it has drawn more and more attention.

Even though many researches have been carried out about the dehumidifier by

simulation and experiment, there are still some limitations. It has been found that most of the previous researches focus on the macroscopic parameter changes of the fluids and the effect of various operating parameters. However, the flow situations and their impacts on heat and mass transfer in the dehumidifier interior are seldom studied. Therefore, this thesis aims to study the coupled flow, heat and mass transfer processes in a typical dehumidifier numerically and experimentally.

Firstly, numerical predictions were conducted to investigate the flow dynamics in the liquid desiccant dehumidifier with the CFD software Fluent. The developed model was validated by existing data from literatures. With the model, the mechanism of the gas-liquid flow in the dehumidifier was illustrated. The velocity profiles, the minimum wetting rate, the effective interfacial areas between the solution and air, the average and local film thickness at different conditions were investigated. Based on the calculation results, it was concluded that the simulation model could predicate the dynamic and local flow conditions in the dehumidifier interior microscopically. It was found that the counter-flow air did change the velocity profile of the LiCl solution along the film thickness due to the drag force. And when the air inlet velocity reached 3.0 m s^{-1}, the impact became very distinct. Under that situation, the air became the dominated factor to decide the velocity field at the interface. Meanwhile, the importance of a suitable solution and air flow rates could be highlighted. The results also explained the reason of the enhancement of mass transfer with film flow.

Then, by adding suitable sources files to Fluent, the coupled flow, heat and mass transfer processes were described comprehensively. In the model, the effect of the velocity field on the heat and mass transfer process has been considered. Meanwhile, the variable physical properties of the desiccant and air, which were taken as constant in almost all existing models, render the simulation more in line with real conditions. In addition, the penetration mass transfer theory was employed to make it possible to observe the dynamic process in the dehumidifier interior. With the established model, the parametric studies were conducted in a range of different flow conditions. Through the simulation, it was found that the air velocity played a critical role on the performance of the dehumidifier, which had to be matched with the channel geometric size for optimization. Besides, titling the plate to keep certain mass transfer gradient in the channel was also essential. Meanwhile, the coupled flow, heat and mass transfer phenomenon was also analyzed.

Secondly, to investigate the hydrodynamics of falling film in the dehumidifier experimentally, the film thickness was measured by a capacitance probe and the flow morphology was captured by a camera. The wetting area under different solution flow rates and plate surface temperatures were investigated. It was found that the minimum solution flow rate to prevent the breakout of the falling film was 0.068 kg m^{-1} s^{-1}, which was of the same order of magnitude of the simulation results (0.071 kg

m^{-1} s^{-1}). The local and temporal film thicknesses under different air velocities were recorded and analyzed for both the upper and lower parts of the falling film. The results showed that the wave was intensified along the flow direction, which also agreed well with the simulation results. In addition, the influence of the air velocity on the film thickness was also investigated. The average film thicknesses were calculated and compared with those of the Nusselt empirical formula. It was found that the Nusselt empirical formula underestimated the film thicknesses in present condition. In addition, the pattern and shape of the typical film flow were presented in the thesis.

Experiments were also designed to investigate the real dehumidification process in a single channel internally-cooled dehumidifier. The absolute humidity change and overall mass transfer coefficient were chosen as the indices to evaluate the performance of the dehumidifier. The influences of various parameters were analyzed in depth. It was found that the overall mass transfer coefficient was higher than that reported in the previous literature due to much higher humidity of the inlet air in the present work. The result fully demonstrated the feasibility and advantages of adopting liquid desiccant dehumidification in Hong Kong. The increase of air velocity in the dehumidifier resulted in the increase of the overall mass transfer coefficient and yet the decrease of the absolute humidity change. The experimental results showed the same tendency with those of the simulation model, which verified

the correctness of employing the penetration mass transfer theory.

Academically, the numerical research provides a novel simulation model to predict the coupled flow, heat and mass transfer processes in a liquid desiccant dehumidifier in this thesis. The model considered the effect of the flow and the variable physical properties of the fluids on the dehumidification process, and enabled the dynamic observation by adopting the penetration mass transfer theory. Secondly, a single channel experimental setup was fabricated to investigate the performance of the dehumidifier. The hydrodynamics of the falling film was studied by investigating the local and temporal film thickness and the flow patterns. Then the effects of various parameters on the performance of the dehumidifier were analyzed in depth. The experimental results verified the correctness of the simulation model to some extent. Thus, the engineers and researchers can employ the model to predict the wetting situation, optimize the operation conditions and design dehumidifiers.

Keywords: flow dynamic; heat and mass transfer; velocity profile; coverage ratio; minimum wetting rate; film thickness; absolute humidity change, mass transfer coefficient; simulation model; experiment method; liquid desiccant dehumidifier

PUBLICATIONS DURING PHD STUDY

Journal papers:

[1] Yimo Luo, Hongxing Yang, Lin Lu. Dynamic and microscopic simulation of the counter-current flow in a liquid desiccant dehumidifier. Applied Energy (in press).

[2] Yimo Luo, Shuangquan Shao, Hongbo Xu, Changqing Tian, Hongxing Yang. Experimental and theoretical research of a fin-tube type internally-cooled liquid desiccant dehumidifier. Applied Energy 133 (2014) 127-34.

[3] Yimo Luo, Hongxing Yang, Lin Lu. Liquid desiccant dehumidifier: development of a new performance predication model based on CFD. International Journal of Heat and Mass Transfer 69 (2014) 408-16.

[4] Yimo Luo, Hongxing Yang, Lin Lu, Ronghui Qi. A review of the mathematical models for predicting the heat and mass transfer process in the liquid desiccant dehumidifier. Renewable and Sustainable Energy Reviews 31 (2014) 587-99.

[5] Yimo Luo, Shuangquan Shao, Fei Qin, Changqing Tian, Hongxing Yang. Investigation on feasibility of ionic liquids used in solar liquid desiccant air conditioning system. Solar Energy 86 (9) (2012) 2718-24.

Conference papers:

[1] Yimo Luo, Shuangquan Shao, Changqing Tian, Hongxing Yang. Investigation of the surface vapor pressure of [DMIM]OAC aqueous solution for solar assisted liquid desiccant dehumidification. Grand Renewable Energy 2014 International Conference and Exhibition July 27-August 1, 2014, Tokyo, Japan.

[2] Yimo Luo, Hongxing Yang, Lin Lu. CFD simulation of the liquid flow on structured packing in the liquid desiccant dehumidifier. The 6th International Conference on Applied Energy, May 30- June 2, 2014, Taipei, Taiwan.

[3] Yi Chen, Yimo Luo, Hongxing Yang. Fresh air pre-cooling and energy recovery by using indirect evaporative cooling in hot and humid region – a case study in Hong Kong. The 6th International Conference on Applied Energy, May 30- June 2, 2014, Taipei, Taiwan.

[4] Yimo Luo, Shuangquan Shao, Hongbo Xu, Changqing Tian, Hongxing Yang. Experimental research of a fin-tube type internally-cooled liquid desiccant dehumidifier. The 12th International Conference on Sustainable Energy technologies, August 26-29th, 2013, Hong Kong, China.

[5] Yimo Luo, Hongxing Yang, Lin Lu. Microscopic simulation of the flow and mass transfer processes in a liquid desiccant dehumidifier. The 5th International Conference on Applied Energy, July 1-4, 2013, Pretoria, South Africa.

[6] Ronghui Qi, Lin Lu, Hongxing Yang, Yimo Luo. Investigation on contact angle of LiCl for liquid desiccant air-conditioning system. The 5th International Conference on Applied Energy 2013, Pretoria, South Africa.

ACKNOWLEDGEMENT

This thesis would never have been possible without my hard work and the help and support from many people.

First and foremost, I would like to express my deepest appreciation and gratitude to my chief supervisor, Prof. Yang Hongxing. During my pursuing of the doctoral degree, he gave me valuable advices, continued encouragement and generous supports. Without him, it was impossible for me to complete the thesis. What's more, his optimism and friendly personality also set an example for my life-long learning.

My special appreciation is also devoted to my co-supervisor, Dr. Lu Lin, for her insightful view and great help on my research and life.

My sincerest gratitude also goes to Dr. Timothy Shedd, who helped me a lot and gave me many valuable instructions on my research when I worked with him in the Multiphase Visualization and Analysis Laboratory at The University of Wisconsin, Madison for a student attachment program.

Furthermore, I would like to express my thanks to all the members in the Renewable Energy Research Group for their help during the PhD study. In particular, I'm deeply indebted to Mr. Wang Meng and Mr. Peng Jinqing for their help with the installation of the test rig and valuable suggestions about the experiment. The advice of Dr. Qi Ronghui is also appreciated. Meanwhile, I have to thank Gong Ming, the Product Manager of Beijing Hi-key Tech Co. Ltd, for his guidance on the simulation work. Moreover, I would like to give my appreciation to the staffs and the technicians from the Department of Building Services Engineering and Industrial Center of The Hong Kong Polytechnic University.

In addition, The Hong Kong Polytechnic University and Hong Kong SAR Government are appreciated for funding my study with the Hong Kong PhD Fellowship. Without the financial support, it would not be possible to complete my PhD study in Hong Kong.

Finally, I would like to give my special thanks to my beloved parents, Mr. Luo Longhua and Ms. Yu Lihua, for their sacrifice for me without expecting any return. I also would like to thank my parents-in-law, and especially my husband Mr. Jin Qiyan. Without their considerate supports and deep love, it is impossible for me to accomplish my PhD study.

TABLE OF CONTENTS

CERTIFICATE OF ORIGINALITY I

ABSTRACT II

PUBLICATIONS DURING PHD STUDY VII

ACKNOWLEDGEMENT X

TABLE OF CONTENTS XII

LIST OF FIGURES XVIII

LIST OF TABLES XXIV

NOMENCLATURE XXV

CHAPTER 1 1

INTRODUCTION 1

1.1 Background of building energy consumption 1

1.2 Introduction of liquid desiccant dehumidification 2

1.3 Objective of the thesis 4

1.4 Organization of the thesis 7

CHAPTER 2 10

LITERATURE REVIEW AND RESEARCH METHODOLOGY 10

2.1 Introduction 10

2.2 Review of existing simulation models 11
2.2.1 Models for adiabatic dehumidifier 12
2.2.2 Models for internally cooled dehumidifier 31
2.3 Review of experiment research 47
2.4 Limitations in the past studies 49
2.4.1 Limitations of simulation models 49
2.4.2 Limitations of experimental research 51
2.5 Review of simulation studies based on CFD 52
2.6 Review of interface tracking methods 56
2.7 Review of mass transfer theories 59
2.7.1 Film theory 60
2.7.2 Penetration theory 62
2.7.3 Surface renewal theory 63
2.8 Review of methods for film thickness measurement 64
2.8.1 Electrical resistance method 64
2.8.2 Electrical capacitance method 65
2.8.3 Laser focus displacement (LFD) sensor measurement 68
2.9 Research methodology of present work 70
CHAPTER 3 74
NUMERICAL SIMULATION OF THE FLOW CHARACTERISTICS 74
3.1 Introduction 74

3.2 Physical model 76
3.3 Mathematical model 77
3.3.1 Governing equations 77
3.3.2 Initial and boundary conditions 81
3.3.3 Meshing and solution scheme 82
3.3.4 Physical properties of the desiccant 84
3.4 Results for the flat plate 85
3.4.1 Validity of the model 85
3.4.2 Velocity profile 88
3.4.3 Minimum wetting rate 91
3.4.4 Interfacial area 95
3.4.5 Film thickness 97
3.5 Results for the corrugated plate 99
3.5.1 Minimum wetting rate 99
3.5.2 Surface axial velocity 99
3.5.3 Surface radial velocity 102
3.5.4 Surface shape under different liquid velocity 103
3.6 Summary 104
CHAPTER 4 108
NUMERICAL SIMULATION OF THE COUPLED FLOW, HEAT AND MASS TRANSFER PROCESSES 108

4.1 Introduction 108
4.2 Physical model 110
4.3 Mathematical model 110
4.3.1 Governing equations 111
4.3.2 Initial and boundary conditions 114
4.3.3 Simulation strategy 114
4.3.4 Physical properties of the fluids 116
4.4 Validity of the model 116
4.4.1 Grid independence study 116
4.4.2 Mass transfer 118
4.5 Results and discussion 119
4.5.1 Example of dynamic description 120
4.5.2 Influence of air velocity 121
4.5.3 Influence of inlet air water concentration 125
4.5.4 Influence of inlet desiccant concentration 127
4.5.5 Influence of inlet desiccant temperature 128
4.5.6 Influence of inlet solution flow rate 132
4.5.7 Influence of internal cooling 134
4.5.8 Influence of variable physical properties 138
4.6 Summary 139
CHAPTER 5 143

EXPERIMENTAL STUDY OF THE FLOW CHARACTERISTICS 143

5.1 Introduction 143

5.2 Description of the test rig and research method 145

5.3 Results and discussion 150

5.3.1 Flow morphology 150

5.3.2 Coverage ratio 152

5.3.3 Minimum wetting rate 155

5.3.4 Film thickness 160

5.4 Summary 175

CHAPTER 6 179

EXPERIMENTAL STUDY OF DEHUMIDIFICATION PERFORMANCE: INTENSIVE ANALYSIS OF INFLUENCING FACTORS 179

6.1 Introduction 179

6.2 Description of experimental bench 180

6.3 Control and measurement instruments 183

6.4 Performance indices and error analysis 187

6.5 Results and discussion 190

6.5.1 Mass and energy conservation analysis 190

6.5.2 Influence of air inlet parameters 193

6.5.3 Influence of solution inlet parameters 198

6.5.4 Influence of cooling water 205

6.6 Summary 207

CHAPTER 7 211

CONCLUSIONS AND RECOMMENDATIONS FOR FUTURE WORK 211

7.1 Conclusions of numerical study 211

7.2 Conclusions of experimental investigation 214

7.3 Comparison of numerical and experimental studies 218

7.4 Recommendations for future research 220

REFERENCES 222

LIST OF FIGURES

Fig. 1.1 Hong Kong's breakdown of electric energy usage in a commercial building (2011) 2

Fig. 1.2 Hong Kong's breakdown of electric energy usage in a residential building (2011) 2

Fig. 2.1 The structure diagram of two dehumidifiers 12

Fig. 2.2 Heat and moisture exchange model in the countercurrent adiabatic dehumidifier 13

Fig. 2.3 Calculation flow chart of the countercurrent pattern 15

Fig. 2.4 Schematic of the cross flow dehumidifier/regenerator 18

Fig. 2.5 A two dimensional schematic of the cross flow dehumidifier/regenerator ... 19

Fig. 2.6 Heat and moisture exchange model in the internally cooled dehumidifier .. 32

Fig. 2.7 Schematic diagram of the cross-flow type plate heat exchanger 33

Fig. 2.8 Schematic diagram of the control volumes considered: (a) primary air-solution; (b) secondary air-water 34

Fig. 2.9 Schematic diagram of the control volume for a counter-flow internally cooled dehumidifier 36

Fig. 2.10 Schematic diagram of control volume for a three-dimensional model.....39

Fig. 2.11 Schematic diagram of control volume for a two-dimensional model.....42

Fig. 2.12 Interface construction schemes: (a) real interface location, (b) donor-acceptor scheme, and (c) geometric reconstruction (PLIC) scheme 59

Fig. 2.13 Schematic diagram of two-film theory 61

Fig. 2.14 Schematic diagram of penetration theory 63

Fig. 2.15 Concept of film thickness measurement technique 64

Fig. 2.16 Sketch of the circuitry.....66

Fig. 2.17 Sketch of the calibration 68

Fig. 2.18 A schematic diagram of an LFD 70

Fig. 2.19 Flow chart of methodology.....73

Fig. 3.1 Schematic of the simplified physical model 76

Fig. 3.2 Sketch map of computational grids 83

Fig. 3.3 Convergence history of velocity at one point in the liquid film 83

Fig. 3.4 Interfacial velocity magnitude with four types of grid 86

Fig. 3.5 Interfacial average velocity magnitude with four types of grids 86

Fig. 3.6 Comparison of liquid film thickness between simulation and Nusselt empirical formula.....87

Fig. 3.7 The comparison between the work with the literature.....88

Fig. 3.8 Velocity profile of LiCl solution along the x axis (y=75mm).....89

Fig. 3.9 Velocity profile of air along the x axis (y=75mm).....90

Fig. 3.10 Stages of film formation during solution flow.....94

Fig. 3.11 Stages of film formation during solution flow on a flat plate (Operating condition No. 7) 95

Fig. 3.12 The ratio of the interfacial area to the geometrical plate surface under different liquid flow rates (u_a=6.0 m s^{-1}).....96

Fig. 3.13 Average film thickness at different LiCl solution flow rates 97

Fig. 3.14 Liquid film thickness profiles at different LiCl solution flow rate.....98

Fig. 3.15 Film thickness *Vs* Axial velocity 101

Fig. 3.16 Film thickness *Vs* Radical velocity.....103

Fig. 3.17 Film shape on the corrugated plate under different liquid flow rate 104

Fig. 4.1 Convergence history of mass fraction of water vapor in outlet air.....114

Fig. 4.2 Convergence history of outlet air temperature 115

Fig. 4.3 Air conditions at the gas outlet with four types of grid 117

Fig. 4.4 Comparison of water vapor concentration of outlet air 119

Fig. 4.5 Stages of film formation and mass transfer in the dehumidifier.....120

Fig. 4.6 Outlet air condition under different inlet air velocity 121

Fig. 4.7 Contour of mass fraction of water vapor under different inlet air velocity 123

Fig. 4.8 Contour of temperature under different inlet air velocity.....124

Fig. 4.9 Contour of mass fraction of water vapor under different water vapor fractions of inlet air 125

Fig. 4.10 Gradient of mass fraction of water vapor at y=0.075m in a range of water

vapor fractions of inlet air 126

Fig. 4.11 Gradient of mass fraction of water vapor at different y values ($x_{a,in}$ =0.020) 127

Fig. 4.12 Liquid film thickness profiles for various inlet desiccant concentrations 128

Fig. 4.13 Mass fraction of water vapor and temperature of outlet air under different inlet desiccant temperature 130

Fig. 4.14 Contour of temperature under different inlet desiccant temperature 131

Fig. 4.15 Interfacial temperature along the liquid flow direction 131

Fig. 4.16 Interfacial average velocity magnitudes under different inlet desiccant temperature 132

Fig. 4.17 Mass fraction of water vapor and temperature of outlet air under different inlet solution flow rate 133

Fig. 4.18 Contours of temperature and mass fraction of water vapor 134

Fig. 4.19 Interface temperature along the flow direction under different heat flux . 135

Fig. 4.20 Temperature of liquid phase under different heat flux 136

Fig. 4.21 Water content in the outlet under different heat flux 137

Fig. 4.22 The profile of interfacial solution concentration along the film flow 139

Fig. 5.1 Sketch of the film flow test: front view and cross section view 145

Fig. 5.2 A sketch of three kinds of solution distributors 146

Fig. 5.3 Picture of calibration devices 147

Fig. 5.4 Calibration curve for the capacitance probe 149

Fig. 5.5 Image of waves occurring on the falling film at Re=66.2 150

Fig. 5.6 Structure of solitary wave 152

Fig. 5.7 Coverage ratios under different surface conditions (T_s=294.8 K) 153

Fig. 5.8 Real pictures of the film flow under different surface conditions 154

Fig. 5.9 Real picture of the breakout of the film flow.....156

Fig. 5.10 Minimum wetting rate of LiCl solution.....158

Fig. 5.11 Viscosity of LiCl solution 158

Fig. 5.12 Comparison between the results of the present experiment and Hartley's empirical formula 160

Fig. 5.13 Mean film thickness under different Reynolds number.....164

Fig. 5.14 Mean film thickness under different air velocity.....166

Fig. 5.15 Mean film thickness of two locations under different air velocity 167

Fig. 5.16 Distinction of mean film thickness between the lower and upper part.....168

Fig. 5.17 Variations of film thickness 169

Fig. 5.18 Temporal film thickness of two different locations 170

Fig. 5.19 Probability density of film thickness with different solution flow rate, u_a=0 172

Fig. 5.20 Probability density of film thickness with different air velocity, Γ_s=0.12 kg m^{-1} s^{-1}.....173

Fig. 5.21 Surface wave velocity with different solution flow rate.....174

Fig. 5.22 Surface wave velocity with different air velocity.....174

Fig. 6.1 Schematic diagram of the single channel liquid desiccant dehumidifier....181

Fig. 6.2 Real picture of the test rig....182

Fig. 6.3 Control devices....183

Fig. 6.4 The appearance of the main test part....184

Fig. 6.5 Measurement devices....187

Fig. 6.6 The meteorological condition within one year in Hong Kong....190

Fig. 6.7 Energy balance of the experiment....192

Fig. 6.8 Effect of air temperature and humidity....195

Fig. 6.9 Effect of air flow rate....197

Fig. 6.10 The effect of solution mass flow rate....199

Fig. 6.11 The effect of solution temperature....202

Fig. 6.12 The surface vapor pressure of the solution under different temperature ..202

Fig. 6.13 The effect of solution concentration....204

Fig. 6.14 Dynamic viscosity with different mass concentration....205

Fig. 6.15 The effect of cooling water temperature....206

LIST OF TABLES

Table 2.1 Comparison of the mathematical models for adiabatic dehumidifier 29

Table 2.2 Detail information of the mathematical models for adiabatic dehumidifier 30

Table 2.3 Detail information of the mathematical models for internally cooled dehumidifier 46

Table 2.4 The introduction of four free boundary methods 57

Table 3.1 Properties of LiCl solution (300 K and 30 % mass concentration).....84

Table 3.2 Wetting situation under different conditions 92

Table 4.1 Summary of calculating conditions.....120

Table 5.1 Relations for mean film thickness based on experiment for tubes ($Re < 1000 - 2000$) (Yu et al. 2012) 162

Table 6.1 Specification of different measuring devices 185

Table 6.2 Summary of the ranges of various parameters 191

NOMENCLATURE

A	specific surface area per unit volume [m^{-1}] or area [m^2]
A_{all}	overall area of the plate [m^2]
A_p	coverage ratio
A_{wet}	wetting area [m^2]
C_p	specific heat [J kg^{-1} K^{-1}]
C_S	standard capacitance [F]
C_{sat}	saturation specific heat [J kg^{-1} K^{-1}]
C_T	parallel plate capacitance [F]
$C_{1\varepsilon}$, $C_{2\varepsilon}$, $C_{3\varepsilon}$	constants
Ca	capillary number [dimensionless]
d_h	hydraulic diameter [m]
D_m	mass diffusion coefficient [m^2 s^{-1}]
D_t	thermal diffusivity [m^2 s^{-1}]
E	energy [J kg^{-1}]
$\boldsymbol{F}$	source term in the momentum equation [N m^{-3}]
F_{ST}	source term due to surface tension [N m^{-3}]
$\boldsymbol{g}$, g	acceleration due to gravity [m s^{-2}]
G	specific mass flow rate [kg m^{-2} s^{-1}]
G'	mass flow rate [kg s^{-1}]

G_k	the generation of turbulence kinetic energy due to the mean velocity gradients [kg m^{-1} s^{-3}]
G_b	the generation of turbulence kinetic energy due to buoyancy [kg m^{-1} s^{-3}]
h	sensible enthalpy [J kg^{-1}] or the distance between the probe and the object [m]
h_e	enthalpy of humid air in equilibrium with liquid desiccant [kJ kg^{-1}]
$h_{e,eff}$	effective saturation enthalpy [kJ kg^{-1}]
h_m	local mass transfer coefficient [kg m^{-2} s^{-1}]
H	height of the dehumidifier [m]
H_{lg}	latent heat of evaporation [J kg^{-1}]
J	mass flux [kg m^{-3} s^{-1}]
k	thermal conductivity [W m^{-1} K^{-1}] or turbulence kinetic energy [m^2 s^{-2}]
K	local overall mass transfer coefficient [kg m^{-2} s^{-1}]
l	liquid flow distance [m]
L	length of the dehumidifier [m]
Le	Lewis number [dimensionless]
m	water condensation rate [g s^{-1}] or per unit cross-sectional area [g m^{-2} s^{-1}] or the number of the species
m^*	capacity ratio similar to the one used in sensible heat exchangers
M	molecular weight [g mol^{-1}]

n	the number of the phases
$\hat{n}$	the divergence of the unit normal
$\hat{n}_w$, $\hat{m}_w$	the unit vectors normal to and tangential to the wall
NTU	number of transfer units
Nu	Nusselt number [dimensionless]
P	pressure [Pa]
$P_{l,b}$, P_a	the partial vapor pressure of the bulk desiccant solution, the atmospheric pressure (Pa) or the partial vapor pressure in air [Pa]
P_s	partial vapor pressure over the solution [Pa] or duct static pressure
P_t	total pressure [Pa]
$\bar{P}$	dimensionless vapor pressure difference ratio
P_v	velocity pressure [Pa]
Q	heat transferred from solution to water [kW m^{-1}]
Re	Reynolds number [dimensionless]
R_ε	additional term [kg m^{-1} s^{-3}]
s	surface replacement rate or cross section of the probe [m^2]
S_E	source term in the energy equation [W m^{-3}]
S_{lg}	mass transfer source at the phase interface [kg m^{-3}]
S_k, S_ε	user-defined source terms [kg m^{-1} s^{-3}]
t	time [s]
t_c	contact time [s]
$\bar{T}$	dimensionless temperature difference ratio
T	temperature [K]
$\boldsymbol{u}$, u	velocity vector [ms^{-1}]

u_{surf}	surface velocity of the liquid film [m s^{-1}]
V	volume [m^3] or the output voltage [V]
V_S	source voltage [V]
W	humidity ratio [kg H_2O kg^{-1} dry air] or the width the dehumidifier [m]
We	Weber number [dimensionless]
W_e	humidity ratio of humid air in equilibrium with liquid desiccant [kmol H_2O $kmol^{-1}$ dry air]
$W_{e,eff}$	effective humidity ratio [kmol H_2O $kmol^{-1}$ air]
$W_{g,b}$, $W_{g,e}$	the humidity ratio of the bulk air and the equilibrium air humidity ratio to the desiccant solution [kg kg^{-1}]
x_a	mass fraction of water vapor in the moist air
x	coordinate axis
$x_{k,q}$	mass fraction of the species k in the q^{th} phase
X	desiccant concentration [kg desiccant kg^{-1} solution]
X_v	concentration of water vapor in air [kg H_2O kg^{-1} air]
X_w	concentration of water in solution [kg water kg^{-1} solution]
Y_M	the contribution of the fluctuating dilatation in compressible turbulence to the overall dissipation rate [kg m^{-1} s^{-3}]

Greek characters

α	the volume fraction of phases
α_C	heat transfer coefficient [W m^{-2} K^{-1}]
α_C'	heat transfer coefficient corrected for simultaneous mass and heat transfer [W m^{-2} K^{-1}]
α_D	mass transfer coefficient [kg m^{-2} s^{-1}]

α'_D	molar mass transfer coefficient [$k\,mol\,m^{-2}\,s^{-1}$]
α^*_D	mass transfer coefficient [m s^{-1}]
α_k , α_ε	the inverse effective Prandtl numbers for k and ε, respectively
δ	film thickness [m]
$\overline{\delta}$	average film thickness [m]
μ	dynamic viscosity [kg m^{-1} s^{-1}]
υ	kinetic viscosity [$m^2\,s^{-1}$]
ρ	density [kg m^{-3}]
σ	surface tension coefficient [$N\,m^{-1}$]
κ	curvature of free surface
ψ	concentration difference ratio
θ_w	the angle between the wall and the tangent to the interface at the wall [$^\circ$]
$\Gamma_{k,q}$	diffusion coefficient of the species k in the q^{th} phase [m^2 s^{-1}]
Γ	mass flow rate [kg m^{-1} s^{-1}]
ε	dissipation rate of turbulence kinetic energy or air side effectiveness
ε_{HE}	heat exchanger effectiveness
ε_o	permittivity of the medium [F m^{-1}]
Δ	change of or difference between parameters
ϑ	dimensionless temperatures $(T-T_r)/\bar{h}$
λ	latent heat of vaporization [kJ kg^{-1}]

Subscripts

a	air
c	critical
eff	effective
f	cooling fluid, like water, air, refrigerant

g	gas phase
i	inlet
i, j	signal of coordinate axis
int	interface
k	the k^{th} species
l	liquid phase or lower part
min	minimum
o	outlet
p	primary air
plate	plate
q	the q^{th} phase
r	secondary (return air)
s	solution
T	turbulence
u	upper part
v	water vapor
w	water

CHAPTER 1

INTRODUCTION

1.1 Background of building energy consumption

At present, a large amount of energy is needed to create a livable indoor environment. It is estimated that the buildings sector consumed 28% ~ 30% of the total final energy in China (China Energy Statistical Yearbook 2013). Especially in Hong Kong, about 90% of total electricity consumption is contributed by buildings as there are very few industrial sectors (http://www.beeo.emsd.gov.hk/en/mibec_beeo.html).

Among all of the power-driven equipment in buildings, the air conditioning system is well-known for its high power consumption. As shown in Fig. 1.1 and 1.2 (Hong Kong Energy End-use Data 2013), the energy consumption for air conditioning takes up about 54% and 23% of the total building's energy consumption in Hong Kong's typical office buildings and residential buildings, respectively, which are sizable. With the acceleration of urbanization and improvement of people's living standard, it is expected that more energy will be required for the air conditioning to keep a comfortable indoor environment.

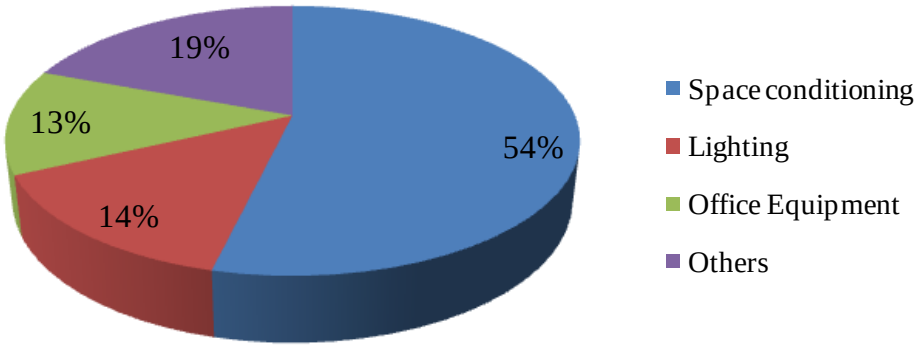

Fig. 1.1 Hong Kong's breakdown of electric energy usage in a commercial building (2011)

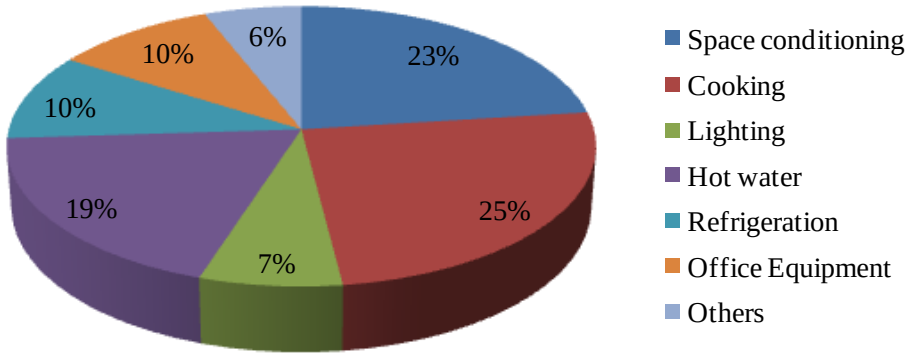

Fig. 1.2 Hong Kong's breakdown of electric energy usage in a residential building (2011)

1.2 Introduction of liquid desiccant dehumidification

Traditional air conditioning systems are notorious as a result of heavy dependence on electric power, limited ability of humidity control, occurrence of wet surface for breeding mildew and bacteria and so on (Oberg and Goswami 1998a). In a moist region like Hong Kong, these problems become even more serious. Thus, to reduce

the energy consumption in buildings and improve the indoor air quality, the desiccant air conditioning system has drawn more and more attention. There are several reasons for its popularity. One is its energy saving due to the separate control of humidity and temperature (Potnis and Lenz 1996). According to the literatures, compared with conventional vapor compression, a desiccant air conditioning system can save up to 40% energy (Oberg and Goswami 1998b). The second reason is that the system could operate under a relatively low regeneration temperature, between 60 and 75 ℃. It means the system can be driven by low-grade thermal energy resources, such as geothermal energy, solar energy, and waste heat (Xie et al. 2008), so as to reduce fossil fuel consumption. In addition, thanks to its independent temperature and humidity control, it can get rid of water condensation and therefore reduce the wet surfaces which are the breeding ground for bacteria and mildew (Jiang and Li 2002).

In light of the state of the desiccant, desiccant air conditioning systems can be divided into two types, which are the liquid desiccant and solid desiccant air conditioning systems. Compared with a solid desiccant system, a liquid desiccant air conditioning system has the following advantages (Xie et al. 2008): 1) due to the fluidness of the liquid desiccants, it is easier to remove the latent heat so as to reduce the irreversible loss; 2) it has more potential of storing chemical energy; 3) it can improve the air quality by absorbing the dust, bacteria, VOC and so on. Thus, the liquid desiccant air conditioning system can be a potential assistance of the traditional vapor compression

air conditioning system.

1.3 Objective of the thesis

The major component of interest in the liquid desiccant air conditioning system is the dehumidifier or the regenerator. On account of the same principle of the two components, the dehumidifier is supposed to be investigated to provide meaningful information. As the dehumidifier is an absorber, where complicated heat and mass transfer processes take place, its performance depends greatly on the heat and mass transfer processes. Thus, the design and operation of the dehumidifier can be optimized by having more comprehensive knowledge of the processes.

Previous researches of the dehumidifier are summarized in Chapter 2. In terms of the simulation models, it has been found that most of the models focus on the macroscopic parameter change of the air and desiccant solution. In addition, lots of assumptions are made to launch the calculation, which is inappropriate sometimes. As for the experiments, the effect of various operating parameters on the performance of the dehumidifier has been analyzed experimentally. The factors include the desiccant fluid properties, the packing type, the flow configuration, the desiccant distribution, the inlet flow rate and condition of the desiccant solution, moist air and cooling media, energy story capacity and so on. However, the flow situations and their impacts on

heat and mass transfer in the dehumidifier interior are seldom observed experimentally. Also, the structures of most of the dehumidifiers are complicated, resulting in big discrepancy between estimated and the real contact areas.

Therefore, the aim of this research is to study the coupled flow, heat and mass transfer process in the liquid desiccant dehumidifier. The main objectives of the project are summarized as follows:

1) To establish two-dimensional transient model to simulate the flow process in the dehumidifier with Computational Fluid Dynamics (CFD) software FLUENT. The desiccant solution flow will be calculated regarding the impacts of gravity, viscosity and surface tension. The mechanism of the gas-liquid flow in the dehumidifier will be illustrated based on the simulation results.

2) To complete the above two-dimensional model by adding suitable heat and mass transfer sources, with which the coupled flow, heat and mass transfer process in the dehumidifier will be described comprehensively. In this way, the effect of the velocity field on the heat and mass transfer process will be incorporated in the model.

3) In order to make it possible to observe the dynamic heat and mass transfer process

in the dehumidifier interior, the penetration mass transfer theory will be employed for the developed simulation model.

4) To render the simulation more in line with real conditions, the real-time changed physical properties of the desiccant and air, which were taken as constant in almost all existing models, will be integrated into the model.

5) A single channel test rig will be established for studying the flow characteristics of the film in the dehumidifier experimentally. In particular, one of the most critical parameters for heat and mass transfer- the film thickness will be measured by an advanced capacitance probe in the present work.

6) By experimental approach, different cases will be measured to reveal the influence of different parameters on the dehumidification performance. These factors, including the inlet air humidity, air temperature, air flow rate, solution concentration, solution temperature, solution flow rate and cooling water temperature, will be analyzed and discussed with the consideration of the flow conditions during the experiment.

1.4 Organization of the thesis

In the first chapter, the background of the building energy consumption is introduced, especially the energy consumption of air conditioning system. As a possible partial substitution of the popular vapor compression air conditioner, the advantages of the liquid desiccant air conditioning system are summarized. The core component, the dehumidifier, is the research target of the thesis. To understand more about the dehumidifier, the general objective is to develop efficient and robust computational and experimental methods/models to study the coupled flow, heat and mass transfer process in the dehumidifier.

Chapter 2 starts with a comprehensive literature review of the simulation and experimental research of the dehumidifier. Based on the summarization, the limitations of previous work are concluded. Then associated models and methods are introduced, including the simulation studies based on CFD, the interface tracking methods, mass transfer theories, and film thickness measurement methods. Then suitable research methodologies are chosen for investigating the unknown area of previous work, especially the flow behavior in a typical dehumidifier.

Chapter 3 focuses on studying the flow dynamics in the liquid desiccant dehumidifier microscopically and dynamically with the CFD software Fluent. The simplified physical model is introduced first. Then the specific simulation method is explained,

including the governing equations, initial and boundary conditions, meshing and solution scheme and physical properties of the desiccant. The model is verified by comparing the calculation results with the Nusselt empirical equations in terms of the film thickness. With the established model, the mechanism of the gas-liquid flow in the dehumidifier will be illustrated. The velocity profiles, the minimum liquid flow rates for wetting the whole surface, the effective interfacial areas between the solution and air, the average and local film thickness at different conditions will be investigated.

Chapter 4 will improve the model proposed in Chapter 3 by adding suitable sources to simulate the coupled flow, heat and mass transfer processes in the dehumidifier. Firstly, the additional information of the mathematical model is given. Before simulation, the model is verified by comparing the results with those of the hand-written program of the finite difference model. With the model, the dynamic process of dehumidification can be described. The dynamic distribution of various parameters in the dehumidifier will be obtained. The effects of various inlet parameters and internally cooling on the dehumidification performance will also be analyzed with the observation of the distribution of various parameters.

Chapter 5 aims to study the flow behavior in a single channel dehumidifier experimentally. The research method is introduced first. With the instruments, the

flow morphology is captured for the solution flow, the coverage ratio is calculated under different conditions of the test surface, and the minimum wetting rate is investigated as well. Most importantly, the temporal film thickness is measured and analyzed, based on which the mean film thicknesses will be calculated. By analysis, the experimental results can validate the correctness of the simulation model in Chapter 3 to some extent.

Chapter 6 investigates the coupled flow, heat and mass transfer performance of the above single channel dehumidifier experimentally. The effects of various inlet parameters, including the inlet air humidity, air temperature, air flow rate, solution concentration, solution temperature, solution flow rate and cooling water temperature and flow rate will be analyzed in-depth by considering the flow condition in the dehumidifier.

Chapter 7 summarizes the major conclusions and achievements of this project and presents several recommendations for the future research.

CHAPTER 2

LITERATURE REVIEW AND RESEARCH METHODOLOGY

2.1 Introduction

It is well known that in a dehumidifier, complicated heat and mass transfer occur. The process can be described in detail: water vapor spreads from the air to the air side surface of the gas-liquid two phase interface, then water vapor condensates on the interface and enters into the liquid phase, and finally the condensed water diffuses from the liquid side of the interface to the desiccant solution. The driving force for heat transfer is the temperature difference between the air and desiccant solution, and for mass transfer is the water vapor pressure difference between the air and the surface of the desiccant solution.

In this chapter, the origins and research methods of present work are presented in detail. Firstly, the existing simulation and experimental studies of the dehumidifier are reviewed in section 2.2 and 2.3. Based on the summarization of the above two sections, the limitations of the previous work are analyzed and listed out in section 2.4. Through the literature, it is found that it is possible to simulate the coupled flow, heat and mass

transfer processes in the dehumidifier with CFD method. Thus, section 2.5 gives a review of the simulation researches of the flow, heat and mass transfer in various devices based on CFD. Section 2.6 summarizes and compares the existing interface tracking methods, which are critical for simulating the two phase flow behaviors. Section 2.7 discusses three classic mass transfer theories, providing information for choosing a suitable mass transfer model. Section 2.8 makes a summary of different methods for measuring the film thickness in previous experimental studies. Finally, according to the present requirements, suitable simulation models and experimental methods are selected and explained in section 2.9.

2.2 Review of existing simulation models

Compared with an experimental research, the simulation method is more time and cost savings. Also, some parameters in the dehumidifier interior can be observed by simulation while it is impossible to be achieved by experiment. Most importantly, the verified simulation models are effective tools to assess and optimize similar dehumidifiers. Therefore, a large amount of studies have been conducted to establish reasonable mathematical models for evaluating the liquid desiccant dehumidifiers.

As for the structure of the dehumidifier, according to whether there is heat output, the dehumidifiers can be classified into adiabatic and internally cooled dehumidifier. The

diagrams of two dehumidifier structures are shown in Fig. 2.1 (Luo et al. 2014a).

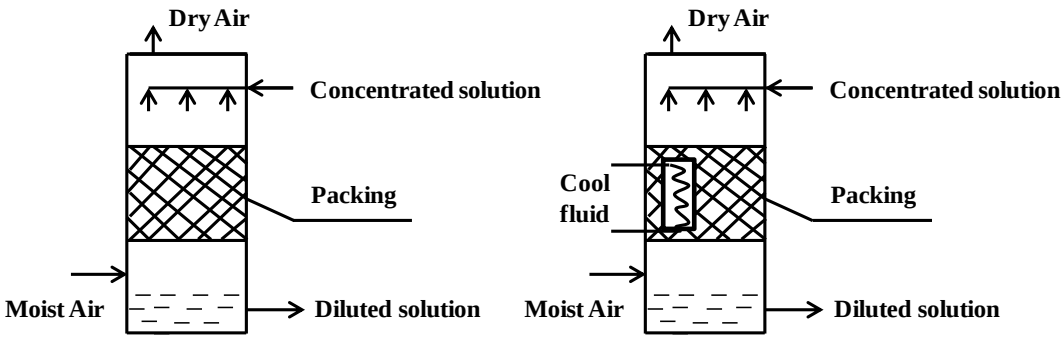

(a) Adiabatic dehumidifier (b) Internally cooled dehumidifier

Fig. 2.1 The structure diagram of two dehumidifiers

2.2.1 Models for adiabatic dehumidifier

There are mainly three types of mathematical models, including the finite difference model, effectiveness NTU ($\varepsilon - NTU$) model and the simplified solutions.

2.2.1.1 Finite difference model

In 1980, Factor et al. (Factor and Grossman 1980) promoted a theoretical model to predict the performance of a countercurrent packed column air-liquid contractor, based on the model for adiabatic gas absorption put forward by Treybal in 1969. In the model, the whole dehumidifier is divided into n parts, as shown in Fig. 2.2.

To simplify the complexity of the heat and mass transfer process, several assumptions were made: 1) the flow of air and desiccant were assumed as the slug flow, 2) the

process was adiabatic, 3) the properties of the gas and liquid were assumed constant across the differential element, which means the gradients only exist at the z direction, 4) and both of the heat and moisture transfer areas were equal to the specific surface area of the packing, 5) it was negligible of the non-uniformity of the air and solution flows, 6) in the flow direction, no heat and moisture transfer occurred, 7) the resistance to heat transfer in the liquid phase was negligible, 8) the interface temperature was equal to the bulk liquid temperature. Based on the above assumptions, the main governing equations were stated.

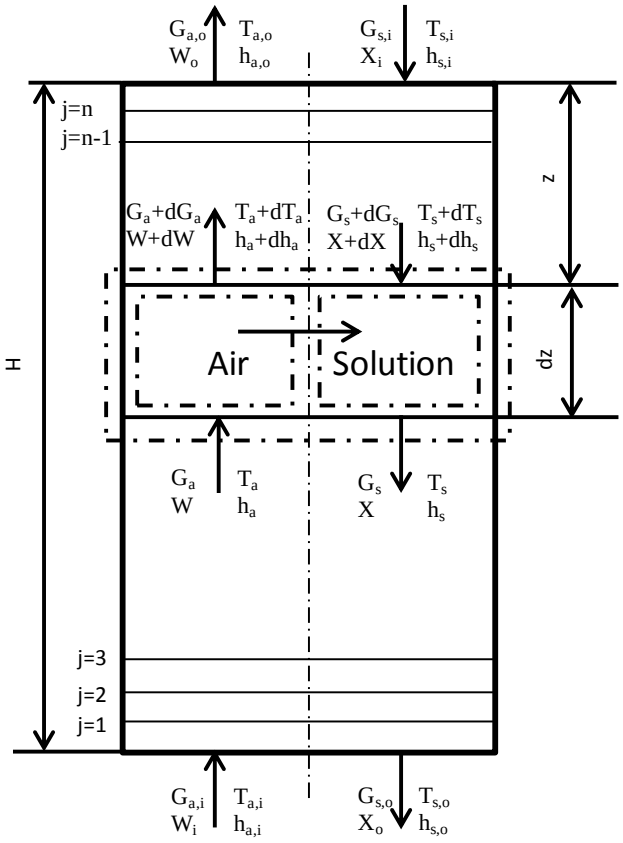

Fig. 2.2 Heat and moisture exchange model in the countercurrent adiabatic dehumidifier

According to the mass balance in the control volume,

$$dG_s = G_a dW \tag{2.1}$$

According to the interface mass and sensible heat transfer rates, the air humidity change was,

$$\frac{dW}{dz} = -\frac{\alpha_D' M_v A}{G_a} \ln\left(\frac{1-P_s/P_t}{1-P_a/P_t}\right) \tag{2.2}$$

According to the interface sensible heat transfer from the air to solution side and the energy balance on the gas side, the air temperature change was,

$$\frac{dT_a}{dz} = -\frac{\alpha'_{C,a} A(T_a - T_s)}{G_a C_{p,a}} \tag{2.3}$$

$$\alpha'_{C,a} A = \frac{-G_a C_{p,v} \frac{dW}{dz}}{1-\exp[G_a C_{p,v} \frac{dW}{dz} / (\alpha_{C,a} A)]} \tag{2.4}$$

where $\alpha_{C,a}$ and $\alpha'_{C,a}$ are the heat transfer coefficient (sensible) of the gas side and that coefficient corrected for simultaneous mass and heat transfer by applying the Ackermann correction, which is one method to take into account the effect of mass transfer on the temperature profile with an Ackermann correction factor. Finally, the boundary conditions were: $z = 0$ $T_s = T_{s,i}$, $G_s = G_{s,i}$, $X = X_i$; $z = H$, $T_a = T_{a,i}$, $G_a = G_{a,i}$, $W = W_i$.

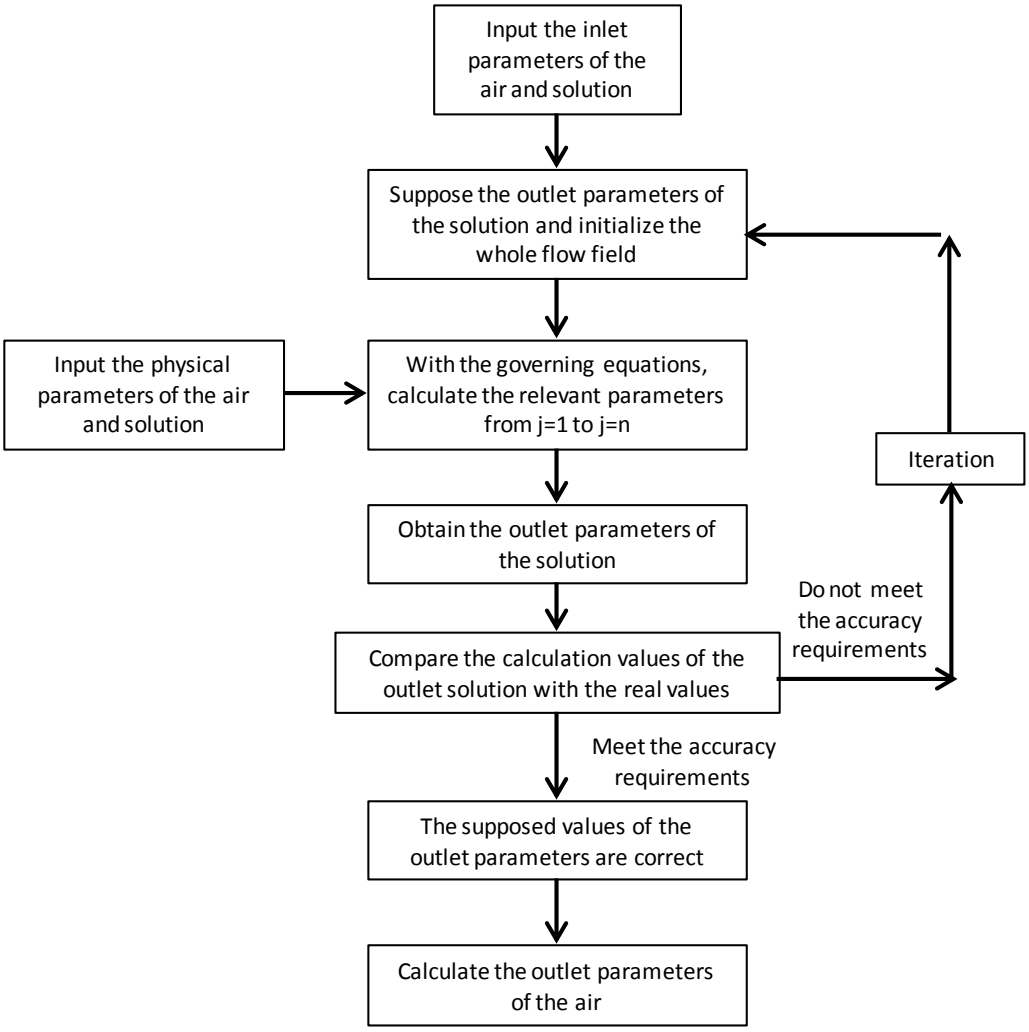

Fig. 2.3 Calculation flow chart of the countercurrent pattern

Since the above differential equations cannot be solved analytically, the most basic solution is a numerical integration along the height of the dehumidifier. To begin the calculation, one end of the dehumidifier must be chosen as the start point. For the countercurrent flow pattern, it needs to presume the outlet conditions for one of the fluids. Solving the above equations from the bottom to the top of the dehumidifier, with the boundary conditions, a set of calculated inlet solution parameters are obtained. By comparing the calculation results with real values, the supposed existing solution

variables are adjusted. The calculation will last until the final results are very close to the real values. A general calculation flowchart for the finite difference model of the counter flow pattern can be summarized in Fig. 2.3.

In the later study, Gandhidasan et al. (Gandhidasan et al. 1987) utilized the similar model to study various parameters on the packing height of the packed tower. Then, Lazzarin et al. (Lazzarin et al. 1999) gave more specific explanation of the calculation method in Appendix A of the literature. Oberg and Goswami (Oberg and Goswami 1998) applied a finite difference model similar to Factor and Grossman's to verify the experimental results. Taking account the insufficiently wetted packing and the different factor when transfer the k-type mass transfer coefficients to the F-type one, Fumo and Goswami (Fumo and Goswami, 2002) improved Oberg and Goswami's mathematical model by modifying the transfer surface with an equation proposed by Onda et al (Onda et al. 1968) with an calculation equation. In addition, a correction factor CF was introduced to modify the correlation of the wetting surface.

All of the above models introduced a coefficient $\alpha'_{C,a}$ to describe the simultaneous heat and mass transfer with the Ackermann correction. Khan and Ball (Khan and Ball 1992) promoted another solution to deal with the simultaneous transfer process. Both heat and mass transfer processes were assumed to be gas controlled, so the interface temperature was the temperature of the bulk liquid and the heat transfer rate across

the air film from the bulk air to the interface was equal to that entering the liquid side,

$$G_{\mathrm{a}} C_{\mathrm{p,a}} dT_{\mathrm{a}} = \alpha_{\mathrm{C,a}} A(T_{\mathrm{s}} - T_{\mathrm{a}}) dz \tag{2.5}$$

Similarly, the mass transfer across the interface was equal to the change in humidity ratio,

$$G_{\mathrm{a}} dW = \alpha_{\mathrm{D,a}} A(W_{\mathrm{e}} - W) dz \tag{2.6}$$

Then, the humid air specific enthalpy change could be written as,

$$dh_{\mathrm{a}} = C_{\mathrm{p,a}} dT_{\mathrm{a}} + dW \cdot [C_{\mathrm{p,v}} (T_{\mathrm{a}} - T_{\mathrm{r}}) + \lambda] \tag{2.7}$$

By substituting equation (2.6) and (2.7) to (2.5), the air enthalpy change along the flow direction was obtained. Here it is rewritten in a simpler way appeared in the later literature,

$$\frac{\partial h_{\mathrm{a}}}{\partial z} = \frac{NTU \cdot Le}{H} [(h_e - h_{\mathrm{a}}) + \lambda (\frac{1}{Le} - 1) \cdot (W_{\mathrm{e}} - W)] \tag{2.8}$$

In the above equations, Le and NTU were defined as,

$$Le = \frac{\alpha_{\mathrm{C}}}{\alpha_{\mathrm{D}} C_{\mathrm{p,a}}} \tag{2.9}$$

$$NTU = \frac{\alpha_{\mathrm{D}} AV}{G_{\mathrm{a}}'} \tag{2.10}$$

In this way, the coupled heat and mass transfer were considered together. In the following research, this handling method is more popular than the Ackermann correction.

The finite difference model has been extensively used for the countercurrent dehumidifier (Gandhidasan et al. 1986; Elsayed et al. 1993; Luo et al. 2011; Luo et al. 2012). For cross flow configuration, Liu et al. (Liu et al. 2007) proposed a model for the heat and mass transfer process in a cross flow adiabatic liquid desiccant dehumidifier/regenerator. The physical and mathematical models are described in Fig. 2.4 and Fig. 2.5, respectively.

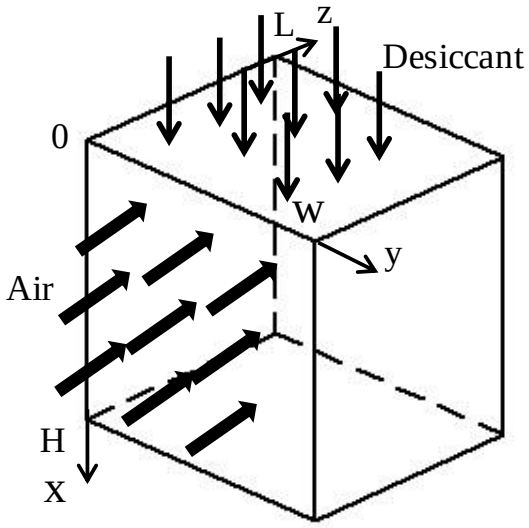

Fig. 2.4 Schematic of the cross flow dehumidifier/regenerator

(Liu et al. 2007)

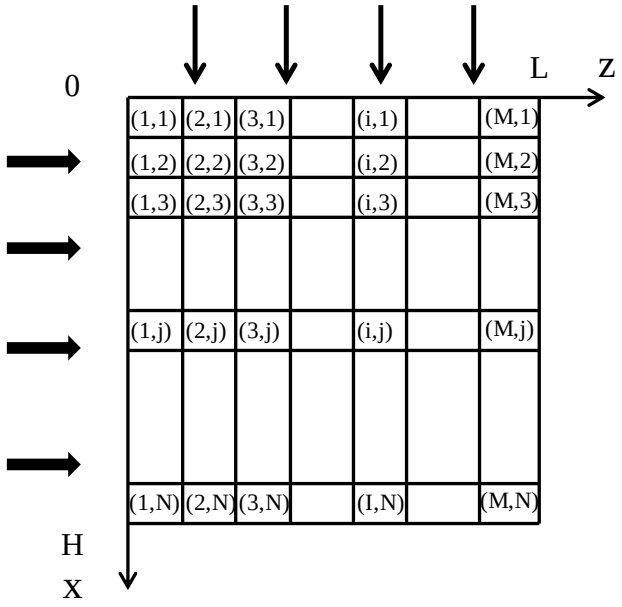

Fig. 2.5 A two dimensional schematic of the cross flow dehumidifier/regenerator (Liu et al. 2007)

The governing equations of energy, water content, and solute mass balances in a differential element were,

$$\frac{G_a^{'}}{H}\cdot\frac{\partial h_a}{\partial z}+\frac{1}{L}\cdot\frac{\partial(G_s^{'}h_s)}{\partial x}=0 \tag{2.11}$$

$$\frac{G_a^{'}}{H}\cdot\frac{\partial W}{\partial z}+\frac{1}{L}\cdot\frac{\partial G_s^{'}}{\partial x}=0 \tag{2.12}$$

$$d(G_s^{'}\cdot X)=0 \tag{2.13}$$

The energy and mass transfer at the interface of air and desiccant solution were expressed in equation (2.8) and the following equation (2.14),

$$\frac{\partial W}{\partial z}=\frac{NTU}{L}\cdot(W_e-W) \tag{2.14}$$

Like some other papers, Le was supposed to be one in the model. However, the value of NTU was correlated based on the corresponding experimental data in the paper.

Niu (Niu 2010) also established a two dimensional mathematical model for the cross-flow adiabatic dehumidifier, and the mass transfer coefficient was gained from the experimental data. Woods and Kozubal (Woods and Kozubal 2012) applied the finite difference model to study the performance of a desiccant-enhanced evaporative air conditioner and the simulation results showed good agreement with the experimental ones.

2.2.1.2 Effectiveness NTU ($\varepsilon - NTU$) model

Stevens et al. (Stevens et al. 1989) reported an effective model for liquid-desiccant heat and mass exchanger, which was developed from a computationally simple effectiveness model for cooling towers (Braun 1988). Except for the assumptions of the finite difference model, two additional assumptions were included. One was the assumption of the linear relationship of saturation enthalpy and temperature. The other one was the neglect of the water loss term for the solution energy balance. In addition, an 'effective' heat and mass transfer process was assumed.

The main equations and calculation process of $\varepsilon - NTU$ model were summarized as follows.

1) Calculated the Number of Transfer Units **(** NTU) by equation (2.10).

2) In terms of the similarity with the heat exchanger, the effectiveness of the countercurrent flow dehumidifier could be expressed as,

$$\varepsilon = \frac{1-e^{-NTU(1-m^*)}}{1-m^* e^{-NTU(1-m^*)}} \tag{2.15}$$

where m^* was a capacitance ratio, defined analogous to the capacitance ratio used in sensible heat exchangers, and it was given in the following equations,

$$m^* = \frac{G_a' C_{sat}}{G_{s,i}' C_{p,s}} \tag{2.16}$$

where C_{sat} was the saturation specific heat, and $C_{sat} = \frac{dh_e}{dT_s}$.

3) With NTU and ε, the air outlet enthalpy could be obtained with the following equation,

$$h_{a,o} = h_{a,i} + \varepsilon(h_e - h_{a,i}) \tag{2.17}$$

4) Used an energy balance to calculate the solution outlet enthalpy.

5) Then an 'effective' saturation enthalpy was found by,

$$h_{e,eff} = h_{a,i} + \frac{h_{a,o} - h_{a,i}}{1-e^{-NTU}} \tag{2.18}$$

6) Using the enthalpy and saturated conditions, the effective humidity ratio $Y_{e,eff}$ could be obtained.

7) Then, by the following equation, the air outlet humidity ratio could be calculated,

$$W_o = W_{e,eff} + (W_i - W_{e,eff})e^{-NTU} \tag{2.19}$$

8) With the mass balance and known inlet and outlet parameters, all of the outlet parameters were acquired.

In the later study, Sadasivam and Balakrishnan (Sadasivam and Balakrishnan 1992) pointed out that the definition of NTU based on the gas mass velocity in Stevens's model was not appropriate when the minimum flow capacity was the liquid (Jaber and Webb 1989). Thus, the gas mass velocity $G_a^{'}$ was changed to the minimal mass velocity of gas and liquid.

As for the $\varepsilon - NTU$ model, there are much fewer literatures than the finite difference model. In the following study, Ren (Ren 2008) developed the analytical expressions for the $\varepsilon - NTU$ model with perturbation technique. The model accounted for the nonlinearities of air humidity ratio and enthalpy in equilibrium with solutions, the water loss of evaporation and the variation of the solution specific heat capacity.

2.2.1.3 The simplified models

It can be found that both the finite difference model and $\varepsilon - NTU$ model require numerical and iterative computations. Thus, both of them are not suitable for hourly performance evaluation.

Khan and Ball (Khan and Ball 1992) developed a simplified algebraic model. With the finite difference model, about 1,700 groups of data were analyzed. The following functions were deduced,

$$W_{\mathrm{o}} = n_0 + n_1 W_{\mathrm{i}} + n_2 T_{\mathrm{s,i}} + n_3 T_{\mathrm{s,i}}{}^2 \tag{2.20}$$

$$W_{\mathrm{o}} = m_0 + m_1 W_{\mathrm{i}} + m_2 T_{\mathrm{a,o}} + m_3 T_{\mathrm{a,o}}{}^2 \tag{2.21}$$

The above two equations can be employed to predict the exit air temperature and humidity ratio easily. However, as they were fitted based on the data with certain operating solution concentration and solution to air mass ratio, they might not be suitable for other conditions.

Liu et al. (Liu et al. 2006) fitted some empirical correlations to estimate the performance of a cross-flow or counter-flow liquid desiccant dehumidifier. The essence of the methodology is obtaining the empirical expression of enthalpy and moisture effectiveness by experiment.

Gandhidasan (Gandhidasan 2004) reported a very simple analytical solution to predicate the rate of moisture removal for the dehumidification process. Referred to previous work (Gandhidasan 1990), the author promoted the dimensionless moisture and temperature difference ratios. By combining the aforementioned two definitions, the energy balance equation could be expressed as follows,

$$C_{p,a}\bar{T}(T_{a,i}-T_{s,i})+\frac{M_v}{M_a}\cdot\frac{\lambda}{P_t}\bar{P}(P_{a,i}-P_{s,i})=\frac{G_s}{G_a}C_{p,s}(T_{s,o}-T_{s,i}) \tag{2.22}$$

According to the literature (Kim et al. 1997), the relationship between the rate of moisture removal m and the partial pressure of water vapor could be deduced as,

$$P_{s,i}=P_{a,i}-\frac{mP_t}{G_a\bar{P}}\frac{M_a}{M_v} \tag{2.23}$$

In addition, the desiccant outlet temperature was easily calculated, as shown in the equation,

$$T_{s,o}=\frac{T_{s,i}-\varepsilon_{HE}T_{c,i}}{(1-\varepsilon_{HE})} \tag{2.24}$$

Finally, substituting equation (23) and (24) to (22), the moisture removal rate m was given as,

$$m=\frac{1}{\lambda}[\frac{G_s{}'C_{p,s}\varepsilon_{HE}}{(1-\varepsilon_{HE})}(T_{s,i}-T_{c,i})-G_a{}'C_{p,a}\bar{T}(T_{a,i}-T_{s,i})] \tag{2.25}$$

The method was rather simple yet it involved lots of assumptions and limitations. Except some common assumptions, it also required that the desiccant inlet temperature was different from the air inlet temperature, and the desiccant temperature leaving the dehumidifier was equal to that of the desiccant entering the heat exchanger.

Chen et al. (Chen et al 2006) constructed an analytical model on the basis of the finite difference model for countercurrent and concurrent flow pattern. The physical model is similar to that of Fig. 2.4. Firstly, a mathematical model was built following the model promoted by Khan and Ball (Khan and Ball 1992). Then, two parameters were introduced for derivation convenience,

$$K_{\mathrm{a}} = Le \cdot C_{\mathrm{p,a}} \cdot T_{\mathrm{a}} + \lambda \cdot W \tag{2.26}$$

$$K_{\mathrm{e}} = Le \cdot C_{\mathrm{p,a}} \cdot T_{\mathrm{s}} + \lambda \cdot W_{\mathrm{e}} \tag{2.27}$$

By combining the mass, energy conservation equations, mass and energy transfer equations at the interface, the change of K_{e} along the flow direction was,

$$\frac{dK_{\mathrm{e}}}{dz} = m^{*}\frac{NTU}{H}[h_{\mathrm{a,i}} + \frac{1}{m^{*}}(K_{\mathrm{e}} - K_{\mathrm{e,o}}) + (Le-1)C_{\mathrm{p,a}} \cdot T_{\mathrm{a}} - K_{\mathrm{e}}] \tag{2.28}$$

By integrating (2.28) from 0 to H or z, K_{e} at the outlet and along z-axis were acquired. Based on the above results, the distribution of air enthalpy, air humidity, and temperature in a countercurrent adiabatic dehumidifier were obtained. Then, the

distribution of the solution parameters can be calculated. In the paper, the analytic solution of the concurrent flow heat and mass transfer process were also given out.

Ren et al. (Ren et al. 2006) derived a new analytical solution from the one-dimensional differential model. By introducing some dimensionless and dimensional groups, the conventional equations of one-dimensional model were transferred to two coupled ordinary differential equations, whose general solution are as follows,

$$\Delta W_{\mathrm{M}} = C_1 e^{\lambda_1 NTU_z} + C_2 e^{\lambda_2 NTU_z} \tag{2.29}$$

$$\Delta \vartheta = -K_1 C_1 e^{\lambda_1 NTU_z} + K_2 C_2 e^{\lambda_2 NTU_z} \tag{2.30}$$

The model is just suitable for the case where the solution flow rate and concentration change slightly as it assumed that the variation of the equilibrium humidity ratio of solution depended only on the change of the solution temperature.

Babakhani and Soleymani developed analytical models for the counter flow adiabatic regenerator (Babakhani and Soleymani 2006) and dehumidifier (Babakhani and Soleymani 2009). The analytical solution was deduced on the basis of the differential equations, including the mass balance, air humidity and temperature change equations listed in (2.1) to (2.3), and liquid desiccant temperature and concentration change derived from the mass and energy conservation equations. To achieve the

simplification, two main assumptions were applied, including the assumptions of the dilute gas phase and constant equilibrium humidity ratio on the interface. Then the above equations could be solved and the integrated analytical solution were,

$$W = W_{\text{int}} + (W_{\text{i}} - W_{\text{int}})\exp(-\alpha \bar{M}\, NTU_{\text{z}}) \tag{2.31}$$

$$T_{\text{a}} = C_1 + C_2\exp(-\theta NTU_{\text{z}}) - \frac{\beta}{(\alpha \bar{M})^2 - \alpha \bar{M}\theta}\exp(-\alpha \bar{M}\, NTU_{\text{z}}) \tag{2.32}$$

$$T_{\text{s}} = \frac{1}{R_{\text{c}}Le}[-C_2\theta\exp(-\theta NTU_{\text{z}}) + \frac{\alpha \bar{M}\beta}{(\alpha \bar{M})^2 - \alpha \bar{M}\theta}\exp(-\alpha \bar{M}\, NTU_{\text{z}})] + T_{\text{a}} \tag{2.33}$$

$$\text{In}\, X = -R_{\text{m}}(W_{\text{i}} - W_{\text{int}})\exp(-\alpha \bar{M}\, NTU_{\text{z}}) + C_3 \tag{2.34}$$

$$G_{\text{s}} = G_{\text{a}}(W_{\text{i}} - W_{\text{int}})\exp(-\alpha \bar{M}\, NTU_{\text{z}}) + C_4 \tag{2.35}$$

With the above solutions, the profiles of the outlet solution and air parameters were available.

Based on the above model, Babakhani (Babakhani 2009) also developed another analytical model which was well suited to the high desiccant flow rate conditions.

Liu et al. (Liu et al. 2008) developed an analytical solution for a similar cross-flow packed bed liquid desiccant air dehumidifier, whose numerical model had been reported in literature (Liu et al. 2007). In the present work, it was regarded that the desiccant mass flow rate and concentration kept constant in the whole process. Thus the equations (2.12), (2.13) and (2.14) were got rid of, and only equations (2.8) and

(2.11) were left for calculation, which were rewritten as,

$$m^* \cdot \frac{\partial h_a}{\partial z} + \frac{H}{L} \cdot \frac{\partial h_e}{\partial x} = 0 \tag{2.36}$$

$$\frac{\partial h_a}{\partial z} = -\frac{NTU}{L} \cdot (h_a - h_e) \tag{2.37}$$

It was found the above control equations had high similarity with those of the cross-flow heat exchanger. Thus the methods in literature (Nusselt 1911; Nusselt 1930) were referred to. As the solution expressions were a litter complicated, here they will not be presented.

Recently, Wang et al. (Wang et al. 2013) developed a simplified yet accurate model for real-time performance optimization. The Levenberg-Marquardt method was used to identify the parameters. The proposed model is suggested to be employed in real-time performance monitoring, control and optimization. Park and Jeong (Park and Jeong 2013) also developed a simplified second-order equation model as a function of operation parameters to study their impact on the dehumidification effectiveness.

2.2.1.4 Summary

To sum up, there are three models to simulate the adiabatic dehumidifiers. The general comparison of them is presented in Table 2.1. As a matter of convenience, the information of some representative models is summarized in detail in Table 2.1.

Table 2.1 Comparison of the mathematical models for adiabatic dehumidifier

Classification	Assumption	Iteration	Accuracy	Applied situation
Finite difference model	Least	Extensive	Best	Component design and operation optimization
$\varepsilon - NTU$ model	More	Less	Better	Component design and operation optimization
Simplified models	Most	No	Worst	Annual assessment

The finite difference model is used most frequently for its accuracy. However, it involves complicated iterative process, so it is only suitable for the component design and operation optimization. The common assumptions have been stated in Factor's model. However, some other simplifications or improvements are made to satisfy the real conditions. It can also be observed that the counter flow configuration is the most commonly used flow pattern, and it can be described by the one-dimensional model. For the dehumidifier with cross flow configuration, the problem is generally solved by the two-dimensional model.

Table 2.2 Detail information of the mathematical models for adiabatic dehumidifier

Classification	Model	Flow pattern	Dimensionality	Treatment of coupled heat and mass transfer
Finite difference model	Factor and Grossman 1980	Counter	One-dimensional	Ackermann correction
	Oberg and Goswami 1998	Counter	One-dimensional	Introduction of Enthalpy
	Fumo and Goswami 2002	Counter	One-dimensional	Ackermann correction
	Khan and Ball 1992	Counter	One-dimensional	Ackermann correction
	Liu et al. 2007	Cross	Two-dimensional	Introduction of Enthalpy
$\varepsilon - NTU$ model	Stevens et al. 1989	Counter	One-dimensional	Introduction of Enthalpy

Classification	Model	Flow pattern	Simplified method
Simplified models	Khan and Ball 1992	Counter	Correlations based on simulation results
	Liu et al. 2006	Counter or Cross	Correlations based on experimental results
	Gandhidasan 2004	Counter	Introduction of dimensionless parameters
	Chen et al. 2006	Counter or Concurrent	Introduction of parameters similar to air enthalpy
	Ren et al. 2006	Counter	Introduction of dimensionless parameters
	Babakhani and Soleymani 2006	Counter	Transfer the differential equations to nonlinear equations
	Liu et al. 2008	Cross	Similar method of cross-flow heat exchanger

For the $\varepsilon - NTU$ model, two additional assumptions are included as mentioned above. Thus, the model is less accurate than the finite difference model. However, compared with the finite difference model, the calculations are dramatically less extensive. Thus, the $\varepsilon - NTU$ model has great potential for saving time. But with the development of the computer technology, the calculated amount of the finite difference model can be accepted due to its accuracy. Therefore, much fewer researches have been done on the $\varepsilon - NTU$ model in the subsequent studies.

From Table 2.2, it is concluded that different dimensionless parameters have been introduced in the deviation processes of the simplified models. Meanwhile, the additive assumptions are needed for simplification. Therefore, they are only applicable for certain operation conditions, and different models can be chosen to be suited to the real situation. The biggest advantage of these models is that the iteration is avoided. As a result of their high efficiency, they are often used to predict the annual energy consumption of an air-conditioning system.

2.2.2 Models for internally cooled dehumidifier

In the internally cooled dehumidifier, some cooling fluid is introduced to remove the heat produced by the vapor condensation, as shown in Fig. 2.6 (Ren et al. 2007). Most of the models for the internally cooled dehumidifier are developed upon the finite difference methods used for the adiabatic dehumidifier. The difference is the

additional consideration of the heat transfer brought by the cooling media. In addition, because of the relatively low solution flow rate in the internally cooled dehumidifier, it is easier for the solution to form a thin film on the surface of the padding wall or plate. Briefly, there are also three types of models for the internally cooled dehumidifier.

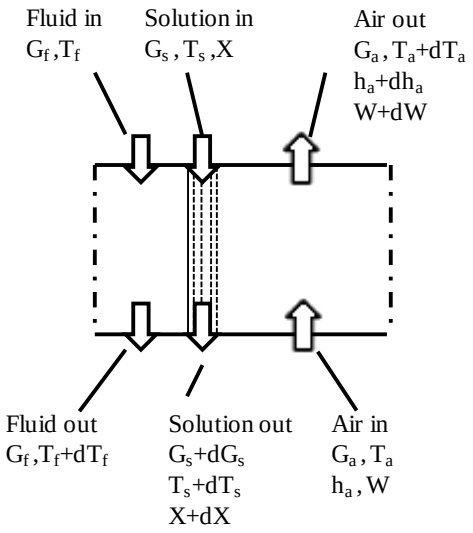

Fig. 2.6 Heat and moisture exchange model in the internally cooled dehumidifier (Ren et al. 2007)

2.2.2.1 Models without considering liquid film thickness

The first type ignores the liquid film thickness. Khan and Martinez (Khan and Martinez 1998) developed a mathematical model to predict the performance of a liquid desiccant absorber integrating indirect evaporative cooling to achieve an almost isothermal operation. The processed air and the solution flowed in countercurrent

direction while the solution and water flowed in parallel direction. Saman and Alizadeh (Saman and Alizadeh 2001) also established a similar model for a cross-flow type plate heat exchanger (PHE) serving as internally cooled dehumidifier. The schematic diagrams of the PHE are presented in Fig. 2.7 and 2.8. It is obvious that it has the same principle with that in literature (Khan and Martinez 1998). The only difference lies in the configuration difference.

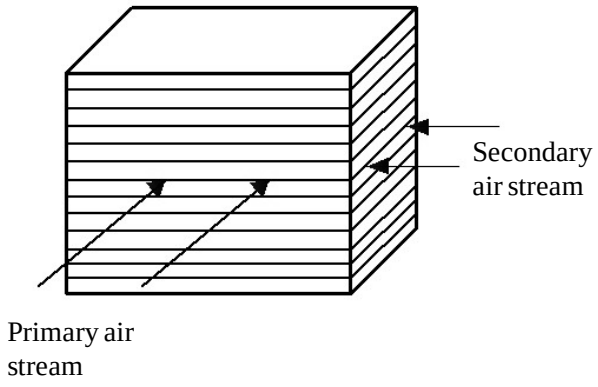

(a)

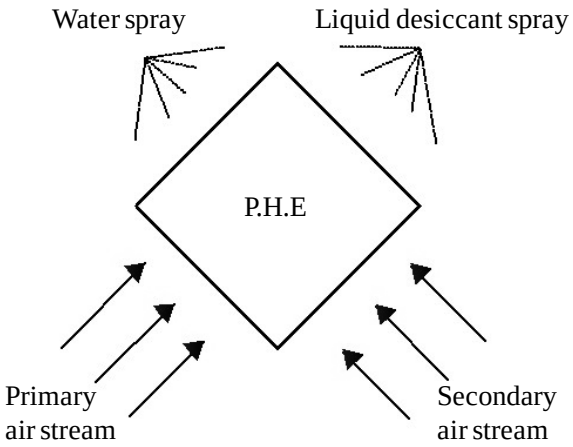

(b)

Fig. 2.7 Schematic diagram of the cross-flow type plate heat exchanger (Ren et al. 2007)

Here, Saman's model will be explained in detail as it is more representative. In the paper, the PHE was divided into a certain number of control volumes in two orthogonal directions. Several assumptions were set, including no heat transfer with the environment, negligible temperature gradient between the solution film and water film, and fully cover of solution and water on the plate.

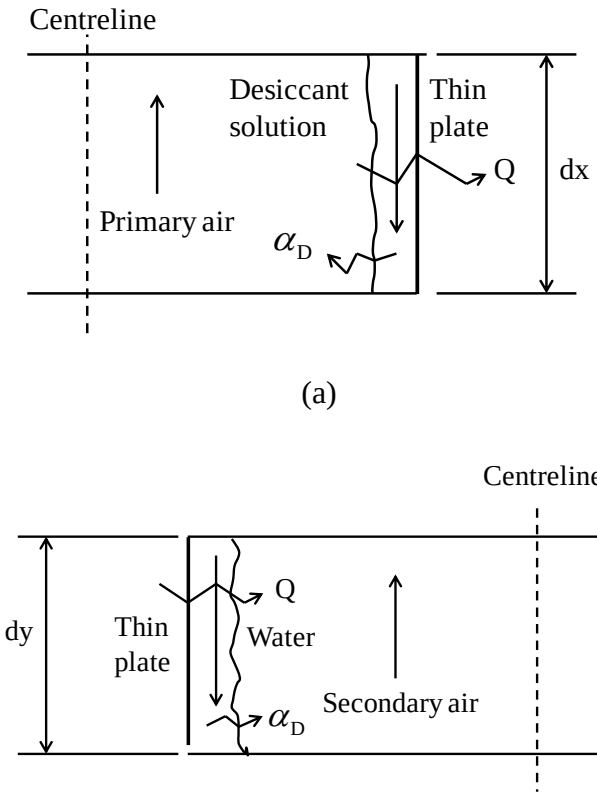

Fig. 2.8 Schematic diagram of the control volumes considered: (a) primary air-solution; (b) secondary air-water

(Saman and Alizadeh 2001)

Thus, the change of the enthalpy and humidity ratio of the primary air were,

$$\frac{dh_{a,p}}{dx} = \frac{NTU_s \cdot Le_s}{H}[(h_{e,s} - h_{a,p}) + \lambda(\frac{1}{Le_s} - 1) \cdot (W_{e,s} - W_p)] \tag{2.38}$$

$$\frac{dW_p}{dx} = \frac{NTU_s}{H} \cdot (W_{e,s} - W_p) \tag{2.39}$$

Also, the mass and energy conservation equations in the control volume were given as,

$$G_{a,p}' \cdot \frac{dW_p}{dx} - \frac{dG_s'}{dx} = 0 \tag{2.40}$$

$$G_{a,p}' \cdot \frac{dh_{a,p}}{dx} - \frac{d(G_s' h_s)}{dx} + Q = 0 \tag{2.41}$$

Similarly, the change of the enthalpy and humidity ratio of the secondary air, and mass and energy conservation equations were expressed as follows,

$$\frac{dh_{a,r}}{dy} = \frac{NTU_f \cdot Le_f}{H}[(h_{e,f} - h_{a,r}) + \lambda(\frac{1}{Le_f} - 1) \cdot (W_{e,f} - W_r)] \tag{2.42}$$

$$\frac{dW_r}{dx} = \frac{NTU_f}{H} \cdot (W_{e,f} - W_r) \tag{2.43}$$

$$G_{a,r}' \cdot \frac{dW}{dy} - \frac{dG_f'}{dy} = 0 \tag{2.44}$$

$$G_{a,r}' \cdot \frac{dh_{a,r}}{dy} - \frac{d(G_f' h_f)}{dy} - Q = 0 \tag{2.45}$$

On the basis of the above governing equations, the discretization equations were derived for each control volume. The calculation method was similar to the flow chart of the finite difference model presented in Fig. 2.3, while it was more complicated as a

result of another iteration started by the advance assumption of the cooling water temperature. In the paper, it is noted that the film thickness was mentioned, but the simulation did not take it into consideration.

Liu et al. (Liu et al. 2009) compared the performances of internally cooled dehumidifiers with various flow patterns. A representative heat and mass transfer model was selected for detail description, as shown in Fig. 2.9. Referred to literature (Khan and Ball 1992), the heat and humidity changes of the air were almost the same with the equation (2.6) and (2.8).

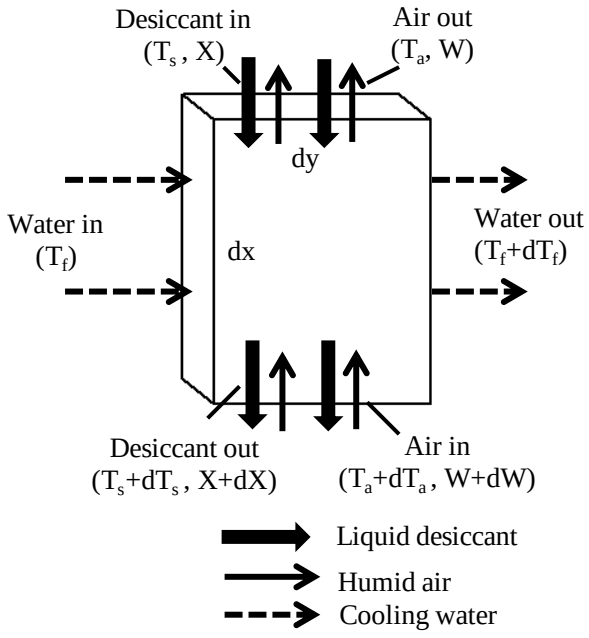

Fig. 2.9 Schematic diagram of the control volume for a counter-flow internally cooled dehumidifier

(Liu et al. 2009)

The energy conservation equation was expressed as,

$$G_{\mathrm{a}}^{'} \cdot \frac{\partial h_{\mathrm{a}}}{\partial x} = \frac{\partial (G_{\mathrm{s}}^{'} h_{\mathrm{s}})}{\partial x} + C_{\mathrm{p,f}} G_{\mathrm{f}}^{'} \frac{L}{H} \frac{\partial T_{\mathrm{f}}}{\partial y} \tag{2.46}$$

As the mass conservation equation has been explained before, here it will not be presented for limited space. And the heat transfer between the desiccant solution and the cooling water was,

$$\frac{\partial T_{\mathrm{f}}}{\partial y} = \frac{NTU_{\mathrm{f}}}{L} \cdot (T_{\mathrm{s}} - T_{\mathrm{f}}) \tag{2.47}$$

Combined the above equations with the inlet conditions, the distribution of the parameters of the air, desiccant solution, and the cooling water could be obtained. The model was applied for analyzing the role of flow patterns in depth, which was seldom reported in previous literatures. In the later study, Zhang et al. (Zhang et al. 2013) employed the above model to predict the performance of an internally-cooled dehumidifier.

Yin et al. (Yin et al. 2009) built a uniform mathematical model for an internally cooled/heated dehumidifier/regenerator which was made up of a plate heat exchanger. It is important to point out that the author took the non-wetted area into consideration by introducing the wetness coefficient. Meanwhile, in a control volume, the transfer process in the channel width was considered to be symmetrical. In addition, to

improve the accuracy of the model, the author also applied the correlation of the mass transfer coefficient fitted out by experiment (Yin et al. 2008).

Based on the one-dimensional differential equations for the heat and mass transfer processes with parallel or counterflow configurations, Ren et al. (Ren et al. 2007) developed an analytical model for internally cooled or heated liquid desiccant-air contact units. To increase the accuracy, the model took the effects of solution film heat and mass transfer resistances, the variations of solution mass flow rate, non-unity values of Lewis factor and incomplete surface wetting conditions into consideration.

Recently, Khan and Sulsona (Khan and Sulsona 1998) developed a two-dimensional and steady-state model for a vapour compression/liquid desiccant hybrid cooling and dehumidification absorber made up of the tube-fin exchanger. To simplify the model, several assumptions were made reasonably. The most critical one was to consider the air and refrigerant flow in countercurrent owing to the large size in the air flow direction.

2.2.2.2 Models considering uniform liquid film thickness

In the second model, the film is considered as a uniformly distributed desiccant film. Park et al. (Park et al. 1994) developed a three dimensional numerical model for simulating the coupled heat and mass transfer in a cross-flow internally cooled/heated

dehumidifier/regenerator. The schematic diagram was presented in Fig. 2.10. Some assumptions were used before listing out the governing equations: the flow was considered as laminar and steady; the physical properties for both solution and air were constant; species thermo-diffusion and diffusion-thermo effects were negligible and thermodynamic equilibrium existed at the solution-air interface. Because of the relatively small absorption, the TEG solution film thickness was simplified as constant and the film mean velocity was also unchanged. Also, the velocity gradient in the liquid solution film at the interface was regarded as zero and the flow of the liquid solution and air was supposed to be fully developed at the start place, as presented in Fig. 2.10.

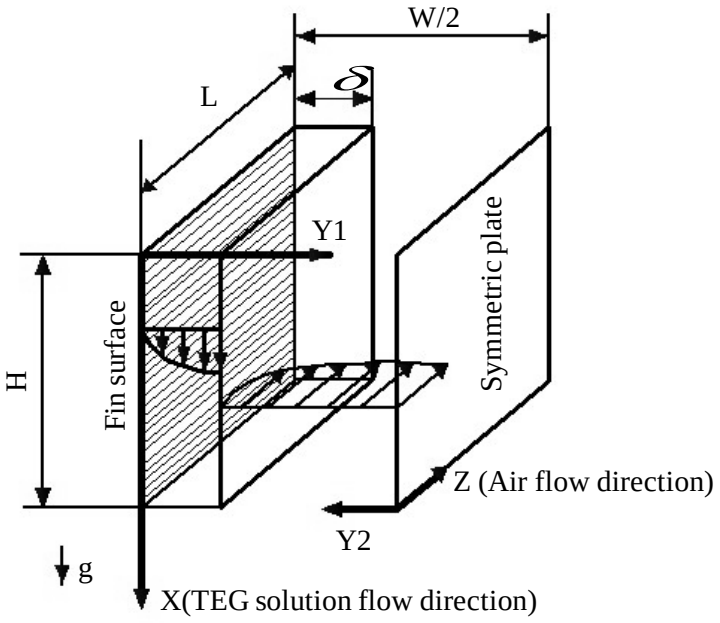

Fig. 2.10 Schematic diagram of control volume for a three-dimensional model (Park et al. 1994)

With the assumptions, the governing equations for the liquid solution flow were,

$$0 = \mu_s \frac{\partial^2 u_s}{\partial y_1^2} + \rho_s g \tag{2.48}$$

$$u_s \frac{\partial T_s}{\partial x} = D_{t,s} \frac{\partial^2 T_s}{\partial y_1^2} \tag{2.49}$$

$$u_s \frac{\partial X_w}{\partial x} = D_{m,s} \frac{\partial^2 X_w}{\partial y_1^2} \tag{2.50}$$

For the air flow, the governing equations were as follows,

$$0 = -\frac{dP}{dz} + \mu_a \frac{\partial^2 u_a}{\partial y_2^2} \tag{2.51}$$

$$u_a \frac{\partial T_a}{\partial z} = D_{t,a} \frac{\partial^2 T_a}{\partial y_2^2} \tag{2.52}$$

$$u_a \frac{\partial X_v}{\partial z} = D_{m,a} \frac{\partial^2 X_v}{\partial y_2^2} \tag{2.53}$$

At the interface, the mass and energy balances also existed,

$$\rho_s D_{m,s} \frac{\partial X_w}{\partial y_1} = -\rho_a D_{m,a} \frac{\partial X_v}{\partial y_2} \tag{2.54}$$

$$-k_s \frac{\partial T_s}{\partial y_1} = k_a \frac{\partial T_a}{\partial y_2} + \rho_a D_{m,a} \frac{\partial X_v}{\partial y_2} \lambda \tag{2.55}$$

The above equations can be discretized along the three different directions. Being combined with the boundary and interfacial conditions, the equations could be solved.

Ali et al. (Ali et al. 2003; Ali et al. 2004; Ali and Vafai 2004) had used the same mathematical model to study the effect of the flow configuration, the inclination angle, the Reynolds numbers, various inlet parameters, cu-ultrafine particles volume fraction, and thermal dispersion on the performance of the dehumidifier/ regenerator.

Mesquita et al. (Mesquita et al. 2006) compared three different numerical models for parallel plate internally cooled liquid desiccant dehumidifier. The second one introduced a constant film thickness. It was assumed that the wall was isothermal so that the water flow could be neglected. On the basis of some other assumptions, the dehumidification process could be described by a two dimensional model, as shown in Fig. 2.11. Being different from the first model which does not consider the film thickness, this model took the momentum equations into consideration. Firstly, the velocity profiles of the air and liquid desiccant were obtained with the momentum equations, presented as follows,

$$\delta = (\frac{3G_s^{'}\nu_s}{\rho_s g})^{1/3} \tag{2.56}$$

$$u_s = \frac{3G_s^{'}}{2\rho_s}(\frac{2y}{\delta^2} - \frac{y^2}{\delta^3}) \tag{2.57}$$

$$u_a = u_s + \frac{dP}{dx}\frac{1}{\mu_a}[\frac{1}{2}(y^2 - \delta^2) + (\frac{W}{2} - y)] \tag{2.58}$$

$$\frac{dP}{dx} = 3\mu_a[\frac{u_s}{(\delta - W/2)^2} + \frac{G_a^{'}}{2\rho_a(\delta - W/2)^3}] \tag{2.59}$$

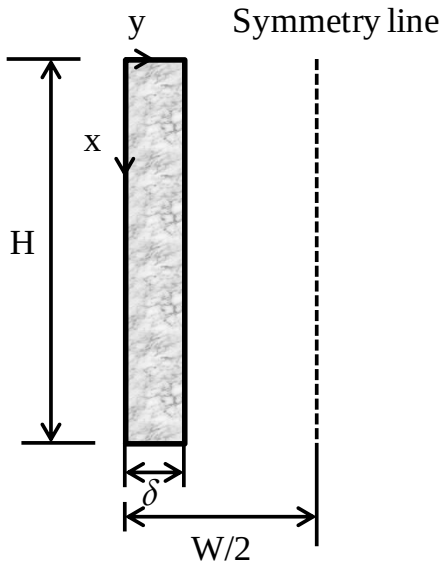

Fig. 2.11 Schematic diagram of control volume for a two-dimensional model (Mesquita 2006)

The energy and species equations of the liquid phase, gas phase, and the energy and species balances equations at the interface are almost the same with those presented in literature (Park and Howell 1994). Then with the velocity values and boundary conditions, all the above equations could be solved numerically and simultaneously with the software package Microsoft EXCEL.

Recently, Dai and Zhang (Dai and Zhang 2004) employed the uniform liquid film thickness to evaluate the performance of a cross flow liquid desiccant air dehumidifier packed with honeycomb papers. The objective of the paper is to analyze the Nusselt and Sherwood numbers in the channels with honeycomb papers as the packing materials.

2.2.2.3 Models considering variable liquid film thickness

The final model introduces a variable film thickness. Except the constant thickness model, Mesquita et al. (Mesquita et al. 2006) also established another variable thickness model for internally cooled liquid-desiccant dehumidifiers. In the model, the film thickness in equation (2.56) varied, thus for every step of calculation, the film thickness was recalculated, so was the liquid velocity profile in equation (2.57). However, to reduce the computational time, the change in the airflow velocity profile was neglected as a result of the small film thickness changes. Compared the results of variable thickness model with the constant thickness model, it was found that the two models converged to the same results at higher desiccant flow rates. However, the constant thickness model underestimated the dehumidification for low desiccant flow rates.

Hueffed et al. (Hueffed et al. 2009) presented a simplified model for a parallel-plate dehumidifier, with both adiabatic and isothermal absorption. The model used a control volume approach and accounted for the film thickness variation by imposing its effect on the heat and mass transfer coefficients. The specific equations of the heat transfer coefficient in terms of the film thickness were listed as,

$$\alpha_{\mathrm{C}} = \frac{Nuk_{\mathrm{a}}}{d_{\mathrm{h}}} \tag{2.60}$$

$$d_{\mathrm{h}} = 2(\mathrm{W}\text{-}2\delta) \tag{2.61}$$

Then the mass transfer coefficient was obtained from the Chilton-Coulburn analogy,

$$\alpha_{\mathrm{D}} = \frac{\alpha_{\mathrm{C}}}{C_{\mathrm{p,a}}}\left(\frac{D_{\mathrm{t}}}{D_{\mathrm{m,a}}}\right)^{-2/3} \tag{2.62}$$

In each control volume, various parameters, including the film thickness δ, hydraulic diameter d_{h}, heat transfer coefficient α_{C}, and mass transfer coefficient α_{D} were calculated on the basis of the inlet conditions. In this way, the impact of the film thickness variation on the heat and mass transfer process was introduced into the model.

Recently, Peng and Pan (Peng and Pan 2009) investigated the transient performance of the liquid desiccant dehumidifier with a one-dimensional non-equilibrium heat and mass transfer model. Unlike the previous study, the local volume average equations of heat and mass transfer were developed in the work, which were solved by *Tri*Diagonal-Matrix Algorithm (TDMA).

In the later year, Diaz (Diaz 2010) also developed a transient two dimensional model for a parallel-flow liquid-desiccant dehumidifier. The geometrical model was almost the same with that of Mesquita et al. (Mesquita 2006). The difference of the governing equations lies in that the present model took the time item into consideration. Some non-dimensional parameters were used to simplify the calculation process. With the model, the variations of some critical variables over time

were illustrated and the effects of oscillatory behavior were analyzed in depth.

2.2.2.4 Summary

The detail information of the mathematical models for the internally cooled dehumidifier is listed in Table 2.3.

The models for internally cooled dehumidifier without considering the film thickness are very similar to those used in the adiabatic dehumidifier. However, the former ones are more complicated due to the involvement of the cooling fluid. These models ignore the effect of the velocity field. Thus, the results of these models have certain discrepancy with the reality, as velocity, mass and energy have strong coupling relationship.

In the models considering uniform film thickness, the film thickness and velocity are usually calculated at the beginning and then keep constant through the whole calculation. The simulation results justified that the constant thickness models under-predicted the dehumidification, especially for low desiccant mass flow rate.

For the models considering variable film thickness, all of the velocity, mass and energy equations are solved together. In the process of each iteration, the film thickness and velocity change, so the influence of the flow on the heat and mass transfer can be demonstrated. Thus, the model is most accurate.

Table 2.3 Detail information of the mathematical models for internally cooled dehumidifier

Classification	Model	Flow pattern (air/desiccant)	Flow pattern (desiccant/cooling fluid)	Cooling fluid
Regardless of film thickness	Khan and Martinez 1998	Counter	Counter	Water and air
	Saman and Alizadeh 2001	Counter	Cross	Water and air
	Liu et al. 2009	Six different configurations		Water
	Yin et al. 2009	Cocurrent	Cocurrent	Water
	Khan and Sulsona 1998	Cross	Cross	Ammonia
	Ren et al. 2007	Four possible flow arrangements		-
Uniform film thickness	Park et al. 1994	Cross	Cross	R22
	Ali et al. (Ali et al. 2003; Ali et al. 2004; Ali and Vafai 2004)	Cocurrent/counter /cross	-	-
	Mesquita et al. 2006	Counter	Counter	Water
	Dai and Zhang 2004	Cross	-	-
Variable film thickness	Mesquita et al. 2006	Counter	Counter	Water
	Hueffed et al. 2009	Cross	-	-
	Peng and pan 2009	Counter	-	-
	Diaz 2010	Cocurrent	-	-

2.3 Review of experiment research

Except for simulation, lots of experiments have been conducted to investigate the heat and mass transfer performance of the dehumidifier.

For the adiabatic dehumidifier, more attention is paid on the packed bed dehumidifier. Chung and Wu (Chung and Wu 1998) pointed out in the packed bed dehumidifier, the liquid flow rate should be higher than the minimum rate calculated from the equilibrium data to be applied in the real operating conditions. Chung et al. (Chung et al. 1995) concluded the heat and mass transfer coefficients of a packed bed dehumidifier and researched on the decontamination function of TEG under different conditions. Oberg and Goswami (Oberg and Goswami 1998) investigated the heat and mass transfer characteristics of a packed bed dehumidifier and assessed its rate of dehumidification and effectiveness, with TEG as desiccant. Lazzarin et al. (Lazzarin et al. 1999) checked the feasibility of applying the packed tower for liquid desiccant systems in air conditioning. It was found that the appropriate choice of flow ratios could improve the dehumidification efficiency. Chung and Wu (Chung and Wu 2000) designed a packed tower with an inverse U-shaped tunnel and the mass transfer coefficient using the vapor pressure of the desiccant solution was developed, with LiCl as desiccant. Fumo and Goswami (Fumo and Goswami 2002) studied the effects of various variables on the rates of dehumidification, regeneration and the relevant effectiveness in packed bed dehumidifier and regenerator, with LiCl as desiccant.

Zurigat et al. (Zurigat et al. 2004) analyzed the variation trend of the moisture removal rate and the effectiveness under the change of various inlet parameters for both the wood and aluminum packings, with TEG as desiccant. Longo and Gasparella (Longo and Gasparella 2005) compared the performance of three different desiccants and found out the new solution H_2O/KCOOH would be a substitute of the traditional desiccants, like LiCl and LiBr solutions. Liu et al. (Liu et al. 2006) studied a cross flow dehumidifier with Celdek structured packings, using LiBr as desiccant. Two indices- moisture removal rate and effectiveness were chosen to evaluate the dehumidifier performance. Xiong et al. (Xiong et al. 2010) developed a two-stage liquid desiccant dehumidification system, whose coefficient of performance and exergy efficiency were elevated both compared with the basic system.

For the internally cooled dehumidifier, less literature are reported than the adiabatic dehumidifier. Chung and Wu (Chung and Wu 1998) added the spray tower with some fin coils of refrigerant flowing, providing the absorber with a lower temperature and resulting in better mass transfer performance. Deng and Ma (Deng and Ma 1999) reported the experimental studies of a film dehumidifier, modifying the Nusselt number by considering the effect of inlet solution concentration. Jain et al. (Jain et al. 2000) introduced two wetness factors to calculate the actual wetting area, by comparing the experimental data with the predicted results. Saman and Alizadeh (Saman and Alizadeh 2002) designed a cross-flow type plate heat

exchanger/dehumidifier. Three different sets of experiments were carried out and it was found that with liquid desiccant, the performance of the heat exchanger was improved. Islam et al. (Islam et al. 2003) invented a film inverting absorber on the basis of the fluid flow characteristics of the film. Compared with the tubular absorber, the novel absorber could increase the vapour mass flux by about 100% at most. Yin et al. (Yin et al. 2008) investigated the behavior of a new internally cooled countercurrent dehumidifier based on the plate-fin heat exchanger by experiment. Bansal et al. (Bansal et al. 2011) compared the moisture removal and effectiveness of an adiabatic dehumidifier and an internally cooled one. In the experiment, the desiccant solution and the air flowed in a cross configuration. It was found the latter performed obviously better than the former.

2.4 Limitations in the past studies

2.4.1 Limitations of simulation models

Through the above detailed description, several shortcomings of the above models can be found.

Firstly, it can be noted that most of the models focus on the macroscopic parameter change of the air and desiccant solution rather than the microscopic heat and mass transfer process in the dehumidifier. Thus, it is understandable that they make a lot of

assumptions in order to launch the calculations. However, the optimal design and operation of the dehumidifier need the understanding of the microscopic and underlying heat and mass transport processes.

Secondly, all of the above models assume the flow to be steady state. But in the real condition, the failing film generally has strong volatility, which affects the heat and mass transfer process significantly. For example, Frisk and Davis (Frisk and Davis 1972) and Goren and Mani (Goren and Mani 1968) have shown that heat/mass transport across a wavy film can increase by as much as 10–100% compared to flat films. On the contrary, after the heat and mass transfer happens at the gas-liquid interface, the temperature and concentration of the solution will change, resulting in the flow change of the film interface. The mutual interaction suggests that the unsteady flow should be considered simultaneously in a coupled manner with the heat and mass transfer processes. Although the model of the heat and mass transfer with the interface fluctuation has been established in the field of chemical engineering, there is no literature about the model applied in dehumidification.

Thirdly, all of the models do not take into account the surface tension between the desiccant solution and the air. However, in some instances, it may be necessary to include the vapor-liquid hydrodynamic interaction in more detail, especially when there are some surface waves.

2.4.2 Limitations of experimental research

In summary, the effect of various design operating parameters and conditions on the performance of the dehumidifier has been analyzed experimentally in previous studies. The factors are evaluated specifically, including the desiccant fluid properties (like density, viscosity, and specific heat capacity and so on), the packing type, the flow configuration, the desiccant distribution, the inlet flow rate and condition of the desiccant solution, moist air and cooling media, energy store capacity and so on. However, there are also several drawbacks to be listed out.

Firstly, the specific flow conditions in the dehumidifier interior were seldom observed experimentally. In addition, the effect of the flow on the heat and mass transfer is also an aspect needed for further research.

Secondly, most of the previous dehumidifiers were complicated in terms of structure, which made it difficult to observe the real contact area for heat and mass transfer. This might result in big error in calculating the mass transfer coefficient.

Finally, the liquid desiccant dehumidifier is very suitable for the hot and humid area. However, its application for this kind of climate is still limited.

2.5 Review of simulation studies based on CFD

To model the coupled flow, heat and mass transfer process in the devices is not an easy target. Firstly, it should consider the hydrodynamic behavior of the flow as it has great influence on the performance of the heat and mass transfer within the absorber. Thus, in the beginning, the research of the hydrodynamic behavior of the flow is introduced. The studies of the film flow date back to the early 20th century. Hopf (Hopf 1910) and Nusselt (Nusselt 1916) investigated the uniform film flow on an inclined plate and proposed the theory of falling film. Then many scholars (Kapitza 1948; Benjamin 1957; Yih 1963; Pierson and Whitaker 1977; Benney 1966; Nakaya and Takaki 1967) carried out the theoretical research of the conditions for interface instability, wave frequency and wave velocity through the linear and nonlinear stability analyze method. With the development of the understanding of the film stability, the research focus has been turned to the relevant knowledge about the wave shape of the liquid film interface, the change rule and the wave internal flow characteristics.

In 2003, Szulczewska et al. (Szulczewska et al. 2003) established a CFD model of the two-phase flow in the plate-type structured packing. The model was intended to estimate the optimum liquid and gas flow rates for wetting the surface. In 2004, Gu et al. (Gu et al. 2004) used the CFD model to study the hydrodynamics of film flow on inclined plates, analyzing the influence of the surface, liquid properties and gas flow rate on the flow action. In 2005, Valluri et al. (Valluri et al. 2005) built a model to study

the dynamic characteristics of waves at low and moderate Reynolds number over corrugated surfaces. The ratio of film interfacial area to that of the substrate could be predicted by the model. In 2005, Hoffmann et al. (Hoffmann et al. 2005) investigated the flow behavior on an inclined plate by means of two and three dimensional numerical simulations. They also did the experiment with the technology of particle tracking speed to verify the correctness of the model. In 2006, Ataki and Bart (Ataki and Bart 2006) simulated the film flow for an X-shape structured packing with the three-dimensional CFD model, and obtained the effective wetting area and liquid holdup. In 2011, Min and Park (Min and Park 2011) studied the wavy laminar flow with the Reynolds number of 200 to 1000 numerically. The results showed good agreement with the experimental one in terms of the wave shape, thus the numerical method was regarded as accurately to predict the wavy film motions. In 2011, Shojaee et al. (Shojaee et al. 2011) pointed out that the gas and liquid flow rates affected the interfacial area of the packed bed significantly. The results of the three-dimensional model showed good agreement with the existing data. To sum up, a large number of studies had been done about the liquid films to analyze the influence of the flow regimes, geometries, and boundary conditions.

There are also a number of literatures reporting the research of the film flow considering the heat and mass transfer. In 1997, Jayanti and Hewitt (Jayanti and Hewitt 1997) studied the hydrodynamics and heat transfer of thin film flow with CFD

techniques. They obtained the velocity and temperature fields and pointed out that waves enhanced the heat transfer rather than determined it. In 2006, Liu et al. (Liu et al. 2006) promoted a complicated computational mass transfer model to investigate the chemical absorption process with heat transfer. The model was capable of predicting the turbulent mass and heat transfer diffusivity. In 2006, Carlo et al. (Carlo, 2006) set up a simple model to assess the dynamics and mass transfer efficiency of distillation columns, proofing that the efficiency of the structured packing could be predicted without the adjustable parameters while the semi-empirical correlations of the pressure drop and absorption coefficient were needed. In 2007, Fard et al. (Fard et al. 2007) studied the hydrodynamic and heat transfer parameters of some distillation column with CFD method. The results of the pressure drop and mass transfer presented good agreement with the experimental ones, which confirmed the value of applying CFD tools in the research. In 2007, Banerjee (Banerjee 2007) applied a numerical model to evaluate the heat and mass transfer from the surface of liquid ethanol. The effect of several variables like the gas inlet velocity, temperature, and vapor mass fraction on the heat and mass transfer characteristics were analyzed in detail. In 2008, Nikou and Ehsani (Nikou and Ehsani 2008) compared the results of the $k-\varepsilon$, RNG $k-\varepsilon$, $k-w$ and BSL turbulence models and concluded that $k-w$ is the best model for simulation in structured packing. In 2010, Haelssig et al. (Haelssig et al. 2010) established the multi-component gas-liquid heat transfer model with the direct numerical simulation method. The model could predict the local

information, which could be applied to large scale process of the equipment. In 2012, Haroun et al. (Haroun et al. 2012) investigated the liquid hold-up and the mass transfer as function of liquid flow rate and structured packing geometry. As for the mass transfer, the exposure time was adjusted by taking physical and geometric parameters into consideration.

To sum up, CFD provides the possibility to analyze the phenomena at temporal and spatial scales. It is capable for predicting the velocity, pressure, temperature and concentration profiles in very complicated systems by solving the continuity, momentum, energy and species equations. Especially, with the rapid development of computer hardware and software, it becomes more available to use the CFD technology to describe accurately the complex behaviors of the gas-liquid two-phase flow and the relevant heat and mass transfer in the absorption and separation process. Moreover, CFD simulation can be a quick and cheap means for design and optimization of the component (Sideman and Moalem-Maron 1982).

Till date, lots of literatures reporting using CFD method to simulate the flow patterns as well as heat and mass transfer within the absorption towers, evaporators, and direct contact condensation units. However, when it comes to the air dehumidifier, seldom literature is reported. In the dehumidifier, the fluid dynamics and vapor absorption by the desiccant solution are mutually coupled, so this case can be used in a CFD

calculation model, where both fluid dynamics and vapor absorption can be treated simultaneously.

2.6 Review of interface tracking methods

For the gas-liquid two-phase flow, it is important to identify the interface dynamics, by which the relevant inter-phase transfer mechanisms can be quantified. However, it is very difficult to investigate the free surface wave characteristics of liquid films for its dynamic and arbitrary nature. Two methods for describing the fluid regions are Euler and Lagrangian representations. The grid is always fixed for Euler method while the grid moves with the interface for the Lagrangian method. For fixed finite difference grids, there are four methods used for embedding free boundaries in finite-difference or finite-element grids, including the Height Functions, Line Segments, Marker Particles and Volume of Fluid (VOF) methods (Hirt and Nichols 1981). Their advantages and disadvantages are listed in Table 2.4.

Among various free boundary methods, the VOF method has been the most popular method to simulate the free surface flow as it is more flexible and efficient than other methods for treating complicated free boundary configurations (Hirt and Nichols 1981).

Table 2.4 The introduction of four free boundary methods

Height Functions	Define the surface	Advantages	Extremely efficient, only requiring a one-dimensional storage array for recording
			Be extendable to three-dimensional situations
		Disadvantages	Not applicable when the boundary slope exceeds the mesh cell aspect ratio
			Not applicable for multiple-valued surfaces problems, like the bubbles or drops
Line Segments		Advantages	Not limited to single-valued surfaces
			More flexible than a Lagrangian mesh line
		Disadvantages	More storage is required
			Not easy for surface intersection and folds
			Not easy for extension to three-dimensional surfaces
Marker Particles	Define the region	Advantages	Simple logically for situations involving interacting multiple free boundaries
			Readily extendable to three-dimensional situations
		Disadvantages	Require significantly more storage
			Require additional time to move all the points to new locations
Volume Of Fluid		Advantages	Require minimum storage
			Avoid the logic problems related to intersecting surfaces
			Applicable for three-dimensional computations
		Disadvantages	Be difficult to calculate the interface curvature
			Inherent numerical smearing

VOF method is on the basis of the volume averaging of the phases and the volume fraction is treated as a single field, which is advected in an Eulerian way. The interface is being reconstructed based on the solution of a transport equation for the volume fraction. The advantages with VOF method are that it requires minimum storage space, treats intersecting free boundaries automatically, and can be rather easily extendable to three-dimensional calculations. According to the literature, the main drawback is it has difficulty for calculating the interface curvature as VOF approach has the possibility of smearing the fraction function due to the false diffusion of numerical scheme (Min and Park 2011).

There are numerous computational techniques to improve the accuracy of surface tracking by VOF. As shown in Fig. 2.12, Hirt and Nichols (Hirt and Nichols 1981) suggested a simple method- the donor and acceptor method in which the portion of each interface in a cell is approximated by a piecewise-constant line, either vertically or horizontally. This technique has been successfully implemented to many complex problems in which several interfaces were present.

The PLIC (Piecewise Linear Interface Calculation) technique suggested by Youngs (Youngs 1982) represents the interfaces more accurately. In this method, the volume fractions of the material in the objective cell and the eight surrounding cells are used to evaluate the slope of the interface. Then the cell is divided into two areas which

match the two volume fractions by adjusting the interface position. As this method determines the interface in each cell independently, the interface is not continuous across the cells. However, the method is found to perform better to represent the interface location (Fluent 6.3 Users Guide).

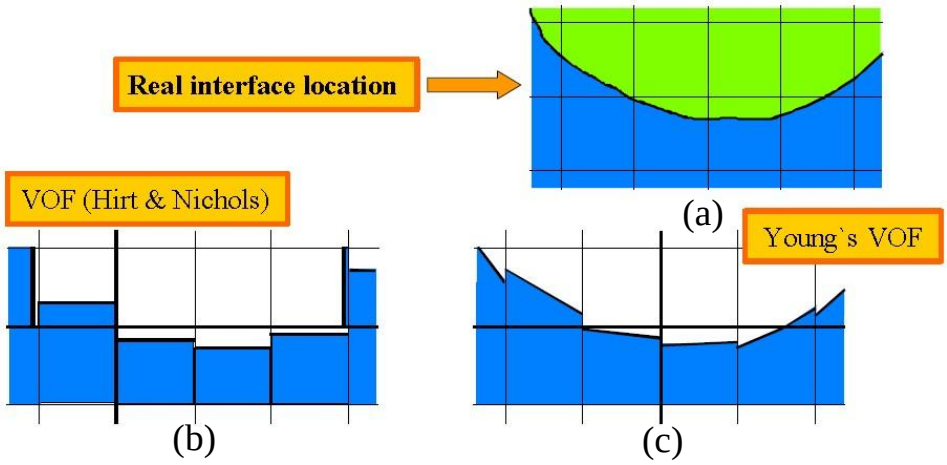

Fig. 2.12 Interface construction schemes: (a) real interface location, (b) donor-acceptor scheme, and (c) geometric reconstruction (PLIC) scheme (Min and Park 2011)

2.7 Review of mass transfer theories

The process of mass transfer is involved in lots of fields, such as distillation, absorption, extraction and so forth. Thus, it is critical to have a good master of the mass transfer mechanism so as to evaluate the specific design of the equipment and optimize its operation conditions. Since the beginning of the previous century, there

have been some models to calculate the interface mass transfer coefficient. Until now, they are still the foundation for mass transfer research, being applied in many practical cases. The most classic and typical theories include film theory, penetration theory and surface renewal theory.

2.7.1 Film theory

It is Nernset (Nernset 1904) who proposed the film theory first in 1904. He assumed that the whole resistance of mass transfer in a given phase lay in a thin and stagnant region of that phase at the interface. This region is called film. Based on it, Whitman (Whitman 1923) developed the two-film theory. It is supposed: 1) at the interphase, there is a state of equilibrium for the two phase, 2) two laminar sub layers exist at both side of the interface and the main transport resistance lies in the two thin and stagnant films, 3) the mass transfer process in the two films can be described by diffusion, 4) the concentrations are uniform for the bulk phases. The specific transport mechanism is shown in Fig. 2.13. Where, P_{A} is the partial pressure of component A in the gas phase and C_{A} is the mole fraction of component A in the liquid phase.

With the known molecular diffusivity and film thickness of the two phases, the mass transfer coefficients can be obtained by,

$$\alpha^*_{D1} = \frac{D_{m1}}{\delta_1} \tag{2.63}$$

$$\alpha^*_{D2} = \frac{D_{m2}}{\delta_2} \tag{2.64}$$

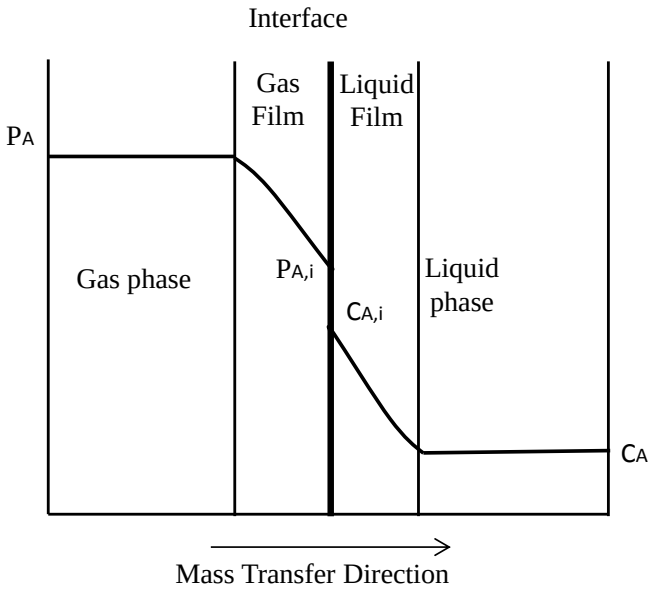

Fig. 2.13 Schematic diagram of two-film theory

The two film theory is very easy to understand and apply, but it has several drawbacks. Firstly, it is not reasonable to predict that the rate of mass transfer is directly proportional to the molecular diffusivity. Secondly, it is difficult to determine the thickness of the two laminar sub layers by experiment. Finally, the convective mass transfer in the thin films is neglected, so the theory is only suitable for the steady mass transfer process.

2.7.2 Penetration theory

The penetration theory was proposed by Higbie in 1935 (Higbie 1935). In the theory, the fluid element moves from the bulk with uniform concentration to the interface. Though a certain contact time t_c with the interface, the element return to the bulk of the fluid, took place by a new element. It is noted that the mass transfer occurs with molecular diffusion at the interface and the process is transient in nature. Fig. 2.14 shows the sketch of mass transfer process.

The mass transfer coefficient of the theory is calculated by,

$$\alpha^*_{\mathrm{D}}=2\sqrt{\frac{D_{\mathrm{m}}}{\pi t_{\mathrm{c}}}} \tag{2.65}$$

It can be found that in the film theory, the mass transfer coefficient is proportional to the molecular diffusivity, that is $\alpha^*_{\mathrm{D}} \propto D_{\mathrm{m}}$. While in the penetration theory, the mass transfer coefficient has a quadratic root relationship with the molecular diffusivity, that is $\alpha^*_{\mathrm{D}} \propto D_{\mathrm{m}}^{1/2}$. According to the experiment, for most of the convective mass transfer process, the relationship of the mass transfer coefficient and the molecular diffusivity can be presented by,

$$\alpha^*_{\mathrm{D}} \propto D_{\mathrm{m}}^{\mathrm{n}},\ (\mathrm{n} = 0.5\text{ -}1.0) \tag{2.66}$$

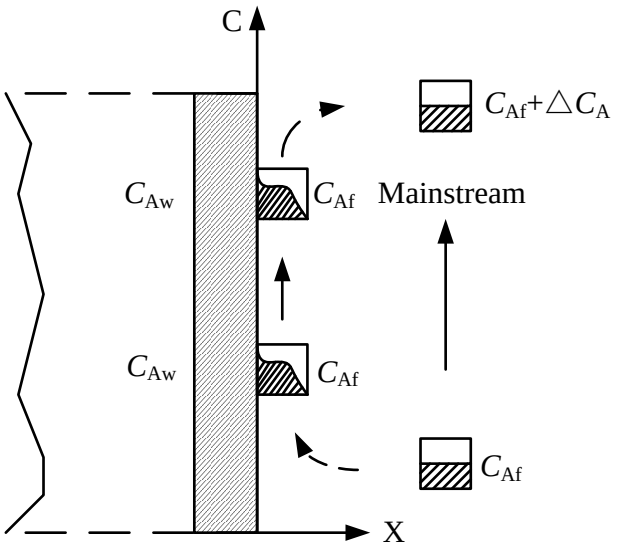

Fig. 2.14 Schematic diagram of penetration theory

2.7.3 Surface renewal theory

As it is not easy to decide the effective contact time t_c, Danckwerts improved the penetration theory by introducing a factor- surface replacement rate (s) in 1951 (Danckwerts 1951). The definition of s is the fraction of elements that is replaced per unit time. It is assumed that in a given time, the chance of a surface element being took place depends on its age. That is to say, each element has an equal chance of being replaced during the next time unit (Westerterp and Wijingaarden 2000). Thus, the mass transfer coefficient is as follows,

$$\alpha^*_D=\sqrt{D_m s} \tag{2.67}$$

Usually, the surface replacement rate is obtained by experiment. It has a great relationship with the dynamic conditions, flow geometry and so on.

2.8 Review of methods for film thickness measurement

With the development of the measurement technologies, it becomes possible to study the flow in micro scale by experiment. Different methods have been used to measure the film flow, including the electrical resistance method, electrical capacitance method, and laser displacement sensor method. In the following, the principle and application are introduced briefly.

2.8.1 Electrical resistance method

The schematic diagram of measuring the film thickness by electrical resistance is presented in Fig. 2.15 (Burns et al. 2003).

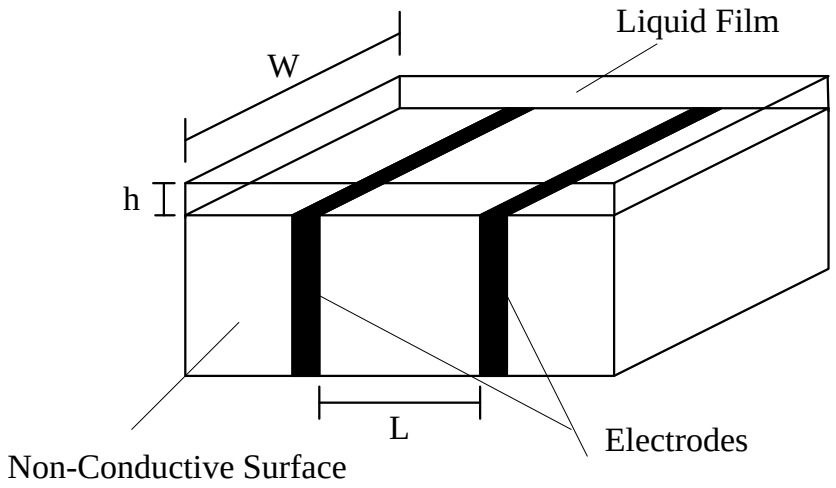

Fig. 2.15 Concept of film thickness measurement technique

(Burns et al. 2003)

The resistance between two electrodes with a distance L can be written as follows,

$$R = \frac{kL}{Wh}\tau \tag{2.68}$$

where k is the resistivity of the liquid. W is the width of the film and h the thickness of the film. τ is the tortuosity of the electrical path between the electrodes.

For the application, Coney (Coney 1973) provided a theory to predict the relationship between the electrical conductance of the probe and the film thickness. Thwaites et al. (Thwaites et al. 1976) used the electrical conductive probes to measure the film properties, like the film thickness, wavy frequency and velocities. Burns et al. (Burns et al. 2003) used the electrical resistance method to measure the liquid film thickness on a spinning disc surface. The method was simple and the results based on the film thickness showed good consistency with a two-dimensional model. Hotta et al. (Hotta et al. 2004) measured the average oil film thickness through the electric resistance method, whose data were utilized to analyze the situation of lubrication state on sliding parts of swash plate type compressors. It is noted that the method is simple and widely used in macro-scale systems. And it requires that the liquid is electrically conducting.

2.8.2 Electrical capacitance method

Fig. 2.16 shows the principle for the capacitance measurement (Zhang et al. 2009). A capacitor consists of two conductive plates, filled with a dielectric medium between

them. When the distance of the gap h or the medium changes, the capacitor voltage changes accordingly.

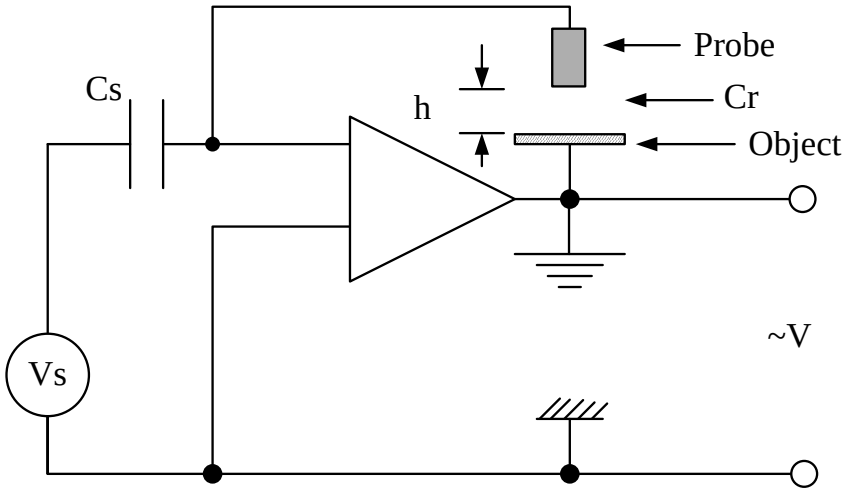

Fig. 2.16 Sketch of the circuitry

(Zhang et al. 2009)

In terms of the feedback operational amplifier, the equation between the source voltage V_S and the output voltage is as follows,

$$V = -\frac{C_S}{C_T} V_S \tag{2.69}$$

where C_S and C_T represent the standard capacitance and parallel plate capacitance, respectively.

C_T is calculated by the theory of parallel plate capacitor,

$$C_T = \frac{\varepsilon_o s}{h} \tag{2.70}$$

where ε_o is the permittivity of the medium, s is the area of the cross section of the

probe, and h is the distance between the probe and the object.

Combining the above two equations,

$$V = -\frac{C_S V_S}{\varepsilon_o s} h \tag{2.71}$$

Through the above equation, it is known that with a certain s, V_S, ε_o (a given medium), the output voltage V is proportional to h.

The schematic diagram of measuring the film thickness by electrical capacitance is depicted in Fig. 2.17. In the process of measurement, the air is the dielectric medium and the liquid surface is one of the two electrodes. When another electrode- the probe is fixed, that is, the distance between the probe and the plate is fixed, the output voltage of the capacitor made up of the probe and the liquid surface is proportional to the film thickness.

In 1992, Klausner et al. (Klausner et al. 1992) proposed a novel method for measuring the liquid film thickness in temperature-dependent flow fields. The results of measuring the film thickness range of 25mm with the capacitance probe were in line with those with a charge coupled device camera. In 2007, Liu et al. (Liu et al. 2007) installed an electrical capacitance sensor with eight electrodes in a two-phase closed thermosyphon. Results are compared with those of the Nusselt theory and

CFD simulation, and it was found agreements and discrepancies were observed for different thresholds. In 2008, Zhang et al. (Zhang et al. 2009) investigated the surface wave and film thickness of the heated falling film with highly sensitive infrared camera system- ThermaCAM^{TM} SC3000 and electrical capacitance method. The Marangoni phenomena and their effect on the flow were analyzed in detail.

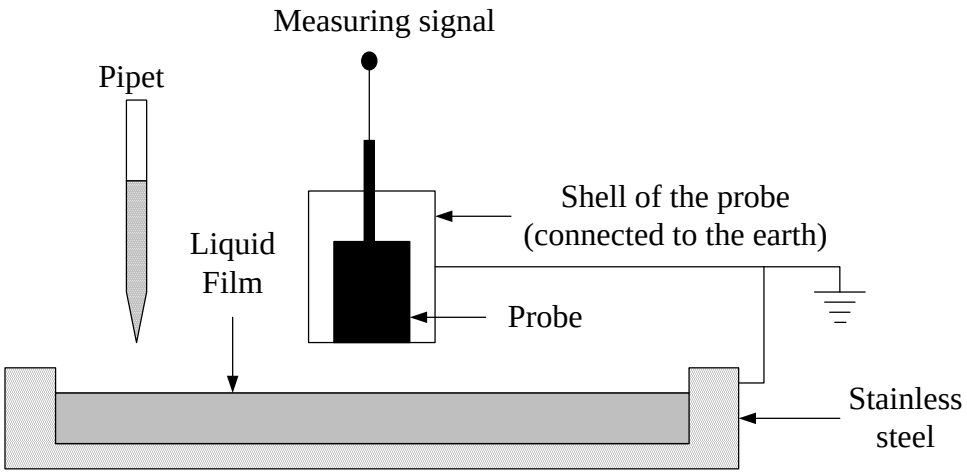

Fig. 2.17 Sketch of the calibration

(Zhang et al. 2009)

2.8.3 Laser focus displacement (LFD) sensor measurement

The device is mainly composed of the semiconductor laser, half-reflection mirror, objective lens, sensitive element, pinhole, diapason, and so on. As shown in Fig. 2.18 (Takamasaa and Hazuku 2000, 1), the conical laser beam gave out by the semiconductor laser goes through the half-reflection mirror and an objective lens, and arrives at the measured surface. Part of the light is reflected by the objective surface,

passes backward through the objective lens, reflected by the mirror, and reaches a pinhole. It is noted that the objective lens can be moved frequently by the diapason and the displacement is detected by a position sensor. According to the mutual-focusing theory, only when the laser beam focus on the objective surface, the reflection beam can be detected by the sensor set up behind the pinhole. Then the displacement of the surface can be related to the displacement of the objective lens. This method is very accurate with high temporal and spatial resolutions.

Takamasa and Hazuku (Takamasaa and Hazuku 2000, 1) presented using two laser focus displacement meters to measure the film flowing down a vertical wall. The sensitivity is 2 μm and 1 kHz of measuring the film thickness. A similar work was done by Takamasa and Hazuku (Takamasa and Hazuku 2000, 2) to study the film thickness of water flowing downwards the inner wall of a vertical tube. Han and Shikazono (Han and Shikazono 2008) used the laser focus displacement meter to measure the thickness of the thin liquid film of a slug flow. The effects of the capillary number, inertia force, bubble length, gravity and so forth on the flow were investigated specifically. Hazuku et al. (Hazuku et al. 2008) continued utilizing LFD to research the interfacial wave structure of the annular two-phase flow. By the experimental data, the minimum film thickness could be predicted by the Reynolds number of the liquid and the interfacial shear stress.

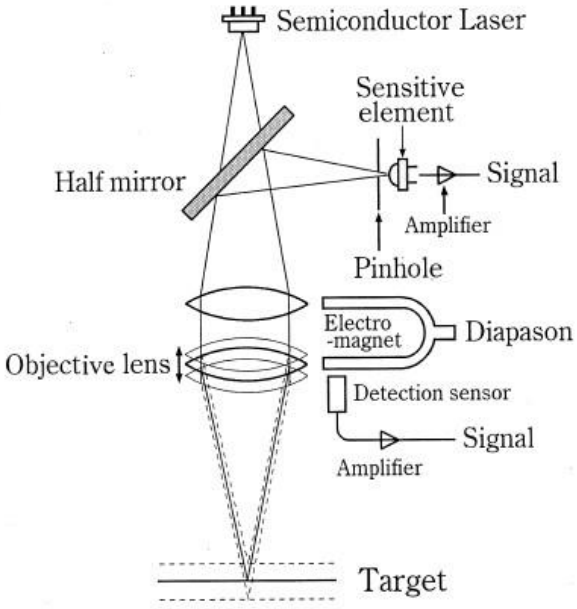

Fig. 2.18 A schematic diagram of an LFD

(Takamasaa and Hazuku 2000, 1)

To sum up, the electrical methods are simple and low cost, which is able to obtain the film's spatially averaged thickness, but not applicable for the film's wavy behaviors, such as the wave frequency, amplitude, and so on. The laser focus displacement sensor has higher temporal and spatial resolutions, yet it is more expensive compared to the electrical methods.

2.9 Research methodology of present work

As mentioned before that CFD is a sophisticated analysis technique to predict the fluid flow behavior, heat and mass transfer performance of the structure or the component. Therefore, CFD software Fluent is utilized for investigation. As the interior structure

of the dehumidifier is rather complicated, it is very difficult to describe the flow and transfer behavior in the whole dehumidifier. Here, the interior structure of the dehumidifier is simplified to a group of parallel and vertical plate channels. Based on the simplification, the two dimensional symmetrical model can be used to simulate the flow and transfer process.

The relevant technologies include: the geometric reconstruction (PLIC) for tracking the interface of the gas and liquid; the continuum surface tension (CSF) model for analyzing the influence of the surface tension; and the species transport model for simulating the mass transfer between the solution and the moist air. The physical properties of the desiccant solution and the mass transfer mechanism are needed to be added to Fluent with user defined files of the C program.

For the experiment, a single channel dehumidifier is designed to observe the flow behavior. A camera will be used to record the images of the liquid film and some flow patterns will be recorded using the video. The pictures will be dealt by the Microsoft Visio and GetData Graph Digitizer to obtain the results of the coverage ratio. The minimum wetting rate will be investigated and compared with the literature and simulation results. The capacitance probe will be employed to measure the temporal film thickness for both of the upper and lower parts of the film. Based on the data, the mean film thickness will be calculated and compared with the results of the literature

and the simulation model. The temporal film thickness for the lower part will be studied with the statistical method.

Then, the performance of the single channel dehumidifier under the climate of Hong Kong will be investigated by analyzing the inlet and outlet parameters of various fluids. The influences of the inlet parameters on the absolute humidity change and mass transfer coefficient will be introduced in detail. The results will be compared with those of the previous studies and explained in terms of the flow behavior as well.

It is important to point out due to time consuming calculation, the geometric size of the simulation model is set smaller than that of the experiment. Even though there exists some discrepancy between the results of the two methods, the same variation tendency can prove the correctness of each other.

For convenient reading, a flow chart of the methodology is summarized and presented in Fig. 2.19.

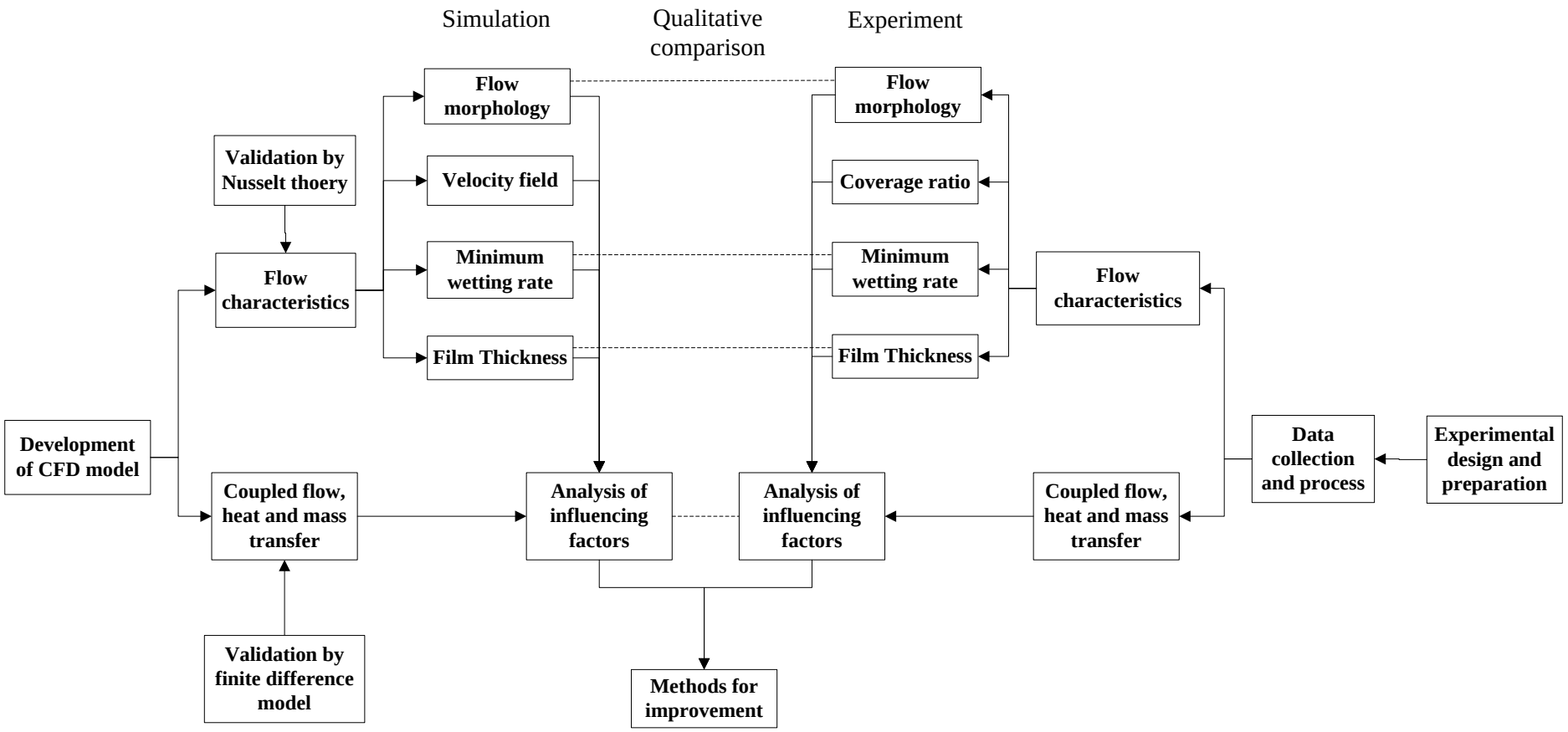

Fig. 2.19 Flow chart of methodology

CHAPTER 3

NUMERICAL SIMULATION OF THE FLOW CHARACTERISTICS

3.1 Introduction

In the interior of the packed bed dehumidifier, a very popular one, the liquid solution flows down along the packing wall under the action of gravity, forming film flow with heat and mass transfer. It is verified that the use of film for mass transport provides small thermal resistance, large contact area and drastic enhancement of mass transport as well (Colinet et al. 2001). Thus, it is extremely important to have a good master of the mechanism of the film flow. However, very few literatures have been reported about its study (Grossman 1983; Grossman 1984). In terms of the research of the dehumidifier, it is found that most of the previous studies focus on the macroscopic parameter changes of the air and desiccant solution, i.e., the outlet values of the variables (Luo et al. 2011; Luo et al. 2012). However, the optimal design and operation of the dehumidifier need the understanding of the microscopic and dynamic flow mechanism. Therefore, the study of the flow situation in the dehumidifier interior is desperately needed.

Computer simulation is a good approach to realize the above target due to its cost and time savings. In fact, according to the literatures, the flow and its impact on mass transfer have been investigated widely with CFD software in the field of chemical engineering and desalination industries. They were verified to be able to describe accurately the complex behaviors of the gas-liquid two-phase flow and the relevant mass transfer in the absorption and separation processes within the evaporators, absorption towers, and direct contact condensation units (Khosravi Nikou and Ehsani 2008; Haelssig and Treblay 2010; Haroun et al. 2012). When it comes to the air dehumidifier, the fluid dynamics and vapor absorption by the desiccant solution are mutually coupled, so that it can also be simulated by CFD software, with which both fluid dynamics and vapor absorption can be dealt with simultaneously.

Therefore, this chapter focused on studying the flow dynamics in the liquid desiccant dehumidifier microscopically and dynamically with the CFD software Fluent. With the established model, the mechanism of the gas-liquid flow in the dehumidifier was illustrated. The velocity profiles, the minimum wetting rate, the effective interfacial areas between the solution and air, the average and local film thickness at different conditions were investigated.

3.2 Physical model

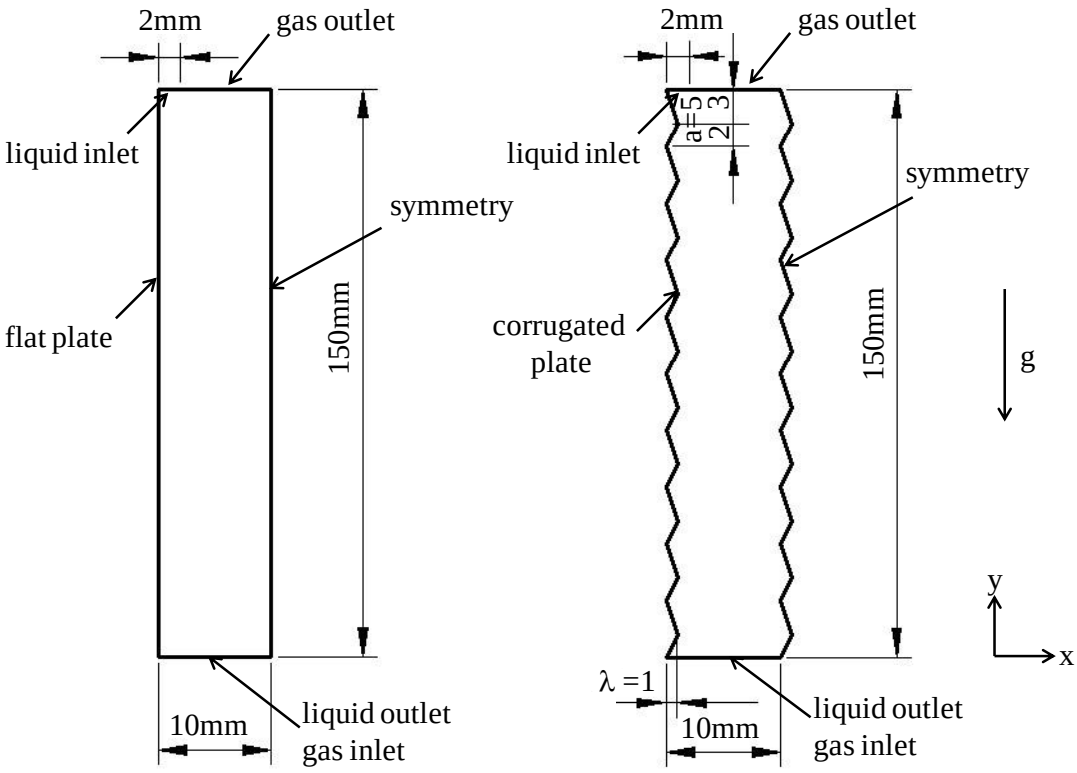

Fig. 3.1 Schematic of the simplified physical model

To improve the capacity of the process equipment, the structured packing Mellapak 250Y has found wide application in the petrochemical, oil and gas industries as well as in the air handling unit. In the paper, a flat plate and a plate-type structured packing Mellapak 250Y were chosen as the modeled objectives. Numerical simulations were conducted for the unsteady two-phase flow with free liquid surface in the channel between two flat or corrugated plates. The simplified geometric constructions are presented in Fig. 3.1. The length of both of the plates was 150 mm and the distance between the plates was 20 mm. The liquid desiccant solution was

supplied to the upper-left hole to the plate while the moist air was introduced by the bottom-right hole. Thus, the liquid and gas flowed counter-currently. The point at the bottom-left corner was set as the origin (0, 0) of the orthogonal coordinates.

3.3 Mathematical model

3.3.1 Governing equations

The VOF (Volume of Fraction) model, especially the one with the PLIC technique, is flexible and efficient to track the free surface of the two phase flow (Youngs 1982). Therefore, it was employed here for simulation. In the following, the VOF method, momentum, energy, species and turbulence equations used in this study are introduced in detail.

(1) VOF model

For the gas-liquid two-phase system, the mass and momentum conservation equations are based on the volume fractions of the gas and liquid. The properties ρ (density) and μ (viscosity) in each computational cell are represented by,

$$\rho = \alpha_{\mathrm{l}}\rho_{\mathrm{l}} + \alpha_{\mathrm{g}}\rho_{\mathrm{g}} \tag{3.1}$$

$$\mu = \alpha_{\mathrm{l}}\mu_{\mathrm{l}} + \alpha_{\mathrm{g}}\mu_{\mathrm{g}} \tag{3.2}$$

If the liquid phase is set as the secondary phase of the VOF model, the movement of

the phase interface will be decided by α_1, which is the volume fraction of the liquid phase. The relationship of the value and the state of the cell is,

$$\begin{cases} \alpha_1 = 1, \text{ the cell is full of the liquid} \\ 0 < \alpha_1 < 1, \text{ the cell contains the interface between the liquid and the gas} \\ \alpha_1 = 0, \text{ the cell is empty of the liquid} \end{cases}$$

Thus, the interface between the gas and liquid can be tracked by solving the following continuity equation for the volume fraction,

$$\frac{\partial \alpha_1}{\partial t} + \boldsymbol{u} \cdot \nabla \alpha_1 = 0 \tag{3.3}$$

Then, the volume fraction for the gas will be achieved by the equation,

$$\alpha_g + \alpha_1 = 1 \tag{3.4}$$

The solution method is similar when choosing the gas phase as the secondary phase in the VOF model.

(2) Mass conservation equation

$$\frac{\partial}{\partial t}(\rho) + \nabla \cdot (\rho \boldsymbol{u}) = 0 \tag{3.5}$$

(3) Momentum conservation equation

$$\frac{\partial}{\partial t}(\rho \boldsymbol{u}) + \nabla \cdot (\rho \boldsymbol{u}\boldsymbol{u}) = -\nabla P + \nabla \cdot (\mu(\nabla \boldsymbol{u} + \nabla \boldsymbol{u}^T)) + \rho \boldsymbol{g} + \boldsymbol{F} \tag{3.6}$$

(4) Turbulence model

In the project, the flow form was gas liquid two phase flow with clear interface. The liquid solution flow $\mathrm{Re_l} < 500$ and the moist air flow $\mathrm{Re_g} < 12000$. Thus according to the literature, the regime of the liquid film was mainly wavy laminar flow and that of the moist air had three kinds of possibilities. But even in the turbulent regime, the Reynolds number of the moist air was not rather high in the present study. As the flow in the work belonged to the one with a relatively low Reynolds number, the RNG (Renormalization group) $k-\varepsilon$ turbulence model was used to describe the flow process of the liquid film (Fluent 6.3 Users Guide).

The turbulence kinetic energy, k, and its rate of dissipation, ε, were obtained from the following transport equations,

$$\frac{\partial}{\partial t}(\rho k) + \frac{\partial}{\partial x_\mathrm{i}}(\rho k u_\mathrm{i}) = \frac{\partial}{\partial x_\mathrm{j}}(\alpha_\mathrm{k} \mu_\mathrm{eff} \frac{\partial k}{\partial x_\mathrm{j}}) + G_\mathrm{k} + G_\mathrm{b} - \rho\varepsilon - Y_\mathrm{M} + S_\mathrm{k} \tag{3.7}$$

$$\frac{\partial}{\partial t}(\rho \varepsilon) + \frac{\partial}{\partial x_\mathrm{i}}(\rho \varepsilon u_\mathrm{i}) = \frac{\partial}{\partial x_\mathrm{j}}(\alpha_\varepsilon \mu_\mathrm{eff} \frac{\partial \varepsilon}{\partial x_\mathrm{j}}) + C_{1\varepsilon} \frac{\varepsilon}{k}(G_\mathrm{k} + C_{3\varepsilon} G_b) - C_{2\varepsilon}\rho \frac{\varepsilon^2}{k} - R_\varepsilon + S_\varepsilon \tag{3.8}$$

(5) Surface tension source term

To simulate the liquid film flow, it is necessary to consider the effect of the surface tension, especially when the liquid layer is very thin. Whether the surface tension has

effect on the flow behavior can be judged by two non-dimensional numbers, which are Re number and Ca number or Re number and We number. The following two equations show how to obtain Ca number and We number,

$$Ca = \frac{\mu u}{\sigma} \tag{3.9}$$

$$We = \frac{\rho L u^2}{\sigma} \tag{3.10}$$

When $\mathrm{Re} << 1$, the Ca number is the main judgment standard. If $Ca >> 1$, the effect of surface tension can be ignored. When $\mathrm{Re} >> 1$, the We number is the prominent factor. If $We >> 1$, the effect of surface tension can be ignored. In the paper, $\mathrm{Re} >> 1$, $We << 1$, thus the effect should be considered in the simulation. In the paper, the continuum surface tension (CSF) model proposed by Brackbill et al. (Brackbill et al. 1992) was utilized for covering the surface tension effect.

The surface tension at the gas-liquid free surfaces is presented as follows,

$$F_{\mathrm{ST}} = \sigma_{\mathrm{ij}} \frac{\rho \kappa_{\mathrm{i}} \nabla \alpha_{\mathrm{i}}}{(\rho_{\mathrm{i}} + \rho_{\mathrm{j}})/2} \tag{3.11}$$

where, σ is the surface tension coefficient, ρ is the volume-averaged density, κ is the free surface curvature defined in terms of the divergence of the unit normal $\hat{n}$ as,

$$\kappa = \nabla \cdot \hat{n} - \frac{1}{|n|}\left[\left(\frac{n}{|n|} \cdot \nabla\right)|n| - (\nabla \cdot n)\right] \tag{3.12}$$

where $\hat{n} = \frac{n}{|n|}$, $n = \nabla \alpha_q$

To adjust the curvature of the surface near the wall, the unit surface normal at the live cell next to the wall is replaced by the dynamic boundary condition, which is expressed as,

$$\hat{n} = \hat{n}_{\mathrm{w}} \cos\theta_{\mathrm{w}} + \hat{m}_{\mathrm{w}} \sin\theta_{\mathrm{w}} \tag{3.13}$$

where $\hat{n}_{\mathrm{w}}$ and $\hat{m}_{\mathrm{w}}$ are the unit vectors normal to and tangential to the wall. The contact angle θ_{w} is the angle between the wall and the tangent to the interface at the wall. The wall adhesion force between solid and liquid resulted from the surface tension can be involved to the CSF model by confirming θ_{w}. θ_{w} not only depends on the fluid properties but also on the smoothness and geometrical characteristic of the wall (Kafka and Dussan 1979).

With the above stated parameters, the surface tension force F_{ST} in Eq. (3.11) was imposed on the momentum conservation equation (3.6) as a source term F.

3.3.2 Initial and boundary conditions

Initially, the whole fluid zone was occupied by the air and there was no liquid phase, which meant that $t = 0$, α_{g} =1, α_{l} =0. As there was not obvious line between the liquid outlet and gas inlet, the whole bottom was set as pressure outlet boundary. The liquid inlet and gas outlet were set as velocity inlet boundary. It is important to point

out that the value of gas outlet velocity was negative to induce the countercurrent flow of the moist air. In addition, the solution concentration and air humidity could also be set by inputting values at the software interface. The wall was no-slip boundary shear condition and the symmetry was set as symmetric boundary conditions.

3.3.3 Meshing and solution scheme

In the simulation, the flow field was meshed by the structured grid. As a result of the thin thickness of the liquid film, the grid density increased gradually from the gas to the liquid phase, as shown in Fig. 3.2. As the gravity force was not negligible, the body force weighted pressure discretization scheme was adopted (Gu et al. 2004). The Semi-Implicit Method for Pressure Linked Equations (SIMPLE) was used for pressure-velocity coupling. The PRESTO! pressure interpolation scheme was utilized, which is highly recommended for pressure-velocity coupling (Fluent 6.3 Users Guide). To accelerate the calculation, the first order upwind differencing was selected as the solution of the momentum, energy, turbulence and species transport equations. The geometric reconstruction scheme was used to solve the VOF equation. Transient simulations were conducted with a time step size of 10^{-4} to 10^{-5} s.

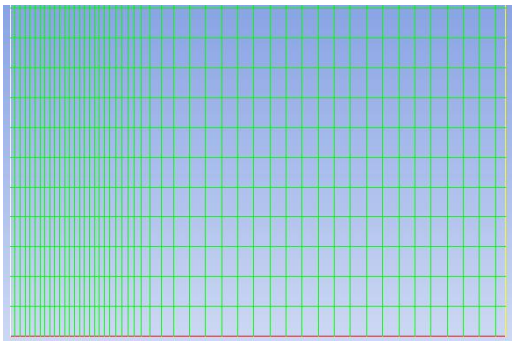

(a) Grid for flat plate

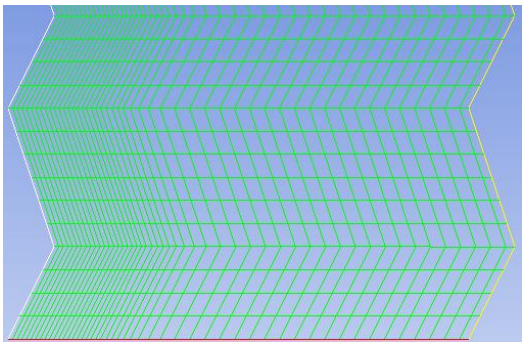

(b) Grid for corrugated plate

Fig. 3.2 Sketch map of computational grids

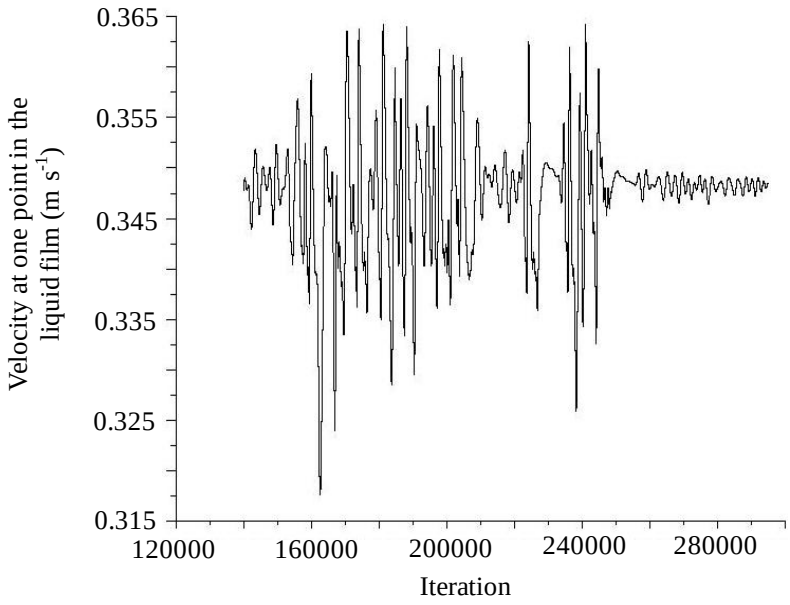

Fig. 3.3 Convergence history of velocity at one point in the liquid film

To judge whether the steady state was achieved, the velocities at several points in the liquid film were monitored. As shown in Fig. 3.3, when the velocity started to oscillate around a certain value, the state was regarded pseudosteady and the calculation was stopped.

3.3.4 Physical properties of the desiccant

Table 3.1 Properties of LiCl solution (300 K and 30 % mass concentration)

	ρ (kg m^{-3})	μ (kg m^{-1} s^{-1})	σ(N m^{-1})	θ_w (°)
LiCl solution	1180	0.00342	0.0891	65.0

According to the literature (Koronaki et al. 2013), Lithium Chloride (LiCl) has the best dehumidifier efficiency, in comparison to other inorganic desiccants, such as lithium bromide (LiBr) and calcium dioxide ($CaCl_2$). Hence, LiCl was chosen to be the desiccant for the dehumidification in the work. The basic state of LiCl solution was set as follows: temperature 300 K and mass concentration 30%. Some important physical properties of LiCl solution at the basic point were calculated referring to the literature (Conde 2004) and listed out in Table 3.1.

3.4 Results for the flat plate

3.4.1 Validity of the model

3.4.1.1 Grid independence study

As mentioned above, the flow field was meshed by the structured grid. Four grids were adopted for the independence study: 49×250, 71×300, 71×500, and 81×500. As a result of the thin thickness of the liquid film, the grid density increased gradually from the gas to the liquid phase. In the x direction, the grid that near the wall had the smallest size (0.04-0.1 mm), and the grid near the symmetry possessed the largest size (0.2-0.3 mm). In the y direction, a uniform grid was employed with sizes 0.6, 0.5 and 0.3 mm, respectively.

To ensure the accuracy of the interfacial description, the grid size in the zone with a distance of 2 mm (the size of the liquid inlet boundary) from the wall should be fine in the work. The grid sizes in the location of the interface were $0.1\text{mm}\times0.6\text{mm}$ for grid 49×250, $0.05\text{mm}\times0.6\text{mm}$ for grid 71×300, $0.05\text{mm}\times0.3\text{mm}$ for grid 71×500, and $0.04\text{mm}\times0.3\text{mm}$ for grid 81×500. The interfacial velocity profiles and average velocity values with four grids are presented in Fig. 3.4 and 3.5. It can be observed that the grid size of 71×500 was fine enough for the calculation by considering the computational accuracy and cost.

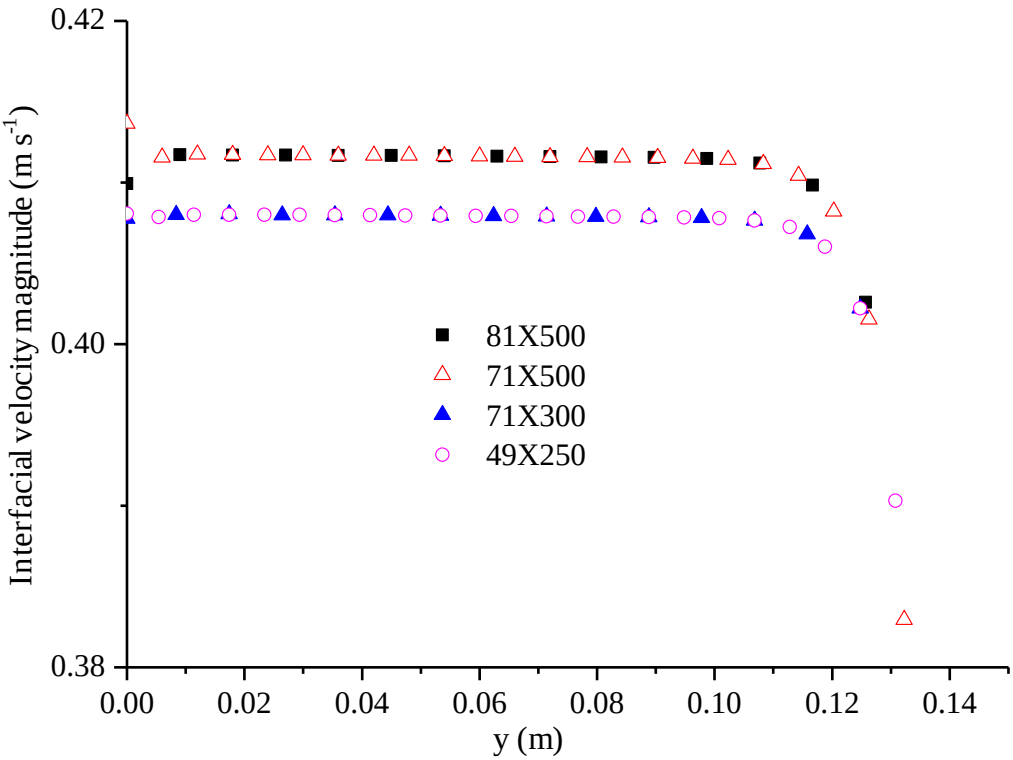

Fig. 3.4 Interfacial velocity magnitude with four types of grid

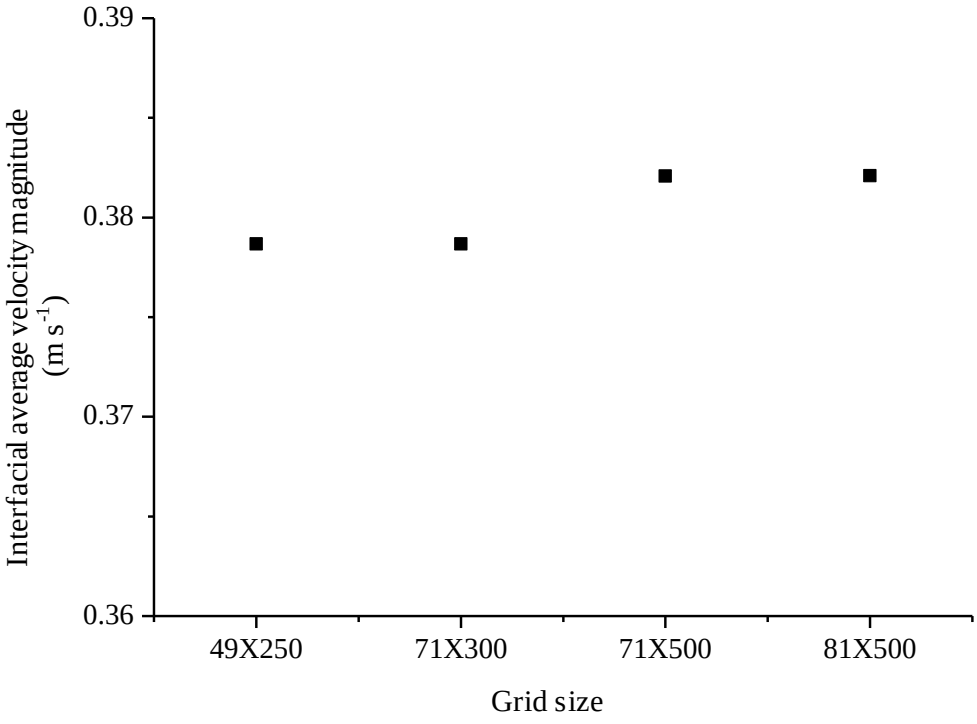

Fig. 3.5 Interfacial average velocity magnitude with four types of grids

3.4.1.2 Film thickness

The flow in the work was mainly wavy laminar one. To verify the correctness of the model, the average film thickness values obtained by the present simulation model were compared with the calculated results of the Nusselt film empirical formula, which is presented in the following equation,

$$\delta = \left(\frac{3\upsilon_s Re_s}{g}\right)^{1/3} \tag{3.14}$$

The results are demonstrated in Fig. 3.6. It shows that the simulation results of the model agree well with those of the empirical formula.

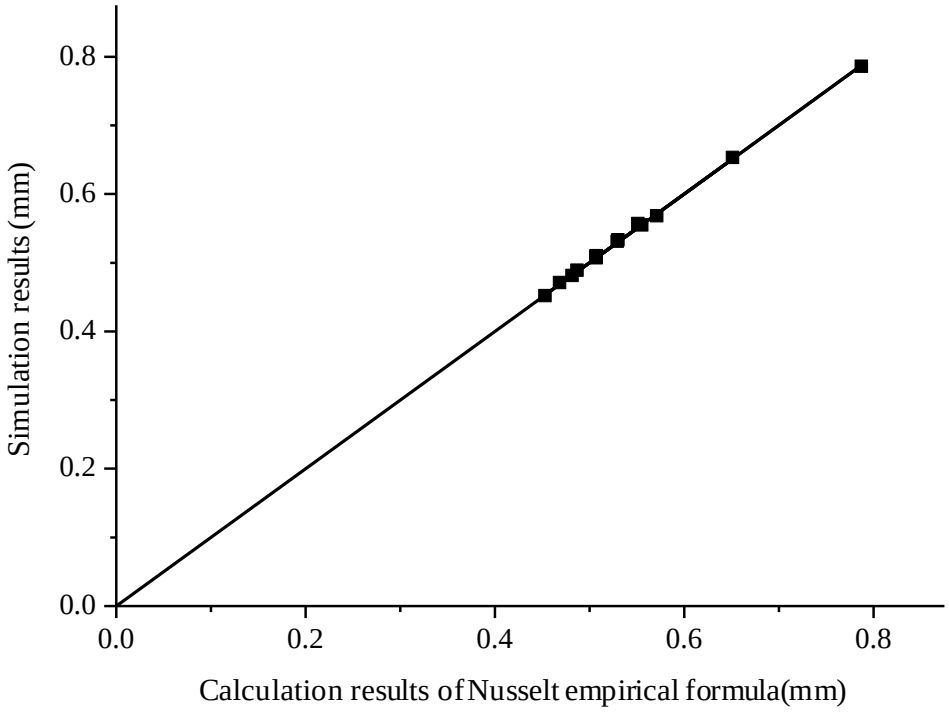

Fig. 3.6 Comparison of liquid film thickness between simulation and Nusselt empirical formula

3.4.1.3 Flow morphology

To further verify the correctness of the calculation method in the work, the results were compared with those of the literature (Gu et al. 2004). The water flowing on an inclined flat plate was simulated in the work. From Fig. 3.7, it can be seen that the results in the work show excellent agreement with the literature under the similar conditions. Thus, it was reliable to continue the calculation with the method.

(a) The results of the literature (Gu et al. 2004)

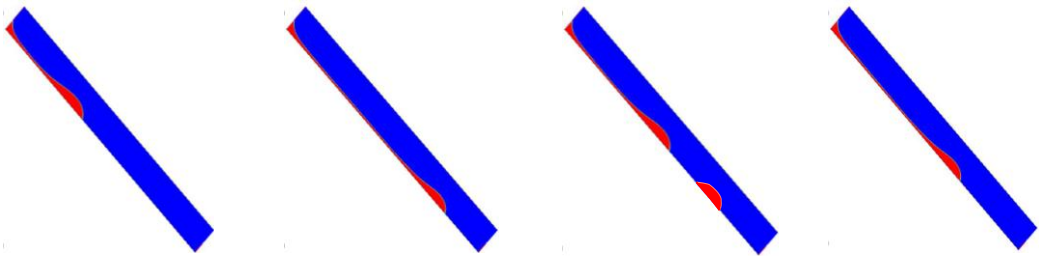

(b) The results in the present work

Fig. 3.7 The comparison between the work with the literature

3.4.2 Velocity profile

The local velocity profile has great influence on the residence time of the liquid and gas phases, which render it a critical factor for the heat and mass transfer process in

the dehumidifier. In the section, the velocity profile in the channel was analyzed.

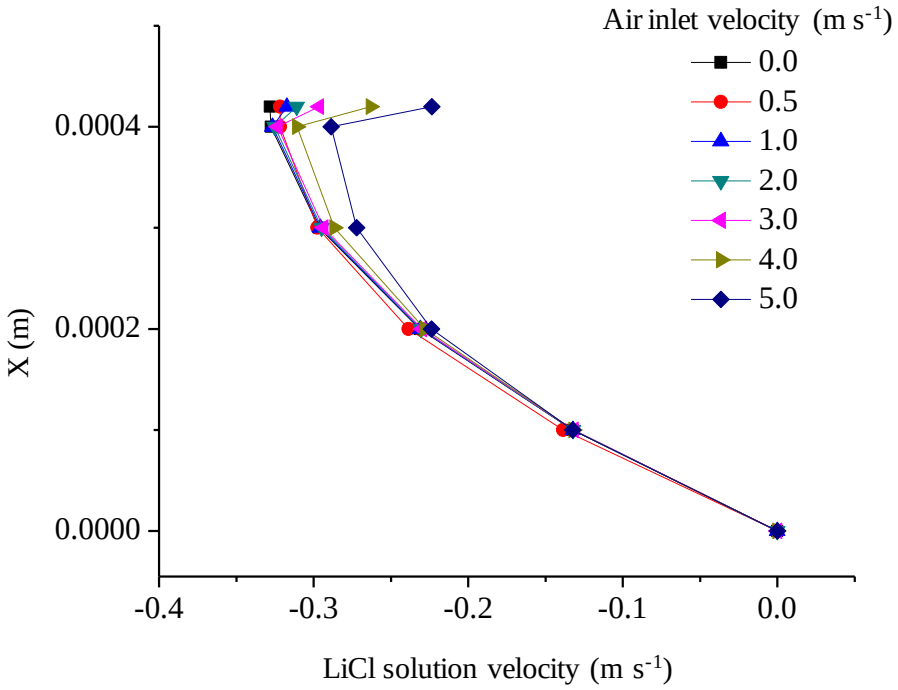

Fig. 3.8 Velocity profile of LiCl solution along the x axis (y=75mm)

Taking the cross section of the channel at y=75mm as an example, as shown in Fig. 3.8, the velocity profiles of LiCl solution under different air inlet velocity are presented. In this paper, the LiCl solution flow and air flow were in a counter-current configuration, thus the velocity of the LiCl solution was negative when the velocity of the air was set as positive. When there was not reverse air flow, the velocity of the LiCl solution showed a semi-parabolic distribution, which increased gradually from the plate surface to the gas-liquid interface. The velocity near the plate was zero for the no-slip boundary condition and there was a peak velocity at the gas-liquid interface. If the air flowed counter-currently to the LiCl solution with different

velocities, the velocity magnitude of the LiCl solution would increase and then decrease, resulting from the drag force of the reversed flow air. With the increase of the air inlet velocity, the influence of the drag force became more and more evident, especially when the air inlet velocity reached more than 3.0 m s^{-1}.

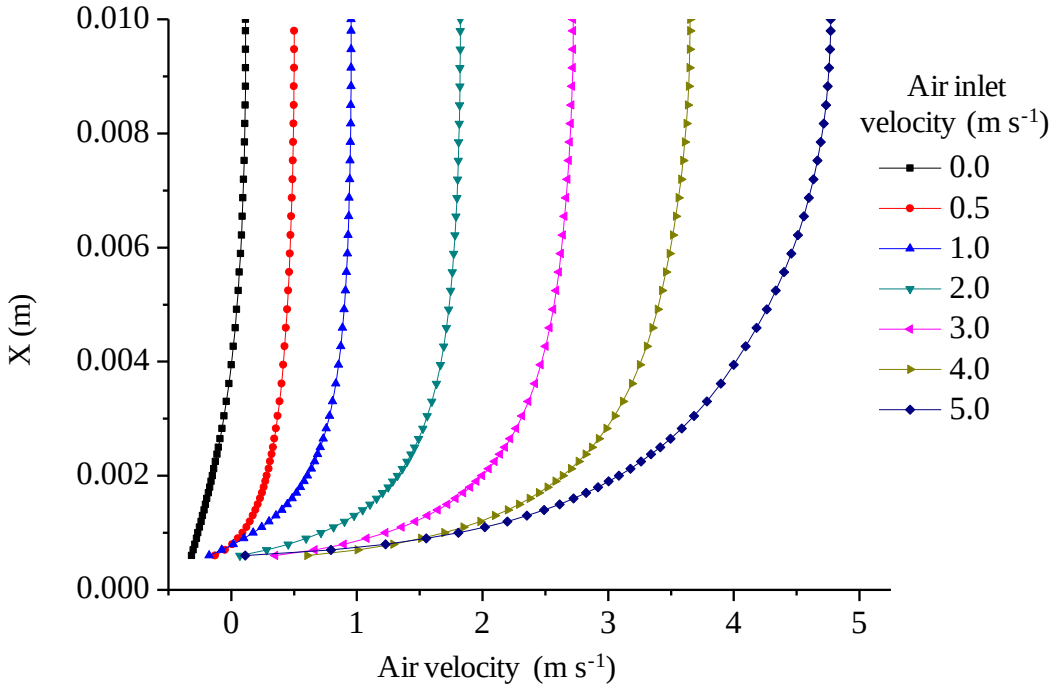

Fig. 3.9 Velocity profile of air along the x axis (y=75mm)

Fig. 3.9 indicates the velocity profiles of the gas phase. As the liquid and gas phases shared the same velocity field in the model, the velocities of the air and LiCl solution were the same at the interface. When the air inlet velocity was zero, the air near the interphase flowed at the same direction with the solution under the function of the

drag force. It was also noted that when the air inlet velocity increased to some point around 3.0 m s^{-1}, the air became the dominated factor to decide the velocity field at the interface and its velocity was no longer following the same direction with the LiCl solution.

3.4.3 Minimum wetting rate

Film breakdown of the falling film flow reduces the contact surface of mass transfer during the dehumidification process, thus it should be avoided as far as possible. It was verified that the critical breakdown point has a strong relationship with the liquid flow rate. In the literature **(**Morison and Tandon 2006), it introduced a parameter, the minimum wetting rate, to quantify the research results. The definition of the minimum wetting rate is the minimum mass flow rate per unit circumference needed to keep the complete falling film of liquid on a surface. In this section, the simulation was to make certain the minimum wetting rate $\Gamma_{s,min}$ at which the plate would be fully covered. The operating conditions are listed in Table 3.2.

It was convenient to observe the stages of film formation through the simulation results. In Fig. 3.10, the stages of film formation during solution flow on a flat plate at different liquid flow rates are reported in detail. Testing the flow with the increase of liquid flow rate (operating conditions from No. 1 to No. 4), it was found that the theoretical minimum wetting rate $\Gamma_{s,min}$ was about 0.071 kg m^{-1} s^{-1} for the LiCl

solution (300 K, 30% concentration).

Table 3.2 Wetting situation under different conditions

Operating conditions	No. 1	No. 2	No. 3	No. 4	No. 5
LiCl solution flow rate (kg m^{-1} s^{-1})	0.047	0.066	0.071	0.118	0.071
Moist air flow rate (m s^{-1})	0.0	0.0	0.0	0.0	4.0
Fully covered (Y/N)	N	N	Y	Y	Y
Operating conditions	No. 6	No. 7	No. 8	No. 9	-
LiCl solution flow rate (kg m^{-1} s^{-1})	0.071	0.071	0.094	0.118	-
Moist air flow rate (m s^{-1})	5.0	6.0	6.0	6.0	-
Fully covered (Y/N)	Y	N	N	Y	-

At the flow rate of 0.066 kg m^{-1} s^{-1}, the liquid solution flowed in a continuous film at the beginning. Then, the liquid congregated in the liquid film forepart under the function of the surface tension and viscous force. To a certain point, the film would break up under the action of gravity. It seemed that the film rupture occurred at the bottom part of the channel cyclically. Thus, it was difficult to form a continuous film at the liquid flow rate of 0.066 kg m^{-1} s^{-1}, not to mention lower liquid flow rates. The reason was that the LiCl solution had very high surface tension and contact angle, both of which reduced its wettability significantly.

It was observed the air flow rate also had an impact on the wetting conditions, especially when the air flowed with relatively high velocity. Keeping the LiCl solution

flow rate at a constant value of 0.071 kg m^{-1} s^{-1} and increasing the air flow rate from the operating condition No. 5 to No. 7, it was found that when the air velocity was up to 6.0 m s^{-1}, some liquid was torn to pieces, as shown in Fig. 3.11. The case had to be avoided as the liquid drop carried over by the air would pollute the indoor environment. Under this condition, to wet the whole surface, the LiCl solution flow rate should be increased to 0.118 kg m^{-1} s^{-1} according to the calculation results of the operating condition No. 9.

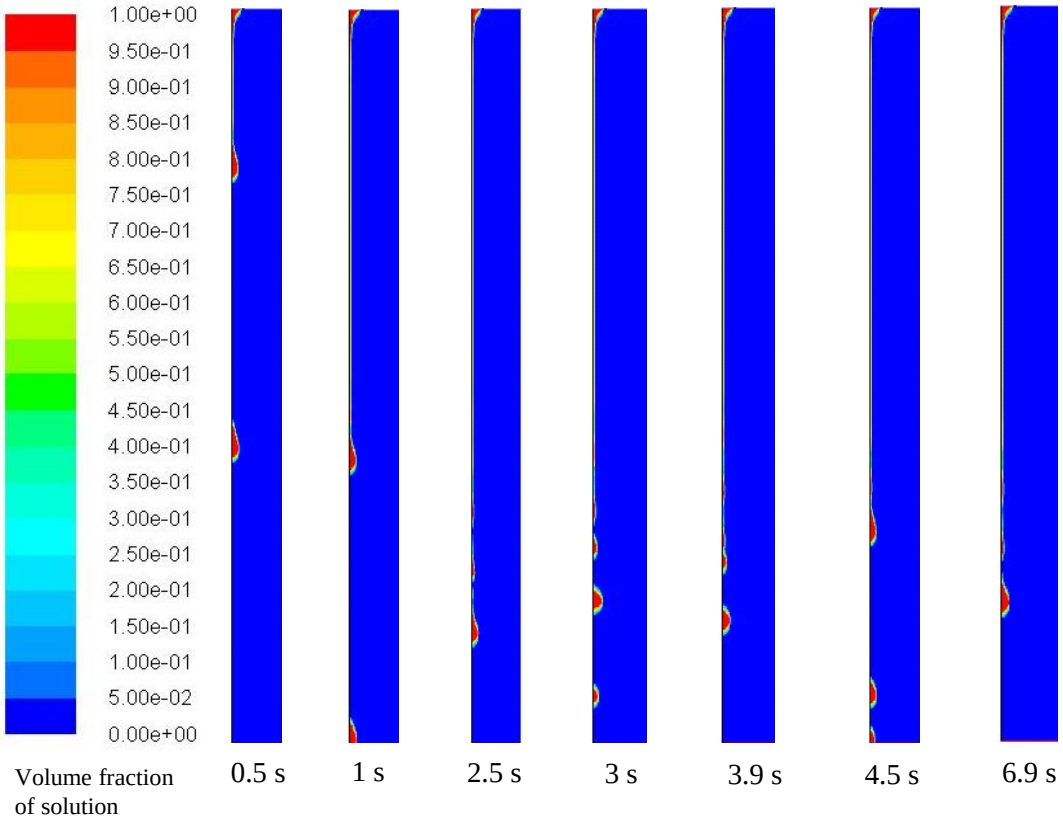

(a) Liquid flow rate: 0.066 kg m^{-1} s^{-1}

(Operating condition No. 2)

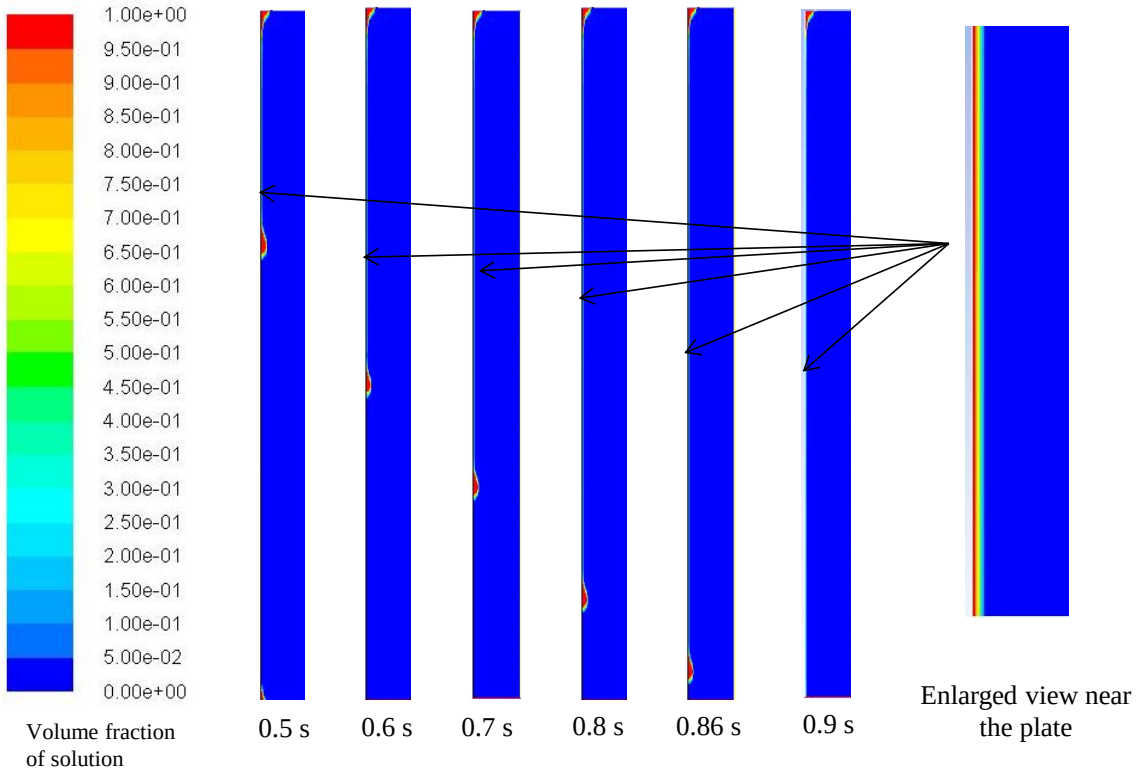

(b) Liquid flow rate: 0.071 kg m^{-1} s^{-1}

(Operating condition No. 3)

Fig. 3.10 Stages of film formation during solution flow

To analyze the influence of the physical properties of the desiccant solution further, an ordinary organic desiccant triethylene glycol (TEG) was chosen for comparison with LiCl solution. According to the calculation results, it was surprisingly found that even at very low liquid flow rate, the TEG could wet the whole plate surface because the TEG solution had very high viscosity and relatively lower contact angle with the surface. In the flow process, the viscous force and surface tension could resist the gravity, which was the main factor causing the liquid film rupture. However,

compared with LiCl solution, it cost much longer time for the TEG solution running through the channel (1.18 s *Vs* 2.54 s) under the same test condition.

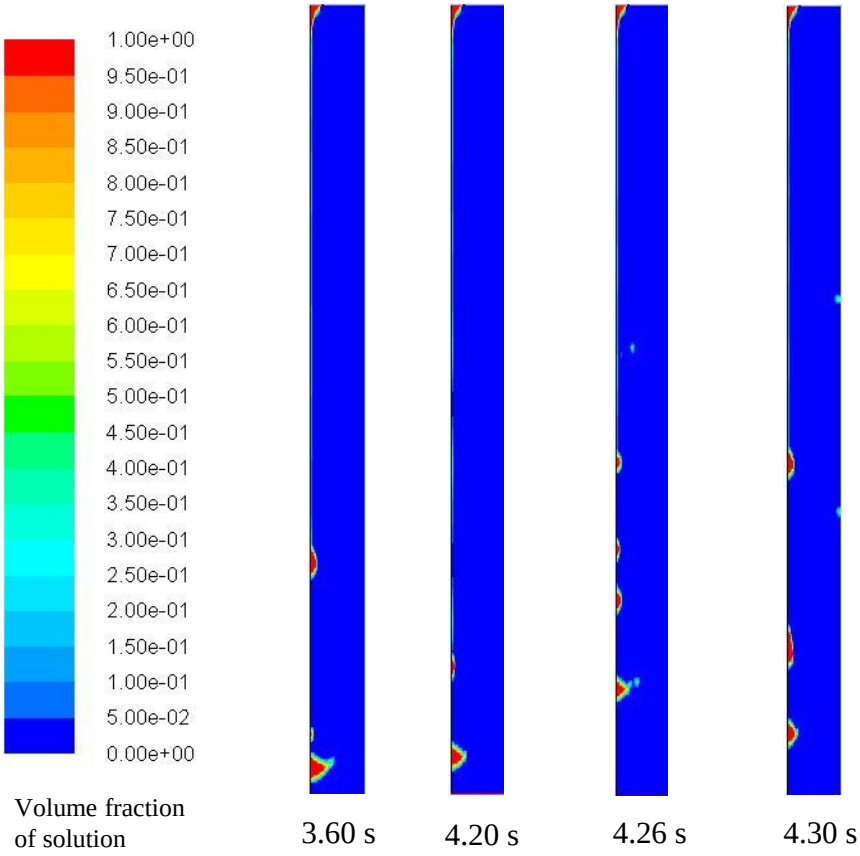

Fig. 3.11 Stages of film formation during solution flow on a flat plate (Operating condition No. 7)

3.4.4 Interfacial area

In this section, the ratio of the interfacial area to the geometrical plate surface as a function of the liquid flow rate was determined. It was noted that the cross section of the flat was the same in the two-dimensional calculations, so the ratio could be obtained. The result is demonstrated in Fig. 3.12.

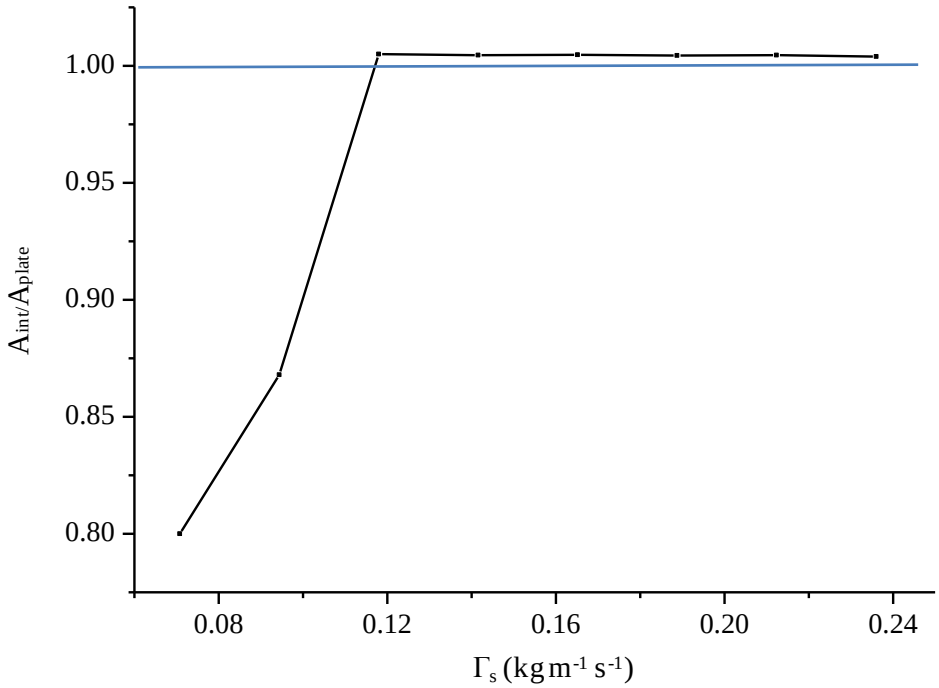

Fig. 3.12 The ratio of the interfacial area to the geometrical plate surface under different liquid flow rates (u_a=6.0 m s^{-1})

Due to the large gas velocity (6 m s^{-1}), it required that the solution flow rate reached a certain value to wet the whole surface of the flat. Thus, when the solution flow rate was low, the ratio of the interfacial area to the geometrical plate surface was less than one. With the increase of the liquid flow rate, the efficient mass transfer area would increase correspondingly. In some cases, the interfacial area could be larger than the plate because of the wave. As the length of the flat plate was only 150 mm, the effective interfacial area was a little bigger than the geometrical plate surface. However, the increased transfer area could be considerable when the plate was longer and there were lots of plates, which was the real situation of the dehumidifier.

Meanwhile, it was also found that when the liquid flow rate achieved a certain value, the increase of the interfacial area would not be recognizable anymore. The results were a little different from those of the literature (Haelssig et al. 2010). The main reason was the different liquid substance employed in the paper.

3.4.5 Film thickness

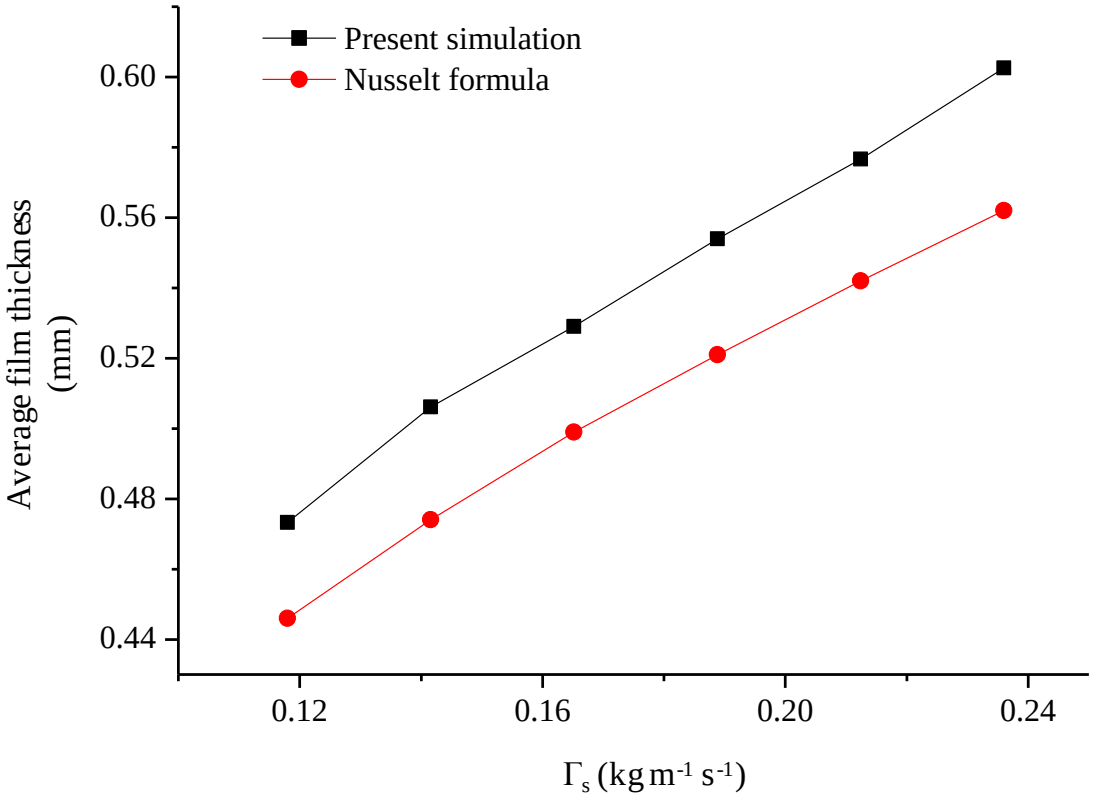

Fig. 3.13 Average film thickness at different LiCl solution flow rates

Film thickness is another important parameter investigated in the paper. From Fig. 3.13, it was concluded that with the increase of the liquid flow rate, the average film

thickness increased accordingly (air velocity was 5.0 m s^{-1}). In Fig. 3.13, it was also found that the average film thicknesses of present work were a litter bigger than those of the Nusselt empirical formula. It might be resulted from the reverse flow of the air.

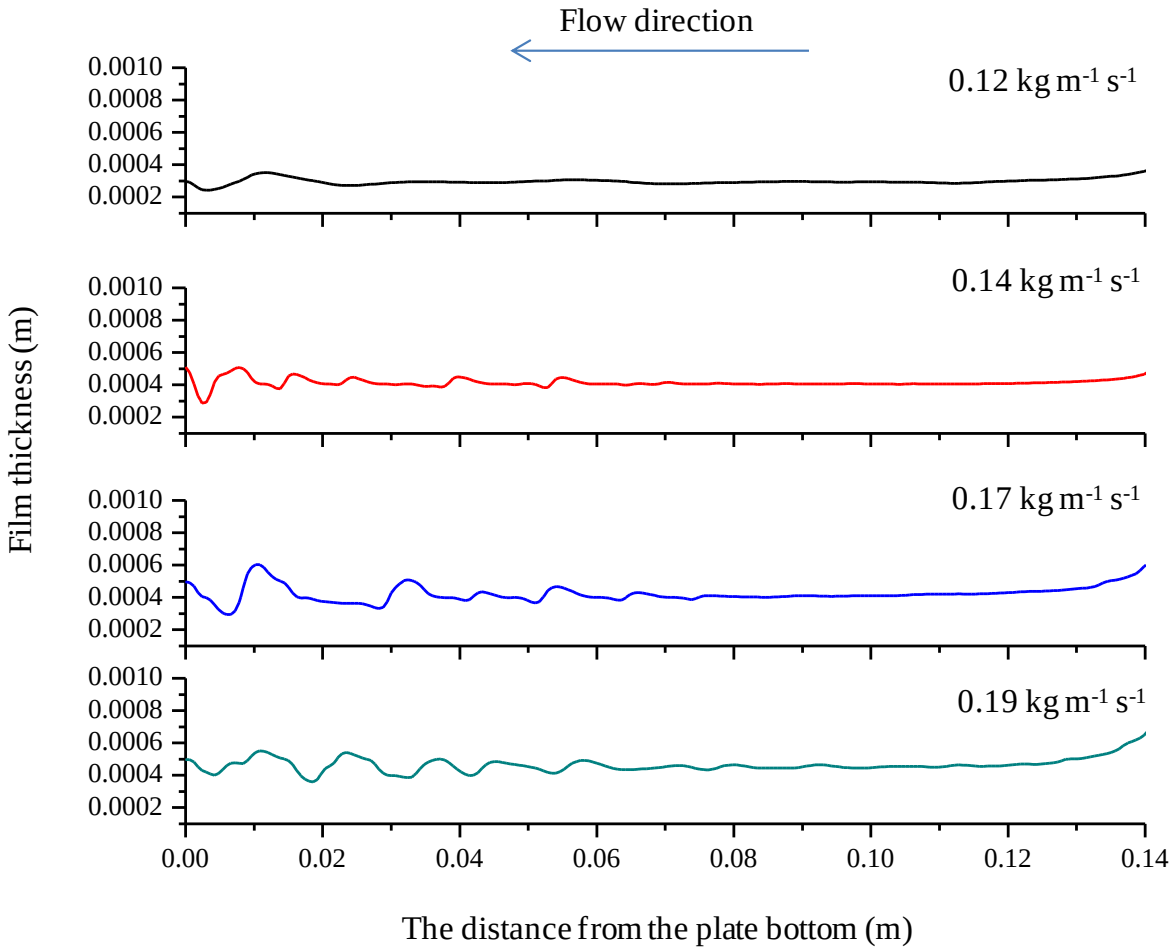

Fig. 3.14 Liquid film thickness profiles at different LiCl solution flow rate

The local film thickness was presented in Fig. 3.14. It could be observed that the fluctuation amplitude increased continuously in the liquid flow direction. The

fluctuation amplitude also rose when the liquid flow rate increased, which explained the increased interface area mentioned in section 3.4.4. Thus, the fluctuation was beneficial to mass transfer in the aspect. Except for the interface area, further research about how the fluctuation affects the mass transfer is needed.

3.5 Results for the corrugated plate

3.5.1 Minimum wetting rate

In section 3.4, it was found that the minimum wetting rate $\Gamma_{s,min}$ was about 0.071 kg m^{-1} s^{-1} for the flat plate. According to the present calculation results, it was concluded that the solution flow rate for the corrugated plate was 0.21 kg m^{-1} s^{-1}, about three times of that of the flat plate under the same simulation conditions. It demonstrated that it was much more difficult to wet a vertical corrugated surface than a flat one. The reason was the accumulation of the liquid solution at the caving of the corrugated plate.

3.5.2 Surface axial velocity

In theory, the wave of the falling film can enhance the mass transfer in two ways, one is by increasing the contact surface, and the other one is by grasping the mass with the rolling wave. Since the surface wave velocities played a great role in determining the film wave, their local distributions were investigated.

The comparisons of the surface velocity between the flat and corrugated plate were carried out under the same conditions: the solution flow rate was 0.472 kg m^{-1} s^{-1}, and the air velocity was 3.0 m s^{-1}.

For a free surface film flow down a vertical flat wall, it is always unstable even under very small Reynolds number. In Fig. 3.15(a), the distribution of the liquid surface axial velocity and the film thickness are presented. As the liquid inlet size of the physical model was 2 mm, there was a sharp change of the film thickness at the liquid inlet. But after that, a flat interface appeared, yet only over some distance at the liquid inlet, following by big fluctuation. It was also observed that the axial velocity increased with the enhancement of the wave, and it would reach the maximum value at the crest of the wave. The results showed consistence with those in the literature (Cui et al. 2012).

For the corrugated plate (Fig. 3.15(b)), the axial velocity was less than that of the flat plate, resulting from the support of the surface. It demonstrated that the corrugated plate could offer much longer contact time for the mass transfer in the dehumidifier. In addition, the change of the axial velocity was also less than that of the flat plate. The corrugated structure could help to stable the liquid flow in the axial direction under the present operating condition.

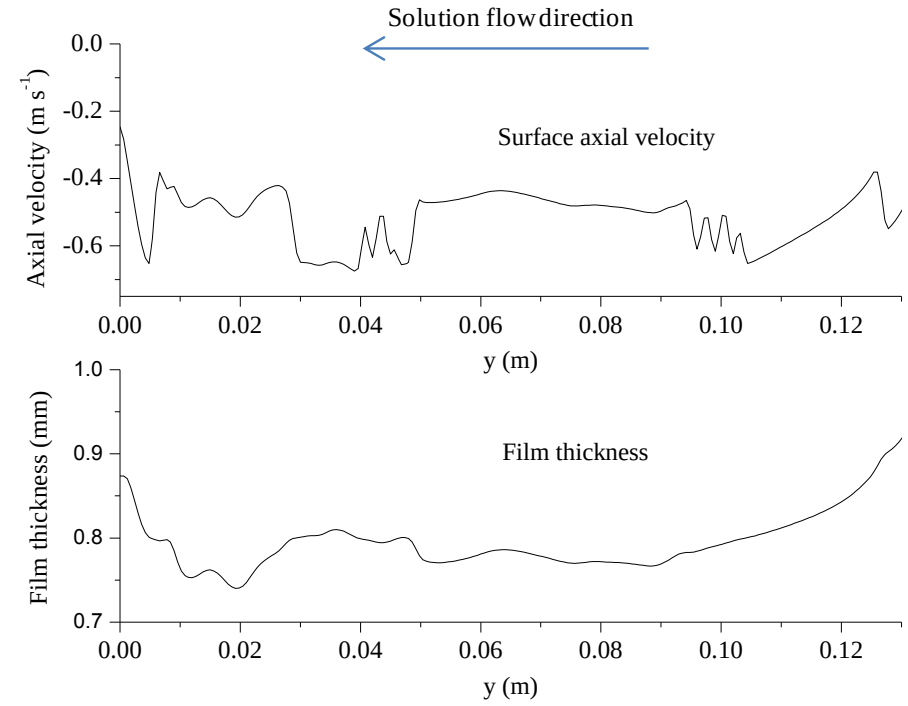

(a) Flat plate

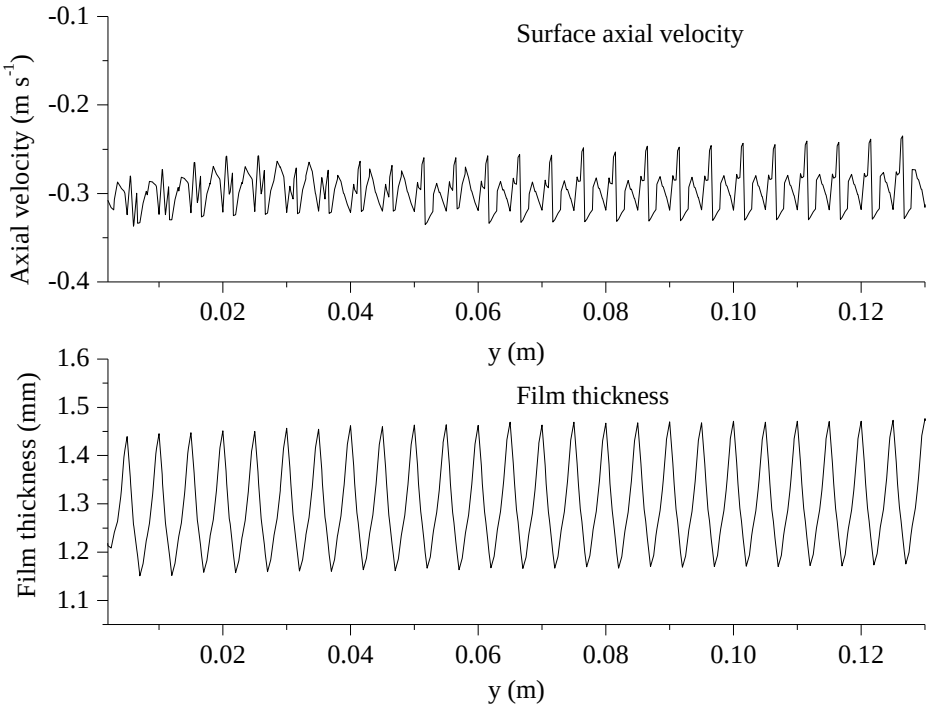

(b) Corrugated plate

Fig. 3.15 Film thickness *Vs* Axial velocity

3.5.3 Surface radial velocity

From Fig. 3.16, it was found that for the flat plate, unlike the surface axial velocity, there was not obvious change of the surface radial velocity. Thus, it was concluded that for the flat plate, the surface wave had a great relationship with the surface axial velocity rather than the radial velocity. On the contrary, the change of the surface radial velocity was much bigger for the corrugated plate, which was determined by the shape of the wall. Whether it will impact on the mass transfer needs further investigation.

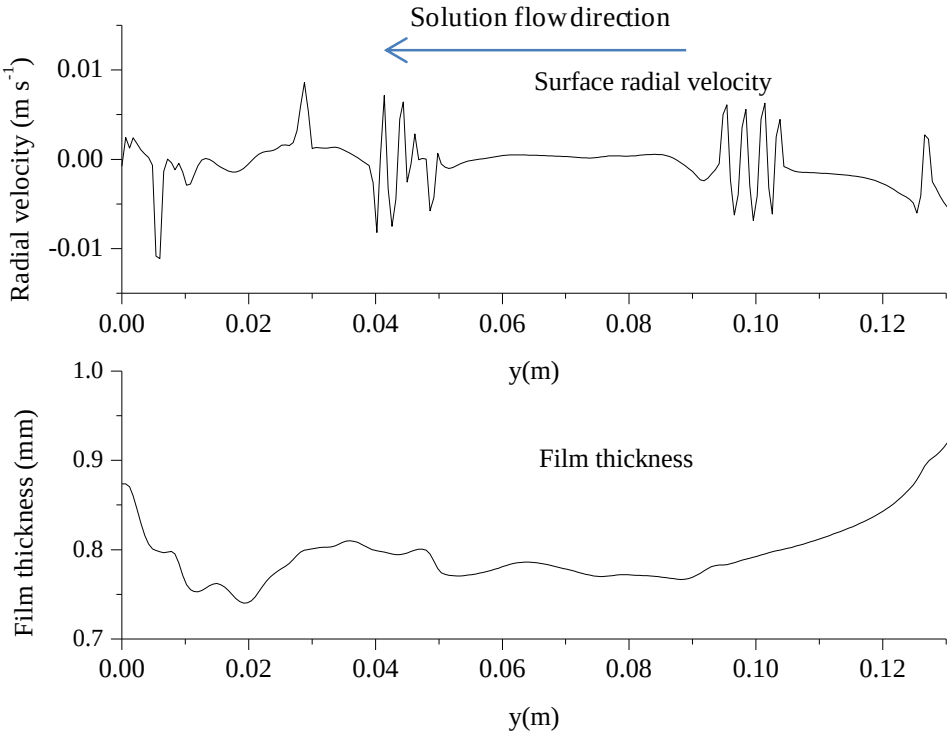

(a) Flat plate

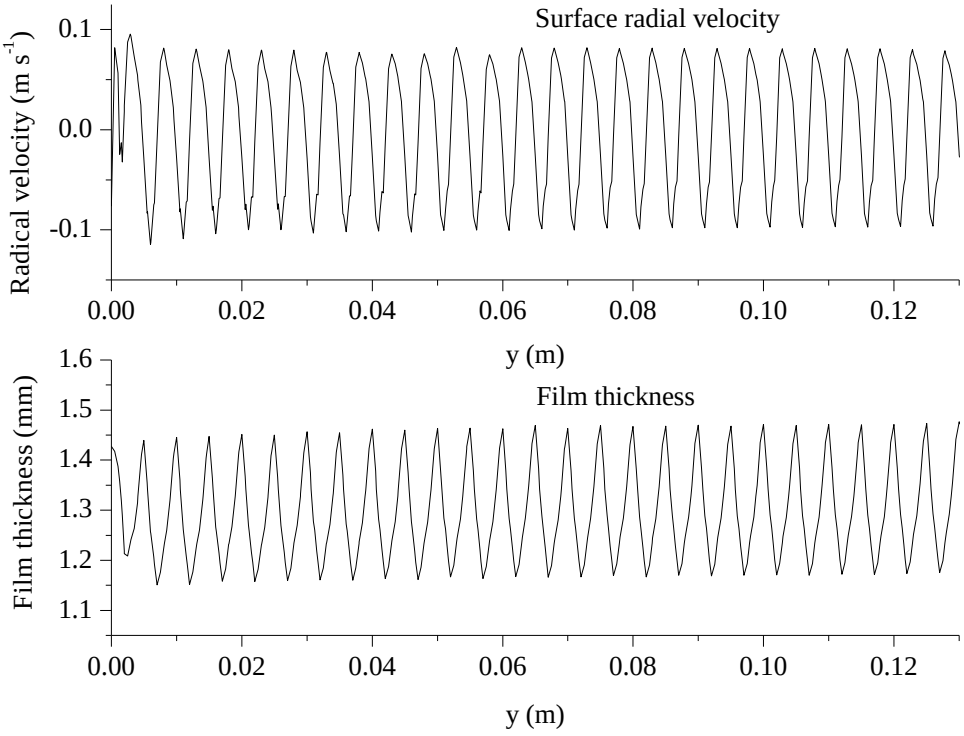

(b) Corrugated plate

Fig. 3.16 Film thickness *Vs* Radical velocity

3.5.4 Surface shape under different liquid velocity

The film shape on the flat plate under different liquid flow rate had been investigated in the previous section. Under the case of a corrugated vertical wall, it was found that the shape of the wave changed periodically (Fig. 3.17). The film thickness would reduce a litter at the beginning and then increased with the increase of the inlet solution flow rate. The similar result was reported in the existing literature (Sun 2012). When the solution flow rate was about 0.307 kg m^{-1} s^{-1}, it seemed easy for the liquid to accumulate on the wall whose surface normal was upward, resulting in the increase of

the liquid holdup for the corrugated plate. In addition, the phase angle decreased with the increase of the inlet solution flow rate. When the solution flow rate reached a certain value, the shape of the liquid film became similar to the wall.

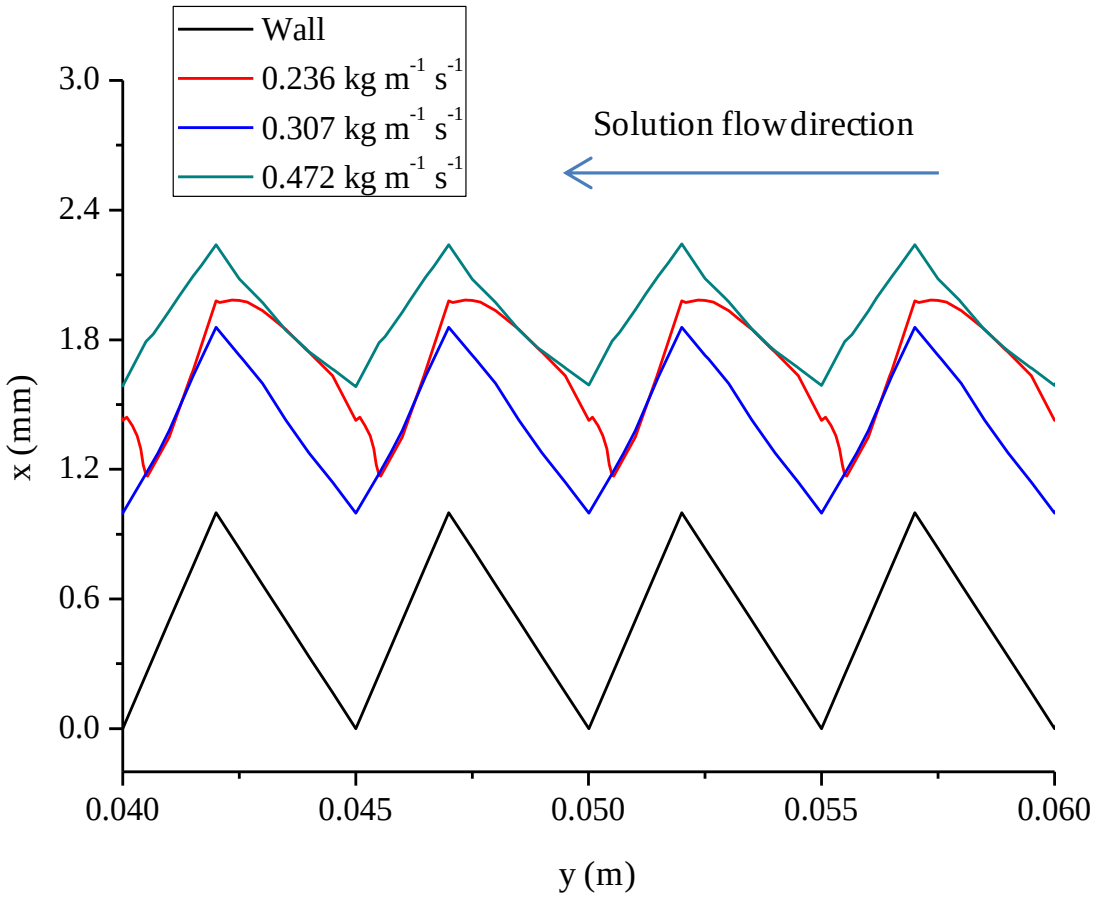

Fig. 3.17 Film shape on the corrugated plate under different liquid flow rate

3.6 Summary

This chapter numerically studied the flow characteristics in the simplified structured dehumidifier. It showed that the simulation model could be an effective tool to

predicate the dynamic and local flow conditions in the dehumidifier. Based on the calculation results, several results can be drawn for the flat plate,

1) The velocity profiles in the dehumidifier were demonstrated. It was found that the counter-flow air did change the velocity profile of the LiCl solution along the film thickness due to the drag force. And when the air inlet velocity reached 3.0 m s^{-1}, the impact became very distinct. Under that situation, the air became the dominated factor to decide the velocity field at the interface.

2) With the model, the importance of suitable solution and air flow rates was highlighted. According to the simulation results, it had been found that if the solution flow rate was too low, the effective interfacial area could be reduced dramatically due to the film breakdown. If the air flow rate was too high, it was possible for the air to carry over the liquid drop, which would be a considerable threaten to the indoor environment. Therefore, the model was an effective way to predicate the optimum flow rates of the solution and air in advance.

3) The results also explained the reason of the enhancement of mass transfer with film flow. It was because with the increase of the liquid flow rate, the fluctuation amplitude and the efficient mass transfer area would increase correspondingly. In some cases, the interfacial area could be larger than the plate because of the wave.

And the increased transfer area was considerable when the plate area was large enough. In this way, the mass transfer in the film flow absorber could be improved significantly.

4) Local film thickness could be obtained for different solution flow rate. For a certain flow rate, the fluctuation amplitude increased continuously along the liquid flow direction. And the fluctuation amplitude also rose with the increase of the liquid flow rate. In addition, the comparison of the average film thickness between the simulation results and those of the Nusselt empirical showed the function of the drag force exerted by the counter-current air flow.

Then the corrugated plate was also studied and the results were compared with the flat plate,

1) The liquid solution flow rate should be larger for wetting the whole surface of the corrugated sheet of packing, compared with the flat plate.

2) For the corrugated plate, the axial velocity was much less than that of the flat plate. It might offer much longer contact time for the mass transfer in the dehumidifier with corrugated packing. In addition, the change of the axial velocity was also less than that of the flat plate. Thus, it was concluded that the corrugated structure

could help to stable the liquid flow in the axial direction under the present operating condition.

3) The change of the surface radial velocity was much bigger for the corrugated plate than the flat plate, which was determined by the shape of the wall.

4) For the vertical corrugated wall, the wave of the film changed periodically. The film thickness would reduce a litter at the beginning and then increased with the increase of the inlet solution flow rate. The phase angle reduced with the increase of the inlet solution flow rate. When the solution flow rate reached a certain value, the shape of the liquid film became similar to the wall.

CHAPTER 4

NUMERICAL SIMULATION OF THE COUPLED FLOW, HEAT AND MASS TRANSFER PROCESSES

4.1 Introduction

Until now, numerous studies have been done about the heat and mass transfer process in the dehumidifier. Several kinds of simulation models have been developed to predict and assess the performance of the dehumidifier, including the finite difference model (Luo et al. 2011; Luo et al. 2012), effectiveness NTU(ε-NTU) model (Ren 2008) and some simplified solutions (Khan and Ball 1992). All of the models are established based on the film theory, which is one of the three most classic and typical theories of mass transfer. The other two mass transfer theories are penetration theory and surface renewal theory. The film theory is very easy to be understood and applied, but it is only suitable for the steady mass transfer process (Whitman 1923). In addition, to simplify the heat and mass transfer process, lots of common assumptions have been made for the above models.

With the rapid development of the computer technology, it becomes more accessible to use the CFD technology to describe the complex behaviors of the heat and mass

transfer in the absorption and separation process. Till now, there are lots of literatures reporting using the CFD method to simulate the heat and mass transfer processes within the evaporators, absorption towers, and direct contact condensation units. Jayanti and Hewitt (Jayanti and Hewitt 1997) studied the hydrodynamics and heat transfer of a thin film flow with CFD techniques. Liu et al. (Liu et al. 2006) promoted a complicated computational mass transfer model to investigate the chemical absorption process with heat transfer. Carlo et al. (Carlo et al. 2006) set up a simple model to assess the dynamics and mass transfer efficiency of distillation columns. Banerjee (Banerjee 2007) applied a numerical model to evaluate the heat and mass transfer from the surface of liquid ethanol. Haroun et al. (Haroun et al. 2012) investigated the liquid hold-up and mass transfer as function of the liquid flow rate and structured packing geometry.

However, the absorption processes of the liquid desiccant dehumidifier modeled with CFD method are seldom reported. In the dehumidifier, the fluid dynamics and vapor absorption of the desiccant solution are mutually coupled, so this case can be simulated with a CFD calculation model, where both fluid dynamics and vapor absorption can be dealt with simultaneously.

In this chapter, a new simulation model was developed on the basis of the one in Chapter 3. In this model, it was taken into consideration that the effect of the

velocity field on the heat and mass transfer process. And the desiccant flow was calculated regarding the impacts of gravity, viscosity and surface tension. Meanwhile, the variable physical properties of the desiccant and air, which were taken as constant in almost all existing models, rendered the simulation more in line with the real condition. In addition, the penetration mass transfer theory was employed to make it possible to observe the dynamic process in the dehumidifier interior (Luo et al. 2014b).

4.2 Physical model

In the paper, the counter-flow configuration was chosen for investigation as it is the most popular one for the liquid desiccant dehumidifier. The simulation was conducted for the unsteady two-phase flow with free liquid surface in the channel between the two flat plates. The simplified geometric construction can be referred to in Fig. 3.1.

4.3 Mathematical model

The flow model had been presented in Chapter 3, thus here they will not be repeated. The equations involved the heat and mass transfer between the solution and air are listed out, including the species transport equation, energy equation and interface mass and energy transfer equations.

4.3.1 Governing equations

4.3.1.1 Species transport equation

$$\frac{\partial}{\partial t}\left(\alpha_{\mathrm{q}}\rho_{\mathrm{q}}x_{\mathrm{k,q}}\right)+\nabla\cdot\left(\alpha_{\mathrm{q}}\rho_{\mathrm{q}}\boldsymbol{u}x_{\mathrm{k,q}}-\alpha_{\mathrm{q}}\Gamma_{\mathrm{k,q}}\nabla x_{\mathrm{k,q}}\right)=S_{\mathrm{lg,k}} \tag{4.1}$$

q=1,.....,n k=1,.....,m

where $x_{\mathrm{k,q}}$ is the mass fraction of the component k in the q^{th} phase. $S_{\mathrm{lg,k}}$ represents the mass transfer source at the phase interface. $\Gamma_{\mathrm{k,q}}$ is the diffusion coefficient.

4.3.1.2 Energy equation

$$\frac{\partial}{\partial t}\left(\rho E\right)+\nabla\cdot\left(\boldsymbol{u}(\rho E+P)\right)=\nabla\cdot\left[k_{\mathrm{eff}}\nabla T-\sum h_{\mathrm{k}}J_{\mathrm{k}}\right]+S_{\mathrm{E}} \tag{4.2}$$

where S_{E} is the energy source term. The definition of the average energy E is as follows,

$$E=\frac{\sum_{q=1}^{n}\alpha_{\mathrm{q}}\rho_{\mathrm{q}}E_{\mathrm{q}}}{\sum_{q=1}^{n}\alpha_{\mathrm{q}}\rho_{\mathrm{q}}} \tag{4.3}$$

E_{q} is obtained according to the specific heat and the temperature of the q^{th} phase.

4.3.1.3 Interface conditions

1) Interface mass transfer

As the mass transfer resistance at the interface can be neglected (Bird et al. 1960), the overall mass transfer coefficient can be written in the form (Zhang et al. 2010),

$$\frac{1}{K_{\mathrm{g}}}=\frac{1}{\alpha_{\mathrm{D,g}}}+\frac{1}{\psi\alpha_{\mathrm{D,l}}} \tag{4.4}$$

where ψ is a function of concentration and temperature of the bulk desiccant solution, and its calculation equation for LiCl solution is as follows,

$$\psi = a_0 + a_1 T_{\mathrm{s}} + a_2 (T_{\mathrm{s}})^2 + a_3 (T_{\mathrm{s}})^3 \tag{4.5}$$

where $a_0 - a_3$ are obtained from the correlations in the literature (Zhang et al. 2010).

Here, the penetration model is used to calculate the local mass transfer coefficients $\alpha_{\mathrm{D,g}}$ and $\alpha_{\mathrm{D,l}}$,

$$\alpha_{\mathrm{D,g}}=2\sqrt{\frac{D_{\mathrm{m.g}}}{\pi t_{\mathrm{c}}}} \tag{4.6}$$

$$\alpha_{\mathrm{D,l}}=2\sqrt{\frac{D_{\mathrm{m,l}}}{\pi t_{\mathrm{c}}}} \tag{4.7}$$

The contact time t_{c} is obtained by the equation,

$$t_{\mathrm{c}} = \frac{l}{u_{\mathrm{surf}}} \tag{4.8}$$

where l is the liquid flow distance. u_{surf} is the surface velocity of the liquid film and it can be calculated by,

$$u_{\text{surf}} = 1.5Q\left(\frac{3\mu Q}{\rho g}\right)^{-1/3} \tag{4.9}$$

With the above equations, the mass transfer source $S_{\text{lg,k}}$, which is imposed to Eq. (4.1) can be achieved by,

$$S_{\text{lg,k}} = K_{\text{g}}(W_{\text{g,b}} - W_{\text{g,e}})A \tag{4.10}$$

where $W_{\text{g,b}}$ is the humidity ratio of the bulk air, $W_{\text{g,e}}$ is the equilibrium air humidity ratio to the desiccant solution, which is obtained from,

$$W_{\text{g,e}} = 0.622\frac{P_{\text{l,b}}}{P_{\text{a}} - P_{\text{l,b}}} \tag{4.11}$$

where $P_{\text{l,b}}$ is the partial vapor pressure of the bulk desiccant solution and P_{a} is the atmospheric pressure.

2) Interface energy transfer

In the dehumidification process, some quantity of heat is given out, including the phase change heat and the dilution heat. Here, the dilution heat can be neglected as compared with the phase change heat of water vapor, it is much smaller (Lowenstein and Gabruk 1992). Then energy source term is the latent heat generated by the mass transfer and is presented as follows,

$$S_{\text{E}} = \sum_{k=0}^{m-1} S_{\text{lg,k}} H_{\text{lg,k}} \tag{4.12}$$

Finally, the energy source term S_{E} is involved into the model by being added to the

Energy equation (4.2).

4.3.2 Initial and boundary conditions

The initial and boundary conditions have been explained in Chapter 3.

4.3.3 Simulation strategy

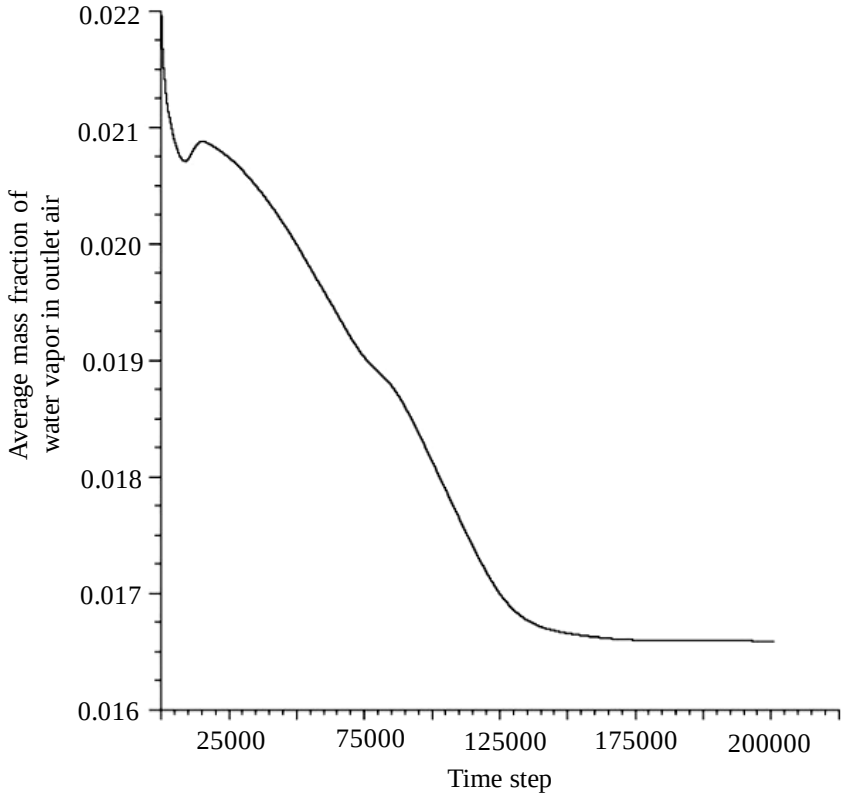

Fig. 4.1 Convergence history of mass fraction of water vapor in outlet air

The CFD software FLUENT was utilized to simulate the two-phase film flow in the 2-D planar vertical channel. The governing equations were solved based on a finite

control volume technique. Quasi-steady state was reached for the total transfer rate of heat and mass in the channel with a flow time of approximately 2 s. Three kinds of parameters were monitored to judge whether the steady state was achieved: the velocities of several points in the liquid film, the average mass fraction of water vapor in the moist air at the gas outlet boundary, and the average temperature of moist air at the gas outlet boundary. As presented in Fig. 3.3, Fig. 4.1 and Fig. 4.2, if the above parameters started to oscillate around a certain value, the state was regarded pseudosteady and the calculation was stopped.

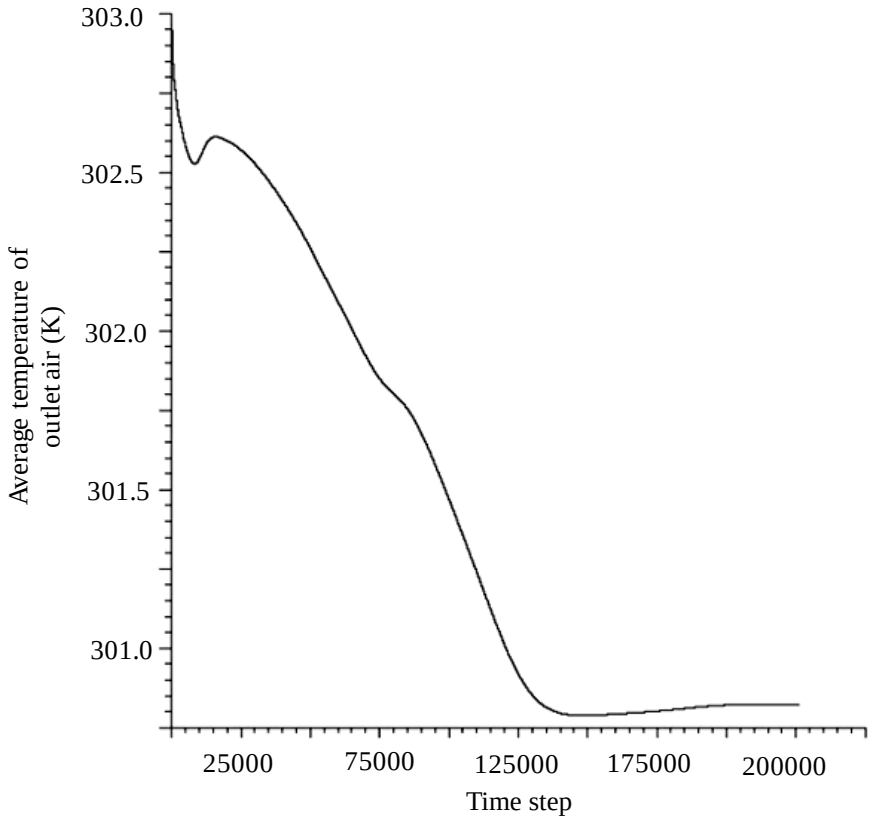

Fig. 4.2 Convergence history of outlet air temperature

4.3.4 Physical properties of the fluids

The basic state of LiCl solution was set as follows: temperature 298 K, mass concentration 30%. In the dehumidification process, due to the heat and mass transfer between the desiccant and air, the properties of the LiCl solution would change all the time. It is fortunate that CFD software Fluent provides the user custom interface where the files of various properties of LiCl solution at different concentrations and temperatures can be compiled with the program, including the density, thermal conductivity, mass diffusivity, viscosity, and so forth.

For the moist air, the database of Fluent contains all of its physical properties. The users only need to set the two components- air and water vapor and mix them together with the relevant formulation contained by the software.

4.4 Validity of the model

4.4.1 Grid independence study

In the simulation, the flow field was meshed by the structured grid. Four grids were selected for the independence study with the flowing elements: 49×250, 71×300, 71×500, and 81×500. As a result of the thin thickness of the liquid film, the grid density increased gradually from the gas to the liquid phase. In the x direction, the grid that near the wall with the smallest size was 0.05-0.1 mm, whereas that near the

symmetry with the largest size was 0.2-0.3 mm. In the y direction, a uniform grid was employed with sizes 0.6, 0.5 and 0.3 mm, respectively. The mass fractions of water vapor in the outlet air were calculated for the above four types of grids under the same inlet boundary condition.

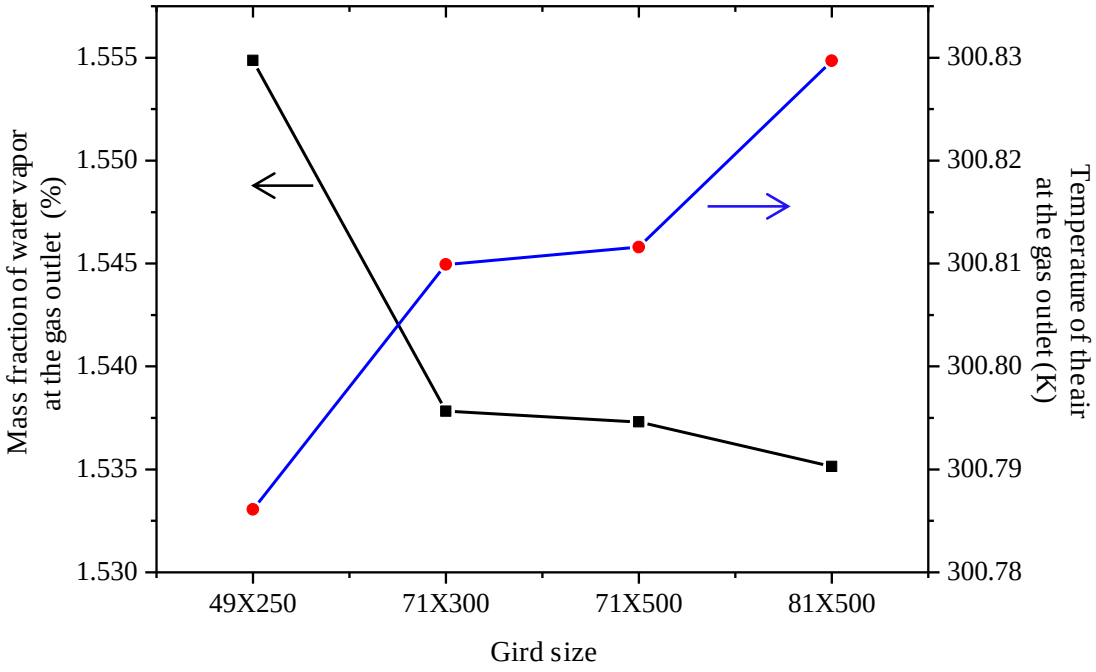

Fig. 4.3 Air conditions at the gas outlet with four types of grid

The simulation results of the four different grids are presented in Fig. 4.3. It can be observed that the grid size does have effect on the final calculation results. The mass fractions of water vapor at the gas outlet of 2.0 s decreased with the increase of the grid size. And the values of the latter three grids were very close. The deviation was within 0.1% for the second and third grid, and 0.3% for the second and fourth grid. As for the outlet air temperature, the difference was so small that the influence of the

grid size could be ignored. Considering the computational accuracy and cost, the grid 71×500 was selected for all the simulations.

4.4.2 Mass transfer

To further justify the established model, the calculation results of present work were compared with those of the hand-written program of the finite difference model. Here it will not spend too much space for introducing the finite difference model as it has been widely used in a large amount of literatures and explained in Chapter 2.

In Fig. 4.4, the results of two methods are compared. It was observed that the majority of the results of moisture content showed an acceptable difference of less than $\pm10\%$ and all of the results within $\pm20\%$. It had been found that the points with bigger discrepancies appeared when the air and desiccant velocities were relatively higher. And the specific tendency was as follows: when the air velocity was higher, the results of present model showed significantly higher water vapor concentration of outlet air than the finite difference model while when the desiccant velocity was higher, the results of present work showed obviously lower water vapor concentration of outlet air than the finite difference model. Therefore, it was concluded that the bigger discrepancies resulted from the different mass transfer theory adopted by the two models. The finite difference model employs the two film theory and the present model uses the penetration theory. As the penetration theory

takes the contact time into consideration, the air and desiccant velocities certainly have great influences on the final result, which will be explained in the next section in detail.

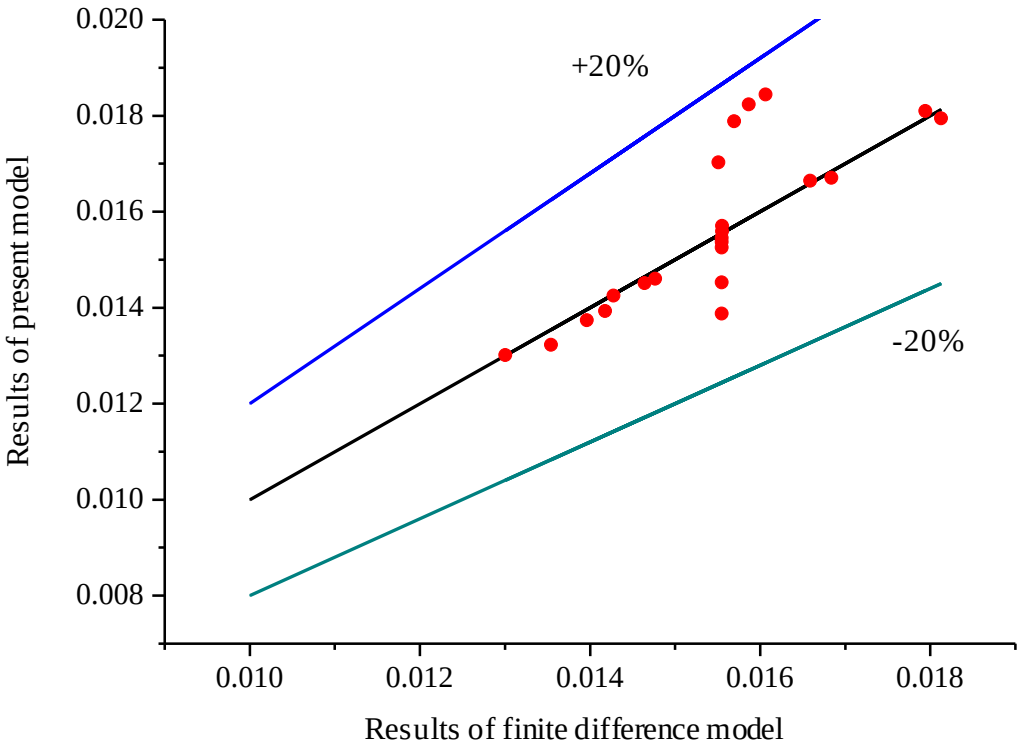

Fig. 4.4 Comparison of water vapor concentration of outlet air

4.5 Results and discussion

With the above established model, the dehumidification processes of the moist air were simulated in a range of different flow conditions. Table 4.1 presents the summary of different calculating conditions.

Table 4.1 Summary of calculating conditions

	Air			Desiccant		
Parameter	$T_{a,in}$ (K)	$x_{a,in}$ (%)	$u_{a,in}$ (m s^{-1})	$T_{s,in}$ (K)	$X_{s,in}$ (%)	$u_{s,in}$ (m s^{-1})
Basic point	303	2.0	0.2	298	30.0	0.07
Range	299-307	1.6-2.4	0.2-2.0	288-308	30.0-45.0	0.05-0.2

4.5.1 Example of dynamic description

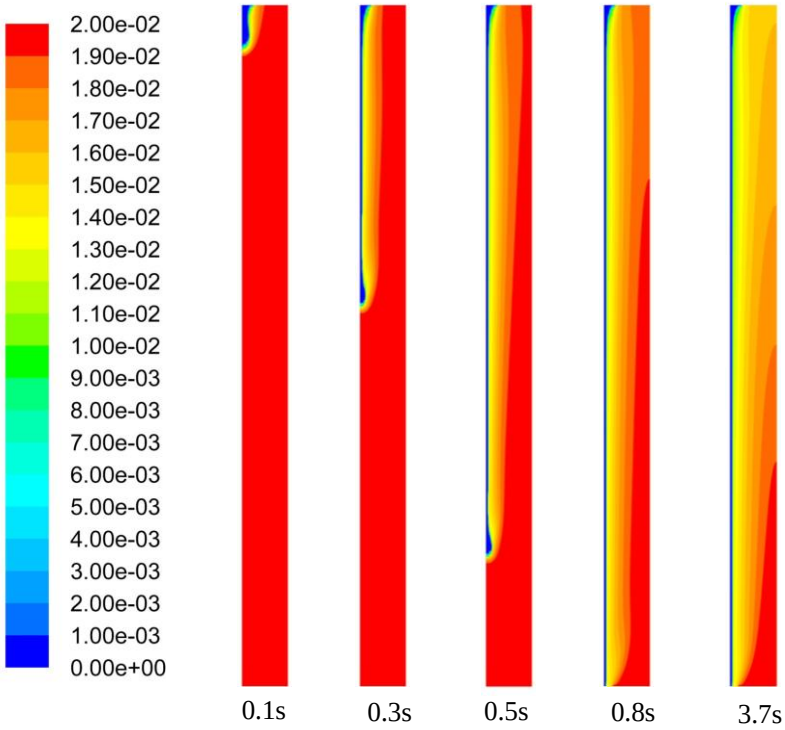

Fig. 4.5 Stages of film formation and mass transfer in the dehumidifier

Results of the model facilitated us to observe the stages of film formation, heat and mass transfer profiles in the dehumidifier interior. Fig. 4.5 gives an example of the dehumidification process. The desiccant solution flowed under the action of surface

tension, viscous force and gravity. In the early stage, the liquid congregation formed in the forepart due to the function of the surface tension and viscous force. As the desiccant velocity was big enough, the liquid solution flowed in a continuous film on the plate in the end. As for the heat and mass transfer, both of the water vapor concentration field and the temperature field in the channel could be observed at any time.

4.5.2 Influence of air velocity

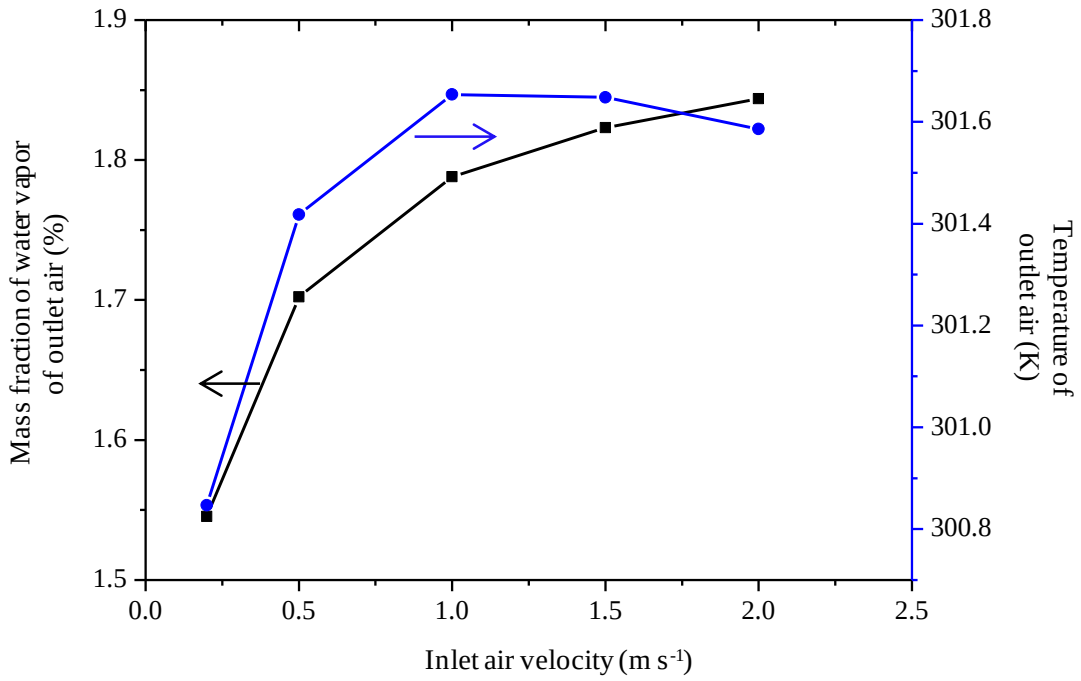

Fig. 4.6 Outlet air condition under different inlet air velocity

In previous researches, the effect of the air flow rate was always investigated. However, in the internally cooled dehumidifier or the adiabatic packed-bed

dehumidifier, where the air and desiccant flow in the channel similar to the geometry shape presented in Fig. 3.1, the air flow rate cannot express directly the air flow condition, as the flow rate depends greatly on the channel size. Thus, here the air velocity was selected for the air flow condition investigation. The results under different air velocities are presented from Fig. 4.6 to 4.8.

In Fig. 4.6, it was found that differences were quite dramatic for different air velocities. With the increase of the air velocity, the average mass fraction of water vapor in the outlet air increased as well. The reason was that when the air velocity was bigger, the contact time between the air and desiccant was shorter, which was bad for the mass transfer process. As far back as the year 1994, Park et al. (Park et al. 1994) had expressed the view of the point that lower air flow rates provided better humidity control and air cooling. Unlike the monotonous relation between the air velocity and outlet air average mass fraction of water vapor, the outlet air average temperature increased first and then decreased a litter with the increase of the inlet air velocity. There were two factors which had effects on the air temperature. On one hand, as the desiccant temperature was lower than that of the air, the air temperature would reduce by sensible heat exchanging with the desiccant. On the other hand, the water condensation of the air produced some latent heat, which would increase the air temperature. The above two factors were coupled, resulting in the outlet air temperature variation tendency.

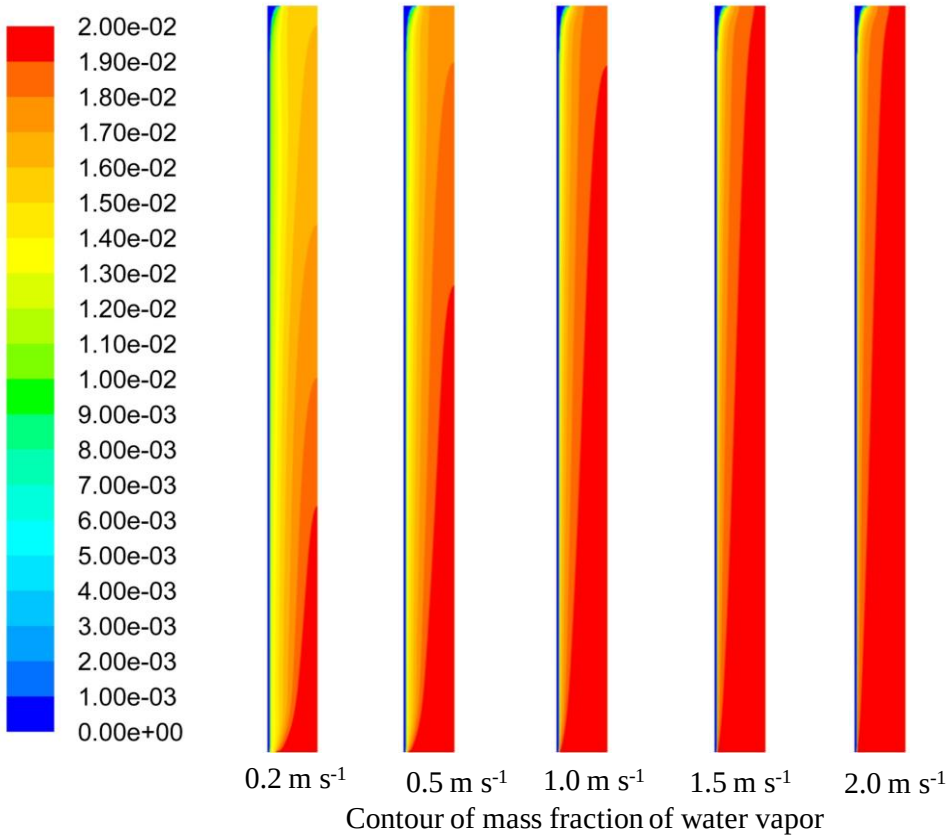

Fig. 4.7 Contour of mass fraction of water vapor under different inlet air velocity

The contour of mass fraction of water vapor in the interior of the dehumidifier is demonstrated in Fig. 4.7. It was concluded that to optimize the operating condition, the air velocity should be set in terms of the channel size, including the channel length and width. Longer channel would certainly provide longer contact time and larger contact area for mass transfer. However, the length could not be too long due to the installation problem and cost consideration. It could be observed that with the same channel length, the air velocity should be matched with the width of the channel. In present condition, it was found that the width of the channel was a litter bigger for air velocity above 1.0 m s^{-1}, as there were big red areas in the contour

diagrams, which manifested no water vapor had been transferred and absorbed by the desiccant. When mixing, it largely increased the humidity ratio of the outlet air.

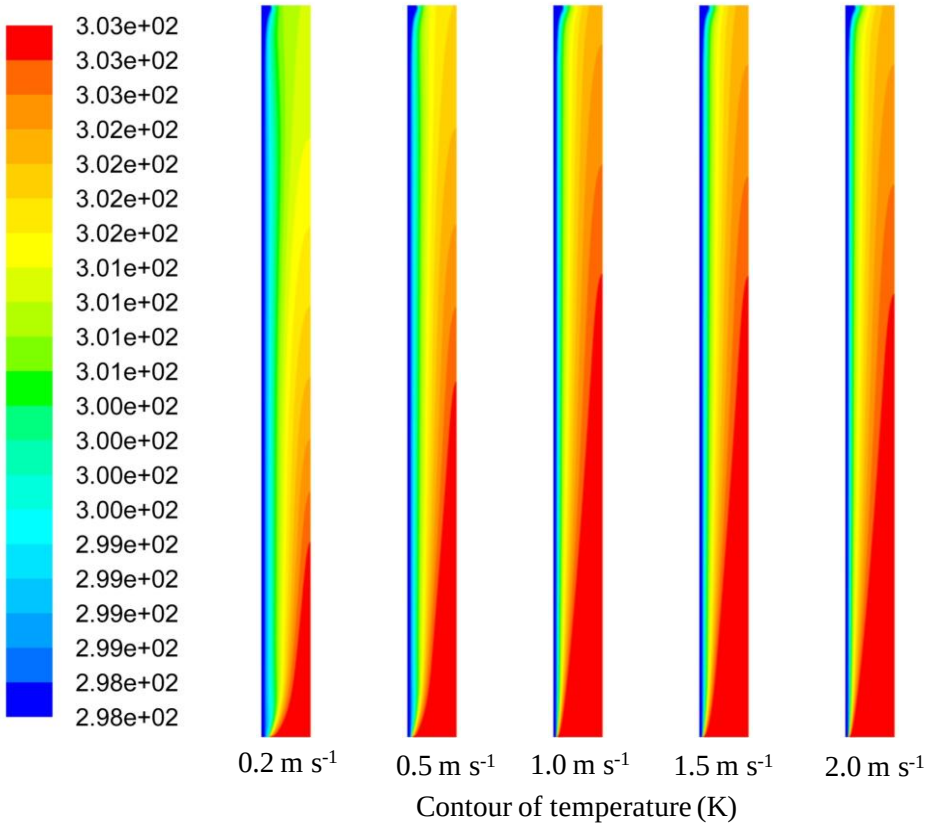

Fig. 4.8 Contour of temperature under different inlet air velocity

Fig. 4.8 presents the temperature distribution in the dehumidifier interior. According to the physical properties of LiCl solution, the thermal diffusion coefficient was much bigger than the mass diffusion coefficient of water in the solution, which explained why the red areas in Fig. 4.8 were smaller than those of Fig. 4.7.

4.5.3 Influence of inlet air water concentration

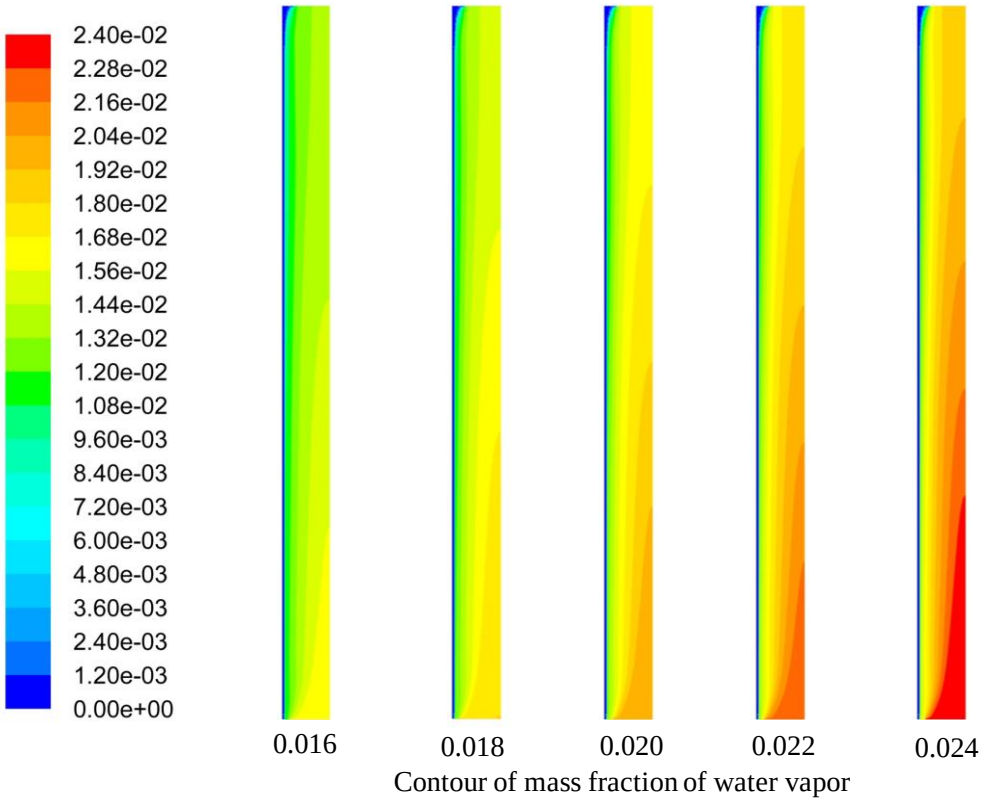

Fig. 4.9 Contour of mass fraction of water vapor under different water vapor fractions of inlet air

Keeping other inlet parameters at the basic point, the increase of the mass fraction of water vapor in the inlet air will enhance the driving force of mass transfer between the air and desiccant. From Fig. 4.9, it was found that the gradient of water vapor concentration became more and more obvious with the increase of the inlet air water vapor concentration. It was also evident to observe the water vapor transportation from the symmetry to the desiccant film.

To make it clearer, the gradient curves of mass fraction of water vapor at the same cross section (y=0.075m) under different inlet water vapor concentrations of inlet air are drawn in Fig. 4.10. There existed a maximum gradient value near the desiccant surface for all the cases, and it reduced along the x direction. In the place far from the liquid film, the mass transfer gradient could be nearly zero, which indicated that no mass transfer happened there.

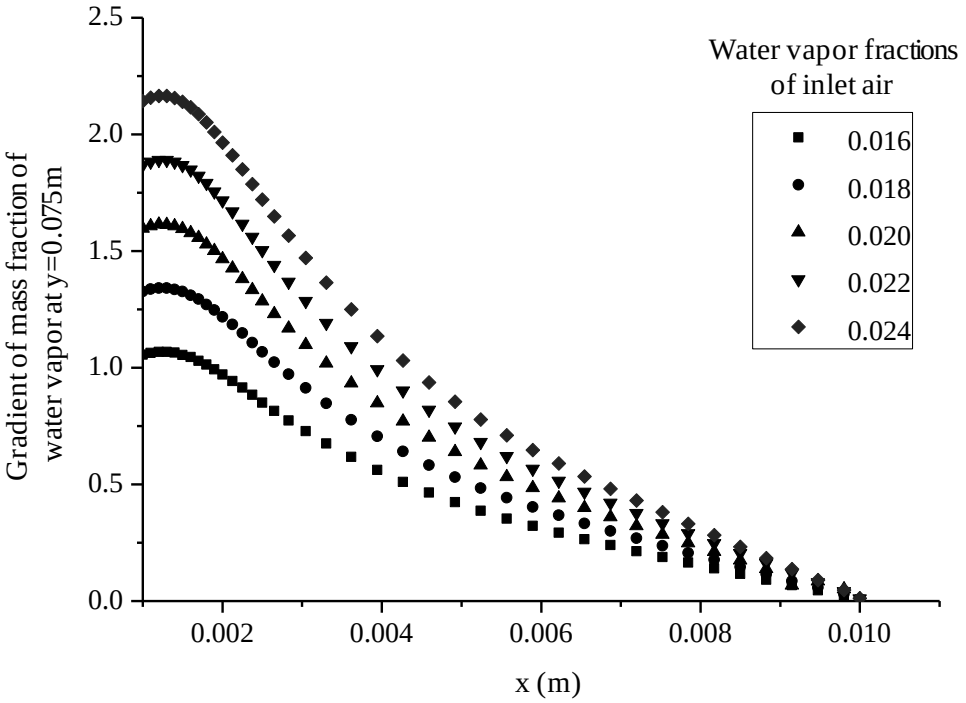

Fig. 4.10 Gradient of mass fraction of water vapor at y=0.075m in a range of water vapor fractions of inlet air

Meanwhile, the gradient of mass fraction of water vapor in the whole channel is also analyzed. The results are demonstrated in Fig. 4.11. Here the locations of the cross sections, the y values, varied from 0.005m to 0.12m. It was discovered that the

gradient curves of mass fraction of water vapor at the lower part of the channel were very different from those of other parts, and the gradients became very small even in the place near the wall surface. So it was recommended to decrease the size of the air entry. To keep the necessary space for mass transfer in the upper part of the channel, a good method is to tilt the plate. In fact, early in 2004, Ali and Vafai [23] had pointed out that the inclination angle played a significant role in enhancing the dehumidification.

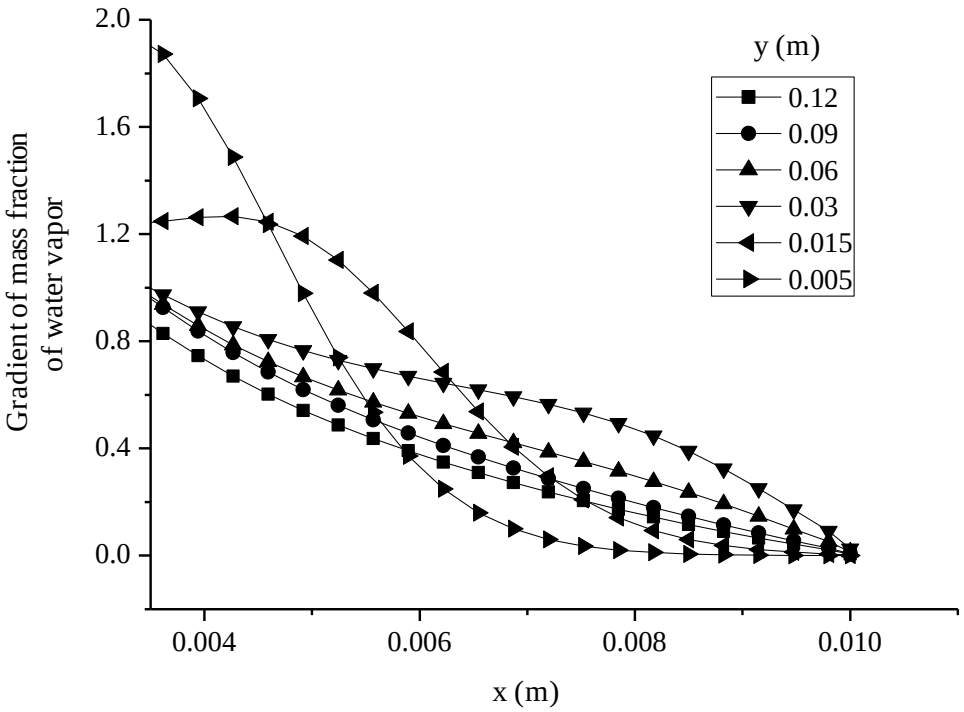

Fig. 4.11 Gradient of mass fraction of water vapor at different y values ($x_{a,in}$ =0.020)

4.5.4 Influence of inlet desiccant concentration

In the section, the local film thickness profiles of the simulations with various inlet

desiccant concentrations are illustrated in Fig. 4.12. It was observed that with a relatively lower desiccant concentration, the liquid films were almost smooth. When the inlet desiccant concentration increased, the liquid film thickness increased and the surface waves became more and more evident correspondingly. It was concluded that the obvious surface waves were generated by the more drastic absorption processes, when significant momentums were exchanged at the vapor-liquid interface.

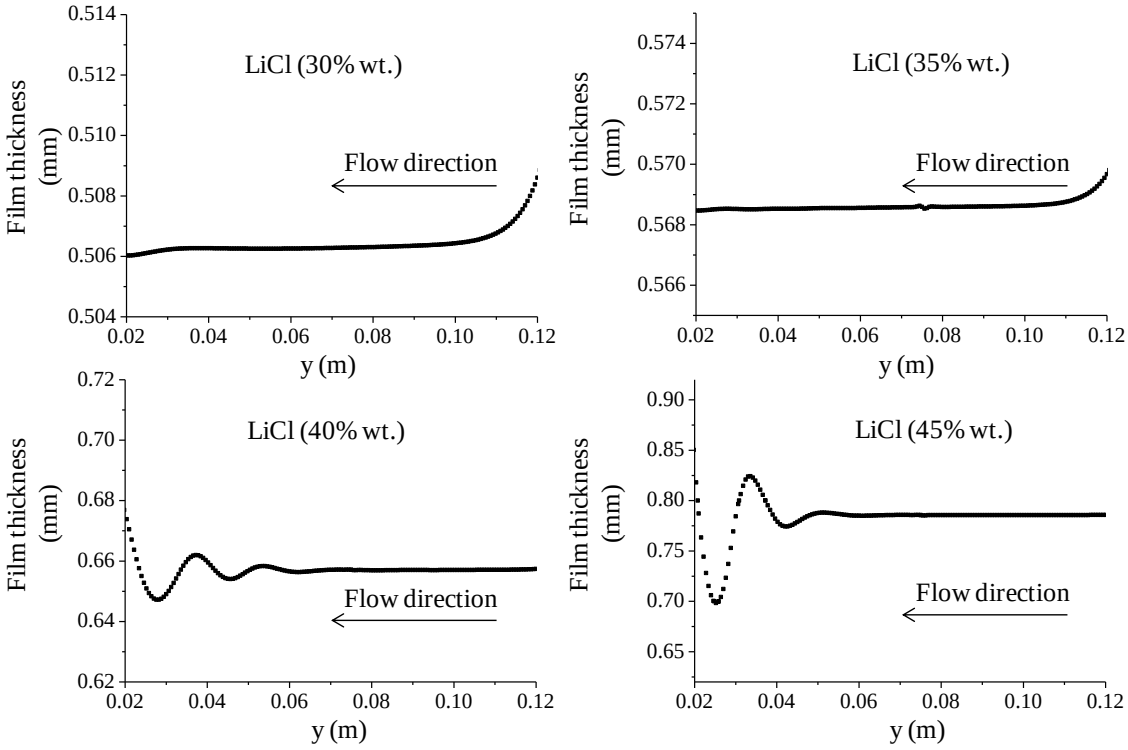

Fig. 4.12 Liquid film thickness profiles for various inlet desiccant concentrations

4.5.5 Influence of inlet desiccant temperature

It was found that the desiccant temperature had great impact on the dehumidification performance. As shown in Fig. 4.13, with the increase of the desiccant temperature,

the water concentration of outlet air increased sharply with a parabolical trend in general. One well known reason was that the surface vapor pressure of the desiccant with higher temperature was higher accordingly. Another reason could be explained by Fig 4.14. It showed the influence of the inlet desiccant temperature on the temperature distribution of the channel. It was easy to observe that the temperature of the air was also affected significantly by the desiccant temperature due to the heat transfer. The above two factors resulted in the parabolical curve in Fig. 4.13. In Fig 4.13, the curve of the outlet air temperature under different inlet desiccant temperatures was also plotted. The results showed that the latent heat of dehumidification played a minor role in determining the outlet air temperature for this channel. However, if the channel was narrower, the situation might be different.

The interfacial temperature along the liquid flow direction is presented in Fig. 4.15. It was observed that the change of the interfacial temperature was not discernible in the dehumidification process, which meant that the desiccant temperature changed a little as well. The latent heat produced for absorption and the sensible heat due to the temperature difference were too small to heat the solution, as the heat capacity of the desiccant was big. On the contrary, the temperature of the moist air changes dramatically along the channel, whose temperature distribution had been shown in Fig. 4.14.

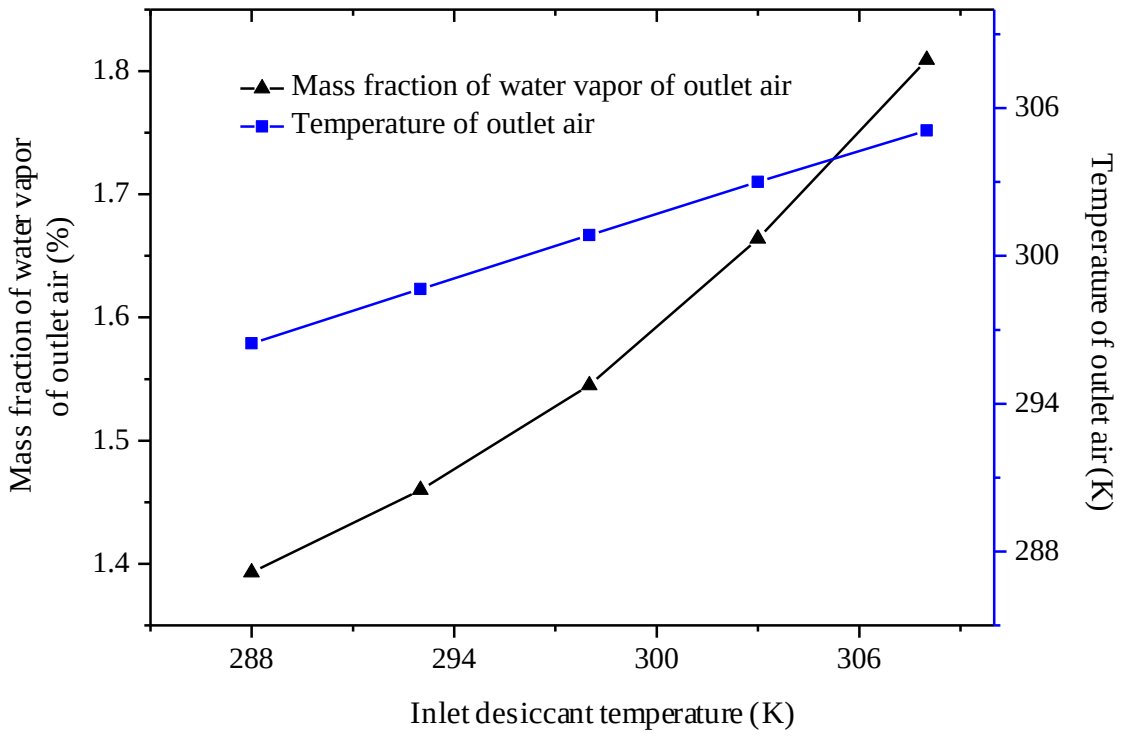

Fig. 4.13 Mass fraction of water vapor and temperature of outlet air under different inlet desiccant temperature

In addition, the interfacial velocities under different inlet desiccant temperature were analyzed, as shown in Fig. 4.16. As the desiccant with higher temperature had lower viscosity, the corresponding interfacial velocity would be larger. The results demonstrated that the increase of the inlet desiccant temperature would enhance the interface velocity. It meant that the high temperature desiccant worsened the dehumidification performance, not only by reducing the mass transfer driving force but also through decreasing the contact time between the desiccant and air.

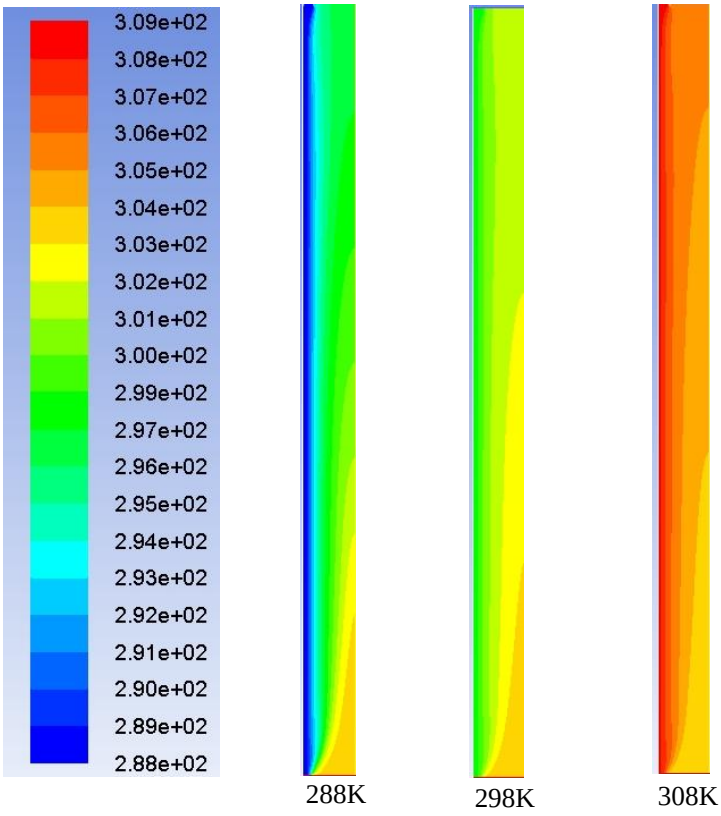

Fig. 4.14 Contour of temperature under different inlet desiccant temperature

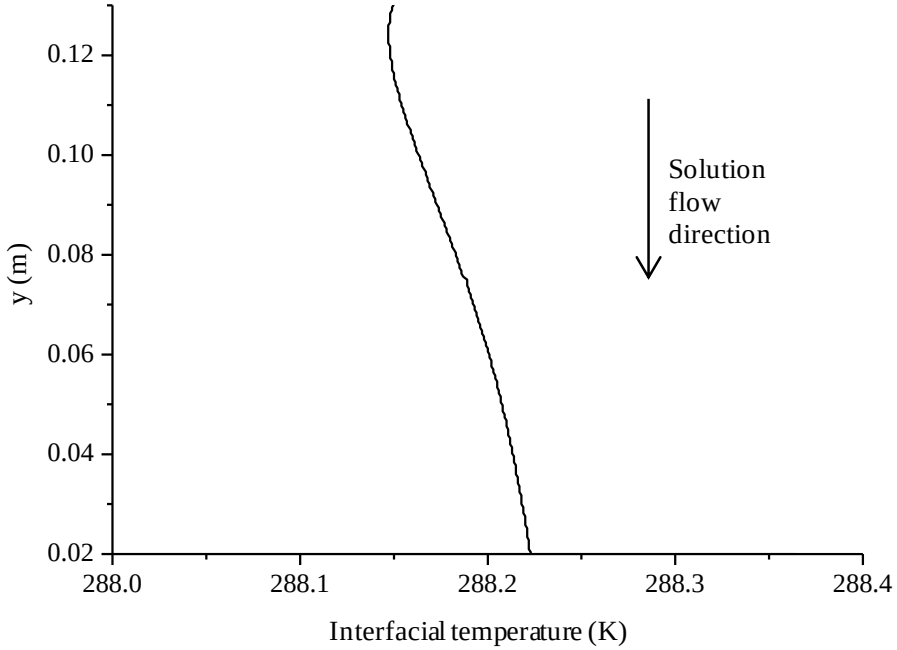

Fig. 4.15 Interfacial temperature along the liquid flow direction

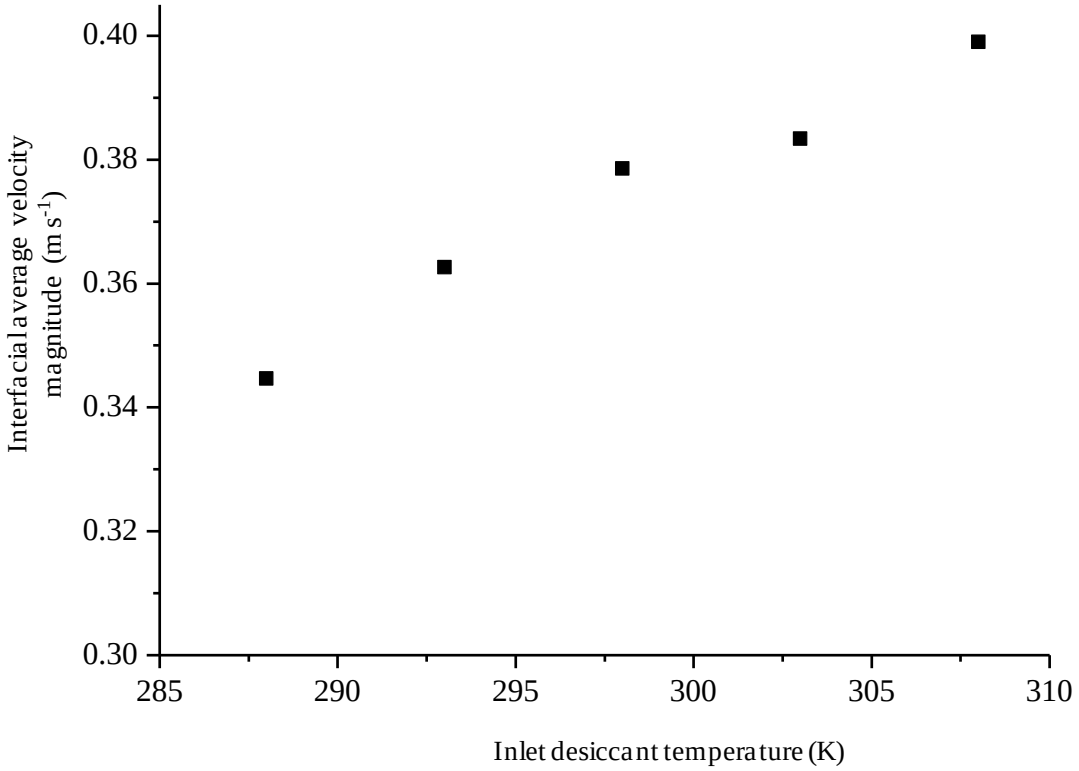

Fig. 4.16 Interfacial average velocity magnitudes under different inlet desiccant temperature

4.5.6 Influence of inlet solution flow rate

Under different inlet solution flow rate, the mass fraction of water vapor and temperature of outlet air had the similar variation trend. As shown in Fig. 4.17, it was observed that the initial increase of inlet solution flow rate would improve the dehumidification performance significantly while the effect would reduce with further increase of inlet solution flow rate. By looking into the contours of temperature and mass fraction of water vapor under different inlet solution flow rate in Fig. 4.18, a common point was found, that is, the thermal diffusion was faster than the mass diffusion. It meant $Le > 1$ for all the cases. In early research, through comparing the

simulation results with the experimental data of Fumo and Goswami (Fumo and Goswami 2002), Babakhani (Babakhani 2009) had pointed out that *Le*=1.1 instead of 1.0 was more preferable for the prediction of the performance of the dehumidifier. Thus, it could be verified that the present model possessed high accuracy.

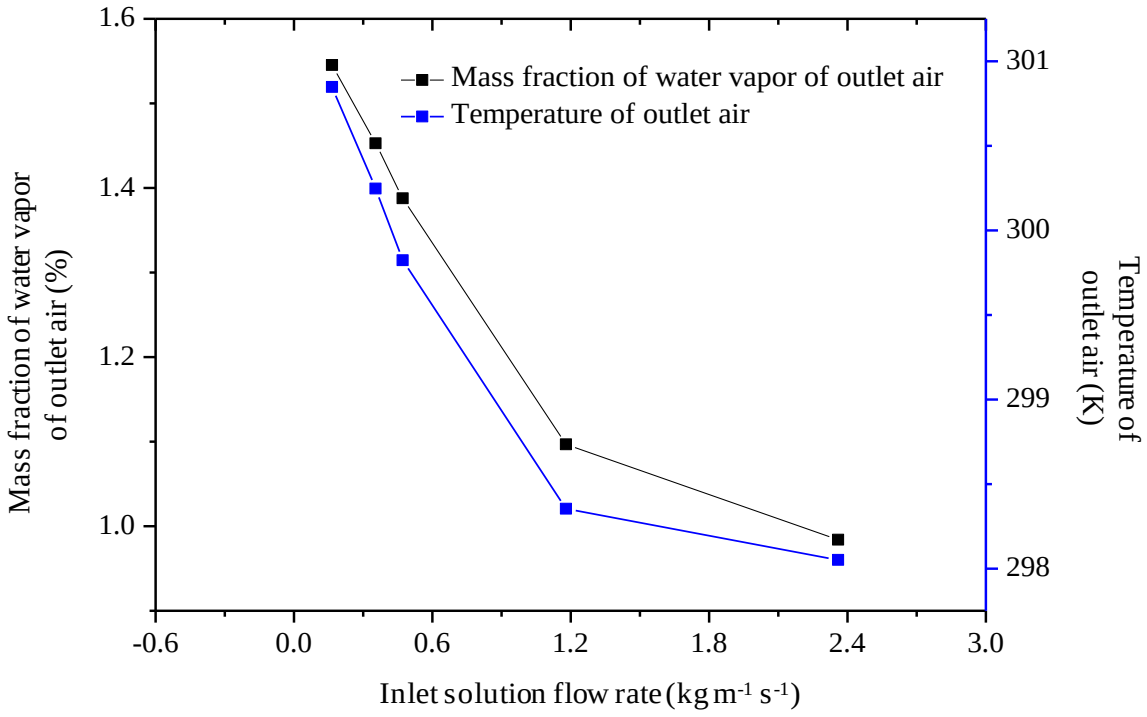

Fig. 4.17 Mass fraction of water vapor and temperature of outlet air under different inlet solution flow rate

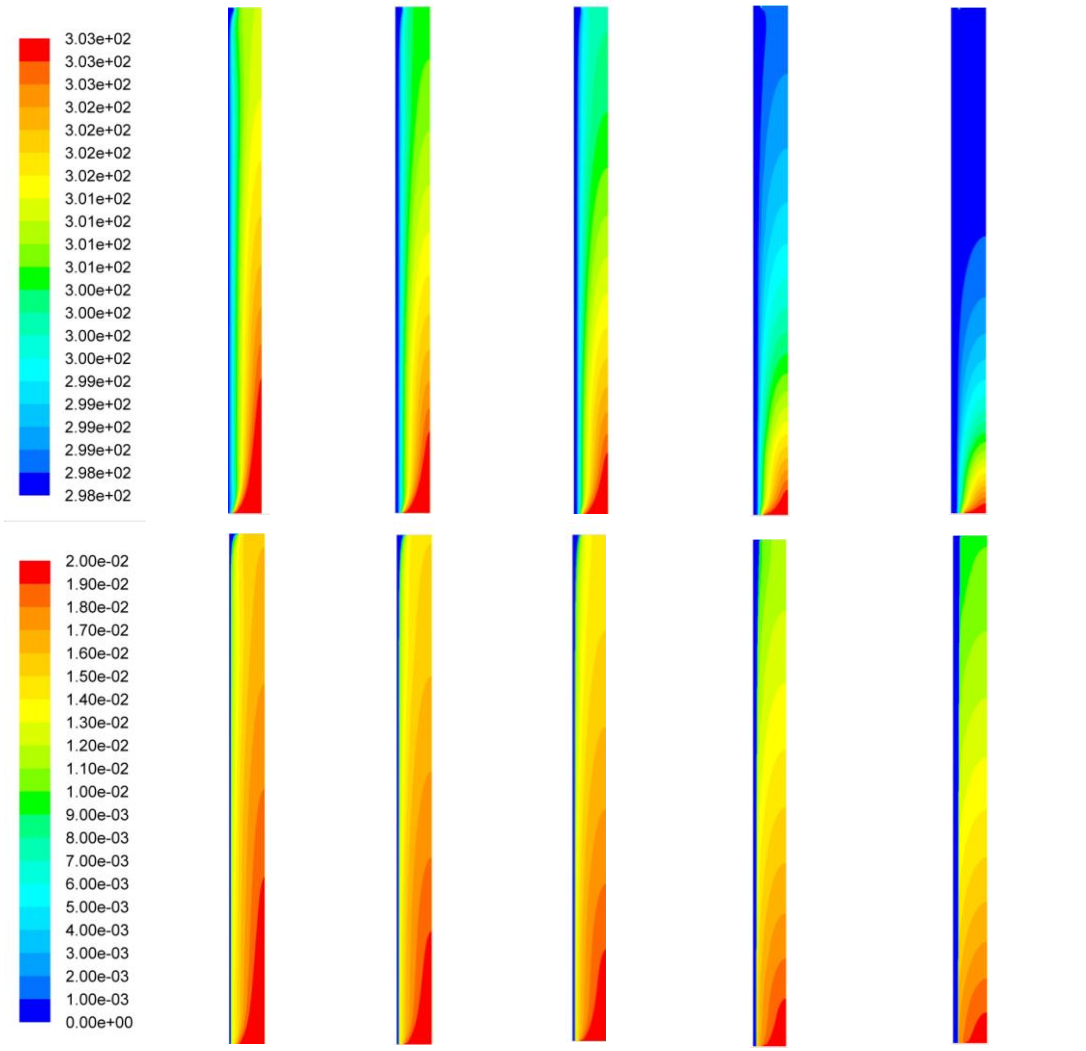

Fig. 4.18 Contours of temperature and mass fraction of water vapor

4.5.7 Influence of internal cooling

In an internally cooled dehumidifier, besides the contact between air and desiccant, some cold source which can provide cool fluid like air or water is added to take away the latent heat produced in the process of dehumidification, which can be regarded as an isothermal process in general. As the latent heat is removed from the dehumidifier, it reduces the temperature rise of the solution and air, resulting in efficiency

improvement. In this section, the dehumidification process with cooling was analyzed.

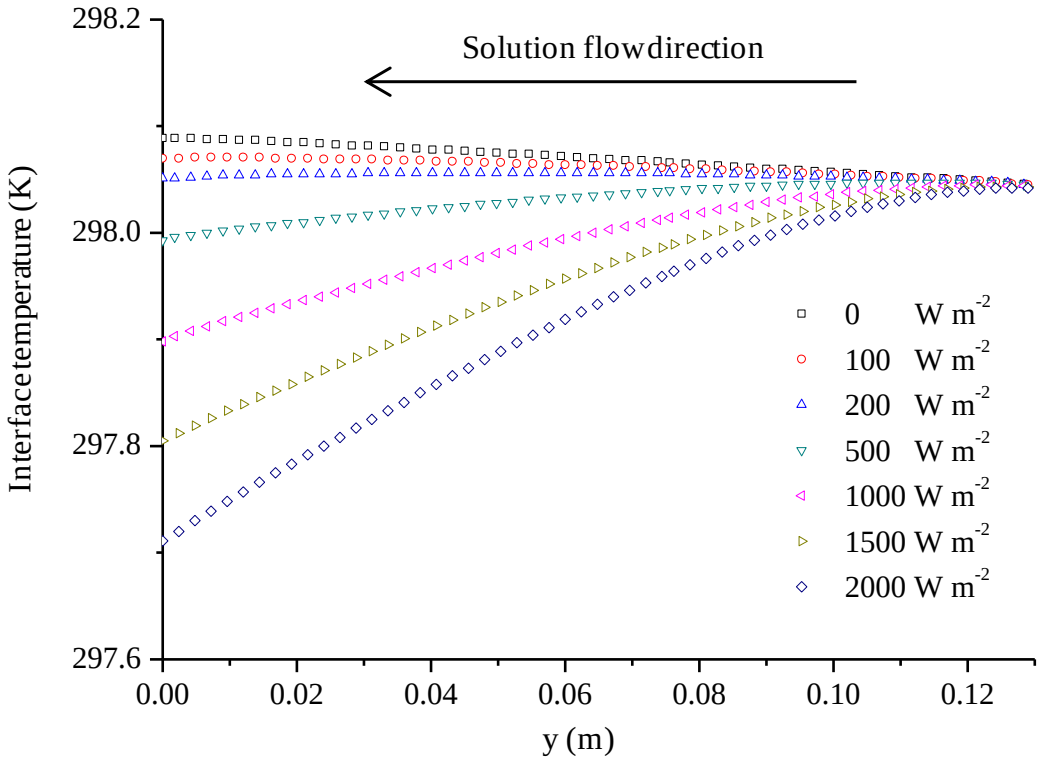

Fig. 4.19 Interface temperature along the flow direction under different heat flux

In Fig. 4.19, the interfacial temperature along the flow direction under different heat fluxes is presented. Here the heat fluxes were set to negative values to achieve cooling. It was observed that when the heat flux was lower, the interface temperature would increase along the flow direction, resulting from the generation of latent heat in the dehumidification process. But when the heat flux reached some value, not only the latent heat was removed, but also the temperature of the fluids in the channel was reduced. As the channel was short, the temperature decrease was not that significant. But it is predicted from the trend that the effect of cooling on the interface temperature

can be great. When the interface temperature decreases, the surface pressure of the solution will decrease so as to enhance the mass transfer.

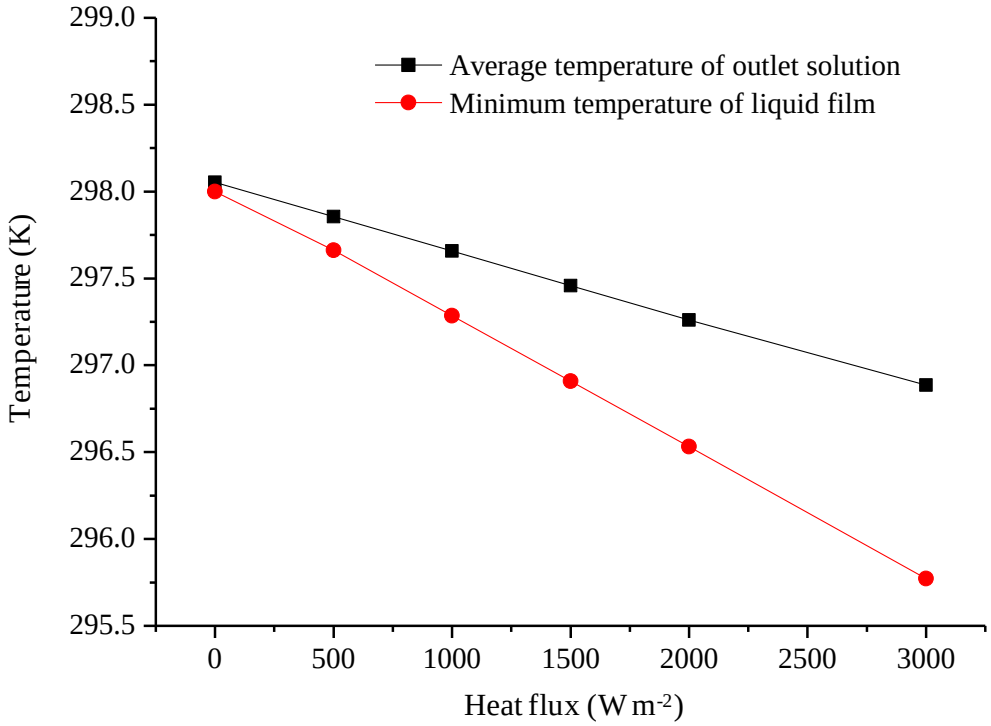

Fig. 4.20 Temperature of liquid phase under different heat flux

As illustrated in Fig. 4.20, it was obvious that the cooling reduced the temperature of the liquid phase significantly. However, it seemed that the cooling did not contribute too much to the dehumidification performance by seeing Fig. 4.21. From Fig. 4.19, it was found that in the flow direction of the air, the temperature difference of the solution between the two cases (with cooling and without cooling) would decrease gradually. The solution temperature with cooling would be lower than that without cooling, which was beneficial for dehumidification. On the other hand, the water

content in the air without cooling would be larger than that with cooling. In the bottom of the channel, the solution temperature was much lower with cooling than without cooling and the water content was equal for both cases, thus the driving force was higher with cooling than without cooling. In the upper part of the channel, the reverse was true. Except for the driving force, the mass transfer coefficient was another factor which decided the mass transfer amount. As the mass transfer coefficient increased with the decrease of the temperature, the mass transfer coefficient with cooling would be greater than that without cooling. Under the function of the above two factors, the dehumidification amount was a litter bigger with cooling than without cooling.

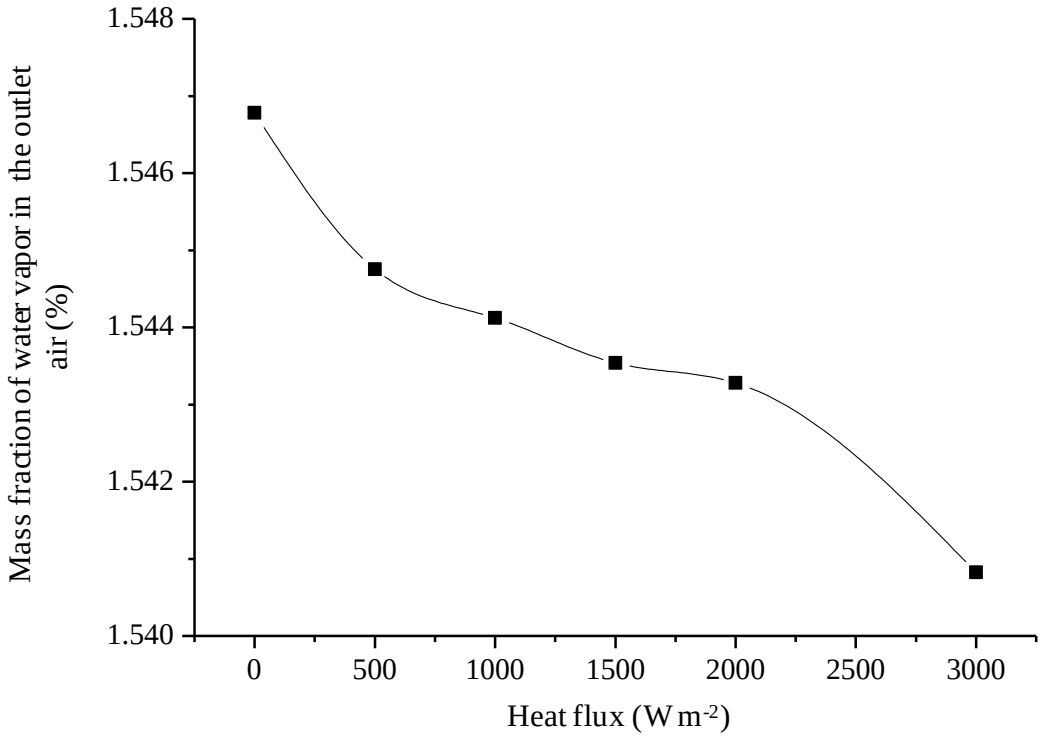

Fig. 4.21 Water content in the outlet under different heat flux

Except for the equal heat flux, it is possible to set other internal cooled boundaries in FLUNET by incorporating the user defined files. Further studies are needed for investigating the influence of the different cooling conditions.

4.5.8 Influence of variable physical properties

It has been mentioned that in most of the previous studies, the properties of the desiccant solution were assumed constant, which is not the actural condition. In the present work, user defined files of various properties of LiCl solution were incorporated into the model, including the density, thermal conductivity, viscosity and so on. During the calculation, the properties of the solution would change simultaneously with the change of the temperature and concentration. In Fig. 4.22, the results for the cases of constant and variable properties are presented. It can be seen that the interfacial solution concentration was lower for variable properties case. Along the flow direction, the desiccant absorbed the moist air, resulting in the increase of the interfacial temperature and decrease of the concentration. As for the constant properties case, the properties of the solution did not change, the surface vapor pressure would keep constant through the process, which would be higher than the variable properties case. Therefore, the amount of water absorption would be higher in the constant properties case, resulting in the lower interfacial solution concentration. The study also demonstrated the necessity of considering the variable properties of the desiccant solution during the simulation.

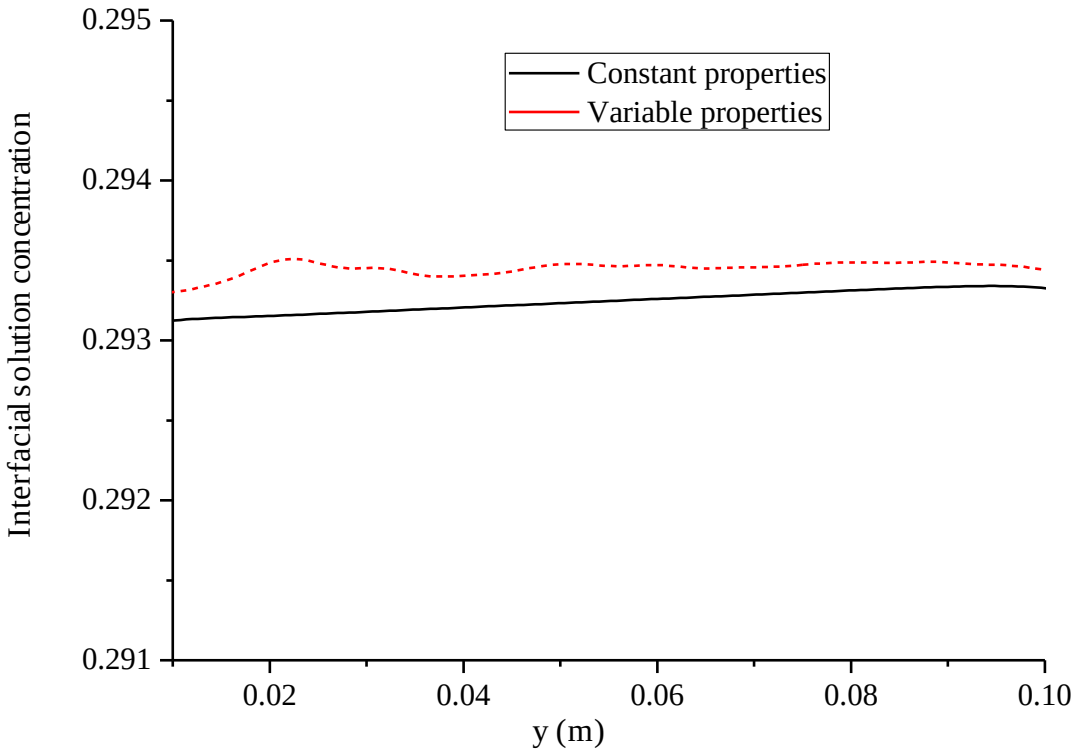

Fig. 4.22 The profile of interfacial solution concentration along the film flow

4.6 Summary

A new simulation model has been developed in this paper for the simultaneous flow, heat and mass transfer processes in a two-dimensional channel of the liquid desiccant dehumidifier. The model was justified to be able to predict the performance of the dehumidifier. Compared with most of the previous models for the dehumidifier, the new model has several advantages,

1) The changed velocity field was calculated by considering the effects of gravity,

viscosity and surface tension, all of which were generally ignored in previous models.

2) The penetration mass transfer theory was used to replace the two film theories, so that it became possible to observe the dynamic heat and mass transfer process of the dehumidifier.

3) Both of the variable physical properties of the desiccant and air were taken into consideration.

4) The simulation results allowed us to predict the water vapor concentration field, temperature field, gradients of water vapor concentration at different places, local film thickness, and the influence of the mass transfer on the film surface waves.

5) The model was also potential for investigating the internally cooled dehumidifier with different cooling conditions.

With the established model, the parametric studies were conducted in a range of different flow conditions. Several important conclusions are summarized as follows,

1) Through the simulation, it was found that the air velocity played a critical role on

the performance of the dehumidifier, and it had to be matched with the channel geometric size for optimization.

2) The gradient of water vapor concentration became more and more obvious with the increase of the inlet air water vapor concentration. It was also evident to see the water vapor transportation from the symmetry to the desiccant film. By analysis, it was suggested to tilt the plate to enhance the mass transfer.

3) With higher solution concentration, the more obvious surface waves were generated by the more drastic absorption processes, when significant momentums were exchanged at the vapor-liquid interface.

4) The desiccant temperature had great impact on the dehumidification performance. Meanwhile, the latent heat of dehumidification played a minor role in determining the outlet air temperature for this channel in the present case. On the basis of the investigation of interfacial velocity, it was concluded that the high temperature desiccant worsened the dehumidification performance, not only by reducing the mass transfer driving force but also through decreasing the contact time between the desiccant and air.

5) By looking into the contours of temperature and mass fraction of water vapor

under different inlet solution flow rate, it was found that $Le > 1$ for the present simulation. The results showed good agreement with the previous experimental study.

CHAPTER 5

EXPERIMENTAL STUDY OF THE FLOW CHARACTERISTICS

5.1 Introduction

The liquid falling film flow on vertical or inclined walls is easily observed no matter in our daily life or the industrial processes. From the research point of view, the falling film flow is a kind of classical free-boundary phenomenon which occupies the strategic position of many applications **(**Kalliadasis et al. 2012). Recently, the dynamics of falling film has drawn more and more attention as it plays a critical role in understanding the nature of the flow. Experimental studies have been carried out to investigate the characteristics of the falling film flows for different geometric structures (Patnaik and Perez-Blanco 1995; Belt et al. 2010; Szulczewska et al. 2003). However, the fundamental researches of the film flow in the dehumidifier are still very limited and information on detailed characteristics is much less reported experimentally.

The specific differences between the flow in the dehumidifier and the general film

flow mainly exist in the two aspects. On the one hand, the properties of the desiccant are different from the previous media. On the other hand, the operating conditions are based on the dehumidification processes, which are different from the previous studies, such as surface temperature, air velocity and so on.

To give a clear and more comprehensive explanation of the film flow in the dehumidifier, the test rig was designed for observing the flow conditions easily in the present work. In the chapter, the following aspects of the experimental results would be reported,

1) The solution flow morphology on a flat plate was described and explained.

2) The coverage ratio was obtained under diverse conditions of the test surface.

3) The minimum wetting rate was investigated and compared with the literature.

4) The mean and temporal film thickness was obtained and compared for the upper and lower part of the film. The temporal film thickness was then analyzed with statistical method.

5.2 Description of the test rig and research method

The sketch of the film flow test is presented in Fig. 5.1. The test surface was a panel made of 316 steel, 400 mm wide (W) and 500 mm long (L), equipped with transparent organic glass side walls to allow the viewing of the liquid film. To make sure the liquid fall vertically and uniformly, several kinds of distributors were designed and tested, as shown in Fig. 5.2. Through test, it was found the design (c) was best for the liquid solution distribution. The solution flowed in the distributor from the upper left import hole. The liquid began to diffuse out once reaching the slot, that is, the solution outlet. As the solution flow was not full pipe flow, there were some bubbles at the exit of the import hole. To try to avoid the disturbance of the bubbles, the hole was opened on the left side of the distributor. In addition, many tiny holes were opened on the upper side of the distributor to release the air bubbles.

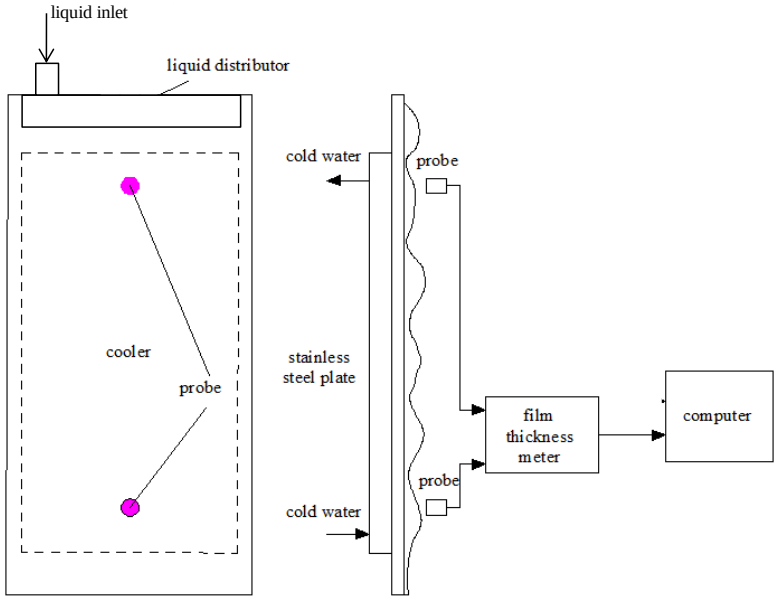

Fig. 5.1 Sketch of the film flow test: front view and cross section view

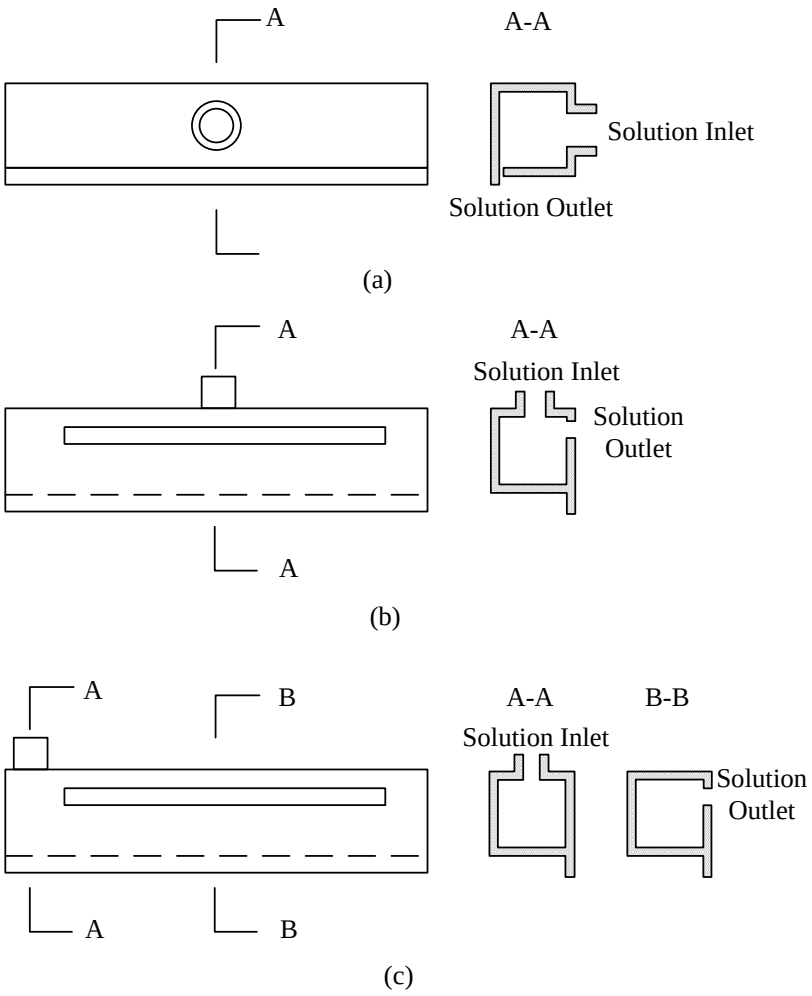

Fig. 5.2 A sketch of three kinds of solution distributors

The JDC-2008 ACCUMEASURE INSTRUMENT developed by Tianjin University was used to measure the film thickness. It is a precision instrument with the resolution of 0.1 μm and the accuracy of 0.8 μm. The principle of the capacitance method has been explained in Chapter 2. The probe was located near the film and oriented perpendicularly to the test surface. In the experiment, the probes were installed at two longitudinal distances (0.15m and 0.35m from the solution inlet).

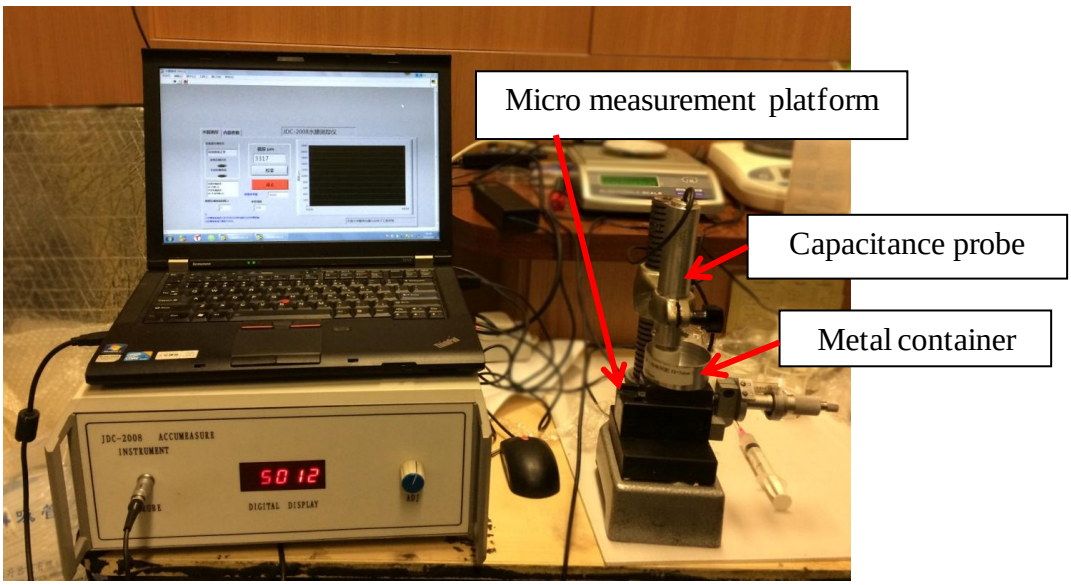

Fig. 5.3 Picture of calibration devices

Before using the device to measure the film thickness, it needed to calibrate it for the solutions with different concentration. Calibration was conducted in static condition, as shown in Fig. 5.3. The calibration process was as follows,

1) Add a certain amount of solution in a metal container. The bottom of the metal container should be covered totally by the solution.

2) Place the metal container horizontally on the micro measurement platform.

3) Adjust the distance between the head of the probe and the liquid surface until the initial voltage reach about 4000mV.

4) Re-zero the film thickness value, and lift the metal container with a certain value (100 μm).

5) Record the film thickness value on the screen.

6) Repeat the step 4) and 5) to obtain the calibration curves.

The calibration results are reported in Fig. 5.4. The LiCl solution with 0.00% and 39.00% concentration were tested. The results showed that the concentration of the solution nearly had no effect on the linear parameter of the instrument. In addition, the accuracy of the device was very high for testing the film thickness of the LiCl solution.

A camera was used to record the images of the liquid film (resolution of 3264×2448), and some flow patterns were recorded using the video (120 fps). By capturing the film flow by the camera, the pictures were dealt by the Microsoft Visio and GetData Graph Digitizer to obtain the results of the coverage ratio. The maximum relative error of coverage ratio was 0.5% by considering the width of an individual pixel in the image and the minimum observed value.

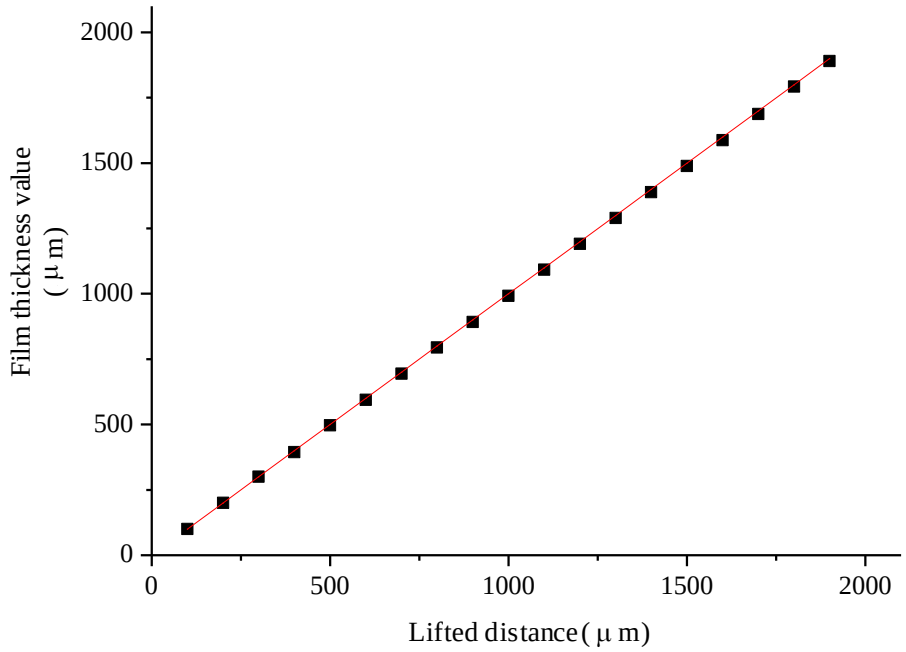

(a) Water

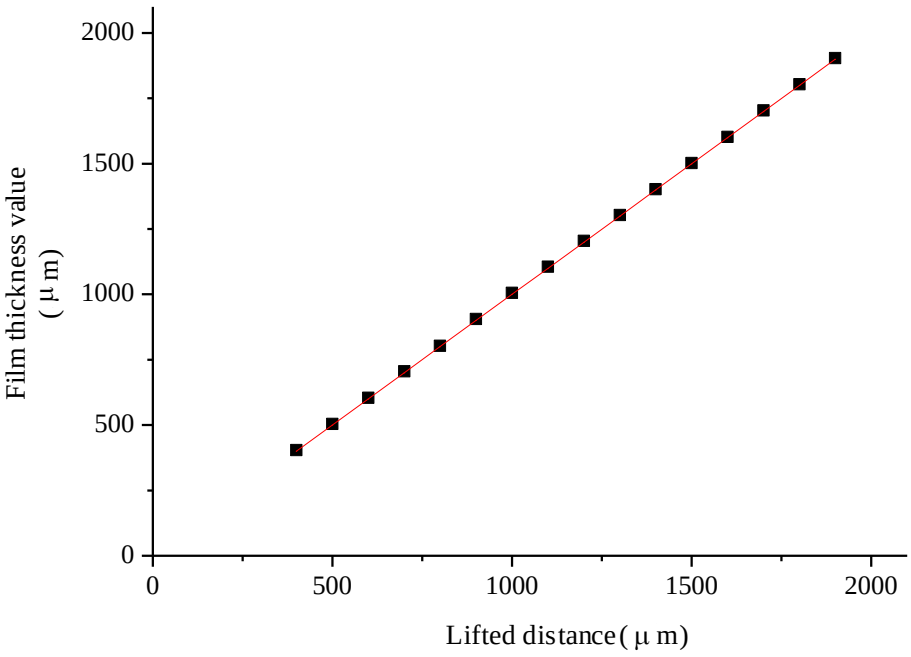

(b) LiCl solution with 39.00% mass concentration

Fig. 5.4 Calibration curve for the capacitance probe

5.3 Results and discussion

5.3.1 Flow morphology

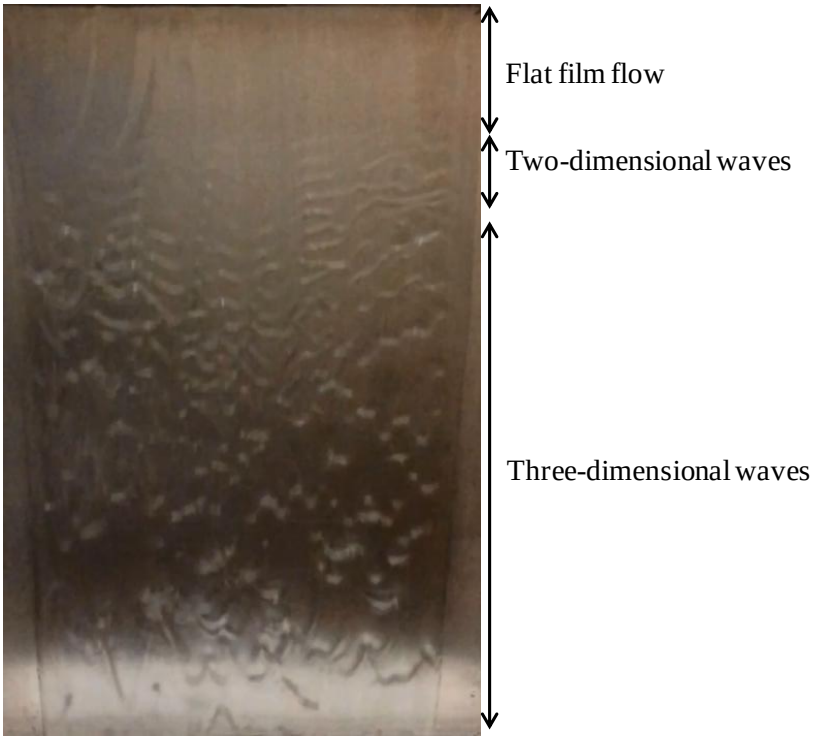

Fig. 5.5 Image of waves occurring on the falling film at Re=66.2

In the section, the dynamics of film flow down the vertical plate was analyzed in detail. As shown in Fig. 5.5, a typical wave evolution with different wavefront patterns can be observed clearly. In the first stage, a smooth surface was visible near the inlet. In the second stage, it is able to find some two-dimensional deformations appeared on the film surface. Due to the perturbation of the import pressure in the left part of the liquid distributor, it is not very easy to observe the two-dimensional deformations as they

developed quickly to the three-dimensional deformations, as presented in the third stage along the film flow direction. In the process, the waves separated, coalesced and interacted with each other, resulting in the complicated surface patterns.

Similar to the literature (Park and Nosoko 2003), the structure of a single large teardrop hump and several small capillary ripples was also found in the present experiment. The snapshot and simulation of the structure were presented in Fig. 5.6. It was found that the large teardrop hump started with a steep front and ended with a relatively smooth surface, which was merged into the film substrate. As the hump carried most of the liquid substance, it played an important role in determining the heat and mass transfer rate in the wave interior, between the wave and the wall, and between the wave and the environment. According to the literature, the structures are often called solitary waves (Chang 1994; Liu and Gollub 1994; Ramaswamy et al. 1996) as they are separated from each other. It was also found that a large amount of horseshoe shapes appeared in the film waterfront patterns, which was consisted of a large curvature head and two legs stretching upward. The pattern was also captured in the existing literature when the Re was above 40.

(a) Snapshot of the structure in the 2-D and 3-D waves at Re=66.2

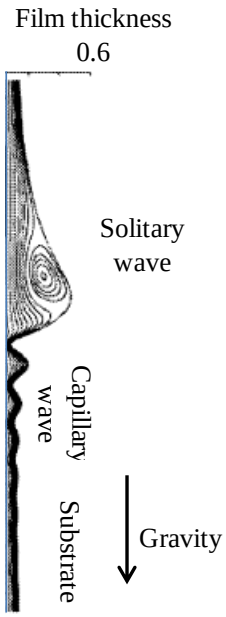

(b) The structure and vortex in the hump of simulation results at Re=36.6 (Nagasaki et al. 2002)

Fig. 5.6 Structure of solitary wave

5.3.2 Coverage ratio

The coverage ratio is important for the heat and mass transfer in the dehumidifier. The definition of coverage ratio in the present work is,

$$A_p = \frac{A_{wet}}{A_{all}} \tag{5.1}$$

where A_{wet} is the wetted area and A_{all} is the overall area of the plate with the slot of the liquid distributor as one side.

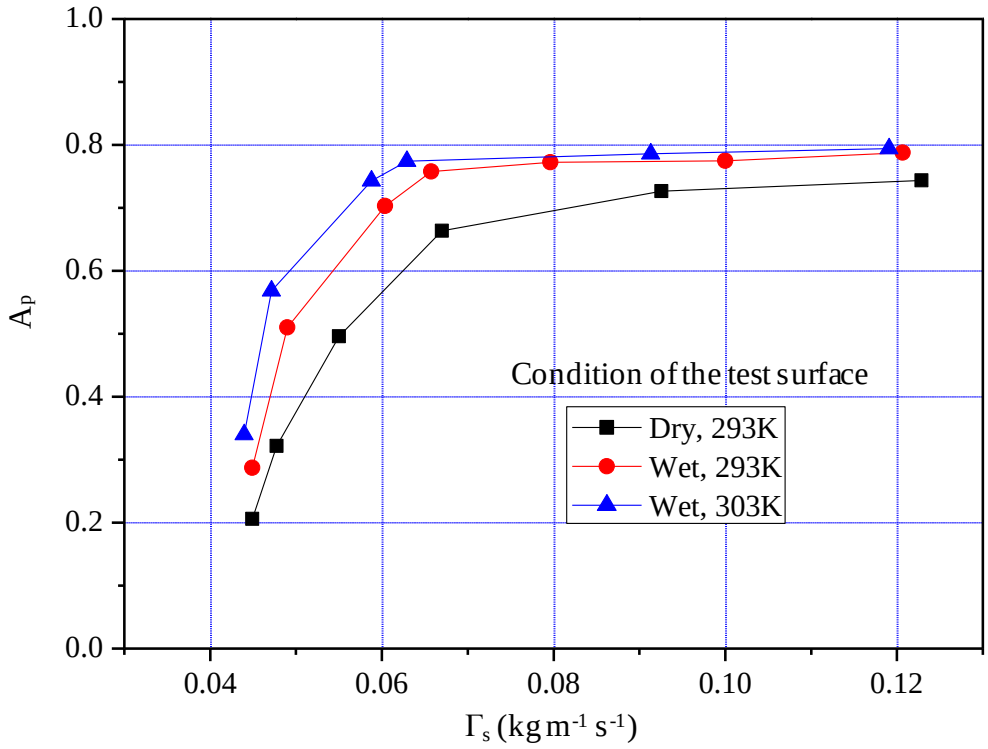

Fig. 5.7 Coverage ratios under different surface conditions (T_s =294.8 K)

The coverage ratios under different surface conditions were investigated, as shown in Fig. 5.7. It was found that on the dry plate, it needed much higher flow rate to achieve high coverage ratio than on the wet plate. As reported in existing literature (Yu et al 2012), the pre-wet of the surface can reduce the contact angle so as to make the surface more hydrophilic. The real pictures of the film flow with the same solution flow rate

were taken for both of the dry and pre-wetted surfaces, presented in Fig. 5.8. It was observed that the edge of the film flow showed different features. For the dry surface, the accumulation of the liquid on the edge of the film was more obvious than the pre-wetted surface. It acted as a dam to prevent the spread of the liquid on the surface.

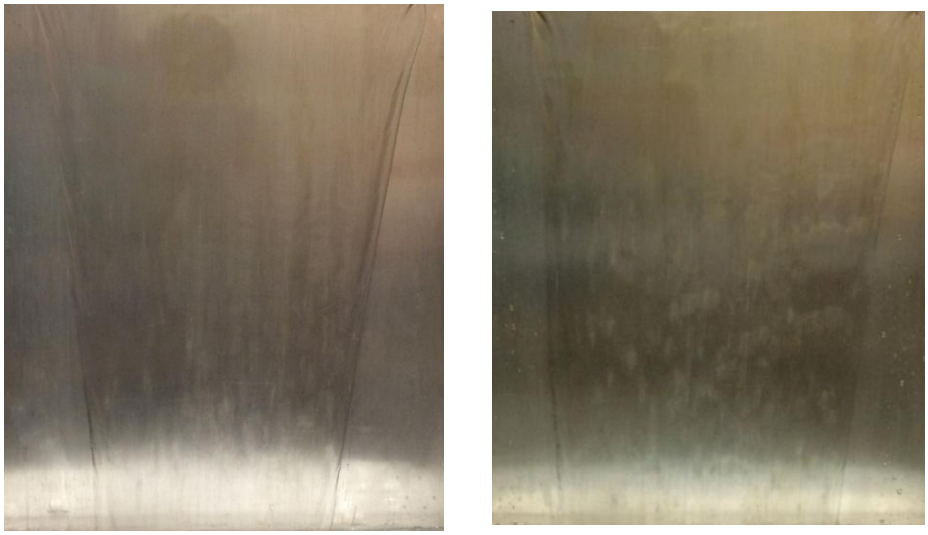

(a) Dry surface (b) Pre-wetted surface

Fig. 5.8 Real pictures of the film flow under different surface conditions (Γ_s = 0.12 kg m^{-1} s^{-1})

The influence of the surface temperature on the coverage ratio was also studied. With the increase of the surface temperature, the coverage ratio increased from 0.1% to 5.1%. It was attributed to the decreased surface tension coefficient of the solution being heated.

Finally, it is inevitable for the film to shrink along the flow direction, which was also reported in the previous research (Yu et al 2012). It was attributed to the gradual increase of the velocity, resulting in the reduction of the flow cross-sectional area. In addition, the big contact angle also enhanced the contraction. They were why the coverage ratio was always less than 1 in the actual experiment.

5.3.3 Minimum wetting rate

From the above section, it was found the mass flow rate should reach some value to guarantee enough coverage ratio. In chapter 3, the minimum wetting rate had been introduced to quantize the research results. According to the literature, there are two types of minimum wetting rate. One is to wet an initially dry surface, and the other is for a complete film where the flow rate is reduced to the point of film breakdown (Hartley and Murgatroyd 1964). The difference is in the latter case, the surface has been wetted first and the contact angle might be reduced significantly.

In the present work, the latter minimum wetting rate was investigated. Therefore, during the experiment, the flow rate was reduced gradually to obtain the minimum wetting rate to prevent the film breakdown. As shown in Fig. 5.9, when the liquid flow rate decreased to some point, the thinning of the film would result in some dry patch, which spread, caused the film breakdown, and decreased the efficiency of the dehumidification.

Fig. 5.9 Real picture of the breakout of the film flow

The minimum wetting rates under different solution inlet temperatures and concentrations were investigated. The temperature differences between the solution and the water behind the plate were kept within 0.5 K to eliminate the influence of the heat transfer between the solution and water. Each group of data was recorded ten minutes after adjusting the flow rate to ensure the stability of the flow.

The influence of solution temperature and concentration were analyzed, as shown in Fig. 5.10. The temperature of the solution varied from 290.7 to 303.3 K and two concentrations were tested in the experiment. It was found that the minimum wetting rate would decrease with the increase of the solution temperature. In the present temperature range, some properties of the solution which were relevant to the flow

almost kept at constant, such as the density and surface tension. However, as shown in Fig. 5.11, the viscosity change was much bigger, that is, nearly 30% within the temperature range. In addition, it was reported that the increase of the solution temperature would result in lower contact angle (Qi et al. 2013). In fact, in the early work (Hartley and Murgatroyd 1954), the equation of the minimum wetting rate for laminar isothermal flow had been developed, as follows,

$$\Gamma_{\min} = 1.69\left(\frac{\mu\rho}{g}\right)^{1/5}[\sigma(1-\cos\theta_w)]^{3/5} \tag{5.2}$$

where μ is viscosity, ρ is density, σ is surface tension coefficient, and θ_w is the contact angle. The equation confirmed that the decrease of the viscosity and contact angle of the solution would reduce the value of the minimum flow rate, which verified the correctness of the experiment.

It was also observed that the minimum flow rate was much bigger with the concentration of 37.5% than 28.9%. The reason could also be explained by analyzing the change of the relevant physical properties of LiCl solution. When the concentration increased, all of the viscosity, density, surface tension coefficient, and contact angle were increased, resulting in the more difficult of wettability of solution on the stainless steel.

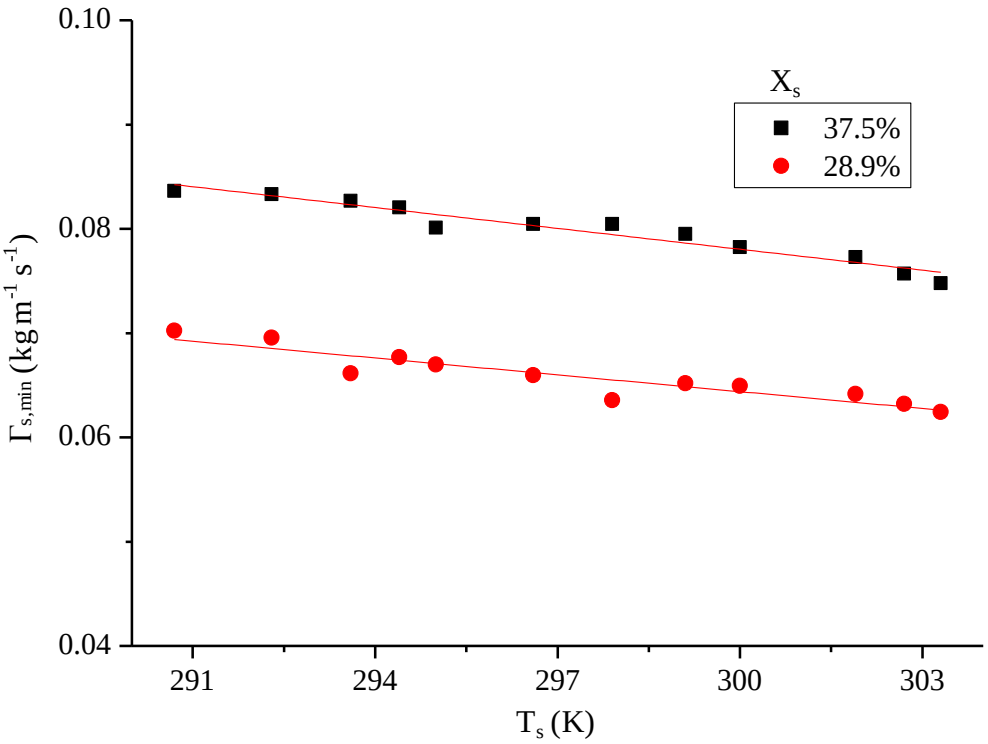

Fig. 5.10 Minimum wetting rate of LiCl solution

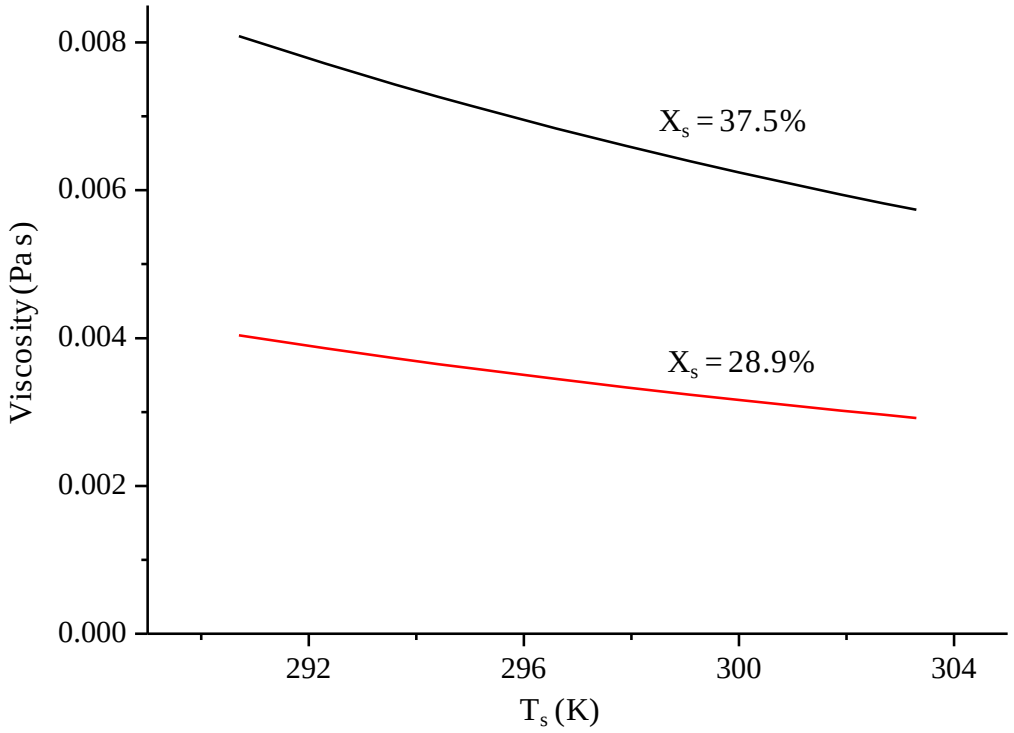

Fig. 5.11 Viscosity of LiCl solution

Then the minimum flow rates were calculated by employing the Hartley's empirical formula. The properties of viscosity, density, and surface tension coefficient were obtained by referring to the literature (Conde 2004), and the contact angle by the literature (Qi et al. 2013). The comparison between the results of the present experiment and Hartley's empirical formula was demonstrated in Fig. 5.12. It was found that the results of Hartley's empirical formula were about four times of those of the experiment. The difference was ascribed to the significant reduction of the contact angle by pre-wetting in the present experiment. Hartley (Hartley and Murgatroyd 1964) had pointed out that the contact angle had a powerful influence on the minimum wetting rate: a change in contact angle from 45^{o} to 20^{o} can reduce the minimum wetting rate by a factor of about ten. Thus, it was suggested pre-wetting the dehumidifier with a relatively higher solution flow rate and then decreasing it to be close to the minimum wetting rate to ensure the sufficient contact surface and lowest energy consumption of the pump. In addition, for predicting the minimum wetting rate with Hartley's empirical formula, it is critical to determine an accurate contact angle.

In chapter 3, the minimum wetting rate was also studied by CFD software Fluent. The simulation was carried out for LiCl solution with 300 K and 30 % mass concentration flowing on the plate of stainless steel. It was predicted that the minimum wetting rate was about 0.071 kg m^{-1} s^{-1} for the case. From Fig. 5.10, through linear interpolation, it could be speculated that the minimum wetting rate for LiCl solution of 300 K and

30 % mass concentration was about 0.068 kg m^{-1} s^{-1} for the experiment. The results demonstrated that the simulation model was reliable for predicting the minimum wetting rate to some extent. In addition, it indicated that the contact angle was decreased by about 25^{o} by pre-wetting the surface in the present work.

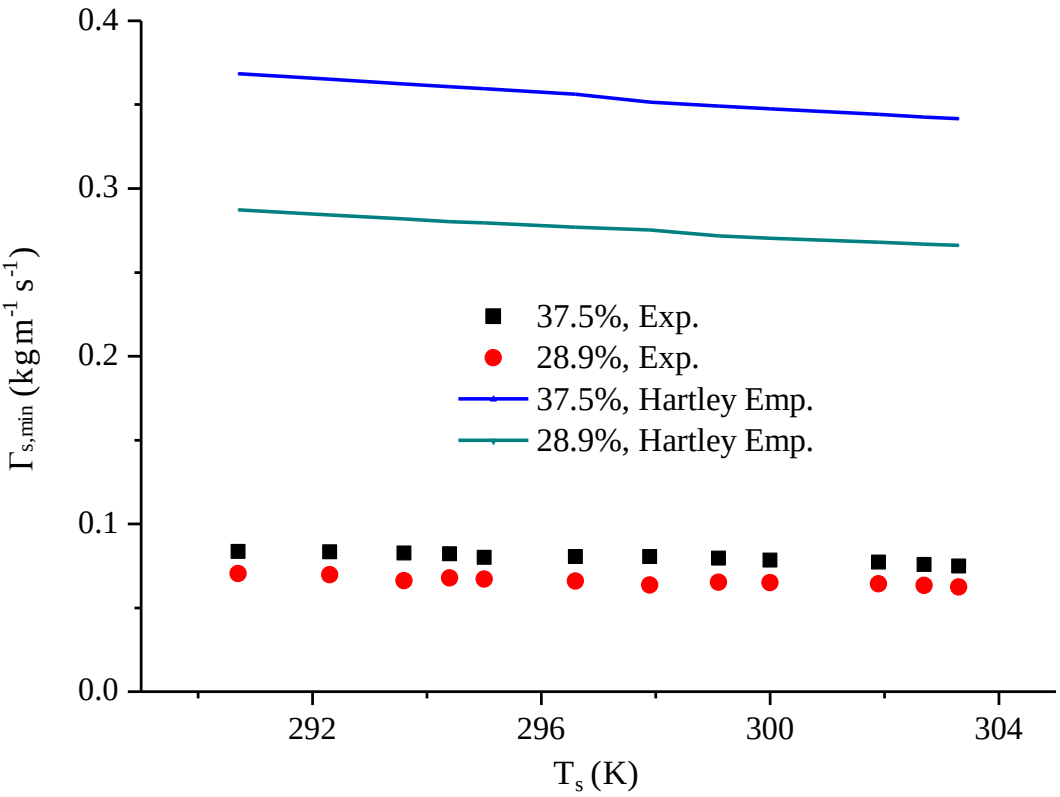

Fig. 5.12 Comparison between the results of the present experiment and Hartley's empirical formula

5.3.4 Film thickness

Film thickness is of great importance to the heat transfer performance of the falling film flow. Thus, it is expected to measure the film thickness accurately (Coney 1973).

In the section, the capacitance probe was installed to obtain the data without disturbing the flow. With the data, the time-average film thicknesses were calculated, and the profiles of the fast-moving waves were recorded. Similar to the above investigation, during the following experiment, the temperature differences between the solution and the water behind the plate were also kept within 0.5 K to eliminate the influence of the heat transfer between the solution and water.

5.3.4.1 Mean film thickness

In 1916, Nusselt proposed an empirical formula to calculate the mean film thickness. It assumed the film flow to be laminar, and the shear stress between the liquid and gas phase was also ignored. However, a large number of studies demonstrate that even with very low Re, the waves still exist in the falling film (Kalliadasis et al. 2012). Moreover, the counter-current gas flow also has impact on the film thickness. Here, Nusselt and other relations for mean film thickness were listed out in Table 5.1. It was found most relations were correlated for the film flow in the tubes. The reason is that the flow inside a tube can eliminate the side-wall effects. In addition, almost all the fluid was water in the previous experimental studies. Therefore, for the dehumidification process, it deserves to acquire the mean film thickness of the desiccant solution flowing on the plate by experiment.

In the present work, the capacitance measurement device was employed to gain the

instantaneous film thickness at the upper and lower part of the film. The mean film thickness is the time and location averaged one, defined as follows,

$$\bar{\delta} = \frac{1}{2n}\left(\sum_{i=0}^{n}\delta_{u} + \sum_{i=0}^{n}\delta_{l}\right) \tag{5.3}$$

where n is the overall recorded numbers during a certain time, and u and l represent the upper and lower part of the film. The film thickness was recorded once in a second.

Table 5.1 Relations for mean film thickness based on experiment for tubes ($Re < 1000-2000$) (Yu et al. 2012)

Researcher	Relation
Nusselt	$\bar{\delta} = 0.909\left(\frac{\upsilon^2}{g}\right)^{1/3} Re^{1/3}$
Brauer	$\bar{\delta} = 0.208\left(\frac{\upsilon^2}{g}\right)^{1/3} Re^{8/15}$
Takahama	$\bar{\delta} = 0.228\left(\frac{\upsilon^2}{g}\right)^{1/3} Re^{0.526}$

In the beginning, the film thickness without counter current gas flow was investigated. The results are shown in Fig. 5.13. Each experimental value plotted in Fig. 5.13 was the average one calculated from three tests.

Firstly, the experimental results had the same trend with those of the Nusselt relation, that was, the increase of the Reynolds number led to a rise of the film thickness. Meanwhile, the relationship of the three different operating conditions also showed

good agreement with the results of the Nusselt relation. Both of the temperature and concentration of the desiccant solution had impact on the film thickness. The increase of the solution concentration would lead to an increase of the film thickness while the increase of the solution temperature had an opposite effect.

Then, it was found that the mean film thickness in the present experiment was about 1.2 times of the results of the Nusselt relation. In the Fig. 13 of the literature (Zhang et al. 2009), the similar experimental results had been reported. In the literature, it was explained by the contraction due to the non-uniform temperature distribution of the film surface. Even though the contraction of the film was also observed in the present experiment (as shown in Fig. 5.8), it was not resulted from the Marangoni flow as the plate was kept isothermal with the solution. For the present experiment, the properties of the desiccant solution might be the main factor to generate the film thickness increase. Compared with the water, the desiccant solution has much higher viscosity, which would decrease the gravity-driven velocity of the film and hence increase the film thickness. Besides, the surface tension coefficient of the desiccant solution was also bigger than that of water, which also enhanced the contraction of the film and made the film thicker. Therefore, the Nusselt relation underestimated the film thickness of the desiccant flow on the flat plate, so did the Brauer and Takahama relation. In fact, even the three relations show large discrepancies in the low Reynolds number region, especially when the Reynolds number is less than 100 (Yu et al. 2012).

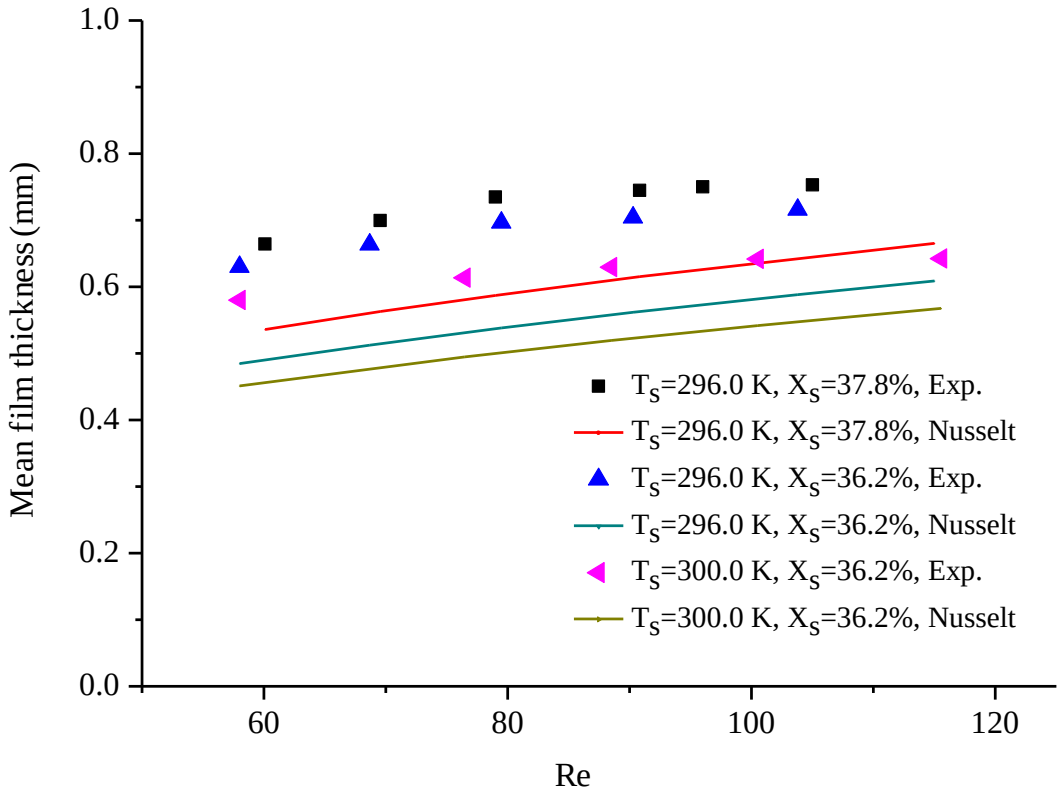

Fig. 5.13 Mean film thickness under different Reynolds number

In the following experiment, the air was introduced to study its influence on the mean film thickness of the upper and lower part, respectively. The mean film thicknesses of the two locations were the time average ones defined as follows,

$$\overline{\delta}_{\mathrm{u}} = \frac{1}{n}\sum_{i=0}^{n}\delta_{\mathrm{u}} \tag{5.4}$$

$$\overline{\delta}_{\mathrm{l}} = \frac{1}{n}\sum_{i=0}^{n}\delta_{\mathrm{l}} \tag{5.5}$$

In Fig. 5.14, the mean film thicknesses are plotted as a function of air flow rate under

three solution flow rates. The solution temperature and concentration were kept around 300 K and 36.2% during the test. It was obvious that the film thickness increased non-linearly with the increase of gas flow rate under the same solution mass flow rate. The similar result was also discovered in the previous study (Steinbrenner et al. 2005; Stockfleth and Brunner 2001). The countercurrent gas flow affected the flow shape of the liquid film. The reason was the gas flow imposed a shear force on the liquid film. According to the mass and momentum balances, the mean film thickness would decrease with the liquid superficial velocity for the present experiment. Due to the shear force exerted by the gas flow, the liquid superficial velocity would reduce. And with the increase of the gas velocity, the shear force would increase and the liquid superficial velocity decrease, resulting in the rise of the film thickness. In Chapter 3, the simulation result showed that the counter-current air flow would reduce the liquid velocity at the interface, especially with a high air velocity. Therefore, the experimental result verified the correctness of the simulation model. In addition, by comparing the mean film thicknesses with and without counter gas flow, it was important to point out that the shear force did have great impact on the film thickness and it needed to be taken into consideration.

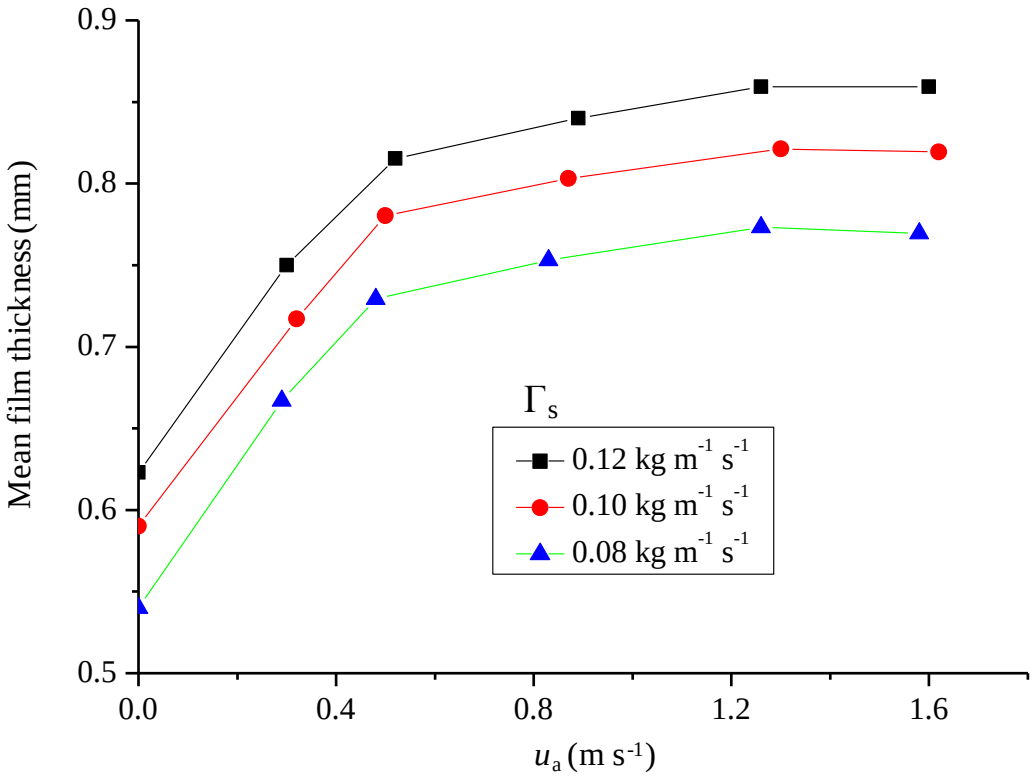

Fig. 5.14 Mean film thickness under different air velocity

In Fig. 5.15, the mean film thicknesses of the upper and lower part are illustrated with different liquid and air flow condition. Firstly, the mean film thickness of the upper part was smaller than that of the lower part. By calculation, the mean film thickness was 10.7%-16.3% thicker at the lower part than at the upper part. The contraction of the film was the main reason of the difference. From Fig. 5.8, it was estimated that the film shrunk about 10 % from the upper location to the lower location. In addition, along the flow direction, the fluctuations were more intense with the development of the film flow, enhancing the increase of the film thickness at the lower part. It could be observed from Fig. 5.5 and also agreed well with the simulation result in chapter 3.

The distinctions under different solution flow rate were presented in Fig. 5.16. When the solution flow rate was lower, the slight increase of the flow rate would result in substantial distinction. When the solution flow rate reached above 0.11 kg m^{-1} s^{-1}, the film thickness distinction approached a maximum value. It demonstrated that the film thickness was more sensitive with a thinner film.

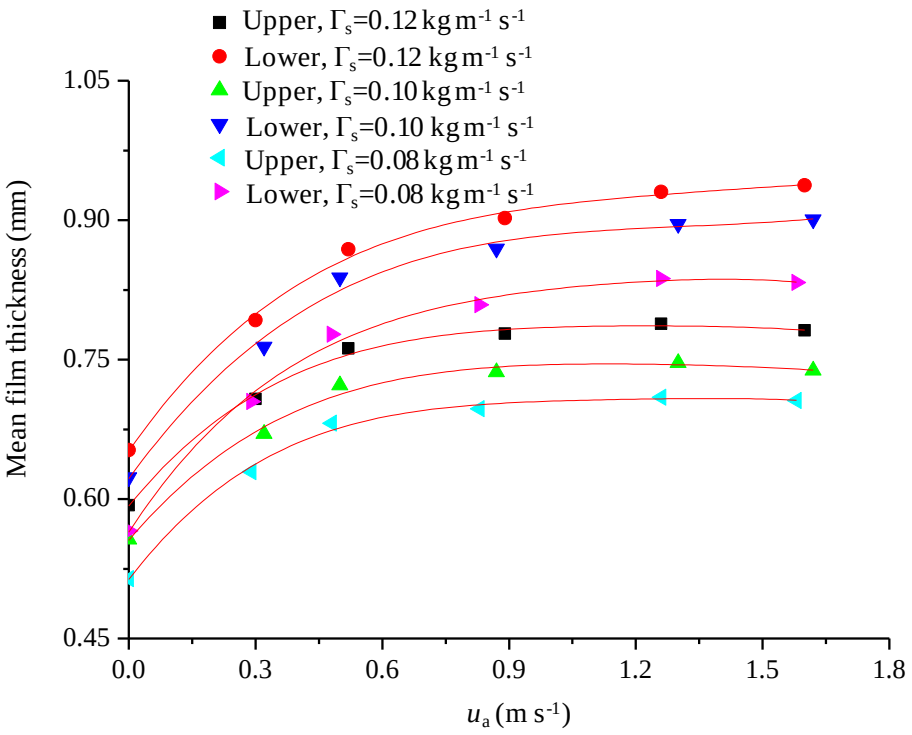

Fig. 5.15 Mean film thickness of two locations under different air velocity

Secondly, from Fig. 5.15, it was found that the air velocity had more significant influence on the mean film thickness of the lower part than that of the upper part. The reason was the slight increase of air velocity enhanced the disturbance of the film in the lower part while the film of the upper part was still almost flat in the present work.

It could be observed from the image of waves occurring on the falling film in section 5.3.1 and also agreed well with the simulation result in chapter 3.

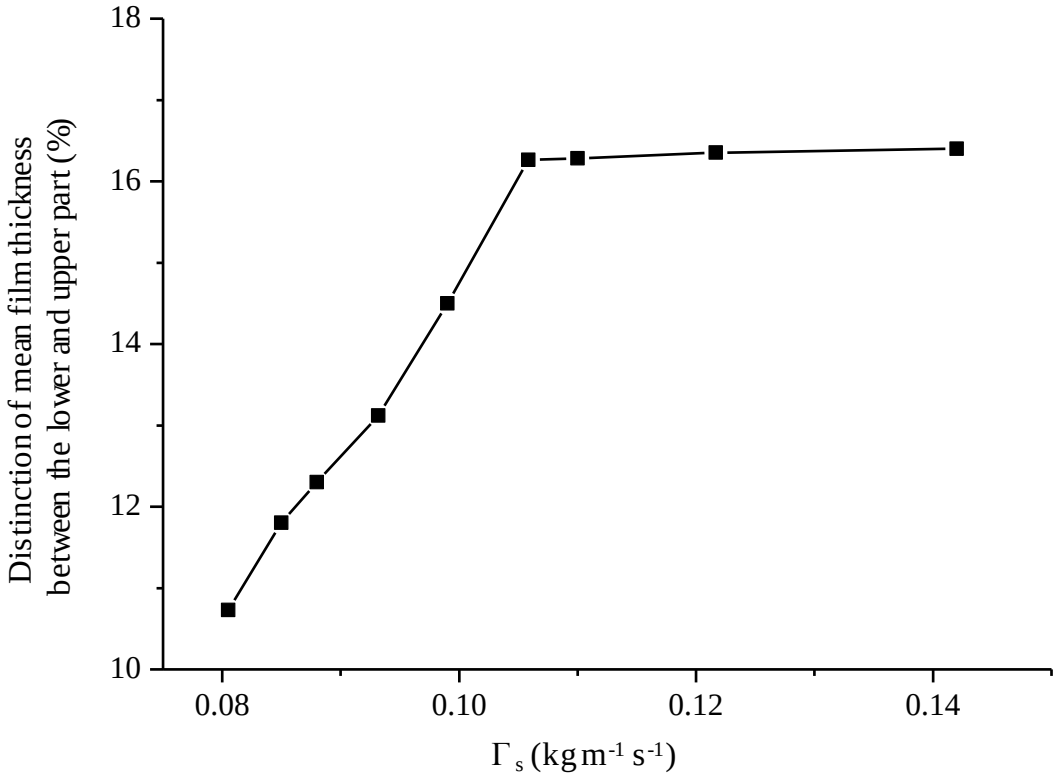

Fig. 5.16 Distinction of mean film thickness between the lower and upper part (u_a=0)

5.3.4.2 Spatial and temporal film thickness

The temporal film thicknesses within 404 seconds at the upper and lower parts of the film without counter-current gas flow are illustrated in Fig. 5.17. The film thickness at a fixed point varied with the time and appeared as sinusoidal waveform, even though the volatility was seemed disorder. It was obvious the fluctuation of the lower part was

more intense, which reflected in the following two aspects. One was that the amplitude of the lower part was about 1.3 times of that of the upper part. Another was that the frequency of the wave was about 21 times of that of the upper part.

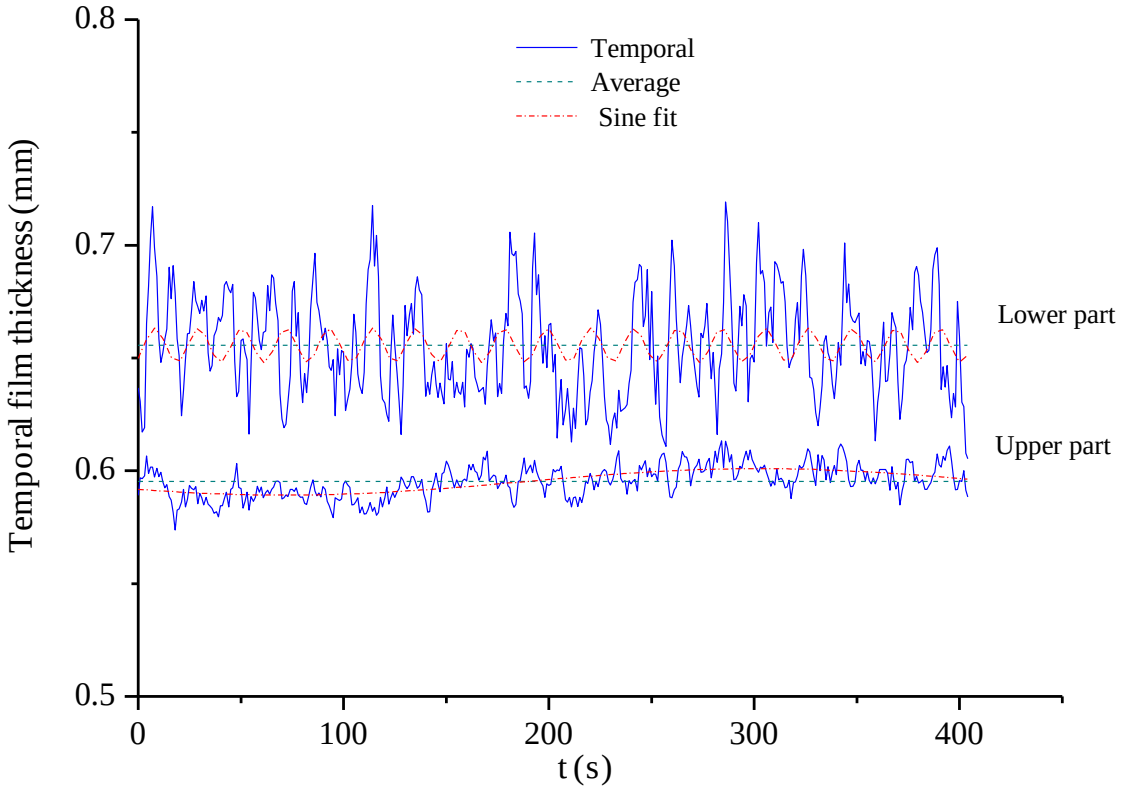

Γ_s (kg m^{-1} s^{-1})	X_s (%)	T_s (K)	u_a(m s^{-1})
0.012	36.2	300	0

Fig. 5.17 Variations of film thickness

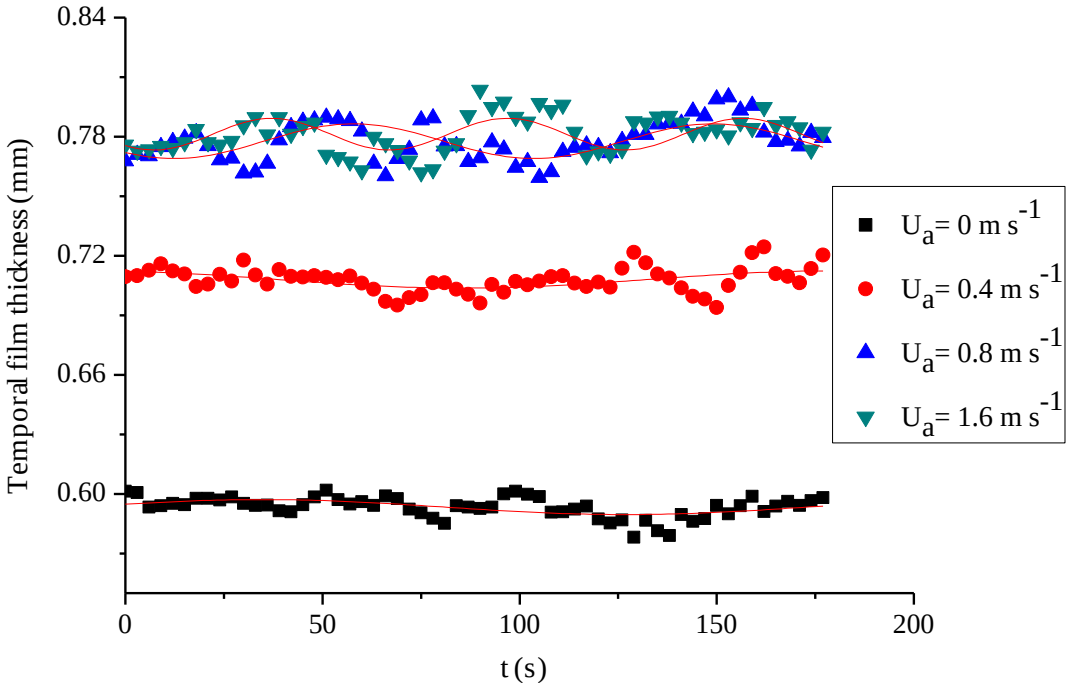

(a) Temporal film thickness of upper part

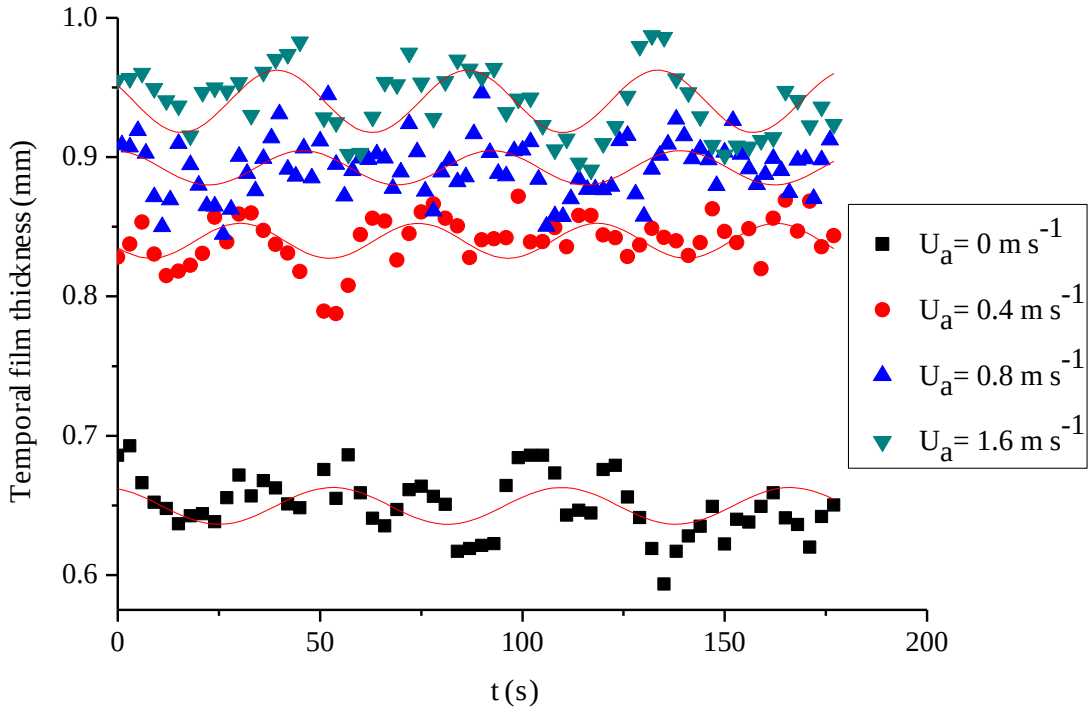

(b) Temporal film thickness of lower part

Γ_s (kg m^{-1} s^{-1})	X_s (%)	T_s (K)
0.012	36.2	300

Fig. 5.18 Temporal film thickness of two different locations

Then the influence of counter-current gas flow on the temporal film thickness was introduced. For the upper part, the increase of the gas velocity would increase the wave height, and enhance the wave both in amplitude and frequency. The similar phenomenon was also found for the film at the lower part. By comparing the curves of Fig. 5.18 (a) and (b), it was easy to find the film wave at the lower point was much more intensive than at the upper point even with different air velocity. There were two reasons for the enhancement. One was the development of the film flow along the flow direction mentioned above. Except for that, it was also expected that the air would have bigger impact on the film at the lower part than the upper part. Due to the counter-current flow, the air velocity decreased gradually in the flow direction, making larger difference at the lower part than at the upper part.

5.3.4.3 Statistical analysis of the lower part

From the above study of the flow morphology, the wave shape of the lower part was regarded to be consisted of large solitary wave, the capillary wave and film substrate. In year 1975, Chu and Dukler (Chu and Dukler 1975) promoted to define the film substract thickness with the statistical analysis, the Probability Density Function (PDF). It was defined by the following equations,

$$P(\delta)=\text{Prob}\{\delta(t)\le\delta\} \tag{5.6}$$

$$f(\delta)=dP(\delta)/d\delta \tag{5.7}$$

The probability density of film thickness with different solution flow rate and zero air flow rate was presented in Fig. 5.19. The curves possessed the following characteristics. Each curve had a peak value, and the maximum value decreased with the increase of the solution flow rate. The corresponding value of x coordinate could be considered as the film substract thickness. The width of the bottom of the curves represented the amplitude of the waves, which meant with the increase of solution flow rate, the wave became intensive.

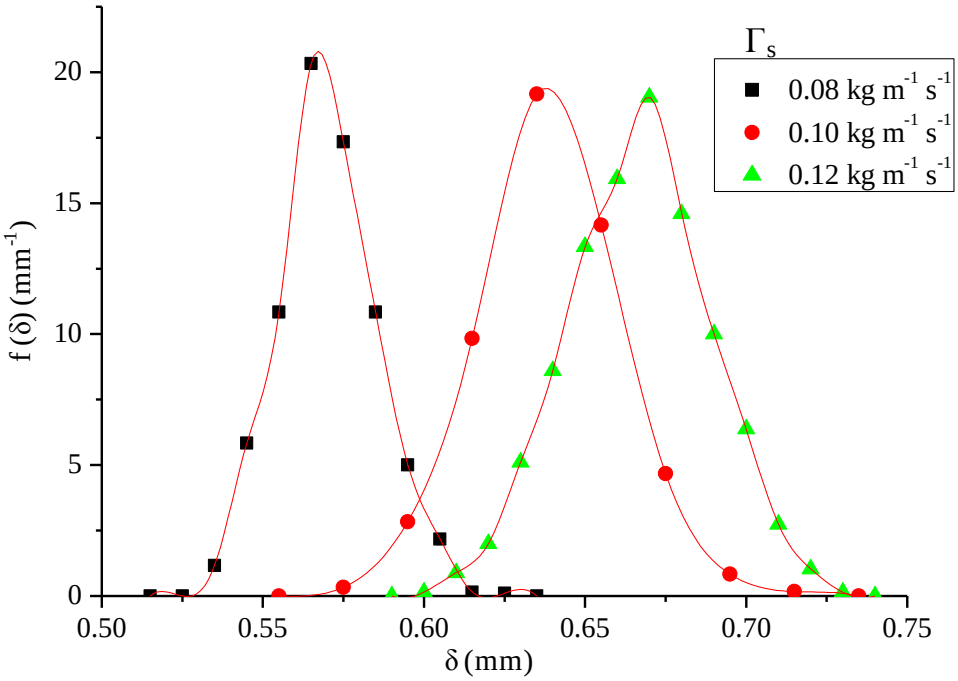

Fig. 5.19 Probability density of film thickness with different solution flow rate, u_a=0

In Fig. 5.20, the probability density of film thickness with different air velocity and one solution flow rate was plotted. The results demonstrated that the increase of air velocity would make the film substract thickness increase and the wave amplitude

increase as well. By comparing the results of statistical analysis to the above study, it showed that the probability density of the film thickness could be an effective tool to describe the flow condition.

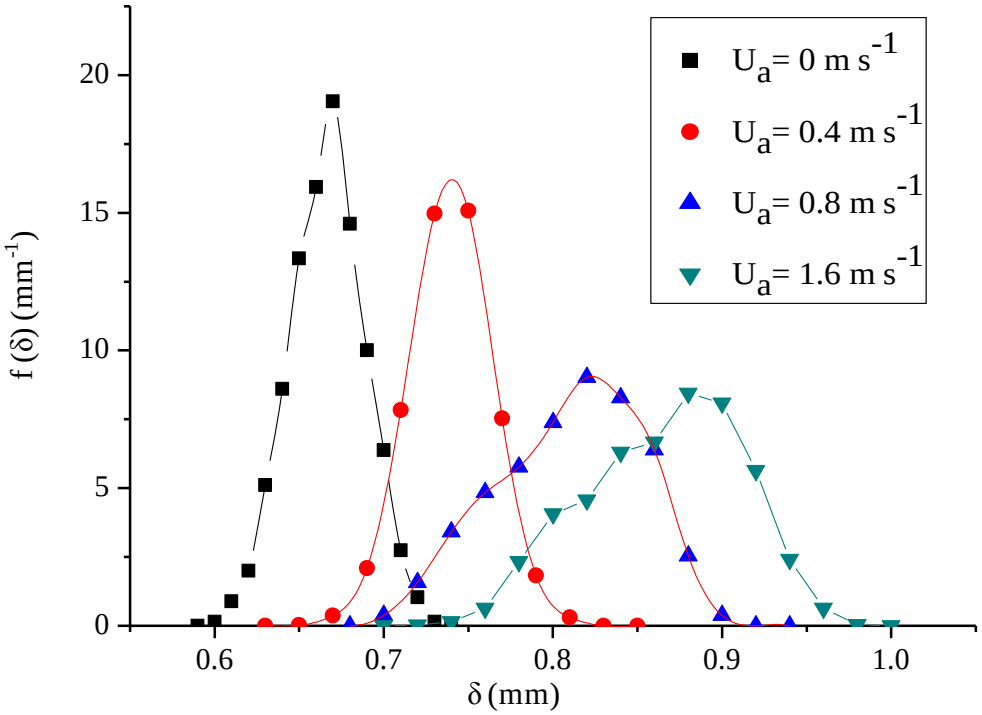

Fig. 5.20 Probability density of film thickness with different air velocity, Γ_s=0.12 kg m^{-1} s^{-1}

Due to the limitation of the measurement devices, it was impossible to measure the wave velocity of the film directly. However, Karapantsios defined the surface wave velocity, $d\delta / dt$, to reflect the wave intensity. It was defined on the basis of the film thickness recorded with the varying time, presented as follows,

$$d\delta / dt \cong \frac{\Delta\delta}{\Delta t} = \frac{1}{\Delta t}[\delta(t+\frac{\Delta t}{2}) - \delta(t-\frac{\Delta t}{2})] \qquad (5.8)$$

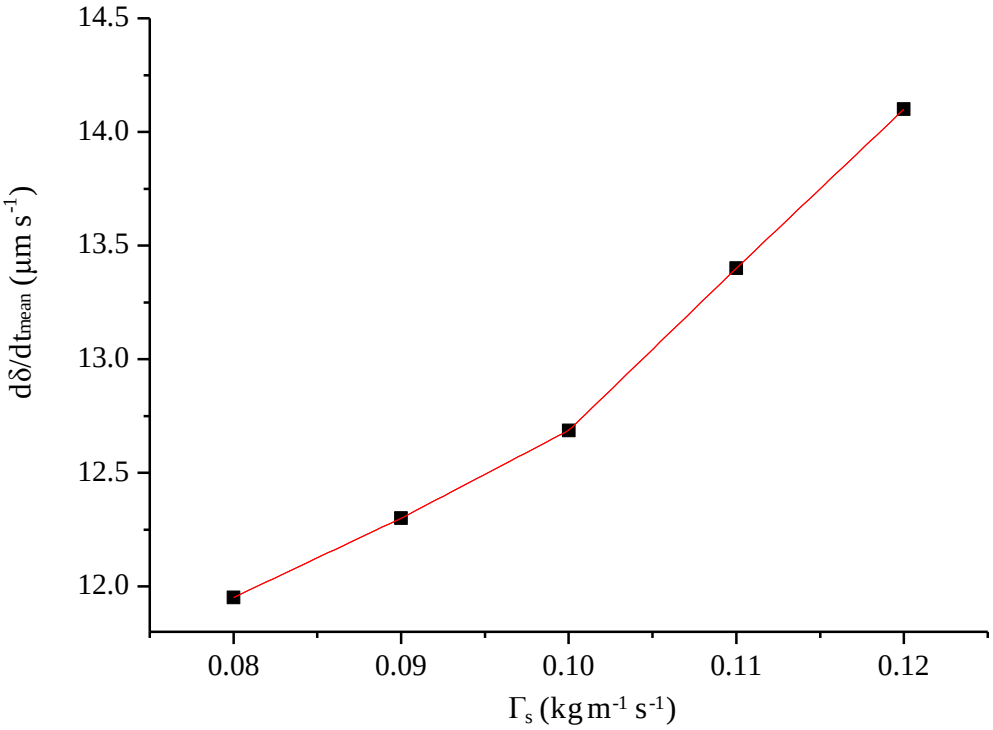

Fig. 5.21 Surface wave velocity with different solution flow rate

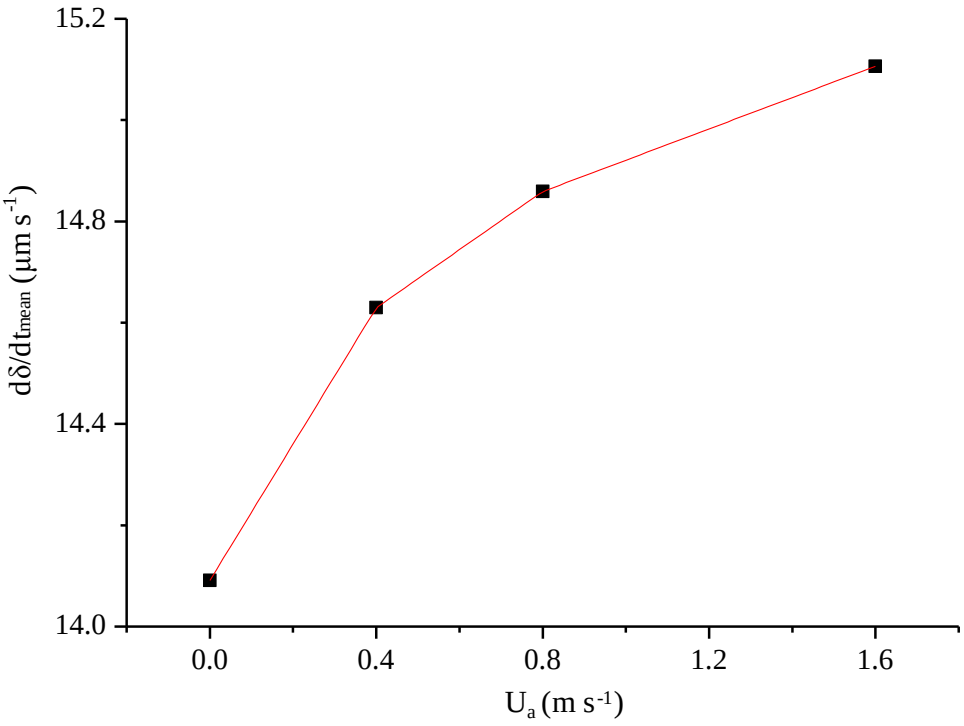

Fig. 5.22 Surface wave velocity with different air velocity

In Fig. 5.21 and 5.22, the influences of the solution flow rate and air velocity on the mean surface wave velocity $d\delta/dt$ of the lower part of the film are illustrated. It showed that both of increase of the solution flow rate and air velocity enhanced the wave intensity.

5.4 Summary

This chapter reported the experimental study of the solution falling film flow on the vertical plate surface. In summary, the following conclusions are obtained,

1) The flow morphology was observed for the solution flow. A typical wave evolution with different wavefront patterns can be seen clearly. It experienced three stages along the flow direction: smooth surface flow, two-dimensional deformation and three-dimensional deformation. In the process, the waves separated, coalesced and interacted with each other, resulting in the complicated surface patterns. In addition, the solitary wave appeared in the present work. The structure played an important role in determining the heat and mass transfer process as the hump carried most of the liquid substance.

2) The coverage ratio was obtained under different conditions of the test surface. It was found that it needed much higher flow rate to achieve high coverage ratio on

the dry plate than on the wet plate. The reason was the pre-wet of the surface could reduce the contact angle so as to make the surface more hydrophilic. Meanwhile, it was found with the increase of the surface temperature, the coverage ratio increased from 0.1% to 5.1%. It was attributed to the decreased surface tension coefficient of the solution being heated.

3) The minimum wetting rate was investigated and compared with the literature and simulation results. The minimum wetting rate would decrease with the increase of the solution temperature and increase with the increase of solution concentration. Both of them had great relationship with the solution properties. Then, it was found the calculation results of Hartley's empirical formula were about four times of those of the experiment, which was attributed to the significant reduction of the contact angle by pre-wetting in the present experiment. In addition, the minimum wetting rate for LiCl solution of 300 K and 30 % mass concentration was about 0.068 kg m^{-1} s^{-1} for the experiment, which showed a good agreement with the simulation value of 0.071 kg m^{-1} s^{-1} in Chapter 3.

4) The mean film thickness was obtained. The experimental results without gas flow had the same trend with those of the Nusselt relation. Then, the influence of air flow rate on the film thicknesses was studied. It was found that the film thickness increased non-linearly with the increase of gas flow rate as a result of the reduction

of liquid superficial velocity due to the shear force exerted by the gas flow. The results agreed well with the simulation results of the superficial film velocity in Chapter 3.

5) The mean film thicknesses of the upper and lower part were illustrated and compared. The results demonstrated that the mean film thickness of the lower part was about 10.7%-16.3% thicker than that of the upper part without air flow. The temporal film thicknesses showed the fluctuation of the lower part was more intense, both in amplitude and frequency of wave. Then the influence of counter-current gas flow on the temporal film thickness was introduced. The increase of the gas velocity would enhance the wave for both of the upper and lower part. It was expected that the air would have bigger impact on the film at the lower part than the upper part. Due to the counter-current flow, the air velocity decreased gradually in the flow direction, making larger difference at the lower part than at the upper part.

6) For the lower part of the film, the probability density of film thickness for different solution flow rate with zero air flow rate, and for different air velocity with one solution flow rate were given out. The film thickness corresponding to the peak value of the curve was the film substract and the width of the bottom of the curves represented the amplitude of the waves. By comparing the results of statistical

analysis to the above study, it showed that the probability density of the film thickness could be an effective tool to describe the flow condition. Finally, the mean surface wave velocity was applied to analyze the influences of the solution flow rate and air velocity. It showed that both of increase of the solution flow rate and air velocity enhanced the surface wave velocity.

CHAPTER 6

EXPERIMENTAL STUDY OF DEHUMIDIFICATION PERFORMANCE: INTENSIVE ANALYSIS OF INFLUENCING FACTORS

6.1 Introduction

The dehumidification process determines the performance of the liquid desiccant system. The experimental study of the dehumidifier had been carried out since the middle 20th century. In the early research, the packed bed dehumidifier was the main objective as a result of its large contact area (Yin et al. 2008). However, as the accumulation of the absorption heat, the solution temperature in this kind of dehumidifier will increase gradually, worsening the effectiveness. It is the main reason for the popularization of the internally cooled dehumidifier, which can remove the latent heat during the dehumidification process. Nevertheless, as far as I am concerned, the work conducted about the details of performance of the internally cooled dehumidifier is still limited as a result of its complexity. As a matter of fact, in most of the internally cooled dehumidifier, the cooling medium are often provided at one side of the tube or plate with the solution flowing at another side. Therefore, one of the

simplest internally cooled dehumidifier is the single channel one, mainly constructed by an air channel, a solid surface and a cooling water channel. The solid surface acts as the contact area for heat transfer between the solution and cooling water, and retains the solution to absorb water vapor and exchange heat with the moist air as well.

In the present study, a single channel test rig was established for the convenient investigation of the fundamental flow, heat and mass transfer process of the dehumidifier. The novel points existed in the following several aspects,

1) The test rig was designed to be easy to observe the heat and mass transfer area, which made the calculation of mass transfer coefficient more accurate.

2) The experimental operating condition was set on the basis of the meteorological condition in Hong Kong.

3) Compared with the previous studies, the influences of various factors were analyzed more intensively in the present work.

6.2 Description of experimental bench

To investigate the hydrodynamics and mass absorption of falling film on the vertical

surface in the dehumidifier, a single channel experimental setup was fabricated, as shown in Fig. 6.1. The test rig was mainly composed of three ways for three different kinds of media, which were desiccant solution, air and water. The real picture of the test rig is also provided in Fig. 6.2.

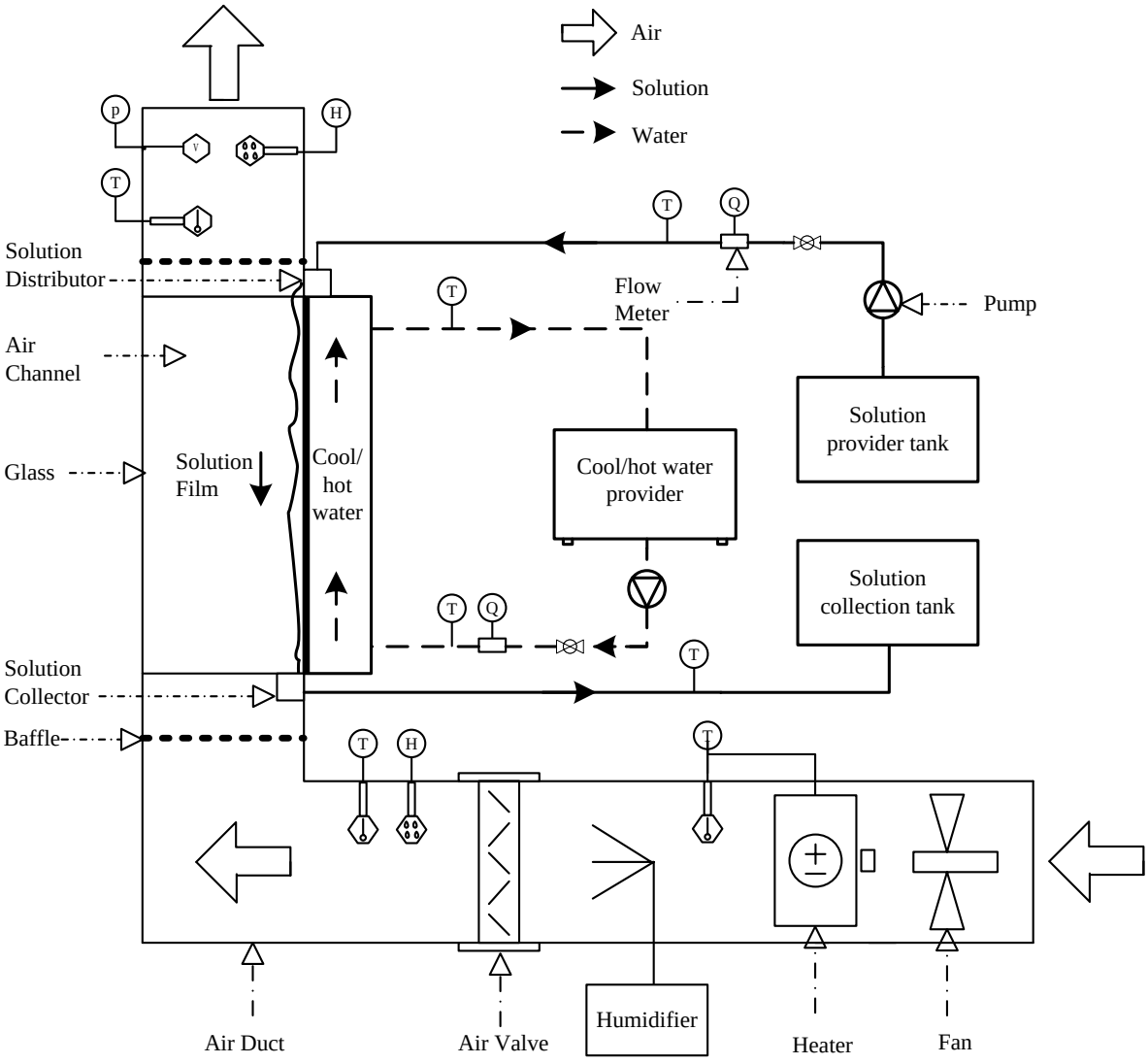

Fig. 6.1 Schematic diagram of the single channel liquid desiccant dehumidifier

Fig. 6.2 Real picture of the test rig

The solution flow loop was designed to enable the delivery of liquid desiccant flow in the test section. It was mainly consisted of a solution provider tank, a solution distributor, a solution collector, a solution collection tank, a pump and some PVC pipes for connection.

The air duct system made the moist air flow in countercurrent way with the desiccant solution, exchanging the moisture and heat with the desiccant. An electrode humidifier and several fin electric heaters were installed to produce the air with certain temperature and humidity.

The water loop offered cold/hot water which flows behind the working surface. It consisted of a cold/hot water producer and some pipes.

6.3 Control and measurement instruments

(a) PID controller

(b) Air valve

(c) DC regulator

(d) Cold/hot water producer

(e) Control board

Fig. 6.3 Control devices

During the experiment, the inlet parameters of the air, solution and water were controlled with certain ranges. The temperature of air and solution could be adjusted to the pre-set values with the PID controllers. The flow rate of air was adjusted by the

air valve with manual operation. The humidity of air was controlled indirectly by the DC regulator, which could provide different DC voltages to decide the water vapor generation amount of the humidifier. The flow rates of the solution and water were regulated by the ball valves installed on the pipelines. The water was supplied by the cold/hot water producer, which was composed of a compressor, evaporator, condenser, throttle and heater. By setting a value on the control panel, the chiller/heater could offer the water to the cavity behind the test surface with a certain temperature. All of the above control devices are presented in Fig. 6.3. To make the operation more convenient and safer, all of the switches were located in the control board.

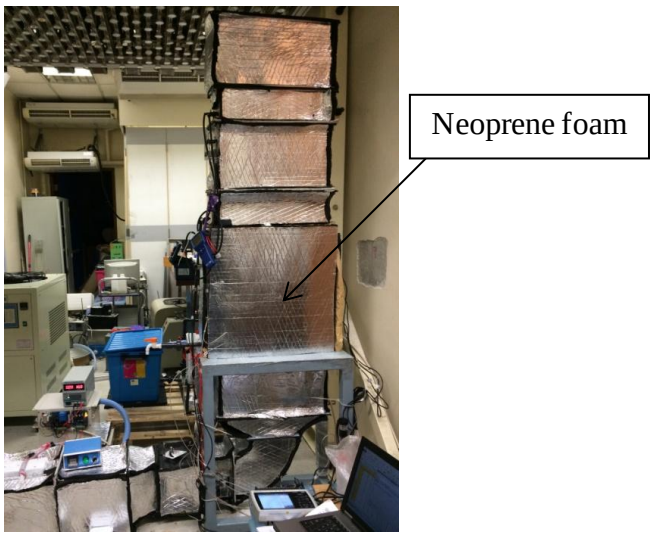

Fig. 6.4 The appearance of the main test part

To reduce the infection of the environment, the whole channel was insulated with neoprene foam, and the main test surface was no exception, as shown in Fig. 6.4.

To evaluate the performance of the dehumidifier, the inlet and outlet parameters of the air, solution and water needed to be measured and recorded, including the inlet and outlet temperatures of all fluids, flow rates of all fluids, air humidity, and solution concentration. The measurement instruments and specifications are shown in Table 6.1 and Fig. 6.5.

Table 6.1 Specification of different measuring devices

Parameter	Device	Accuracy	Operational range
Air dry/wet bulb temperature	Pt RTD sensors	±0.1 K	273-693 K
Air velocity	Standard nozzles plus manometer (DP-CALC 5825)	±1% of reading	-3735～3735 Pa
Solution density	Specific gravity hydrometer (DH-300X)	1 kg m^{-3}	1-99999 kg m^{-3}
Solution flow rate	Turbine flow rate sensor (Gems Sensors 173936-C-RS)	±3% of reading	0.5-7.5 L min^{-1}
Solution temperature	Pt RTD sensors	±0.1 K	273.0-693.0K

Some Pt resistance temperature detectors (RTDs) were used to measure the inlet and outlet temperatures of air, solution and water, with the accuracy of 0.1 K. The flow rates of solution and water were measured by the turbine flow rate sensors, with the accuracy of ±3% of reading. The flow rate or velocity of the air was obtained by the

standard nozzles plus manometer. The principle of the above device is to measure the static pressure and total pressure in the air duct to obtain the velocity pressure, which had a relationship with the air velocity. For non-standard air condition, the formula is,

$$u = 1.291\sqrt{\frac{1000}{P_a} \times \frac{T}{289} \times \frac{100000}{100000 + P_s} \times P_v} \tag{6.1}$$

where u is the velocity, P_v is the velocity pressure, P_a is the atmospheric pressure, and P_s is the duct static pressure.

With the formula, the velocity of the air with different temperature and humidity can be calculated by the velocity pressure. The accuracy of the device was $\pm 1\%$ of reading in the range of 3735 Pa. The humidity of air was calculated with the dry-bulb and wet-bulb temperatures of the air, measured by the Pt RTDs. The maximum error for temperature was 0.1 K and the estimated error for the absolute humidity was about 0.2 g kg^{-1} in the present operation range. All of the data are recorded automatically by the data logger once per second. A specific gravity hydrometer was used to obtain the density of the solution, with the accuracy of 1 kg m^{-3}. Then, the solution concentration could be determined with the density and temperature of the solution. The error for the solution concentration was about 0.15 % by calculation.

(a) Air flow (standard nozzles plus manometer)

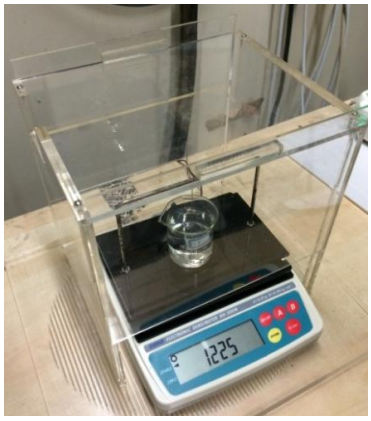

(b) Specific gravity hydrometer

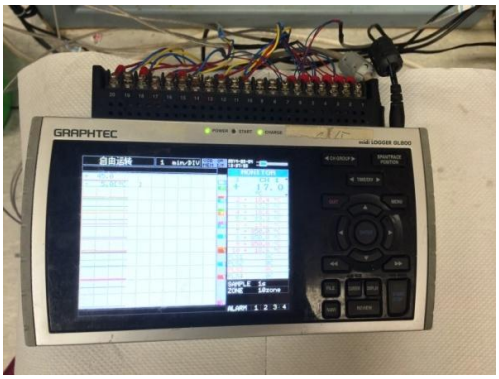

(c) Data logger (GRAPHTEC GL820)

(d) Turbine flow rate sensor

Fig. 6.5 Measurement devices

6.4 Performance indices and error analysis

The performance of the dehumidifier was evaluated from the air absolute humidity change and overall mass transfer coefficient.

The absolute humidity change is defined by,

$$\Delta W = W_{\mathrm{i}} - W_{\mathrm{o}} \tag{6.2}$$

It is the most intuitive, but also one of the most important indicators of the dehumidifier performance.

The overall mass transfer coefficient is presented as (Saman and Alizadeh 2002),

$$\alpha_{\mathrm{D}} = \frac{G_{\mathrm{a}}^{'}}{A}\frac{W_{\mathrm{i}} - W_{\mathrm{o}}}{W_{\mathrm{i}} - W_{\mathrm{e}}} \tag{6.3}$$

here, A is the actual wetted area of falling film recorded in the experiments, and W_{e} is the absolute humidity of the surface air in equilibrium with the solution at its temperature and concentration.

The maximum relative error of individual parameter could be calculated by,

$$e_{i,\max}(\%) = \frac{E_i}{P_{\min}} \tag{6.4}$$

where E_i means the measurement error of individual device. $P_{\min}$ is the minimum value of the measured parameter, where the maximum relative error occurs.

The uncertainties of the experimental results were caused by errors in the measurement. According to the literature (Coleman and Steele 2009), if an

experimental result Y is given by the equation,

$$Y = Y(X_1, X_2, ..., X_j) \tag{6.5}$$

where $X_1, X_2, ...,$ and X_j are the measured variables, the uncertainty can be determined by the following equation,

$$U_Y = [(\frac{\partial Y}{\partial X_1} U_{X_1})^2 + (\frac{\partial Y}{\partial X_2} U_{X_2})^2 + \cdots + (\frac{\partial Y}{\partial X_j} U_{X_j})^2]^{1/2} \tag{6.6}$$

where U_Y is the uncertainty of the result, and U_{X_1}, U_{X_2} …and U_{X_j} are the uncertainties of the independent variables.

The data collected to evaluate the performance index ΔW mentioned in Eq. (6.2) were measured by temperature sensors, whose accuracy is ± 0.1 K. As mentioned in the last sector, the error for the absolute humidity was about 0.20 g kg^{-1} by calculation in the present operation range. Thus, the maximum relative error of absolute humidity was about 1.40%. Finally, the uncertainty calculated for ΔW was 1.98%.

The data collected to evaluate the performance index α_D mentioned in Eq. (6.3) were measured by temperature sensors, manometer, specific gravity hydrometer, and camera, whose accuracy are ± 0.1 K, 1 $kg \cdot m^{-3}$. With the similar method, the uncertainty calculated for α_D is 5.32%.

6.5 Results and discussion

6.5.1 Mass and energy conservation analysis

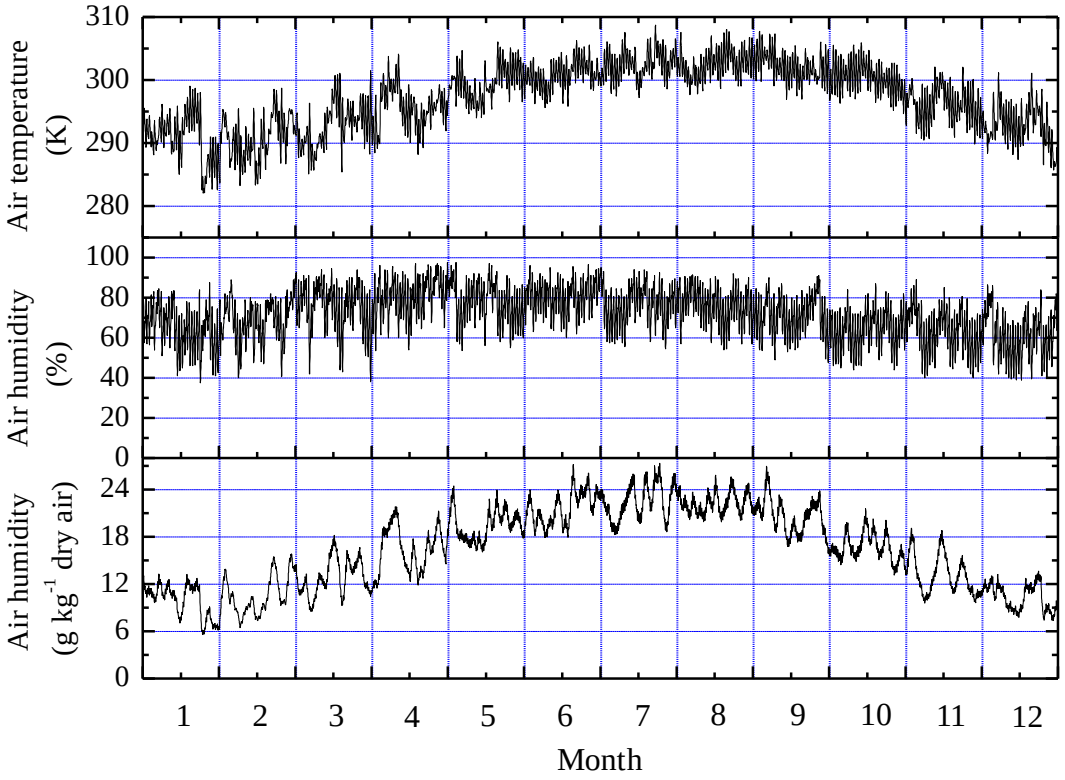

Fig. 6.6 The meteorological condition within one year in Hong Kong

The experiment was carried out with different inlet parameters to explore their influences. The operating conditions of the air were set on the basis of the climate in Hong Kong. As shown in Fig. 6.6, the meteorological condition within one year of Hong Kong is provided by the software TRNSYS, including the air temperature, relative and absolute air humidity. The data illustrates that the weather is hot and humid in Hong Kong. Especially in most of the time from April to September, the air

temperature is more than 297.0 K, the relative humidity is more than 70.0%, and the absolute humidity is more than 18.00 g kg^{-1} dry air. Based on the above data, the specific inlet condition of the air was set for the experiment. In Table 6.2, the detailed ranges of various parameters were listed out.

Table 6.2 Summary of the ranges of various parameters

Parameter	Symbol	Unit	Range
Air temperature	T_a	K	297.0-308.5
Air humidity	W_a	g kg^{-1} dry air	18.0-24.0
Air flow rate	G'_a	kg s^{-1}	0.01-0.09
Solution temperature	T_s	K	290.3-303.3
Solution concentration	X_s	%	33.7-40.7
Solution flow rate	G'_s	kg s^{-1}	0.037-0.047
Cooling water flow rate	G'_w	kg s^{-1}	0.038
Cooling water temperature	T_w	K	291.0-297.5

The mass and energy balances needed to be investigated before analyzing the data. According to the mass and energy conservation, the moisture absorbed by the solution should be equal to that removed from the solution, and the enthalpy change of the air should be equal to the change of the solution and cooling water. They are expressed in Eq. (6.7) and (6.8),

$$G'_{a}(W_{a,o}-W_{a,i})=G'_{s,i}X_{s,i}(\frac{1}{X_{s,i}}-\frac{1}{X_{s,o}}) \tag{6.7}$$

$$G'_{a,i}h_{a,i}-G'_{a,o}h_{a,o}=(G'_{s,i}h_{s,i}-G'_{s,o}h_{s,o})+(G'_{w,i}h_{w,i}-G'_{w,o}h_{w,o}) \tag{6.8}$$

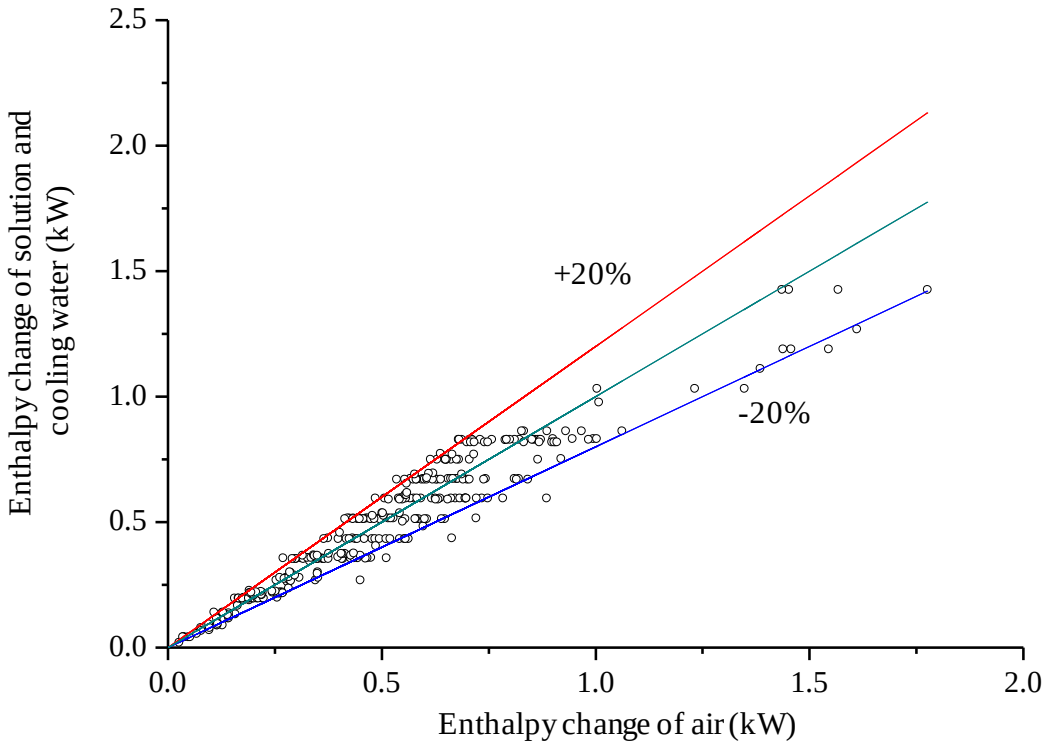

Fig. 6.7 Energy balance of the experiment

As in the present experiment, the change of the solution concentration was too small to be tested accurately, it became hard to judge whether Eq. (6.7) was satisfied or not. Thus, here only the energy conservation was checked and shown in Fig. 6.7. It can be found that most of the deviations between the energy change of the air and that of the solution and cooling water were kept within ±20% for 360 groups of experimental results. Therefore, it was acceptable for employing the test rig for the further study.

6.5.2 Influence of air inlet parameters

6.5.2.1 Air temperature and humidity

As the air temperature and humidity were interacted on each other, it was hard to adjust one parameter without changing another parameter when dealing with the inlet air. Thus, during the experiment, more than 200 groups of experiments with different inlet air temperature and humidity were done to find the discipline.

As shown in Fig. 6.8 (a), it was found that the inlet air humidity had great effect on the change of the absolute humidity. It was reasonable that the humid air possesses high potential for mass transfer. On the other hand, it was a surprise that the increase of the inlet air temperature would reduce the performance so greatly. As far as I am concerned, the air with the same absolute humidity has the same water vapor pressure. That is to say, when contacting with the solution, the driving force is supposed to be the same. Thus, what resulted in the large difference? According to the previous literature, some of them simply pointed out that the reason is the different temperature rises of the solution (Gandhidasan et al. 2002). However, it was discovered that the temperature rise of the inlet and outlet solution in the work was only a little bigger when the inlet air temperature is higher.

By deeper analysis, it was speculated that as the film had a certain thickness, even though the difference of the overall temperature rise was small, the temperature

increases of the solution at the surface could be much bigger with higher inlet air temperature. As the solution acting as absorber were those at the surface of the film, their temperature were of great importance. The reason for introducing the internal cooling for dehumidifier was to reduce the solution temperature. However, it seemed that the key to the problem was to reduce the surface temperature of the solution. Two ways could be adopted. One was to enhance the heat transfer in the film by reinforcing the disturbance of the liquid film. Another one was to enhance the heat transfer between the film surface and the cooling media by reducing the film thickness.

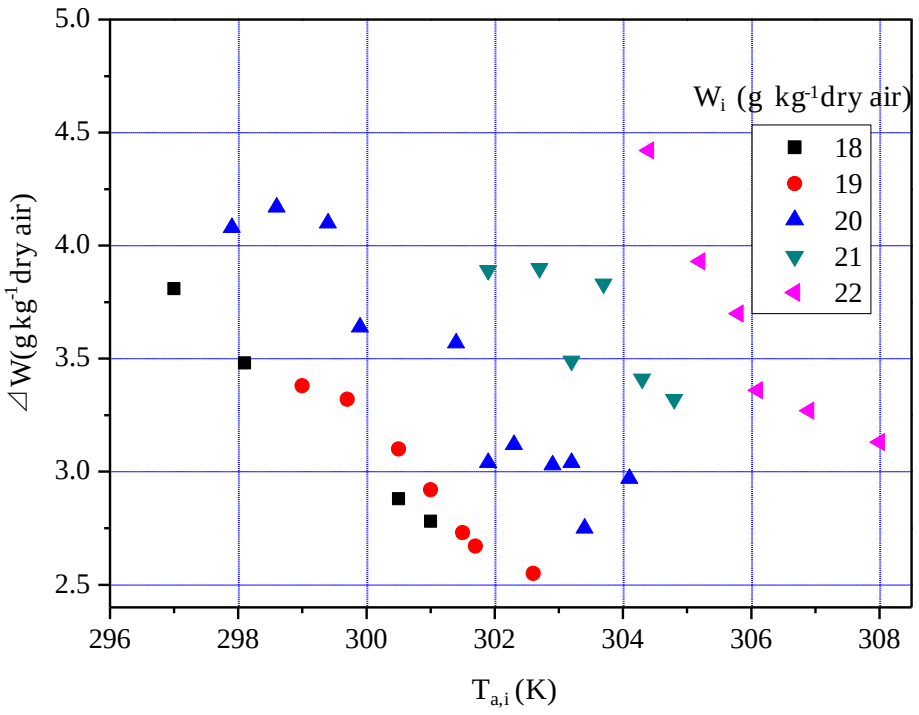

(a) Absolute humidity change

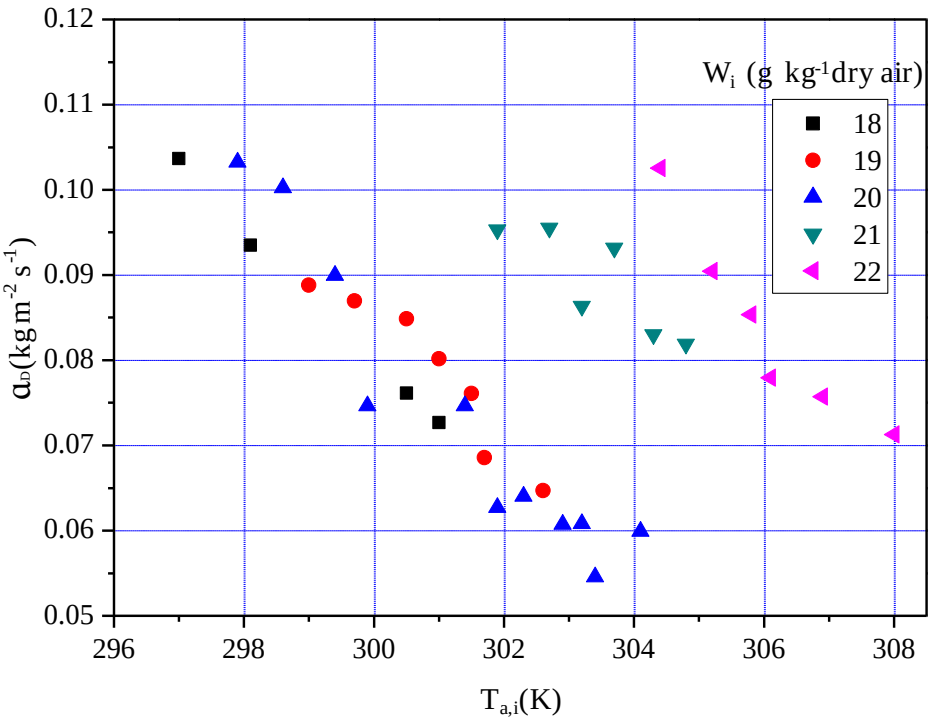

(b) Mass transfer coefficient

G'_s (kg s^{-1})	X_s	T_s(K)	G'_a (kg s^{-1})	G'_w (kg s^{-1})	T_w (K)
0.045	0.38	293.2	0.06	0.038	293.0

Fig. 6.8 Effect of air temperature and humidity

As shown in Fig. 6.8 (b), the results of the mass transfer coefficient are illustrated. In terms of the air temperature, the results showed similar trend with the absolute humidity change. However, it was observed that the function of the humidity was different when the inlet air humidity was relatively small. It could be explained by analyzing the Eq. (6.3). With the increase of the inlet air humidity, the absolute humidity change (one of the numerators of Eq. (6.3)) would increase accordingly. On the other hand, the denominator was also increased. Thus, the final results of the mass transfer coefficient were decided by the extent of the changes of the two factors.

In present work, it showed smaller effect on the mass transfer coefficient when the inlet air humidity was relatively lower.

Here, the results were also compared with the literature (Zhang et al. 2013). It is found that the mass transfer coefficient was higher than the result reported. In our opinion, the main reason was the inlet air humidity adopted in the present work was much higher than those of the literatures. It demonstrates that the liquid dehumidifier performs very well in hot and humid areas such as Hong Kong.

6.5.2.2 Air flow rate

The experiments were carried out for different air mass flow rates. The influence of the air flow rate on the absolute water vapor absorption was illustrated in Fig 6.9 (a). Similar to the simulation results in chapter 4, with the increase of the air flow rate, the absolute water vapor absorption would reduce. The reason was that when the channel was short, if the air flowed in relatively high velocity, there was not enough contact time for the air and solution.

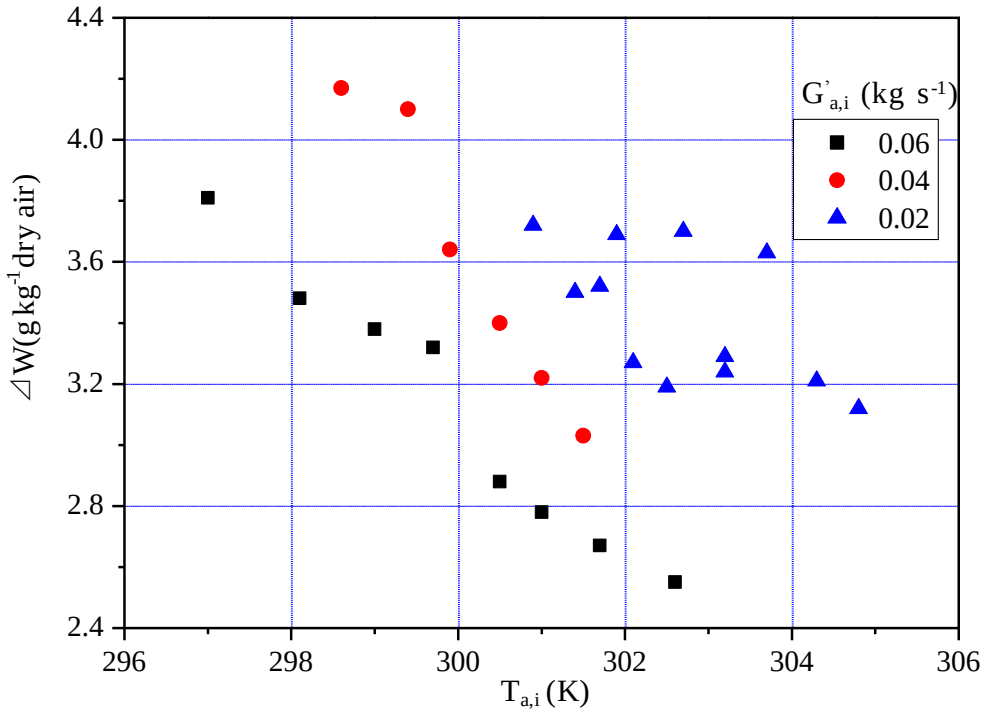

(a) Absolute humidity change

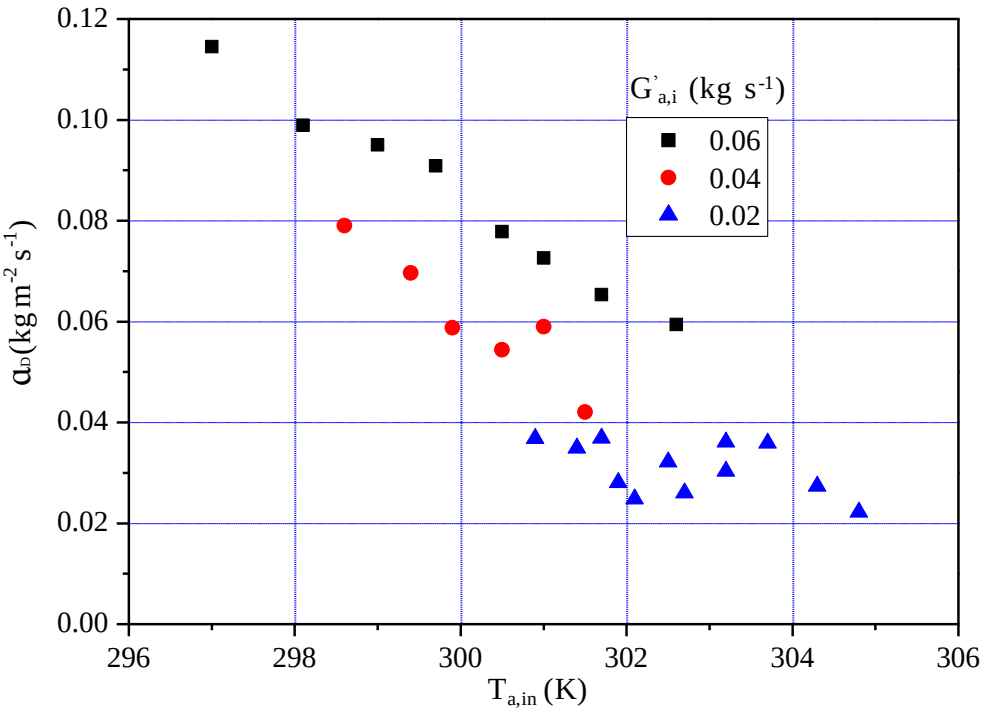

(b) Mass transfer coefficient

G's (kg s^{-1})	Xs	Ts(K)	W (g kg^{-1} dry air)	G'w (kg s^{-1})	Tw (K)
0.045	0.38	293.20	19.00	0.038	293.0

Fig. 6.9 Effect of air flow rate

The results of the mass transfer coefficient are shown in Fig. 6.9 (b). In contrast to the absolute humidity change, the mass transfer coefficient increased with the increase of the air flow rate. The same results had been reported in previous research (Zhang et al. 2010). By analysis, the reason was that when the air flow rate increased, even the change of the absolute humidity reduced, the overall water vapor removal increased. The change of the latter was bigger than the former, which resulted in the gradual increase of the mass transfer coefficient.

6.5.3 Influence of solution inlet parameters

6.5.3.1 Solution flow rate

From Fig. 6.10, the increase of the solution flow rate gave rise to bigger absolute humidity change and mass transfer coefficient. The results seemed to be popular and predictable in the previous research. In most of the previous experiments, the contact area was assumed to be the same, but that has not always been the case. Therefore, it was speculated that the increase of the absolute humidity change and mass transfer coefficient might be due to the increased contact area with the increase of the solution flow rate.

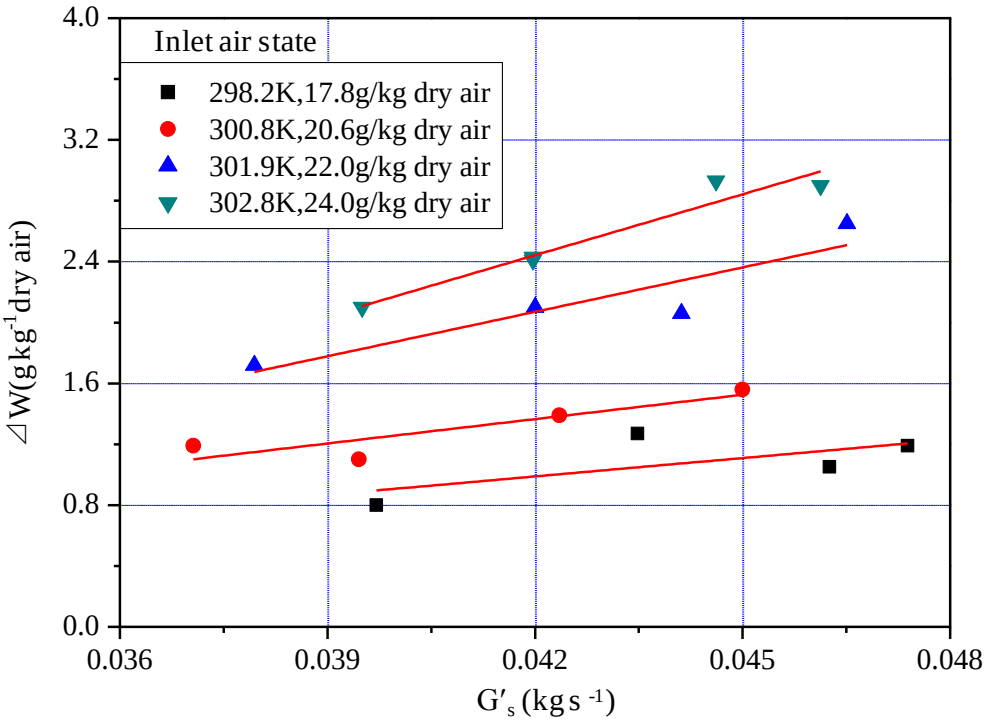

(a) Absolute humidity change

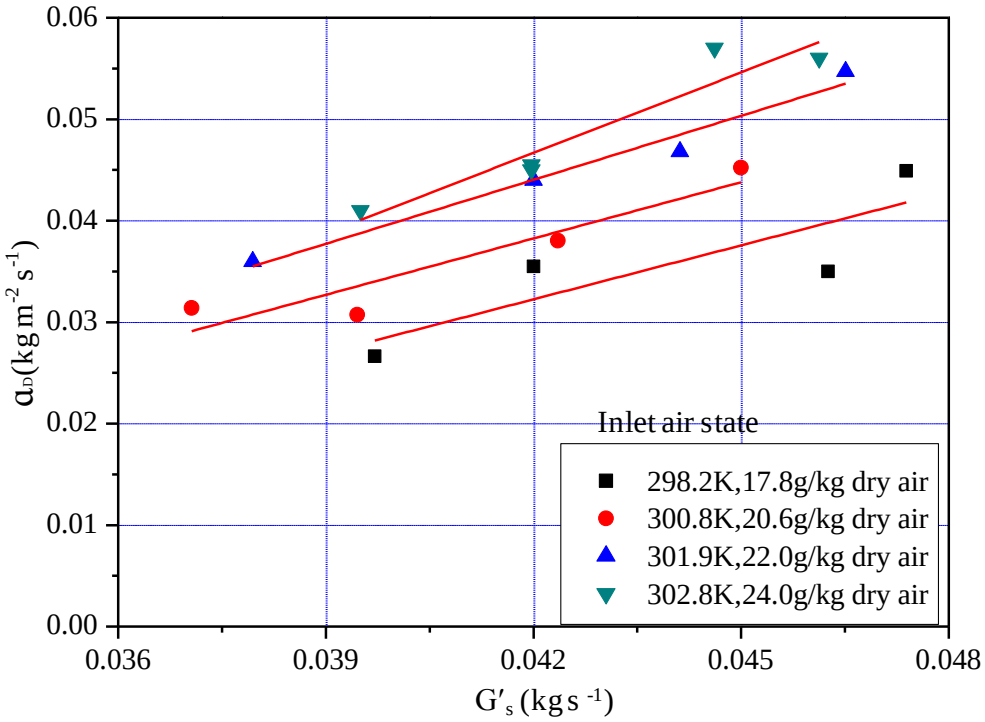

(b) Mass transfer coefficient

G'_a (kg s^{-1})	X_s	T_s(K)	G'_w	T_w (K)
0.06	0.37	297.20	0.038	294.50

Fig. 6.10 The effect of solution mass flow rate

During the present experiment, the mass flow rate of the solution was kept large enough to prevent the film breakout. Therefore, the contact area was almost the same for investigating the effect of the solution flow rate. From the slopes of the above curves, it was found that unlike the previous research, both of the absolute humidity and mass transfer coefficient changed very slowly when the solution flow rate increased. There were two factors which would influence the final results. Due to the fluctuation and disturbance of the liquid, the solution concentration would be higher after absorbing the same amount of water vapor with relatively higher flow rate. On the other hand, for the internally cooled dehumidifier, the higher solution flow rate resulted in thicker film thickness, which would make the removal rate of latent heat slower. The experimental results showed that the outlet solution temperature was about 0.2-0.5 K lower when the solution flow rate was smaller. Thus, the two factors had the opposite effect on the final results. For the present work, the first factor prevailed so the performance was a little better with higher solution flow rate. However, it was predicted that the case would be different if the flow channel was longer, where the solution temperature rise was more serious with higher solution flow rate.

6.5.3.2 Solution temperature

The influence of solution temperature on the performance is presented in Fig. 6.11. Compared with the solution flow rate, the solution temperature had far more of an

effect on the absolute humidity change and mass transfer coefficient. The reason could be explained by Fig. 6.12. It is observed that with a certain concentration, the surface vapor pressure of LiCl solution increases exponentially with the increase of the temperature. It means that the driving force of mass transfer was reduced significantly when the inlet temperature of the solution was increased. In particular, along the flow direction, due to the heat exchange with the high temperature moist air and latent heat of absorption, the effect of the solution temperature rise on the surface vapor pressure would be more serious. Therefore, the higher inlet solution temperature not only reduced the initial capacity of absorption, but also deteriorated the whole dehumidification process.

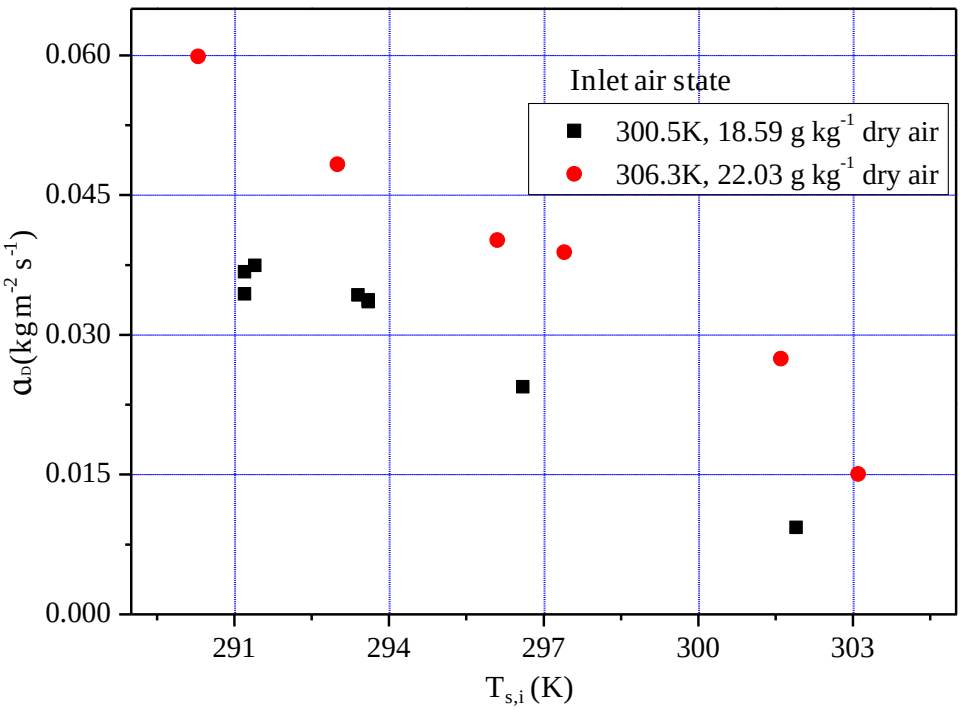

(a) Absolute humidity change

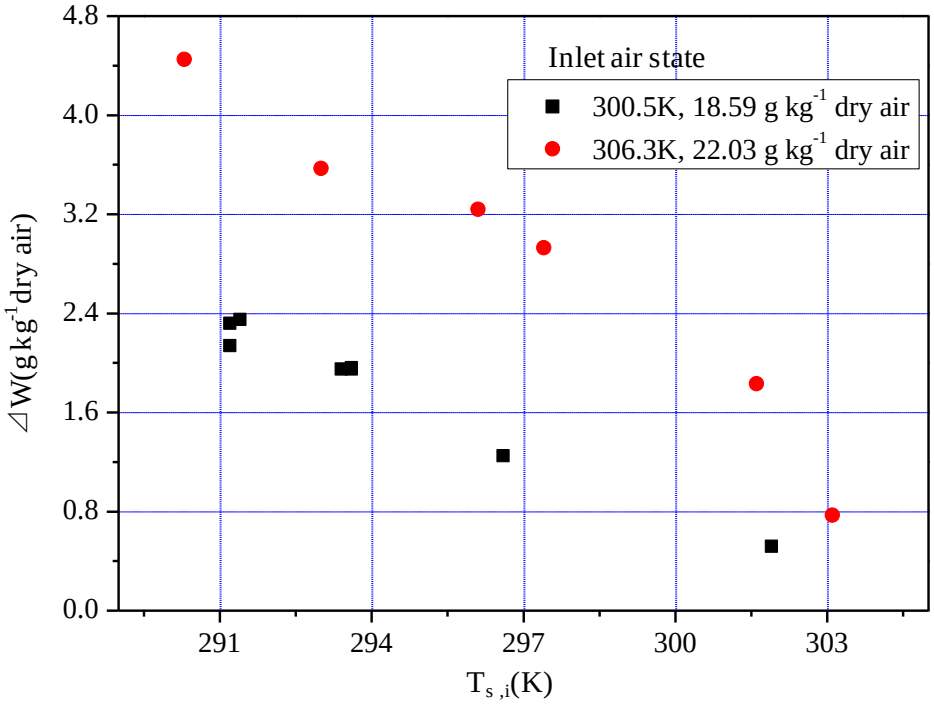

(b) Mass transfer coefficient

G'_a (kg s^{-1})	X_s	G'_s (kg s^{-1})	G'_w	T_w (K)
0.04	0.39	0.03	0.038	294.50

Fig. 6.11 The effect of solution temperature

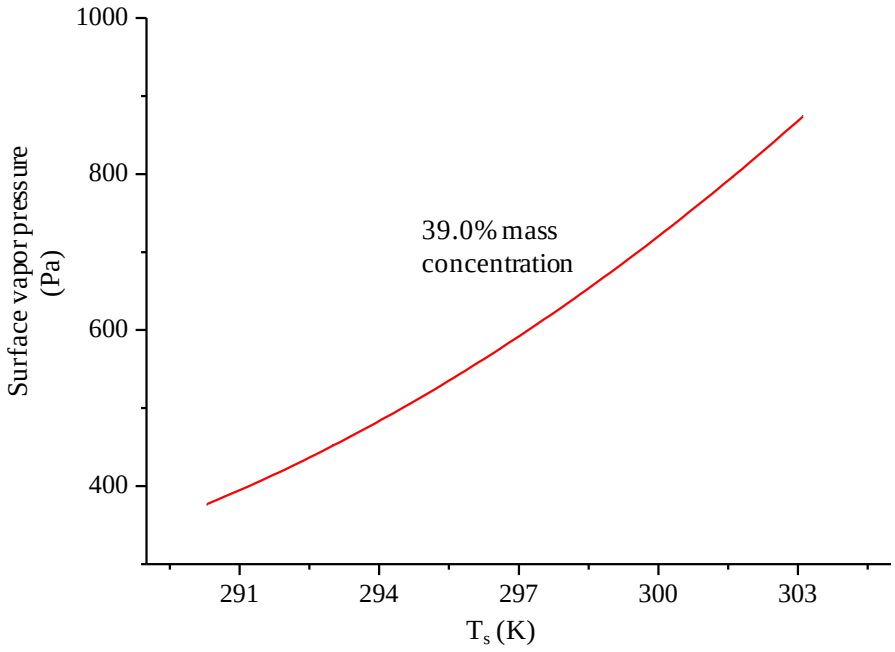

Fig. 6.12 The surface vapor pressure of the solution under different temperature

6.5.3.3 Solution concentration

The absolute humidity change and mass transfer coefficient under different solution concentration were studied in this section. From Fig. 6.13, it was obvious that the increase of the solution concentration would result in bigger water vapor absorption and mass transfer coefficient, as the higher solution concentration represented higher driving force of mass transfer.

The tendency of the curves showed that the influence of the concentration varied in different range. As a result of the limitation of the test rig design, the contact time and area were relatively smaller in the present work. Therefore, when the solution concentration was smaller than 35.0%, the dehumidifying effect was not obvious. Later, the increase of the concentration from 36.0% to 39.0% gave rise to a fast promotion of the performance. However, the further increase made much smaller difference to the result. Even though the higher concentration is beneficial for the water vapor absorption, it is unfavorable for the transportation of the desiccant solution. As shown in Fig. 6.14, the viscosity of the solution shows a parabolic increase with the concentration, which means that it needs much more energy to transport the solution with a higher concentration. During the experiment, it had been found that the maximum flow rate of water was larger than that of the solution with the same pump. Therefore, the balance should be found to optimize the operating conditions.

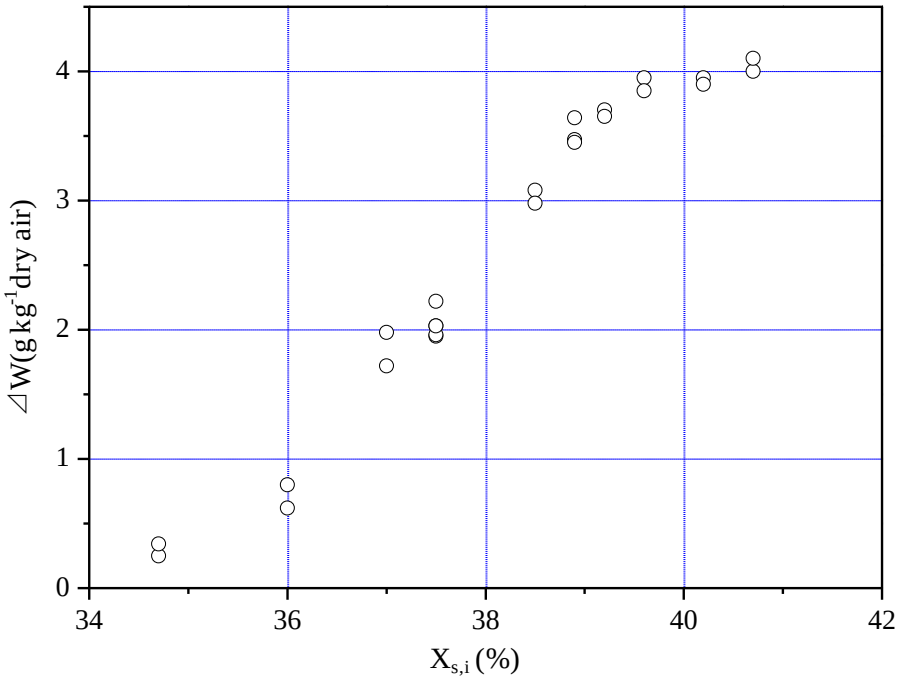

(a) Absolute humidity change

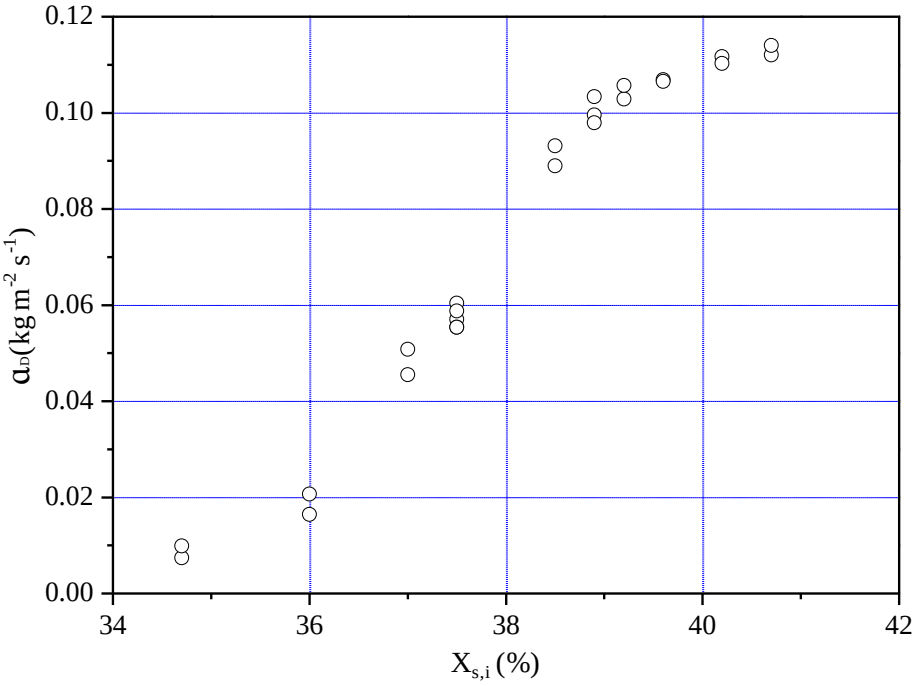

(b) Mass transfer coefficient

T_a(K)	W_a (g kg^{-1} dry air)	G'_a (kg s^{-1})	T_s	G'_s (kg s^{-1})	G'_w	T_w (K)
297.3	18.6	0.06	296.8	0.03	0.038	294.5

Fig. 6.13 The effect of solution concentration

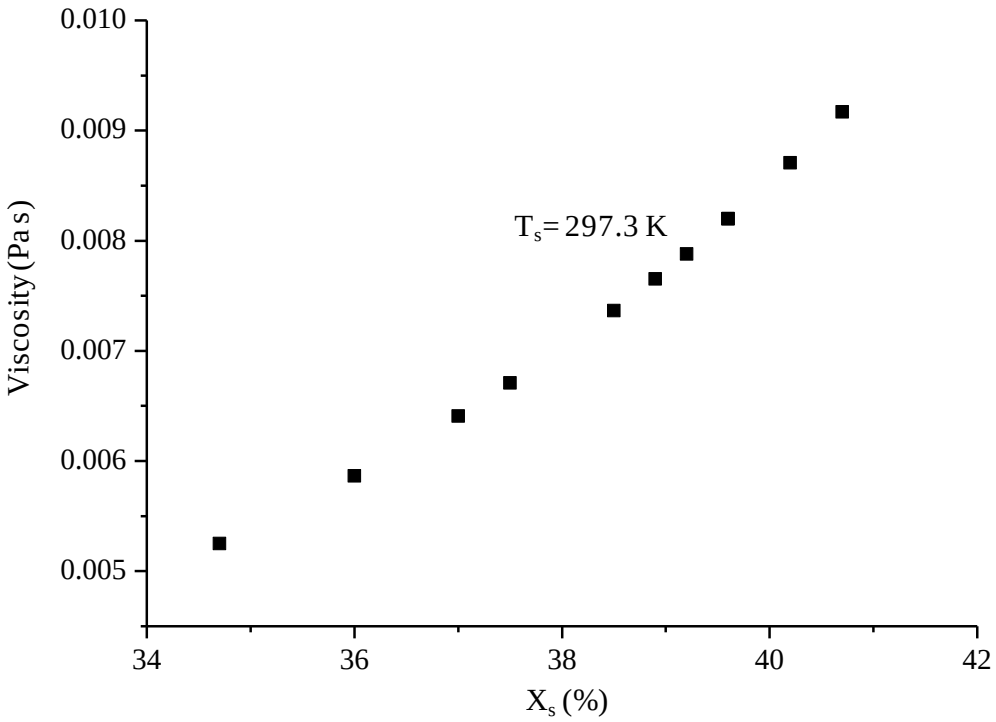

Fig. 6.14 Dynamic viscosity with different mass concentration

6.5.4 Influence of cooling water

In the experiment, it was found that the cooling water flow rate had not distinct effect on the performance of the dehumidifier for the present design. However, its temperature did change the dehumidification results. The high cooling water temperature would deteriorate the performance. With a higher cooling water temperature, the surface vapor pressure was higher, which reduced the mass transfer driving force between the desiccant and the moist air.

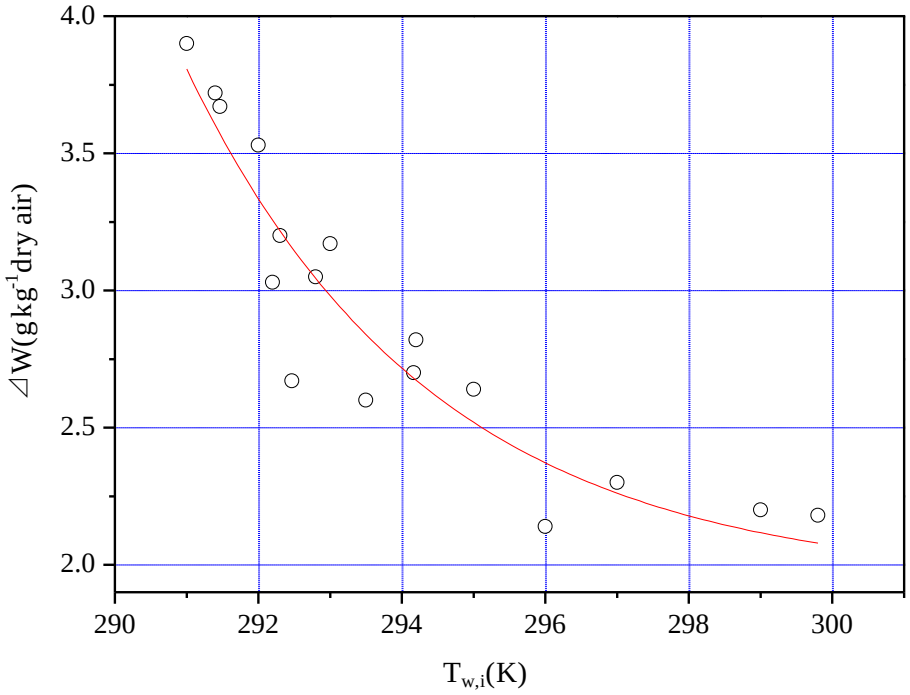

(a) Absolute humidity change

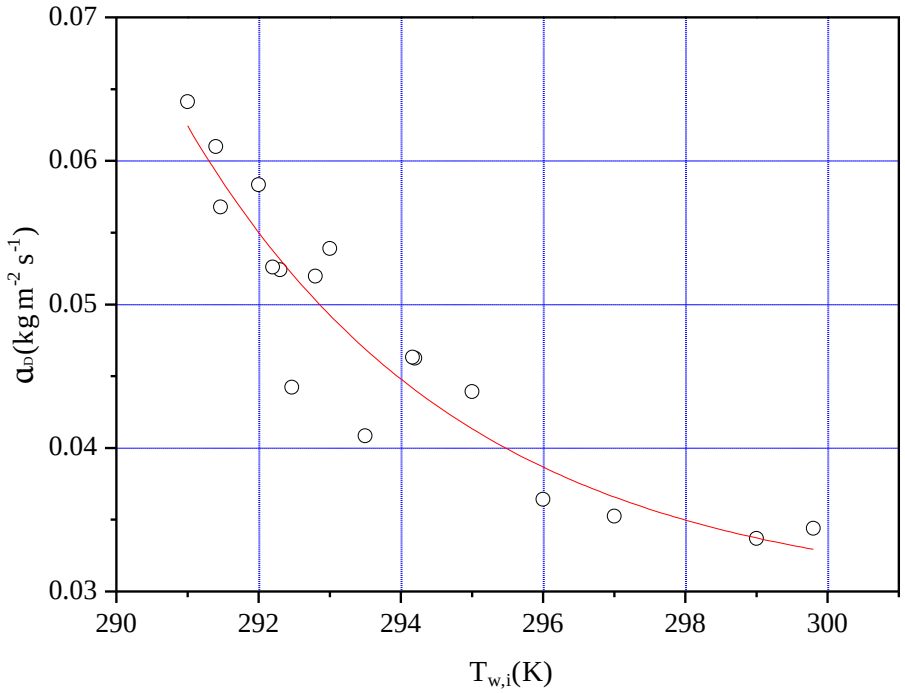

(b) Mass transfer coefficient

T_a(K)	W_a (g kg^{-1} dry air)	G'_a(kg s^{-1})	T_s (K)	X_s (%)	G'_s (kg s^{-1})	G'_w
301.4	21.3	0.04	299.2	39.6	0.03	0.038

Fig. 6.15 The effect of cooling water temperature

Fig. 6.15 showed that the decrease of the cooling water temperature would engender the exponential increase of the absolute water vapor absorption and mass transfer coefficient. Except for the increase of the mass transfer driving force due to the reduction of the solution temperature, it was found that there was some condensation water dissolved out from the moist air at the non-wetted place of the plate, as the temperature of the plate surface was lower than the dew-point temperature of the moist air. Under the influence of the two factors, the above mentioned exponential increase took place. In the hot and humid region, like Hong Kong, the condensation was likely to occur. Therefore, the combination of the liquid desiccant dehumidification and condensation dehumidification would happen simultaneously under this kind of situation. However, in some of the previous studies (Liu et al. 2009; Gao et al. 2013), the condensation had not been taken into consideration. It was also observed when the cooling water temperature reached around 296 K, its effect became weak. The main reason was the relatively short channel, which inhibited the cooling effect of the water. The result would be better with a longer flow channel as expected.

6.6 Summary

In the chapter, a single channel test rig was established for the convenient investigation of the fundamental flow, heat and mass transfer process of the dehumidifier. The absolute humidity change and mass transfer coefficient were

employed to describe the combined flow, heat and mass transfer performance of the internally cooled dehumidifier. Obtained results were summarized as follows,

1) The inlet air humidity has great positive effect on the absolute humidity change and mass transfer coefficient. By comparison, the mass transfer coefficient was about ten times of those in the previous studies. It was attributed to the higher inlet air humidity, set based on the climate condition in Hong Kong. Therefore, it demonstrates the liquid dehumidifier was very suited to the hot and humid areas.

2) It was supervising to find that the increase of the inlet air temperature reduced the performance so greatly. Most of the previous studies simply pointed out that the reason was the different temperature rises of the solution. However, it is discovered that the temperature rise of the inlet and outlet solution in the work is only a little bigger when the inlet air temperature is bigger. By an indepth analysis, the reason was the surface temperature of the liquid film would be higher with higher inlet air temperature. Therefore, the key technology to improve the performance was to reduce the surface temperature of the solution. Two ways can be adopted. One is to enhance the heat transfer in the film by reinforcing the disturbance of the liquid film by increasing the solution flow rate. Another one is to enhance the heat transfer between the film surface and the cooling media by reducing the solution flow rate.

3) Similar to the simulation results, with the increase of the air flow rate, the absolute water vapor absorption would reduce as a result of the reduction of contact time. On the contrary, the mass transfer coefficient increased as the overall water vapor removal increased even greater.

4) Unlike the previous research, both of the absolute humidity and mass transfer coefficient changed very slowly when the solution flow rate increased. The big changes reported in the previous studies might result from the changed wetting area in the complicated dehumidifier.

5) Compared with the solution flow rate, the solution temperature had far more of an effect on the absolute humidity change and mass transfer coefficient. It is observed that with a certain concentration, the surface vapor pressure of LiCl solution increases exponentially with the increase of the temperature. In particular, along the flow direction, due to the heat exchange with the high temperature moist air and latent heat of absorption, the effect of the solution temperature rise on the surface vapor pressure would be more serious. Therefore, the higher inlet solution temperature not only reduced the initial capacity of absorption, but also deteriorated the whole dehumidification process.

6) The tendency of the curves showed that the influence of the concentration varied

in different range. For the present experiment, when the solution concentration was smaller than 35.0%, the dehumidifying effect was not obvious. Later, the increase of the concentration from 36.0% to 39.0% gave rise to a fast promotion of the performance. However, the further increase made much smaller difference to the result. Even though the higher concentration is beneficial for the water vapor absorption, it is unfavorable for the transportation of the desiccant solution.

7) It showed that the decrease of the cooling water temperature would engender the exponential increase of the absolute water vapor absorption and mass transfer coefficient. Except for the increase of the mass transfer driving force due to the reduction of the solution temperature, it was found that there was some condensation water dissolved out from the moist air at the non-wetted place of the plate. However, in some of the previous studies, the condensation had not been taken into consideration.

CHAPTER 7

CONCLUSIONS AND RECOMMENDATIONS FOR FUTURE WORK

This thesis presents the numerical and experimental studies of a simplified liquid desiccant dehumidifier. A new numerical model and experimental approach have been developed to reveal the phenomena of the coupled flow, heat and mass transfer processes in the dehumidifier. The factors influencing the performance were discussed by numerical and experimental methods. A summary of the conclusions is given below.

7.1 Conclusions of numerical study

A new simulation model based on the CFD was developed in this thesis for describing the simultaneous flow, heat and mass transfer processes in a two-dimensional liquid desiccant dehumidifier. The developed model has been verified by comparing its results with those obtained by the finite difference model. Then the model was employed to analyze various influencing factors. In the following, some highlighted results are listed out:

1) It was found that the counter-flow air did change the velocity profile of the LiCl solution along the film thickness due to the drag force. And when the air inlet velocity reached 3.0 m s^{-1}, the impact became very distinct. The air velocity also played a critical role in the performance of the dehumidifier, and it had to be matched with the channel geometric size for optimization.

2) For a certain flow rate, the fluctuation amplitude increased continuously along the liquid flow direction. And the fluctuation amplitude also rose with the increase of the liquid flow rate. In addition, the comparison of the average film thickness between the simulation results and the Nusselt empirical equation showed the function of the drag force exerted by the counter-current air flow.

3) For the corrugated plate, the liquid solution flow rate should be larger for wetting the whole surface of the corrugated sheet of packing. In addition, it was concluded that the corrugated structure could help to stable the liquid flow in the axial direction under the present operating condition.

4) The gradient of water vapor concentration became more and more obvious with the increase of the inlet air water vapor concentration. It was also evident to see the water vapor transportation from the symmetry to the desiccant film. By analysis, it was suggested to tilt the plate to enhance the mass transfer.

5) With higher solution concentration, more obvious surface waves could be generated by more drastic absorption processes, when significant momentums were exchanged at the vapor-liquid interface.

6) It was concluded that the high temperature desiccant worsened the dehumidification performance, not only by reducing the mass transfer driving force but also through decreasing the contact time between the desiccant and air.

7) By looking into the contours of temperature and mass fraction of water vapor under different inlet solution flow rate, it was found that Le>1 for the present simulation. The results showed good agreement with the previous experimental study.

Academically, the numerical study contributed an efficient CFD model for simulating the coupling flow, heat and mass transfer processes in the liquid desiccant dehumidifier. Compared with most of the previous models for the dehumidifier, the new model has several advantages: 1) The changed velocity field was calculated by considering the effects of gravity, viscosity and surface tension, all of which were generally ignored in previous models. 2) The penetration mass transfer theory was used to replace the two film theories, so that it became possible to observe the

dynamic heat and mass transfer process of the dehumidifier. 3) Both of the variable physical properties of the desiccant and air were taken into consideration. 4) The simulation results allowed us to predict the water vapor concentration field, temperature field, gradients of water vapor concentration at different places, local film thickness, and the influence of the mass transfer on the film surface waves. 5) The model was also potential for investigating the internally cooled dehumidifier with different cooling conditions.

7.2 Conclusions of experimental investigation

In terms of experiment, a single channel test rig was well designed for investigating the fundamental flow, heat and mass transfer processes of the dehumidifier. Some experimental results could verify the developed simulation model to some extent.

In chapter 5, the flow behavior was studied in detail. In summary, the main findings are as follows,

1) The film flow experienced three stages along the flow direction: smooth surface flow, two-dimensional deformation and three-dimensional deformation. In addition, the solitary wave appeared in the present work, which played an important role in determining the heat and mass transfer process as the hump

carried most of the liquid substance.

2) The plate surface condition had great impact on the coverage ratio. It needed much higher flow rate to achieve high coverage ratio on the dry plate than on the wet plate. Meanwhile, it was found the coverage ratio increased from 0.1% to 5.1% with the increase of the surface temperature.

3) The minimum wetting rate would decrease with the increase of the solution temperature and increase with the increase of solution concentration. The experimental minimum wetting rate for LiCl solution of 300 K and 30 % mass concentration was about 0.068 kg m^{-1} s^{-1}, which showed a good agreement with the simulation value of 0.071 kg m^{-1} s^{-1} in Chapter 3.

4) The film thickness increased non-linearly with the increase of gas flow rate as a result of the reduction of liquid superficial velocity due to the shear force exerted by the gas flow. The results showed good agreement with the simulation results of the superficial film velocity in Chapter 3.

5) The fluctuation of the lower part was more intense, both in amplitude and frequency of the wave. The increase of the gas velocity would enhance the wave for both of the upper and lower part, and the air would have bigger impact on the

film at the lower part than the upper part.

6) For the lower part of the film, the probability density of film thickness for different solution flow rate with zero air flow rate, and for different air velocity with one solution flow rate were given out.

Then the combined flow, heat and mass transfer performance of the internally cooled dehumidifier were described by the absolute humidity change and mass transfer coefficient. The highlighted results were summarized as follows,

1) The state points of the inlet air were set based on the climate of Hong Kong. Under the hot and humid conditions, the mass transfer coefficient was relatively higher than the results in the previous studies. Therefore, it demonstrated the liquid dehumidifier was very suited to hot and humid areas.

2) Similar to the simulation results, the absolute water vapor absorption would reduce with the increase of the air flow rate as a result of the reduction of contact time. On the contrary, the mass transfer coefficient increased as the overall water vapor removal increased even greater.

3) Unlike the previous research, both of the absolute humidity and mass transfer

coefficient changed very slowly when the solution flow rate increased. It was speculated that the big changes reported might result from the changed wetting area in the complicated dehumidifier.

4) The higher inlet solution temperature not only reduced the initial capacity of absorption, but also deteriorated the whole dehumidification process.

5) The influence of the solution concentration varied in different range. For the present experiment, the increase of the concentration from 36.0% to 39.0% gave rise to a fast promotion of the performance, while the further increase made much smaller difference to the result.

6) The decrease of the cooling water temperature would engender the exponential increase of the absolute water vapor absorption and mass transfer coefficient. There was some condensation water dissolved out from the moist air at the non-wetted place of the plate when the temperature was lower. However, in some of the previous studies, the condensation had not been taken into consideration.

Academically, the contributions of the experimental studies were reflected by the following novel points: 1) The test rig was designed to be easy to observe the heat and mass transfer area, which made the calculation of mass transfer coefficient more

accurate. 2) The experimental operating condition was set on the basis of the meteorological condition in Hong Kong. 3) Compared with the precious studies, the influences of various factors were analyzed more intensively in the present work.

7.3 Comparison of numerical and experimental studies

It is noted that in the project, the dimension sizes of the simulation model and test rig are different. The reason for the mismatch is that the calculation of physical model with bigger size is very time consuming while it is difficult to observe and monitor the phenomena with test bench of small size. Thus, it is a pity that quantitative comparisons have been conducted rather than the qualitative analysis. Even so, the consistency of the experiment and simulation results can still be reflected by the following aspect.

1) Flow morphology

It can be concluded that the film flow experienced a similar process for both of the simulation and experiment. That is, the first stage of the flow showed a flat film, followed by the wave fluctuation. The results demonstrated the instability of film flow on the flat plate.

2) Minimum wetting rate

The minimum wetting rate was investigated with the solution of 300 K and 30% concentration by simulation and experiment. The calculation value of minimum wetting rate $\Gamma_{s,min}$ was 0.071 kg m^{-1} s^{-1} while 0.068 kg m^{-1} s^{-1} for the experiment. The same order of magnitude demonstrated that the simulation model was reliable for predicting the minimum wetting rate to some extent. In addition, the results also indicated that the contact angle was decreased by about 25^{o} by pre-wetting the surface in the present work.

3) Film thickness

Both of simulation and experimental results manifested that the Nusselt empirical formula underestimated the mean film thickness, especially when there was reversed air flow. Also, the simulation results showed that the wave was enhanced along the flow direction, which was also verified by the measured data of the time and location dependent film thickness.

4) Influencing factor

The factors influencing the performance of the dehumidifier were studied in detail. The absolute humidity absorption presented the same change trend for the simulation and experimental results. Especially, the effect of the air velocity embodied the importance of its matching with the size of the dehumidification channel. Also, the simulation results explained fully the better performance of the dehumidifier with the

higher inlet air humidity. In addition, the analysis of the experimental data benefited a lot from the observation of the simulated temperature and humidity distributions in the channel.

To sum up, the simulation and experiment results supported each other.

7.4 Recommendations for future research

It has been verified that the liquid desiccant air conditioning system can be a potential substitute for the traditional vapor compression air conditioning system, especially in the hot and humid area. However, before its wide application, a more comprehensive understand is needed for the coupled flow, heat and mass transfer processes in the interior of the dehumidifier, one of the key components.

Compared with the experimental research, the simulation method is more time and cost savings. Recently, CFD tools have been developing fast for simulating the two-phase absorption process. Due to the time limitation, only the two-dimensional model has been established in the thesis. Thus, a stable three dimensional model is required to be more in line with the reality. Correspondingly, the contact time of the penetration theory is needed to be made certain, which is not easy for the three dimensional model. Also, in the real practice, the inlet conditions will change with the

environment, thus the simulation with time dependent boundary conditions is suggested.

For the experimental study, the range of the experiments is limited to low Re for the film flow. The flow behavior for high Re number is recommended to be conducted and compared with that of the low Re. Due to the limitation of the experiment, the quantitative analysis of the flow on the heat and mass transfer is not realized. Therefore, it is looking forward to improving the test rig to finish it and to compare the results with the simulation results. In addition, to study the energy consumption of the system, further comprehensive measurement can be conducted to discover the pressure drop of both of the air and solution sides.

REFERENCES

Ali A, Vafai K. An investigation of heat and mass transfer between air and desiccant film in an inclined parallel and counter flow channels. International Journal of Heat and Mass Transfer 2004;47:1745-60.

Ali A, Vafai K, Khaled ARA. Analysis of heat and mass transfer between air and falling film in a cross flow configuration. International Journal of Heat and Mass Transfer 2004;47:743-55.

Ali A, Vafai K, Khaled ARA. Comparative study between parallel and counter flow configurations between air and falling film desiccant in the presence of nanoparticle suspensions. International Journal of Energy Research 2003;27:725-45.

Ataki A, Bart H. Experimental and CFD Simulation Study for the Wetting of a Structured Packing Element with Liquids. Chemical Engineering & Technology 2006;29(3):336-47.

Babakhani D. Developing an application analytical solution of adiabatic heat and mass transfer processes in a liquid desiccant dehumidifier/regenerator. Chemical Engineering & Technology 2009;32(12):1875-84.

Babakhani D, Soleymani M. An analytical solution for air dehumidification by liquid desiccant in a packed column. International Communications in Heat and Mass

Transfer 2009;36:969-77.

Babakhani D, Soleymani M. Simplified analysis of heat and mass transfer model in liquid desiccant regeneration process. Journal of the Taiwan Institute of Chemical Engineers 2006;41:1509-16.

Banerjee R. A numerical study of combined heat and mass transfer in an inclined channel using the VOF multiphase model. Numerical Heat Transfer Part A 2007; 52:163-83.

Bansal P, Jain S, Moon C. Performance comparison of an adiabatic and an internally cooled structured packed-bed dehumidifier, Applied Thermal Engineering 2011;31:14-9.

Belt RJ, Van't Westende JMC, Prasser HM, Portela LM. Time and spatially resolved measurements of interfacial waves in vertical annular flow. International Journal of Multiphase Flow 2010;36:570-87.

Benjamin TB. Wave formation in laminar flow down an inclined plane. Journal of Fluid Mechanics 1957;2:554-57.

Benney DJ. Long waves on liquid films. Journal of Mathematical Physics. 1966;45:150-5.

Bird RB, Stewart WE, Lightfoot EN. Transport Phenomena, Wiley, New York, 1960.

Brackbill JU, Kothe PB, Zemach C. A continuum method for modeling surface tension. Journal of Computational Physics 1992;100:335-54.

Braun JE. Methodologies for the design and control of chilled water systems. Ph.D.

Thesis in Mechanical Engineering, University of Wisconsin-Madison, 1988.

Burns JR, Ramshaw C, Jachuck RJ. Measurement of liquid film thickness and the determination of spin-up radius on a rotating disc using an electrical resistance technique. Chemical Engineering Science 2003;58:2245-53.

Carlo LD, Olujic Z, Paglianti A. Comprehensive Mass Transfer Model for Distillation Columns Equipped with Structured Packings. Industrial & Engineering Chemistry Research 2006;45:7967-76.

Chang H. Wave Evolution on a Falling Film. Annual Review of Fluid Mechanics 1994;26:103-36.

Chen XY, Li Z, Jiang Y, Qu KY. Analytical solution of adiabatic heat and mass transfer process in packed-type liquid desiccant equipment and its application. Solar Energy 2006;80:1509-16.

Chu KJ, Dukler AE. Statistical characteristics of thin, wave films Ⅲ. Structure of the large waves and their resistance to gas flow. AIChE Journal 1975;21(3):583-93.

Chung TW, Ghosh TK, Hines AL, Novosel D. Dehumidification of moist air with simultaneous removal of selected indoor pollutants by triethylene glycol solutions in a packed-bed absorber. Separation Science and Technology 1995;30(7):1807-32.

Chung TW, Wu H. Dehumidification of air by aqueous triethylene glycol solution in a spray tower. Separation Science and Technology 1998;33:1213-24.

Chung TW, Wu H. Mass transfer correlation for dehumidification of air in a packed absorber with an inverse U-shaped tunnel, Separation Science and Technology

2000;35(10):1503-15.

Coleman HW, Steele WG. Experimentation, validation, and uncertainty analysis for engineers. Third Edition, A John Wiley & Sons, Inc., 2009.

Colinet P, Legros JC, Velarde MG. Nonlinear dynamics of surface-tension-driven instabilities. Wiley-VCH, New York, 2001:512.

Conde MR. Properties of aqueous solutions of lithium and calcium chlorides: formulations for use in air conditioning equipment design. International Journal of Thermal Sciences 2004;43:367-82.

Coney MWE. The theory and application of conductance probes for the measurement of liquid film thickness in two-phase flow. Journal of Physics E: Scientific Instruments 1973;6: 903-10.

Cui XT, Li XG Li, Sui H, Li H. Computational fluid dynamics simulations of direct contact heat and mass transfer of a multicomponent two-phase film flow in an inclined channel at sub-atmospheric pressure. International Journal of Heat and Mass Transfer 2012;55:5808-18.

Dai YJ, Zhang HF. Numerical simulation and theoretical analysis of heat and mass transfer in a cross flow liquid desiccant air dehumidifier packed with honeycomb paper. Energy Conversion and Management 2004;45:1343-56.

Danckwerts PV. Significance of liquid-film coefficients in gas absorption. Journal of Industrial and Engineering Chemistry 1951;43:1460-67.

Deng SM, Ma WB. Experimental studies on the characteristics of an absorber using

LiBr/H2O solution as working fluid. International Journal of Refrigeration 1999;22:293-301.

Diaz G. Numerical investigation of transient heat and mass transfer in a parallel-flow liquid-desiccant absorber. Heat Mass Transfer 2010;46:1335-44.

E2 Singapore (http://www.e2singapore.gov.sg)

Elsayed MM, Gari HN, Radhwan AM. Effectiveness of heat and mass transfer in packed beds of liquid desiccant system. Renewable Energy 1993;3(6-7):661-68.

Factor HM, Grossman G. A packed bed dehumidifier/regenerator for solar air conditioning with liquid desiccants. Solar Energy 1980;24(6):541-50.

Fluent 6.3 Users Guide, Fluent Inc., 2006.

Frisk DP, Davis EJ. The enhancement of heat transfer by waves in stratified gas–liquid flow. International Journal of Heat and Mass Transfer 1972;15:1537-52.

Fumo N, Goswami DY. Study of an aqueous lithium chloride desiccant system: air dehumidification and desiccant regeneration. Solar energy 2002;62(4):351-61.

Gandhidasan P. A simplified model for air dehumidification with liquid desiccant. Solar Energy 2004;76:409-16.

Gandhidasan P. Reconcentration of aqueous solutions in a packed bed: a simple approach. Transactions of the ASME Journal of Solar Energy Engineering 1990;112:268-72.

Gandhidasan P, Al-Farayedhi AA, and Antar MA. Investigation of heat and mass transfer in a gauze-type structured packing liquid desiccant dehumidifier. International

Journal of Energy Research 2002;26:1035-44.

Gandhidasan P, Kettleborough CF, Ullah MR. Calculation of heat and mass transfer coefficients in a packed tower operating with a desiccant-air contact system. Journal of Solar Energy Engineering 1986;108:123-28.

Gandhidasan P, Ullah MR, Kettleborough CF. Analysis of heat and mass transfer between a desiccant-air system in a packed tower. Journal of Solar Energy Engineering 1987;109:89-93.

Goren SL, Mani PVS. Mass transfer through horizontal liquid films in wavy motion, AIChE Journal 1968;14:57-61.

Grossman G. Simultaneous heat and mass transfer in film absorption under laminar flow. International Journal of Heat and Mass Transfer 1983;26(3):357-71.

Grossman G. Simultaneous heat and mass transfer in absorption of gases in turbulent liquid films. International Journal of Heat and Mass Transfer 1984;27(12):2365-76.

Gu F, Liu CJ, Yuan XG, Yu GC. CFD simulation of liquid flow on inclined plates. Chemical Engineering & Technology 2004;27(10):1099-104.

Haelssig JB, Tremblay AY, Thibault J, Etemad SG. Direct numerical simulation of interphase heat and mass transfer in multicomponent vapour-liquid flows. International Journal of Heat and Mass Transfer 2010;53:3947-60.

Haghshenas Fard M, Zivdar M, Rahimi R, Nasr Esfahany M, Afacan A, Nandakumar K, Chuang KT. CFD simulation of mass transfer efficiency and pressure drop in a structured packed distillation column. Chemical Engineering & Technology

2007;30(7):854-61.

Han Y, Shikazono N. Thickness of liquid film formed in slug flow in micro tube. ECI International Conference on Heat Transfer and Fluid Flow in Microscale Whistler, September 21-26, 2008.

Haroun Y, Raynal L, Legender D. Mass transfer and liquid hold-up determination in structured packing by CFD. Chemical Engineering Science 2012;(75):342-48.

Hartley DE, Murgatroyd W. Criteria for the break-up of thin liquid layers flowing isothermally over solid surfaces. International Journal of Heat and Mass Transfer 1964;7:1003-15.

Hazuku T, Takamasa T, Mastumoto Y. Experimental study on axial development of liquid film in vertical upward annular two-phase flow. International Journal of Multiphase Flow 2008;34:111-27.

Higbie R. The rate of absorption of a pure gas into a still liquid during short period of exposure. Transaction of AlChe Journal 1935;31:365-88.

Hirt CW, Nichols BD. Volume of Fluid (VOF) Method for the dynamics of free boundaries. Journal of Computational Physics 1981;39:201-25.

Hoffmann A, Ausner I, Repke J, Wozny G. Fluid dynamics in multiphase distillation processes in packed towers. Computers and Chemical Engineering 2005;29:1433-37.

Hong Kong Energy End-use Data 2013, Electrical & Mechanical Services Department, Hong Kong.

Hopf L. Turbulenz bei einem slusse. Annals of Physics 1910;32:777.

Hotta T, Inoue T, Matsuda M, Ueda M. Measurement of oil film between swash plate and shoe for swash plate type compressor. International Compressor Engineering Conference at Purdue, July 12-15, 2004.

http://www.beeo.emsd.gov.hk/en/mibec_beeo.html.

Hueffed AK, Chamra LM, Mago PJ. A simplified model of heat and mass transfer between air and falling-film desiccant in a parallel-plate dehumidifier. Journal of Heat Transfer 2009;131(5): 052001-1-052001-7.

Jaber H, Webb RL. Design of cooling towers by the effectiveness-NTU method. Journal of Heat Transfer 1989;111:837-43.

Jain S, Dhar PL, Kaushik SC. Experimental studies on the dehumidifier and regenerator of a liquid desiccant cooling system. Applied Thermal Engineering 2000;20:253-67.

Jayanti S, Hewitt GF. Hydrodynamics and heat transfer of wavy thin film flow. International Journal of Heat and Mass transfer 1997;40(1):179-90.

China Energy Statistical Yearbook, Compiled by Department of Energy Statistics, National Bureau of Statistics, People's Republic of China, 2013.

Jiang Y, Li Z. Dehumidification air conditioning method and systems. 2002. (In Chinese)

Kafka FY, Dussan VEB. On the interpretation of dynamic contact angles in capillaries. Journal of Fluid Mechanics 1979;95:539-65.

Kalliadasis S, Ruyer-Quil C, Scheid B, Velarde MG. Falling Liquid Films. Applied

Mathematical Sciences. 2012;176.

Kapitza PL. Wave flow of thin viscous liquid films. Zhur. Experi. Teor. Fiz. 1948;18:3.

Khan AY, Ball HD. Development of a generalized model for performance evaluation of packed-type liquid sorbent dehumidifiers and regenerators. ASHRAE Transactions 1992;98:525-33.

Khan AY, Martinez JL. Modelling and parametric analysis of heat and mass transfer performance of a hybrid liquid desiccant absorber. Energy Conversion and Management 1998;39(10):1095-112.

Khan AY, Sulsona FL. Modelling and parametric analysis of heat and mass transfer performance of refrigerant cooling liquid desiccant absorbers. International Journal of Energy Research 1998;22(9):831-32.

Khosravi Nikou MR, Ehsani MR. Turbulence models application on CFD simulation of hydrodynamics, heat and mass transfer in a structured packing. International Communications in Heat and Mass Transfer 2008;35:1211-9.

Kim KJ, Ameel TA, Wood BD. Performance evaluation of LiCl and LiBr for absorber design applications in the open-cycle absorption refrigeration system. Transactions of the ASME Journal of Solar Energy Engineering 1997;119:165-73.

Klausner JF, Zeng LZ, Bernhard DM. Development of a film thickness probe using capacitance for asymmetrical twophase flow with heat addition. Review of Scientific Instruments 1992;63(5):3147-52.

Koronaki IP, Christodoulaki RI, Papaefthimiou VD, Rogdakis ED. Thermodynamic

analysis of a counter flow adiabatic dehumidifier with different liquid desiccant materials. Applied Thermal Engineering 2013;50:361-73.

Islam MR, Wijeysundera NE, Ho JC. Performance study of a falling-film absorber with a film-inverting configuration. International Journal of Refrigeration 2003;26:909-17.

Lazzarin RM, Gasparella A, Longo GA. Chemical dehumidification by liquid desiccants: theory and Experiment. International Journal of Refrigeration 1999;22:334–47.

Legislating Green Buildings in Singapore (http://www.futurarc.com)

Liu XH, Chang XM, Xia JJ, Jiang Y. Performance analysis on the internally cooled dehumidifier using liquid desiccant. Building and Environment 2009;44:299-308.

Liu J, Gollub JP. Solitary Wave Dynamics of Film Flows. Physics of Fluids 1994;6(5): 1702-12.

Liu XH, Jiang Y, Qu KY. Analytical solution of combined heat and mass transfer performance in a cross-flow packed bed liquid desiccant air dehumidifier. International Journal of Heat and Mass Transfer 2008;51:4563-72.

Liu XH, Jiang Y, Qu KY. Heat and mass transfer model of cross flow liquid desiccant air dehumidifier/regenerator. Energy Conversion and Management 2007;48:546-54.

Liu S, Li J, Chen Q. Visualization of low pattern in thermosyphon by ECT. Flow Measurement and Instrumentation 2007;18:216-22.

Liu XH, Qu KY, Jiang Y. Empirical correlations to predict the performance of the

dehumidifier using liquid desiccant in heat and mass transfer. Renewable Energy 2006;31:1627-39.

Liu GB, Yu KT, Yuan XG, Liu CJ, Guo QC. Simulations of chemical absorption in pilot-scale and industrial-scale packed columns by computational mass transfer, Chemical Engineering Science 2006;61:6511-29.

Liu XH, Zhang Y, Qu KY, Jiang Y. Experimental study on mass transfer performances of cross flow dehumidifier using liquid desiccant. Energy Conversion and Management 2006;47:2682-92.

Longo GA, Gasparella A. Experimental and theoretical analysis of heat and mass transfer in a packed column dehumidifier/regenerator with liquid desiccant. International Journal of Heat and Mass Transfer 2005;48:5240-54.

Lowenstein AI, Gabruk RS. The effect of absorber design on the performance of a liquid-desiccant air conditioner. ASHRAE transaction 1992:712-770.

Luo YM, Shao SQ, Xu HB, Tian CQ. Dehumidification performance of [EMIM]BF_4. Applied Thermal Engineering 2011;31(14-15):2772-77.

Luo YM, Shao SQ, Qin F, Tian CQ, Yang HX. Investigation of feasibility of ionic liquids used in solar liquid desiccant air conditioning system. Solar Energy 2012;86:2718-24.

Luo YM, Yang HX, Lu L. Liquid desiccant dehumidifier: development of a new performance predication model based on CFD. International Journal of Heat and Mass Transfer 2014;69:408-16.

Luo YM, Yang HX, Lu L, Qi RH. A review of the mathematical models for predicting the heat and mass transfer process in the liquid desiccant dehumidifier Renewable and Sustainable Energy Reviews 2014;31:587-99.

Mesquita LCS., Harrison SJ, Thomey D. Modeling of heat and mass transfer in parallel plate liquid-desiccant dehumidifiers. Solar Energy 2006;80:1475-82.

Min JK, Park S. Numerical study for laminar wavy motions of liquid film flow on vertical wall. International Journal of Heat and Mass Transfer 2011;54:3256-66.

Morison KR, Tandon G. Minimum wetting rates for falling films on stainless steel. Developments in Chemical Engineering and Mineral Processing 2006;14(1-2):153-62.

Nagasaki T, Akiyama H, Nakagawa H. Numerical analysis of flow and mass transfer in a falling liquid film with interfacial waves. Thermal Science and Engineering 2002;10(1):17-24.

Nernst W. Theory of reaction velocity in heterogenous systems. International journal of research in physical chemistry and chemical physics 1904;47:52-5.

Niu RP. Modeling and numerical simulation of dehumidifier using LiCl solution as the liquid desiccant. International conference on electrical engineering and automatic control 2010, Shandong.

Nusselt W. Der Warmeubergang im Kreuzstrom. Zeitschrift des Vereines Deutscher Ingenieure 1911;55:2021-24.

Nusselt W. Die oberflachenkondensation des wasserdampfes. VDI Zeitschrift

1916;60:569-78.

Nusselt W. Eine neue Formel fur den Warmedurchgang im Kreuzstrom. Technische Meahanik und Thermodynamik 1930;1:417-22.

Oberg V, Goswami DY. Experimental study of the heat and mass transfer in a packed bed liquid desiccant air dehumidifier. Journal of Solar Energy Engineering 1998;120(4):289-97.

Oberg V, Goswami DY. Advances in solar energy: an annual review of research and development. American Solar Energy Society Inc. 1998;12:431-70.

Onda K, Takeuchi H, Okumoto Y. Mass transfer coefficients between gas and liquid phases in packed columns. Journal of Chemical Engineering of Japan 1968;1:56-62.

Park MS, Howell JR, Vliet GC, Peterson J. Numerical and experimental results for coupled heat and mass transfer between a desiccant film and air in cross-flow. International Journal of heat & mass transfer 1994;37(Suppl.):395-402.

Park JY, Jeong JW. A Simplified Model for Predicting Dehumidification Effectiveness of a Liquid Desiccant System. AEI 2013:516-23.

Park CD, Nosoko T. Three-dimensional wave dynamics on a falling film and associated mass transfer. AIChe Journal 2003;79(11):2715-27.

Patnaik V, Perez-Blanco H. Roll waves in falling films: an approximate treatment of the velocity field. International Journal of Heat and Fluid Flow 1996;17(1):63-70.

Peng SW, Pan ZM. Heat and mass transfer in liquid desiccant air-conditioning process at low flow conditions. Commun Nonlinear Sci Numer Simulat 2009;14:3599-607.

Pierson FW, Whitaker S. Some theoretical and experimental observations of the wave structure of falling liquid films. Industrial & Engineering Chemistry Fundamentals 1977;16(4):401-8.

Potnis SV, Lenz TG. Dimensionless Mass-Transfer Correlations for Packed-Bed Liquid Desiccant Contactors. Industrial & Engineering Chemistry Research 1996;35 (11): 4185-93.

Qi RH, Lu L, Yang HX, Luo YM. Investigation on contact angle of LiCl for liquid desiccant air-conditioning system. The 5th International Conference on Applied Energy, July 1-4, 2013.

Ramaswamy B, Chippada S, Joo SW. A Full-Scale Numerical Study of Interfacial Instabilities in Thin-Film Flows. Journal of Fluid Mechanics 1996;325:163-94.

Ren CQ. Corrections to the simple effectiveness-NTU method for counterflow cooling towers and packed bed liquid desiccant–air contact systems. International Journal of Heat and Mass Transfer 2008;51:237-45.

Ren CQ, Jiang Y, Zhang YP. Simplified analysis of coupled heat and mass transfer processes in packed bed liquid desiccant-air contact system. Solar Energy 2006;80(1):121-31.

Ren CQ, Tu M, Wang HH. An analytical model for heat and mass transfer processes in internally cooled or heated liquid desiccant-air contact units. International Journal of Heat and Mass Transfer 2007;50:3545-55.

Sadasivam M, Balakrishnan AR. Effectiveness-NTU method for design of packed bed liquid desiccant dehumidifiers. Chemical Engineering Research & Design 1992;70:572-77.

Saman WY, Alizadeh S. An experimental study of a cross-flow type plate heat exchanger for dehumidification/cooling. Solar Energy 2002;73(1):59-71.

Saman WY, Alizadeh S. Modelling and performance analysis of a cross-flow type plate heat exchanger for dehumidification/cooling. Solar Energy 2001;70(4):361-72.

Shojaee S, Hosseini SH, Rafati A, Ahmadi G. Prediction of the effective area in structured packings by computational fluid dynamics. Industrial & Engineering Chemistry Research 2011;50:10833-42.

Sideman S, Moalem-Maron D. Direct contact condensation, Advances in Heat Transfer. 1982;15:227-81.

Steinbrenner JE, Hidrovo CH, Wang FM, Vigneron S, Lee Es, Kramer TA, Cheng CH, Eaton JK, Goodson KE. Measurement and modeling of liquid film thickness evolution in stratified two-phase microchannel flows. Heat SET 2005 Heat Transfer in Components and Systems for Sustainable Energy Technologies, April 5-7, 2005.

Stevens DI, Braun JE, Klein SA. An effectiveness model of liquid-desiccant system heat/mass exchangers. Solar Energy 1989;42(6):449-55.

Stockfleth R, Brunner G. Film thickness, flow regimes, and flooding in countercurrent annular flow of a falling film at high rressures. Industrial & Engineering Chemistry Research 2001;40:6014-20.

Sun FD. Numerical simulation on liquid flow characteristics of the wavy plate. Modern Chemical Industry 2012;32(1):90-3.

Szulczewska B, Zbicinski I, Gorak A. Liquid flow on structured packing: CFD simulation and experimental study. Chemical Engineering and Technology 2003;26(5):580-4.

Takaki CR. Non-linear stability of liquid flow down an inclined plane. Journal of the Physical Society of Japan. 1967;23(3):638-45.

Takamasaa T, Hazuku T. Measuring interfacial waves on film flowing down a vertical plate wall in the entry region using laser focus displacement meters. International Journal of Heat and Mass Transfer 2000;43:2807-19.

Takamasaa T, Hazuku T. Measuring interfacial waves on film flowing down tube inner wall using laser focus displacement meter. International Journal of Multiphase Flow 2000;26:1493-507.

Thwaites GR, Kulov NN, Nedderman RM. Liquid film properties in two-phase annular flow. Chemical Engineering Science 1976;(31):481-86.

Valluri P, Matar OK, Hewitt GF, Mendes MA. Thin film flow over structured packings at moderate Reynolds numbers. Chemical Engineering Science 2005;60:1965-75.

Wang XL, Cai WJ, Lu JG, Sun YX, Ding XD. A hybrid dehumidifier model for real-time performance monitoring, control and optimization in liquid desiccant dehumidification system. Applied Energy 2013;111:449-55.

Westerterp KR, Wijingaarden RJ. Principles of chemical reaction engineering.

Ullmann's Encyclopedia of Industrial Chemistry, 2000.

Whitman W. The two-film theory of gas absorption. Chemical Metallic Engineering 1923;29(4):146-8.

Woods J, Kozubal E. A desiccant-enhanced evaporative air conditioner: Numerical model and experiments. Energy Conversion and Management 2012;65:208-20.

Xie XY, Jiang Y, Tang YD, Yi XQ, Liu SQ. Simulation and experimental analysis of a fresh air-handling unit with liquid desiccant sensible and latent heat recovery. Building Simulation 2008;1:53-63.

Xiong ZQ, Dai YJ, Wang RZ. Development of a novel two-stage liquid desiccant dehumidification system assisted by CaCl2 solution using exergy analysis method, Applied Energy 2010;87:1495-504.

Yin YG, Zhang XS, Peng DG, Li XW. Model validation and case study on internally cooled/heated dehumidifier/regenerator of liquid desiccant systems. International Journal of Thermal Sciences 2009;48:1664-71.

Yin YG, Zhang XS, Wang G, Luo L. Experimental study on a new internally cooled/heated dehumidifier/regenerator of liquid desiccant systems. International Journal of Refrigeration 2008;31:857-66.

Yih CS. Stability of liquid flow down an inclined plane. Physics of Fluids 1963;6(3):321-34.

Youngs DL. Time-dependent multi-material flow with large fluid distortion. Numerical Methods for Fluid Dynamics 1982;24:273-85.

Yu YQ, Wei SJ, Yang YH, Cheng X. Experimental study of water film falling and spreading on a large vertical plate. Progress in Nuclear Energy 2012;54:22-8.

Zhang L, Hihara E, Massuoka F, Dang CB. Experimental analysis of mass transfer in adiabatic structured packing dehumidifier/regenerator with liquid desiccant. International Journal of Heat and Mass Transfer 2010;53:2856-63.

Zhang T, Liu XH, Jiang JJ, Chang XM, Jiang Y. Experimental analysis of an internally-cooled liquid desiccant dehumidifier. Building and Environment 2013;60:1-10.

Zhang F, Peng J, Geng J, Wang ZX. Thermal imaging study on the surface wave of heated falling liquid films. Experimental Thermal and Fluid Science 2009;33:424-30.

Zurigat YH, Abu-Arabi MK, Abdul-Wahab SA, Air dehumidification by triethylene glycol desiccant in a packed column. Energy Conversion and Management 2004;45:141-55.